


1993

## A study of molecular order and motion in nematic liquid crystal mixtures

Jon Michael Goetz  
*College of William & Mary - Arts & Sciences*

Follow this and additional works at: <https://scholarworks.wm.edu/etd>

 Part of the [Atomic, Molecular and Optical Physics Commons](#), [Condensed Matter Physics Commons](#), and the [Polymer Chemistry Commons](#)

---

### Recommended Citation

Goetz, Jon Michael, "A study of molecular order and motion in nematic liquid crystal mixtures" (1993). *Dissertations, Theses, and Masters Projects*. William & Mary. Paper 1539623842. <https://dx.doi.org/doi:10.21220/s2-280v-pv92>

This Dissertation is brought to you for free and open access by the Theses, Dissertations, & Master Projects at W&M ScholarWorks. It has been accepted for inclusion in Dissertations, Theses, and Masters Projects by an authorized administrator of W&M ScholarWorks. For more information, please contact [scholarworks@wm.edu](mailto:scholarworks@wm.edu).

## **INFORMATION TO USERS**

**This manuscript has been reproduced from the microfilm master. UMI films the text directly from the original or copy submitted. Thus, some thesis and dissertation copies are in typewriter face, while others may be from any type of computer printer.**

**The quality of this reproduction is dependent upon the quality of the copy submitted. Broken or indistinct print, colored or poor quality illustrations and photographs, print bleedthrough, substandard margins, and improper alignment can adversely affect reproduction.**

**In the unlikely event that the author did not send UMI a complete manuscript and there are missing pages, these will be noted. Also, if unauthorized copyright material had to be removed, a note will indicate the deletion.**

**Oversize materials (e.g., maps, drawings, charts) are reproduced by sectioning the original, beginning at the upper left-hand corner and continuing from left to right in equal sections with small overlaps. Each original is also photographed in one exposure and is included in reduced form at the back of the book.**

**Photographs included in the original manuscript have been reproduced xerographically in this copy. Higher quality 6" x 9" black and white photographic prints are available for any photographs or illustrations appearing in this copy for an additional charge. Contact UMI directly to order.**

# **U·M·I**

University Microfilms International  
A Bell & Howell Information Company  
300 North Zeeb Road, Ann Arbor, MI 48106-1346 USA  
313/761-4700 800/521-0600



**Order Number 9429674**

**A study of molecular order and motion in nematic liquid crystal mixtures**

**Goetz, Jon Michael, Ph.D.**

**The College of William and Mary in Virginia, 1993**

**U·M·I**  
300 N. Zeeb Rd.  
Ann Arbor, MI 48106



A STUDY OF MOLECULAR ORDER AND MOTION  
IN NEMATIC LIQUID CRYSTAL MIXTURES

---

A Dissertation

Presented to

The Faculty of the Department of Physics  
The College of William and Mary in Virginia

In Partial Fulfillment

Of the Requirements for the Degree of  
Doctor of Philosophy

---

by

Jon Michael Goetz

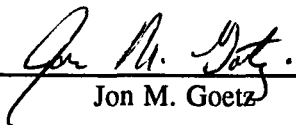
1993

---

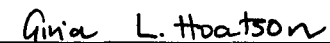
APPROVAL SHEET

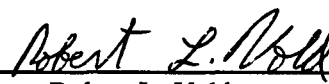
This dissertation is submitted in partial fulfillment of  
the requirements for the degree of


Doctor of Philosophy


  
Jon M. Goetz

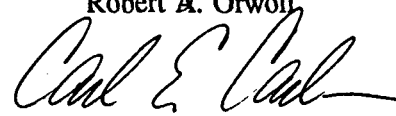
Approved, August 1993

  
Gina L. Hoatson

  
Robert L. Vold

  
Harlan E. Schone

  
Robert A. Orwoll

  
Carl E. Carlson

## TABLE OF CONTENTS

Preliminaries	
Acknowledgements .....	v
List of Tables .....	vi
List of Figures .....	vii
Abstract .....	ix
1. Introduction .....	2
1.1 Structure .....	2
1.2 Orientational Order .....	5
1.3 Molecular Theories .....	8
1.4 Measurement of Orientational Order .....	12
1.5 Measurement of Molecular Motion .....	14
1.6 Magnetic Resonance Spectroscopy .....	15
1.7 A Study of Molecular Order and Motion in Liquid Crystal Mixtures .....	18
2. Orientational Order in a Binary Liquid Crystal Mixture .....	22
2.1 The Quadrupolar Hamiltonian .....	22
2.2 Spin Dynamics .....	26
2.3 The Quadrupolar Echo Pulse Sequence .....	29
2.4 $^2\text{H}$ -NMR Spectra of Nematic Molecules in Liquid Crystal Phases .....	32
2.5 Sample Preparation and Experimental Setup .....	42
2.6 $^2\text{H}$ -NMR Experimental Results .....	44
2.7 A Mean Field Theory of Binary Mixtures .....	54
2.8 Interpretation of Fits to the Mean Field Theory .....	57
3. Phase Diagrams of Binary Mixture .....	65
3.1 Symmetry of the Nematic Phase .....	65
3.2 Cartesian Order Tensors .....	67
3.3 The Ordering Potentials .....	69
3.4 A Geometric Mean Assumption .....	70
3.5 Statistical Mechanics of Binary Mixtures .....	72
3.6 Temperature Dependence of Orientational Order in a Single Component System .....	76
3.7 Temperature-Concentration Phase Diagrams of Binary Mixtures .....	89
3.8 Conclusions .....	92



4. Molecular Motions of Nematic Liquid Crystals . . . . .	102
4.1 Pulse Sequences . . . . .	103
4.2 Relaxation Theory . . . . .	108
4.3 Relaxation Rates and Spectral Densities . . . . .	118
4.4 Models of Molecular Reorientation . . . . .	119
4.5 Experimental Determination of Rotational Dynamics . . . . .	129
4.6 Reorientational Dynamics in a Liquid Crystal Mixture . . . . .	154
5. Appendix . . . . .	175
6. References . . . . .	180
Vitae . . . . .	191

## ACKNOWLEDGEMENTS

I would like to thank my advisor, Dr. Gina Hoatson, for her hard work, dedication, understanding and guidance throughout the years. If I have acquired any of her organization skills, tenaciousness, physical insights, scientific writing skills or sense of humor, my time as her graduate student has been well spent. The amount of care and effort she has put forth to make my graduate career productive and successful is well appreciated. I would also like to thank Dr. Bob Vold for his helpful suggestions and physical insights; it has been a real treat to be able to work in the same lab with such an eminent researcher. I also need to thank the other students in the Hoatson group for all their input and help: Tak Tse, April Baugher, Marco Brown, Kim Bell, Sam Varner and Brian Peko. I feel lucky that I had the pleasure to work with you.

Of course, physics is not all there is to happiness. I also would like to thank the people who made my years in Williamsburg some of the happiest of my life. First, to all the members of the Physics volleyball, football, softball, walleyball and hard fighting basketball teams: thanks. Man, those were good times. I also would like to thank Jenny Poor for being an ever supporting friend; Pam Dawson for helping me be the best person I can; Allan Greer for being a great roommate and solid friend; and April Baugher for her humor, friendship, and fun in these last months and for all the help getting the thesis to the committee on time.

Finally, I would like to thank my parents for their support and encouragement. This difficult achievement would not have been possible without the strong home foundation which they constructed for me.

## LIST OF TABLES

<u>Table</u>	<u>page</u>
2.1 Location of the EFG tensor in fluorene . . . . .	39
2.2 Experimental quadrupolar splittings . . . . .	46
2.3 Order Parameters for FLOC and p-Xy . . . . .	47
2.4 Theoretical asymmetry parameter contributions . . . . .	52,53
4.1 Spin operators $A_{2M}$ . . . . .	116
4.2 Spectral densities . . . . .	116
4.3 Redfield relaxation matrix elements . . . . .	117
4.4 Quadrupolar splittings of pure FLOC . . . . .	132
4.5 Relaxation rates for pure FLOC . . . . .	135
4.6 Relaxation rates for pure FLOC . . . . .	136
4.7 Fits to the third rate model . . . . .	150
4.8 Quadrupolar splittings of FLOC and p-Xy in mixture . . . . .	155
4.9 Relaxation rates for FLOC and p-Xy in mixture . . . . .	159
4.10 Relaxation rates for FLOC and p-Xy in mixture . . . . .	160
4.11 Fits to the third rate model for FLOC in mixture . . . . .	169
4.12 Fits to the third rate model for p-Xy in mixture . . . . .	170

## LIST OF FIGURES

<u>Figure</u>	<u>page</u>
1.1 The Nematic Phase . . . . .	4
1.2 Euler Angles . . . . .	7
1.3 Components of the binary mixture . . . . .	9
2.1 Energy level diagram . . . . .	25
2.2 Quadrupolar echo pulse sequence . . . . .	31
2.3 Site assignments for FLOC and p-Xy . . . . .	37,38
2.4 Block diagram of a spectrometer . . . . .	43
2.5 Order parameters of FLOC and p-Xy . . . . .	48,49
2.6 Fits to mean field theory . . . . .	59-61
3.1 Orientational order parameters of a biaxial nematic liquid crystal . . . . .	77-81
3.2 Orientational distribution of a rod-like nematogen . . . . .	77-81
3.3 Orientational distribution of a plate-like nematogen . . . . .	83-85
3.4 Phase diagram of a mixture of rod-like liquid crystals . . . . .	91
3.5 Phase diagram of a mixture of plate-like liquid crystals . . . . .	93
3.6 Phase diagram of a mixture of rod-like and plate-like liquid crystals . . . . .	94
3.7 Phase diagram of a mixture of rod-like and plate-like liquid crystals . . . . .	95
3.8 Phase diagram of a mixture of rod-like and asymmetric plate-like liquid crystals . . . . .	96
3.9 Phase diagram of a mixture of asymmetric rod-like and asymmetric plate-like liquid crystals . . . . .	97
3.10 Free energy density as a function of concentration . . . . .	98,99
4.1 Pulse sequences used to investigate motion . . . . .	105
4.2(a) Stacked plots from an inversion-recovery experiment . . . . .	109
4.2(b) Stacked plots from a broad-band Jeener-Broekaert experiment . . . . .	110
4.3 Molecular reorientational motion . . . . .	126
4.4 Order parameters for pure FLOC . . . . .	113
4.5 Spectral densities for pure FLOC . . . . .	137-142

4.6	Constant $\Delta\chi^2$ boundary . . . . .	144-146
4.7	Arrhenius plot of motional correlation times for pure FLOC . . . . .	151
4.8	The collision parameter for pure FLOC . . . . .	152
4.9	Order parameters of FLOC - p-Xy mixture . . . . .	156,157
4.10	Spectral densities of FLOC and p-Xy in mixture . . . . .	161-167
4.11	Arrhenius plot of motional correlation times for FLOC in mixture . . . . .	181
4.12	A selective inversion experiment . . . . .	182

## ABSTRACT

Materials which flow like fluids, but possess anisotropic properties like molecular crystals, are called 'liquid crystals'. Studies of liquid crystals contribute to our understanding of how molecular orientation influences macroscopic properties. This thesis presents experimental and theoretical investigations of molecular order and dynamics in nematic liquid crystal systems. First, deuterium nuclear magnetic resonance is used to determine the degree of orientational order of both components of a liquid crystal mixture simultaneously. The temperature dependence of the four order parameters is interpreted using a newly developed mean field theory of nematic binary mixtures composed of biaxial molecules. Next, mean field theory is applied to predict the phase behavior of arbitrarily shaped nematogens. For single component liquid crystals, the four order parameters needed to quantify orientational order of biaxial molecules in a biaxial nematic phase are calculated as a function of temperature for both rod-like and plate-like liquid crystals. For binary mixtures, temperature-concentration phase diagrams for a variety of molecular shapes are calculated. These theoretical predictions suggest that binary mixtures of highly asymmetric molecules with opposite shape anisotropies may display stable biaxial nematic phases. Last, deuterium nuclear magnetic spin relaxation rates are measured as a function of temperature to investigate the molecular motion of a liquid crystal and a liquid crystal binary mixture. These experimental results are interpreted using an anisotropic viscosity model of molecular reorientation. The temperature dependence of the correlation times for the molecular motions is examined and discussed. It is demonstrated that mixing probe molecules into a liquid crystal has a profound effect on the molecular motion of the liquid crystal.

**A STUDY OF MOLECULAR ORDER AND MOTION  
IN NEMATIC LIQUID CRYSTALS**

## 1. INTRODUCTION

The three common forms of matter are the solid, the liquid and the gas phase. In 1888, German chemists [1-3] observed an intermediate phase in some esters of cholesterol. These materials flowed like a viscous liquid but possessed anisotropic optical properties characteristic of solid crystals. Studying these esters using a polarization microscope, Otto Lehmann reported in 1889 of observing a "fliessende kristalle" or "liquid crystal" phase [2]. Materials which have these intermediate phases or mesophases are called liquid crystals, mesogens or mesomorphs. Most liquid crystal molecules are organic compounds having elongated shapes. These long molecules tend to align parallel to each other on average, this alignment gives liquid crystals their anisotropic, crystal-like properties. Liquid crystal systems can be produced by dissolving amphiphilic molecules, such as salts of higher fatty acids, in a carefully controlled amount of solvent, usually water. This class of materials are called **lyotropic** liquid crystals. Lyotropics are usually formed by aggregates of molecules; examples include soaps, detergents and biological membranes. Systems that show mesomorphic behavior in a definite temperature range are called **thermotropic**.

### 1.1 Structure

Both lyotropic and thermotropic liquid crystals are classified according to their structure. The **nematic** phase is a turbid, low viscosity state. Nematic liquid crystals give thread-like textures when viewed through a polarizing microscope, and *Nemat* is Greek for thread-like. Liquid crystal molecules in the nematic phase have long



range orientational order, but the centers of mass of the molecules are distributed at random. Nematic liquid crystals or nematogens come in a variety of shapes. Rod shaped liquid crystal molecules form calamitic nematic phases (*calamos* is Greek for rod). The calamitic nematic phase is uniaxial with all rods pointing in a particular direction on average. This class of compounds has been the most extensively investigated and is the most important for technological applications [4,5]. As of 1990, there were approximately 20,000 rod-like mesogenic compounds known to exist, and typically 1,000 new calamitic liquid crystalline compounds are synthesized each year [6]. In 1977, two groups independently discovered that disk-like molecules form nematic liquid crystal phases [7,8]. Since disks have rotational symmetry, the discotic nematic phase is uniaxial. Recently, a number of groups have claimed to obtain a biaxial nematic phase with highly asymmetrically shaped molecules [9,10,11]. For these biaxial nematogens, rotations about the long axis are sufficiently hindered that there is orientational order in two orthogonal directions. Illustrations of these phases are presented in Figure 1.1.

Although this work will concentrate on thermotropic liquid crystals in the nematic phase, other liquid phases exist. Many mesogens form more highly ordered liquid crystal phases as temperature is lowered (for thermotropics) or as concentration of the amphiphilic molecules is increased (for lyotropics). **Smectic** mesophases (*smektikos* is Greek for soap-like) are characterized by positional order in at least one dimension in addition to average orientational alignment. The centers of mass of the molecules align in layers giving a one dimensional density fluctuation. There are many different kinds of smectic phases, indicated with the subscripts  $S_A$ ,  $S_B$ , ... ,  $S_1$  [12]. These phases differ

---

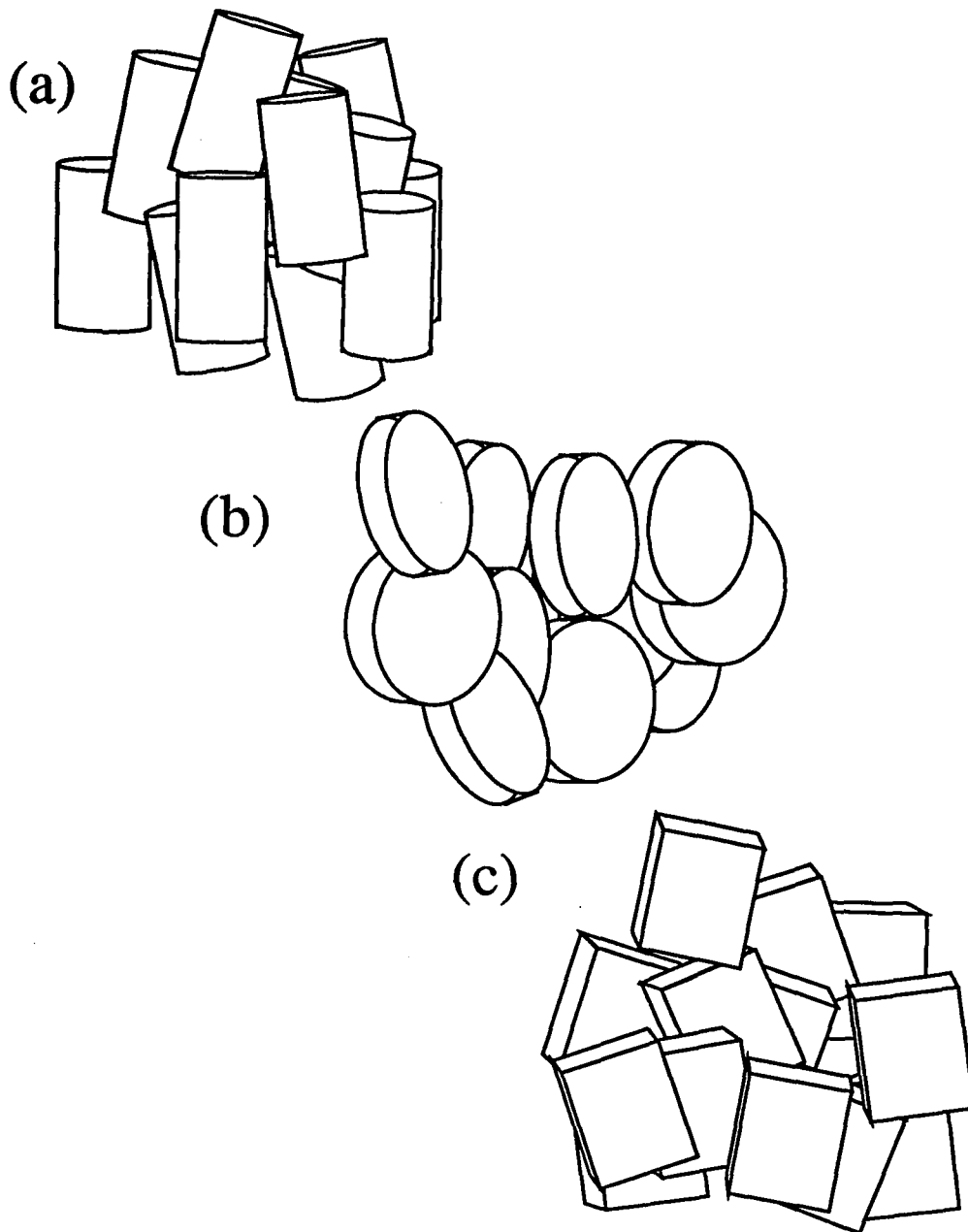


Figure 1.1 The nematic phase is sketched.

- (a) The calamitic nematic phase composed of rod-like molecules.
- (b) The discotic nematic phase composed of disk-like molecules.
- (c) The biaxial nematic phase composed of brick-like molecules.

in (i) the orientation of the preferred direction of the molecules with respect to the layer normal (orthogonal and tilted smectic phases), and (ii) the organization of the centers of mass of the molecules within the layers. Some discotic liquid crystal molecules also tend to stack in ordered columns which are arranged in a hexagonal or rectangular array. These smectic-like phases called columnar discotic phases. The experimental determination of the liquid crystal phase is performed using a variety of techniques. X-ray diffraction results obtained from powders and single crystal samples can be used to determine the structure of the mesophase [12]. Observations of mesogens using a polarizing microscope give textures which are indicative of the symmetry of the phase [13]. Finally, miscibility studies can help classify the phase of a liquid crystal by taking advantage of the fact that complete miscibility is found only for phases of equal or closely related structures [14].

## 1.2 Orientational Order

Anisotropic properties of liquid crystals depend crucially on the degree of orientational order of the constituent molecules. All present day applications of liquid crystals exploit dielectric, diamagnetic, optical, or viscosity anisotropies which are manifestations of the orientational order [4,5]. A measure of the degree of alignment in liquid crystals is needed to quantify this order. The average orientation of liquid crystal molecules can be described statistically by defining a distribution function  $f(\Omega)$  such that  $f(\Omega)d\Omega$  is the probability of finding a molecule within a solid angle  $d\Omega$  centered at  $\Omega$ .  $\Omega$  represents the three Euler angles  $(\alpha, \beta, \gamma)$  which describe the orientation of the molecule in the lab frame, as shown in Figure 1.2. The orientational distribution function can be

---

expanded using Wigner rotation matrix elements as the basis [15],

$$f(\Omega) = \sum_{J,m,n} \frac{2J+1}{8\pi} \langle D_{mn}^{(J)}(\Omega) \rangle D_{mn}^{(J)*}(\Omega). \quad (1.1)$$

The coefficients of this expansion,  $\langle D_{mn}^{(J)}(\Omega) \rangle$ , are thermal averages called **order parameters** which are usually determined experimentally rather than  $f(\Omega)$  itself.

Restricting the discussion to nematic liquid crystals, experiments show that nematic mesophases exhibit  $D_{\infty h}$  symmetry [16] even if the molecules do not. Phases with  $D_{\infty h}$  symmetry have a plane of symmetry perpendicular to the direction of average alignment (the director,  $\mathbf{n}$ , is a unit vector pointing in the direction of average alignment). For systems possessing  $D_{\infty h}$  symmetry,  $\langle D_{mn}^{(J)}(\Omega) \rangle$  with  $J$  odd are zero.

The scalar order parameter,  $Q$ , describes orientational order in a uniaxial phase of cylindrically symmetric molecules. Unfortunately, some authors prefer the notation  $Q$  [17], while other use  $S$ ,  $S_{zz}$ ,  $P_2(\cos\theta)$ , or  $\overline{D_{00}^2(\Omega)}$  to stand for the same quantity [15]. In this thesis, the convention of Bergersen et al. [17] will be adopted, and this order parameter will be called  $Q$ .

$$Q = S_{zz} = \langle P_2(\beta) \rangle = \langle D_{00}^{(2)}(\Omega) \rangle = \left\langle \frac{3}{2} \cos^2\beta - \frac{1}{2} \right\rangle. \quad (1.2)$$

The uniaxial order parameter,  $Q$ , is zero for randomly oriented isotropic fluids, and it can range from 1 for perfectly aligned rods to  $-\frac{1}{2}$  for completely aligned plates. Most experiments only measure this second rank order parameter, although some estimates of the fourth rank order parameter  $\langle P_4(\beta) \rangle$  have also been published [18,19]

$$\langle P_4(\beta) \rangle = \langle D_{00}^{(4)}(\Omega) \rangle = \left\langle \frac{35}{8} \cos^4\beta - \frac{15}{4} \cos^2\beta - \frac{3}{8} \right\rangle. \quad (1.3)$$

In reality, all rod-like nematogens deviate from cylindrical symmetry in

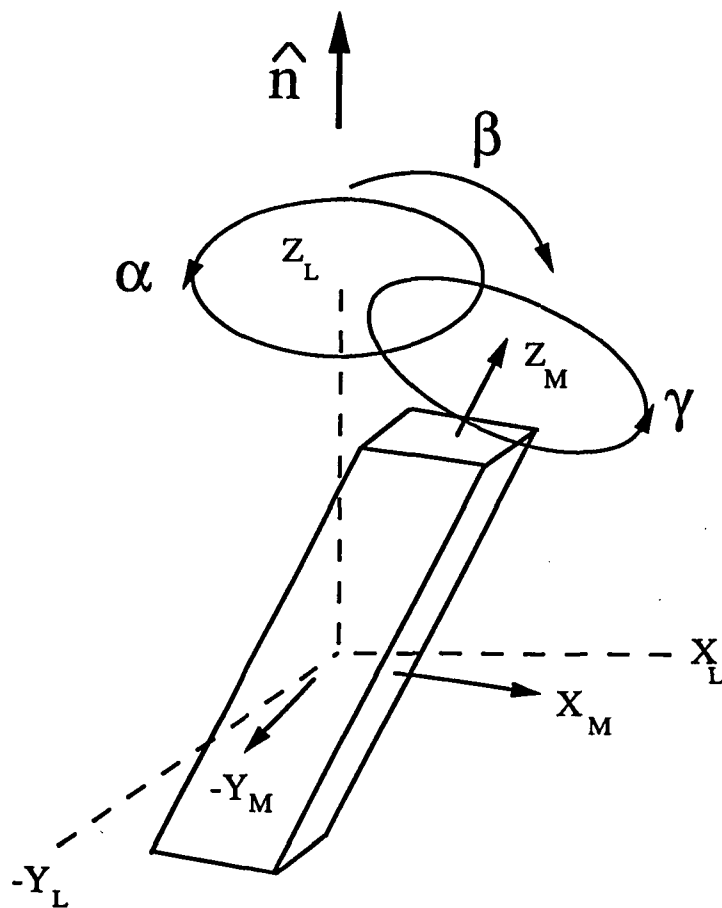


Figure 1.2 The three y-convention Euler angles ( $\Omega = (\alpha, \beta, \gamma)$ ) which describe the orientation of a liquid crystal molecule in the laboratory frame.

some degree, so although the phase may be uniaxial, the two sides of the brick-like molecule will have different probabilities of orienting along the director. A second order parameter describing this molecular anisotropy is  $(S_{xx}-S_{yy})$  or  $D$  [15,17],

$$D = (S_{xx}-S_{yy}) = \left\langle \frac{3}{2} \sin^2 \beta \cos 2\gamma \right\rangle = \sqrt{\frac{3}{2}} \left\langle D_{02}^{(2)}(\Omega) + D_{0-2}^{(2)}(\Omega) \right\rangle. \quad (1.4)$$

For a biaxial nematic phase of non-cylindrically symmetric particles, four order parameters are required to describe the orientational order [17,20]. These are the uniaxial phase order parameters given above,  $Q$  and  $D$ , and two biaxial phase order parameters given below,  $P$  and  $C$ .

$$P = \left\langle \frac{3}{2} \sin^2 \beta \cos 2\alpha \right\rangle = \sqrt{\frac{3}{2}} \left\langle D_{20}^{(2)}(\Omega) + D_{-20}^{(2)}(\Omega) \right\rangle \quad (1.5)$$

$$C = \frac{2}{3} \left\langle D_{2-2}^{(2)}(\Omega) + D_{-22}^{(2)}(\Omega) - D_{22}^{(2)}(\Omega) - D_{-2-2}^{(2)}(\Omega) \right\rangle$$

$$C = \frac{3}{2} \left\langle (1 + \cos^2(\beta)) \cos(2\alpha) \cos(2\gamma) - 3 \cos(\beta) \sin(2\alpha) \sin(2\gamma) \right\rangle \quad (1.6)$$

$$= \frac{3}{2} \left\langle (1 + \cos^2(\beta)) \cos(2\alpha) \cos(2\gamma) - 3 \cos(\beta) \sin(2\alpha) \sin(2\gamma) \right\rangle$$

### 1.3 Molecular Theories

Why do liquid crystals align? Molecular theories of liquid crystals attempt to understand the behavior of mesogenic systems in terms interactions among the component molecules. Ideally, molecular dynamics simulations of large systems of particles with realistic intermolecular potentials would be used. Reasonably accurate pair potentials exist for simple molecules such as inert gases, methane, nitrogen, water, oxygen and benzene [21]. These potentials have been determined experimentally and have been used in computer simulation studies of gases and liquids. To date, the molecular complexity of nematogens have prevented the determination of reliable pair potentials and

their subsequent use in computer simulation experiments. Currently, model potentials must be introduced in order to approximate the relevant characteristics of the interactions. Using these approaches, a qualitative understanding of liquid crystals from a molecular point of view can be developed.

The Onsager molecular field theory [22] ascribes the origin of nematic ordering to the anisotropic shape of the molecules, i.e. to short range, hard core, repulsive interactions. The stability of the nematic phase is given in terms of the excluded volume of hard rods with the shape of spherocylinders or ellipsoids of revolution. An analytic expression for the free energy is derived as a function of the length to breadth anisotropy, the order parameter  $Q$ , and the packing fraction. Analytical solutions for the order parameters can be obtained using statistical mechanics, and the solution which gives the minimum free energy of the system is taken to be equilibrium. For long, thin rods with a length to breadth ratio of 100, this approach gives very high predictions for the order parameters ( $Q \approx 0.78$ ) and over estimates the density change ( $\Delta\rho = 21\%$ ) at the isotropic-nematic transition compared to experimentally determined values ( $Q \approx 0.3$  and  $\Delta\rho = 4\%$ ) [23]. Smaller length to breadth ratios give more reasonable results. If this ratio is 3,  $Q = 0.62$  and  $\Delta\rho < 1\%$ .

Landau-DeGennes theory is an alternate approach in which any attempt to calculate the partition function from the intermolecular potential is forsaken. Instead, the free energy is written as an expansion in terms of parameters of importance in characterizing the transition of interest. For liquid-gas transitions, the relevant order parameter is the density, for ferromagnets it is the magnetization, for superconductors it

is the Cooper pair potential, and for liquid crystals it is the order parameter. Landau's original work was successful in describing second order phase transitions. The nematic-isotropic transition is first order because the order parameters and the entropy of transition change discontinuously at the transition. DeGennes [16] extended Landau's theory to predict the order parameters near weakly first order transitions. In 1991, the Swedish Academy of Sciences presented DeGennes with a Nobel prize in Physics in part for this theory which "has shown that phase transitions in such apparently different physical systems as magnets, superconductors, polymer solutions and liquid crystals can be described in mathematical terms of surprisingly broad generality" [27].

Many other interesting theories of liquid crystal order in nematics have been developed. The Lebwohl-Lasher model [28] is a Monte-Carlo type calculation in which molecules, placed on a fixed lattice, interact via the potential  $U_{ij} = -\epsilon_{ij} P_2(\cos\theta)$ , where  $\theta$  is the angle between the long axes of molecules  $i$  and  $j$ , here  $\epsilon_{ij}$  is finite if  $i$  and  $j$  are nearest neighbors and 0 otherwise. This model predicts a first order phase transition from the liquid state to the nematic, with  $Q=0.333\pm 0.009$  [29]. The Lebwohl-Lasher model is presently being used to investigate order in small droplets (microns) dispersed in a polymer matrix where surface boundary conditions have a profound effect on the orientation of the molecules [30]. Other Monte Carlo simulations in which hard particles are allowed to move rotationally and translationally have been performed, giving results similar to Onsager techniques [31]. Finally, hybrid van der Waals-type theories which consider both short range and long range interactions for liquid crystals have also been proposed [32,33]. The addition of a long term attractive term to hard core term in the



potential lowers the  $Q$  at the transition by 0.10 to 0.15, while the change of density at the transition is unaffected [33].

In this thesis, a highly successful molecular theory called mean field theory will be used to interpret experimental results and to predict the behavior of binary mixtures of biaxial nematogens. Mean field theory, first formulated by Maier and Saupe [24], attributes nematic ordering to anisotropic, soft, long range attractive interactions. The mean field approach assumes that any molecule in the system interacts with a mean field generated by all the other molecules. In the original treatment, attractive pair-wise London dispersion forces (induced dipole-induced dipole) were assumed which led to a mean field pseudopotential  $U(\Omega)$  [24],

$$U(\Omega) = -CQ \left[ \frac{3}{2} \cos^2\beta - \frac{1}{2} \right] \quad (1.7)$$

here  $C$  is a temperature independent constant,  $\beta$  is the Euler angle between the molecular  $z$ -axis and the director shown in Figure 1.2, and  $Q$  is the orientational order parameter. Later it was realized that any pair potential of the form  $U(r_{12}, \beta) = -u(r_{12}) P_2(\cos\beta)$ , where  $u(r_{12})$  is some scalar function of distance, will give this pseudopotential [25]. Classical statistical mechanics gives the orientational order parameter  $Q$  as function of this pseudopotential, and this equation can be solved self-consistently to find a solution for the order parameter as a function of temperature. The free energy density, entropy density and internal energy density of the system can also be calculated, and the order parameter solution which gives the minimum free energy density at a given temperature gives the stable equilibrium state of the system. Results of this theory are in qualitative agreement with experiment. Using Maier-Saupe mean field theory, the order parameter

at the transition isotropic-nematic transition  $T_{NI}$  has been calculated to be  $Q = 0.4289$ , and the entropy of transition is  $\Delta S = 3.47 \text{ J/mol}^\circ\text{K}$  (experiments which measure the latent heat of transition give  $\Delta S \approx 2.5$  to  $3.4 \text{ J/mole K}$ ) [26].

Mixtures of liquid crystals are often used in applications. The aim is to get a nematic phase having specific physical properties related to the orientational order parameter (birefringence, dielectric susceptibility, diamagnetic susceptibility) appropriate for the application, over a reasonably wide temperature range around the ambient. Binary mixtures of liquid crystals have been treated theoretically using extensions of mean field lattice models [34,35], Onsager theories [36,37], van der Waals-type theories [32], lattice models of hard rods [38], and extended Maier-Saupe models [39-41]. In the first two chapters of the thesis, a recently developed extension of Maier-Saupe theory of binary mixtures of biaxial molecules [41] will be used to interpret experimentally measured orientational order parameters in a nematic liquid crystal binary mixture, and to predict phase stability and orientational order in binary mixtures of biaxial nematogens.

#### **1.4 Measurement of Orientational Order**

The uniaxial order parameter,  $Q$ , can be determined by measuring a number of anisotropic physical properties of liquid crystals. The magnetic susceptibility  $\chi$  is defined as  $\chi = \mu_0 \mathbf{M}/\mathbf{B}$  (SI units), where  $\mu_0$  is the permeability of the vacuum,  $\mathbf{B}$  is the magnetic induction and  $\mathbf{M}$  is the magnetization. An external magnetic field induces a magnetization  $\mathbf{M}$  in a sample by changing the orbital motion of the electrons on constituent molecules. Most mesogens are diamagnetic, in these materials the induced currents tend to lower the magnetic field in the sample, hence  $\chi$  is negative. The

orientational order parameter  $Q$  can be estimated by subtracting the susceptibility measured along the director from that measured perpendicular to it [42]. The dielectric susceptibility,  $\chi^e = \epsilon_0^{-1} \mathbf{P}/\mathbf{E}$ , where  $\epsilon_0$  is the permittivity of vacuum, and  $\mathbf{P}$  is the polarization induced by the electric field  $\mathbf{E}$ , have also been used to measure  $Q$ . The dielectric susceptibility anisotropy can be estimated optically with measurements of refractive indices and electrically with capacitance measurements [42].

Optical spectroscopies have also been used to quantify molecular order in liquid crystal systems. Raman spectroscopy involves the inelastic scattering of a photon. In 1928, Raman observed that a small proportion of radiation passing through a substance emerges with an increase or decrease in frequency. This occurs when a molecule in the ground state is excited to a virtual electronic state and instantaneously (lifetimes of the virtual excited states are about  $10^{-12}$  s) emits a photon as it returns to some vibrational or rotational level in the ground electronic state. The scattered light is analyzed spectroscopically. A study of the polarization of the Raman lines can give, with the aid of somewhat oversimplified models, both the second and the fourth moment of the orientational distribution function ( $Q$  and  $\langle P_4(\beta) \rangle$ ) [43,44]. With fluorescence spectroscopy, radiant energy is absorbed and an electron is elevated into an excited singlet state. A photon is emitted after a singlet state lifetime of  $\tau \approx 10^{-9}$  s, and the electron falls from the lowest vibrational level of the first excited singlet state to the ground state. Since most mesomorphic molecules do not fluoresce appreciably, the technique in general uses a fluorescent probe molecule. The anisotropy in the polarization of the emitted radiation from these probe molecules is used to determine the static order parameters  $Q$

and  $\langle P_4(\beta) \rangle$  [45]. With infrared spectroscopy, photons are absorbed resulting in vibrational excitation of the molecule. Any molecular vibration which modulates the molecular dipole moment can cause absorption and reemission of infrared light. A given normal mode of vibration will absorb the radiation at a particular vibrational frequency. The order parameter  $Q$  can be measured by observing the absorbance of infrared light polarized parallel to and perpendicular to the nematic director at an appropriate normal mode frequency [43,44].

### 1.5 Measurement of Molecular Motion

Molecular motion can also be measured with scattering and spectroscopic experiments. With fluorescence depolarization, the degree of polarization of the fluorescence emission depends on the reorientational dynamics of the liquid crystal molecules. If the lifetime of the singlet state,  $\tau_f$ , is much less than the molecular reorientational relaxation time,  $\tau_r$ , then the results of the experiment can only be used to measure orientational order parameters. In the other extreme where  $\tau_r \ll \tau_f$ , the molecular system approaches dynamical equilibrium before emission takes place, and again only static information is accessible. The most interesting case is when  $\tau_r \approx \tau_f$ , then the molecular motion strongly influences but does not totally destroy the degree of polarization of the fluorescence emission. Time resolved fluorescence spectroscopy can be used to measure  $\tau_r$  using pulsed light experiments and the ratio  $\tau_r/\tau_f$  using steady state experiments [43-46]. For Raman and infrared spectroscopy, the bandshape of the observed frequencies is influenced by both vibrational and reorientational motion. The basic problem for measuring molecular motion with these methods is the separation of

broadening mechanisms due to rotation from that due to vibrations. Because the bandshape is a convolution of two different relaxation processes [47], the Fourier transform is simply a product of the two separate correlation functions. Models of the motion can be used to interpret these correlation functions and give relaxation rates [43]. One scattering experiment which can probe the dynamics of liquid crystals involves reflecting a beam of neutrons from an aligned liquid crystal. By measuring the intensity of the scattered neutrons as a function of momentum and energy, translational and rotational diffusion rates have been estimated using models for the molecular motion which assume uncorrelated vibrational, rotational and translational motions [48,49].

### **1.6 Magnetic Resonance Spectroscopy**

Magnetic resonance spectroscopy is a powerful, widely used technique for studying both the dynamics and structural properties of nematic liquid crystals. The phenomenon of magnetic resonance is due to the interaction of an external magnetic field with the intrinsic spin of a nucleus or an electron. Although the fundamental behavior of nuclei and electrons in a magnetic field is very much alike, the experimental apparatus used to study these interactions and the types of information accessible is quite different. These differences have led to a division of the subject of magnetic resonance into two broad categories: (1) electron spin resonance (ESR) and (2) nuclear magnetic resonance (NMR).

To investigate liquid crystal systems using ESR techniques, groups of atoms with unpaired electrons (usually nitroxide radicals) are chemically attached to probe molecules, and these probes are diluted into the host mesogen. It is possible to derive a

theoretical expression for the ESR line position as a function of the orientational order parameter  $Q$  [50] and even  $\langle P_4 \rangle$  of the probe molecules in the host matrix [51]. Relaxation rates of these paramagnetic states are on the order of the  $10^{-9}$  sec, thus spectral lineshapes are very sensitive to rotational motions of the spin tagged solute. In order to interpret the lineshapes, a numerical solution of the stochastic Liouville Equation (a density operator form of the time dependent Schrödinger equation with a randomly fluctuating Hamiltonian) is solved with explicit models for the reorientational motion [52]. Information obtained using this technique is of course restricted to the dynamics of the tagged solute, and can not be used to infer the motion of the liquid crystal molecules themselves.

Nuclear magnetic resonance (NMR) refers to the resonant absorption of electromagnetic radiation by a system of atomic nuclei placed in a magnetic field. The frequency of the resonance,  $\nu_0$ , is the Larmor precession frequency of the nuclei in a magnetic field. For a nucleus possessing both spin angular momentum  $\hbar I$  and a proportional magnetic moment  $\mu = \gamma \hbar I$ , the Larmor frequency is proportional to the intensity of the magnetic field,  $\nu_0 = \gamma B_0$ , where  $\gamma$  is the gyromagnetic ratio in Hertz per Tesla. An exact quantum calculation using the Zeeman Hamiltonian:

$$H_z = -\gamma \hbar B_0 I_z, \quad (1.8)$$

yields an energy separation between adjacent levels of  $E_0 = h\nu_0$ . There are  $2I+1$  eigenstates with eigenvalues  $E_m = -h\nu_0 m$ , where  $m$  is the z component angular momentum quantum number which takes integer values between  $-I$  and  $I$ . The actual energy levels are perturbed because of interactions with other nuclei and electrons. These perturbing

interactions make NMR spectroscopy a powerful tool for probing molecular structure, order and dynamics.

NMR studies of liquid crystals commonly use the hydrogen ( $^1\text{H}$ ), carbon ( $^{13}\text{C}$ ) and deuterium ( $^2\text{H}$ ) nuclei. For  $^1\text{H}$ -NMR studies, the Zeeman interaction is perturbed by direct, through space, dipole-dipole couplings. The fact that each hydrogen nucleus interacts with each of its many neighbors makes interpretation of the spectra difficult, although multiple quantum techniques have been developed to simplify the analysis of the highly complicated spectra [53]. For  $^{13}\text{C}$ -NMR, the dominant perturbations on the Zeeman interaction are chemical shielding anisotropies and  $^{13}\text{C}$ - $^1\text{H}$  dipolar couplings. Proton decoupling can provide simple, high resolution spectra of liquid crystals, but this requires high radio frequency power making temperature control difficult [54].  $^2\text{H}$ -NMR is uniquely suited for studying molecular static and dynamics. Unfortunately the natural abundance of deuterium is low ( 0.015% ) [55], which makes the use of isotopically enriched substances necessary. For  $^2\text{H}$  nuclei, coupling between electric field gradients generated by neighboring electrons and the nuclear quadrupole moment is the dominant interaction.

A  $^2\text{H}$ -NMR spectrum consists of a simple doublet for each inequivalent deuterated site, and the size of the quadrupolar splittings in Hertz,  $2\nu_Q$ , gives site specific orientational information. Once the sites have been assigned, and the geometry of the molecule determined, expressions for the splitting in terms of order parameters for the liquid crystal can be derived [56].  $^2\text{H}$ -NMR has been used to measure the static orientational order parameter  $Q$  ( $S_{zz}$ ) and  $D$  ( $S_{xx}-S_{yy}$ ) [57-61]. Unfortunately, since the

---

electric quadrupolar interaction is second rank, the fourth rank order parameter  $\langle P_4 \rangle$  and higher rank order parameters can not be measured with this technique. Often for liquid crystal systems,  $^2\text{H-NMR}$  experiments spectral widths ( $<200$  kHz) are quite narrow on the scale of the typical frequencies for reorientational dynamics of liquid crystal molecules ( $>10$  MHz). In this limit, nuclear spins experience a time averaged interaction, and the lineshape is "motionally narrowed". In this case, the line shape of the spectrum does not give detailed motional information, however pulsed  $^2\text{H-NMR}$  relaxation experiments, which measure the relaxation rates of spin states, are capable of giving information about the molecular dynamics [59,60]. The relaxation rates can be expressed in terms of spectral density functions which characterize the spectrum of molecular fluctuations. These spectral densities, which are Fourier transforms of autocorrelation functions, can be interpreted using models of the molecular motion [61,62].

### 1.7 A Study of Molecular Order and Motion in Liquid Crystal Mixtures

This thesis will be presented in three parts. In the first section,  $^2\text{H-NMR}$  spectra were measured as a function of temperature in a binary mixture of the mesogen 2-fluorenyl-4'-tetradecyloxy benzoate- $\text{d}_{10}$  (FLOC) and a solute probe para-xylene- $\text{d}_{10}$  (p-Xy) shown in Fig. 1.3 [58]. The molecular structure of FLOC is typical of many classical rod-like liquid crystals. FLOC has flat, rigid fluorene core [62] with a 14 carbon tail attached. This long, alkoxy chain is flexible and can exist in many ( $3^{13}$ ) configurations. Both molecules were deuterated: the FLOC was selectively deuterated on the rigid fluorene moiety while the p-Xy was perdeuterated. In the  $^2\text{H-NMR}$  experiment, the quadrupolar splittings allow the unambiguous determination of the order parameters  $Q_i$



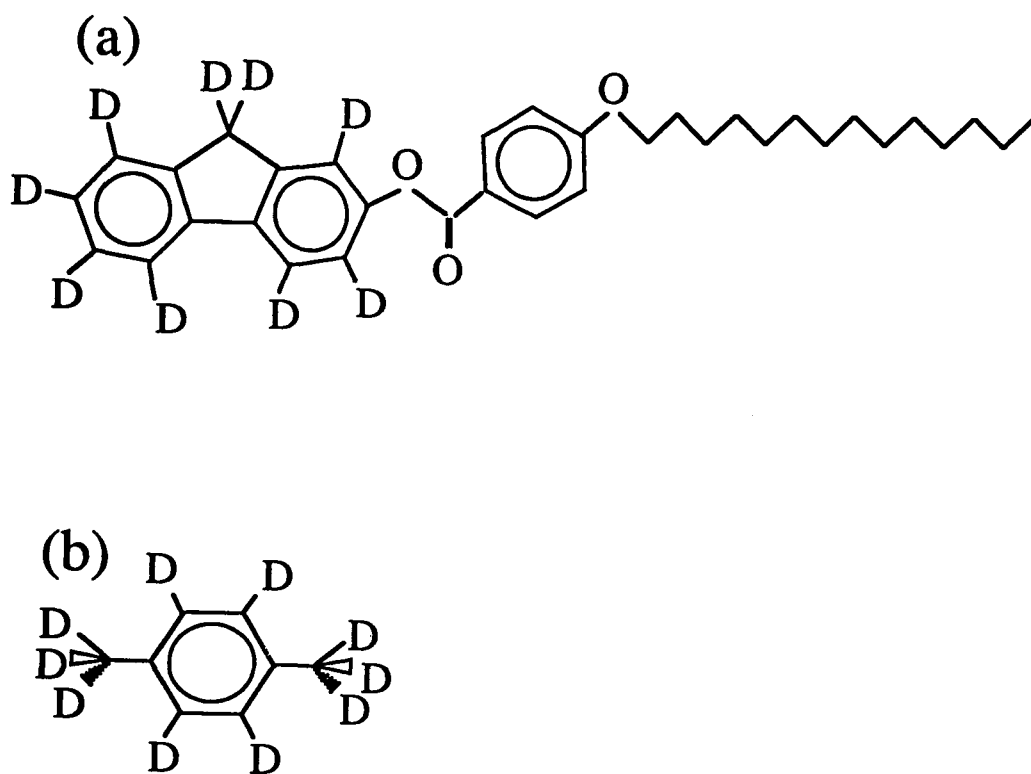


Figure 1.3 The molecular structures of the two components of the binary mixture.

(a) FLOC.

(b) p-Xy.

and  $D_i$  of both species ( $i=1,2$ ). These are the first results to provide this information on the degree and asymmetry of orientational order of both components of a binary mixture in the nematic phase [58]. The temperature dependence of the order parameters are interpreted using a new mean field theory of binary mixtures of biaxial particles [41]. There is good agreement between the theoretical predictions and the four order parameters determined from the  $^2\text{H-NMR}$  over the entire temperature range studied. Furthermore, an identical analysis of pure FLOC data give results which are consistent with those obtained from the binary mixture of FLOC and p-Xy.

The second section presents the results of a theoretical study of binary mixtures of biaxial particles using a newly developed mean field theory [41]. In this section, a general pseudopotential consistent with the  $D_{2h}$  symmetry of the constituent particles is used to calculate the eight order parameters ( $Q_i, D_i, P_i, C_i$  for  $i=1,2$ ) which describe order in binary mixtures of uniaxial and biaxial nematic phases. For a single component, the model only requires one parameter,  $r_2$ , a ratio of anisotropic interaction strengths, to predict the temperature dependence of the four order parameters. The temperature dependence for all four order parameters is presented and interpreted for both rod-like and plate-like liquid crystals. Three anisotropic interaction strengths,  $r_1$ ,  $r_2$  and  $r_3$ , are needed to calculate the order parameters of both components of a binary mixture as a function of concentration and temperature. Once the order parameters have been calculated, the free energy of the system is evaluated to predict the stability of the mixture. By systematically varying the anisotropic interaction strengths, temperature-concentration phase diagrams for a variety of molecular shapes are presented. These

theoretical predictions suggest that binary mixtures of molecules with highly asymmetric shapes will display stable biaxial nematic phases [63].

The last section of the thesis will present the results of a  $^2\text{H}$ -NMR relaxation experiment performed to investigate the molecular motion of the nematogen FLOC [61] and a FLOC : p-Xy binary mixture. Pulse sequences have been designed to measure spin relaxation rates of quadrupolar order and Zeeman order in two separate experiments [59]. Using Redfield theory [64], a formalism applicable in the fast motion regime, this combination yields spectral densities,  $J_1^k(\omega_0)$  and  $J_2^k(2\omega_0)$ , for each site  $k$  on the molecule. The spectral density data are interpreted by fitting the experimental results with an anisotropic viscosity model of molecular motion in liquid crystal molecules. This model of molecular reorientation requires three independent correlation times corresponding to rotations of the liquid crystal molecule about specific axis and a collision parameter related to the angular jump size of rotations about the long molecular axis [65]. The temperature and frequency dependence of the correlation times are examined and discussed. Finally, results of a similar experiment on a mixture of p-Xy and FLOC are presented which provide a description of the dynamics of both components of a binary mixture simultaneously.

## 2. ORIENTATIONAL ORDER IN A LIQUID CRYSTAL BINARY MIXTURE

This section of the thesis will describe how deuterium nuclear magnetic resonance ( $^2\text{H-NMR}$ ) has been used to measure the temperature dependence of the orientational order parameters of both components of a liquid crystal binary mixture, and how these experimental results are interpreted using a mean field theory of binary mixtures of liquid crystals [58,66]. Many methods of measuring liquid crystal order parameters rely on the assumption that the ordering and dynamics of dissolved probe molecules mimic their liquid crystal hosts [67-69], this work is useful for evaluating the validity of these assumptions.

### 2.1 The Quadrupolar Hamiltonian

$^2\text{H-NMR}$  takes advantage of the fact that electrons in orbit about a nucleus have an effect on the energy required to reorient it. All nuclei with spin  $I > 1/2$  have an electric quadrupole moment  $eQ$  [70]. If these non-spherical nuclei experience an electric field gradient generated by the local electron density, the electrostatic energy varies with nuclear orientation. The Hamiltonian,  $H_Q$ , describing this quadrupolar interaction is

$$H_Q = \frac{1}{6} \sum_{\alpha\beta} V_{\alpha\beta} Q_{\alpha\beta} \quad (2.1)$$

Where  $V_{\alpha\beta}$  is the electric field gradient tensor in Cartesian coordinates

$$V_{\alpha\beta} = \left( \frac{\partial^2 V(\mathbf{x})}{\partial x_\alpha \partial x_\beta} \right)_{r=0} \quad (2.2)$$

and  $Q_{\alpha\beta}$  is the nuclear quadrupole moment tensor

$$Q_{\alpha\beta} = \int (3x_\alpha x_\beta - r^2 \delta_{\alpha\beta}) \rho(x) d^3x. \quad (2.3)$$

Here  $\alpha, \beta = x, y, z$ ,  $V(x)$  is the electrostatic potential, and  $\rho(x)$  is the nuclear charge density at  $x$ . These expressions appear to be extremely difficult to evaluate because they involve distribution functions of nuclear particles. However, since only the spatial orientation of the nucleus is of interest and not actual distributions of nucleons, only the diagonal matrix elements  $\langle I | Q_{\alpha\beta} | I \rangle$  need to be calculated. For these elements, the Wigner-Eckart theorem can be applied to reexpress the quadrupole Hamiltonian in terms of the spin operators  $I_{\alpha\beta}$  [71]

$$H_e = \frac{eQ}{6I(2I-1)} \sum_{\alpha,\beta} V_{\alpha\beta} \left[ \frac{3}{2} (I_\alpha I_\beta + I_\beta I_\alpha) - \delta_{\alpha\beta} I^2 \right]. \quad (2.4)$$

For the analysis to follow, it will be convenient to use spherical tensor notation. Spherical tensor matrix elements are simply linear combinations of Cartesian tensor elements [72]. As demonstrated in Appendix I, each of the 9 elements of any second rank spherical tensor can be presented in terms of an equivalent Cartesian tensor. Reexpressing the Cartesian tensor  $V_{\alpha\beta}$  as a spherical tensor  $T_{l,m}$  gives

$$\begin{aligned} T_{2,0} &= \frac{1}{4} eQ V_{zz}, & T_{2,\pm 1} &= -\frac{1}{4} eQ [V_{xz} \pm V_{yz}], \\ T_{2,\pm 2} &= \frac{1}{8} eQ [V_{xx} - V_{yy} \pm 2iV_{xy}]. \end{aligned} \quad (2.5)$$

The spin part of the quadrupolar Hamiltonian becomes  $A_{l,m}$  in spherical tensor notation

$$A_{2,0} = 3I_z^2 - I^2, \quad A_{2,\pm 1} = I_z I_\pm + I_\pm I_z, \quad A_{2,\pm 2} = I_\pm^2. \quad (2.6)$$

Here  $e$  is the electronic charge and  $eQ$  is the electric quadrupole moment of a deuteron.

An expression for the electric quadrupolar Hamiltonian,  $H_Q$ , can be derived in terms of the scalar contraction of the two spherical tensors  $T$  and  $A$

$$H_Q = \sum_{m=-2}^2 (-1)^m A_{l,m} T_{l,-m}. \quad (2.7)$$

In a typical  $^2\text{H}$ -NMR experiment, the quadrupolar nuclei are placed in a strong static external magnetic field. The full Hamiltonian can be written as

$H = H_Z + H_Q$ , where  $H_Z$  is the Zeeman Hamiltonian and  $H_Q$  is the quadrupolar term. For deuterons in a strong (i.e. 7 Tesla) external magnetic field, the quadrupolar term in the Hamiltonian ( $E_Q/h \leq 250$  kHz) is much smaller than the Zeeman Hamiltonian ( $E_Z/h = 46$  MHz). Thus, the quadrupolar interaction is treated as a perturbation on the dominant Zeeman Hamiltonian. Neglecting terms of order  $(e^2qQ/\gamma\hbar\mathbf{B})^2$ , perturbation theory gives a first order approximation to energy levels of the system

$$E \approx -m\gamma B_0 + \frac{3m^2 - I(I+1)}{I(2I-1)} \langle T_{2,0}^L \rangle. \quad (2.8)$$

The superscript  $L$  in the term  $\langle T_{2,0}^L \rangle$  denotes that the derivatives are evaluated in the laboratory frame in which the  $z$ -axis is parallel to  $\mathbf{B}_0$ . The brackets indicate that the field gradients are time averaged. Figure 2.1 illustrates the perturbation of the Zeeman energy levels by the electric quadrupolar terms in the Hamiltonian, and it shows the transitions responsible for a symmetric spectrum with peaks at  $\nu_0 \pm \nu_Q$ . Each inequivalent deuteron presents is a set of symmetric peaks in frequency space separated by  $2\nu_Q$ . The following discussion outlines the pulse NMR experimental techniques used to measure these quadrupolar splittings.

## SPIN I=1

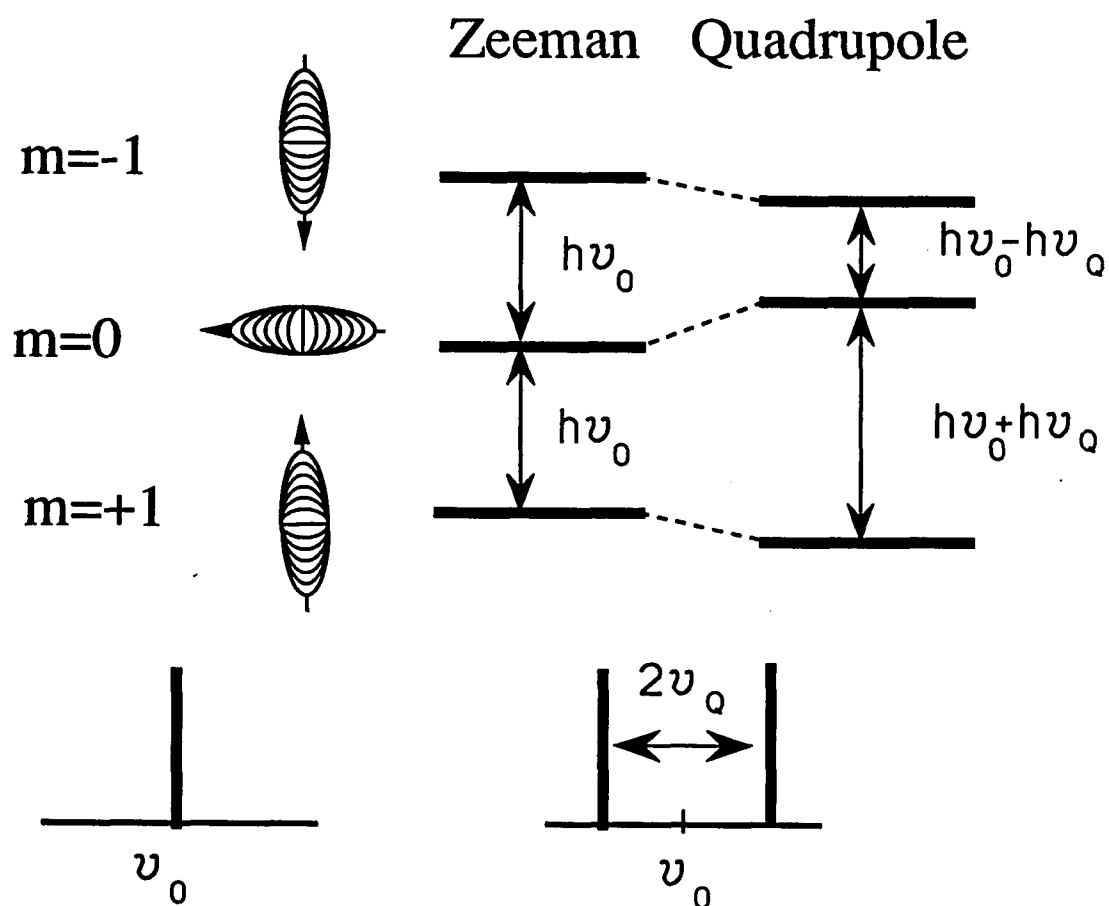


Figure 2.1 Energy level diagram for a spin  $I = 1$  in a magnetic field  $B_0$ . The deuterium quadrupolar interaction is treated as a perturbation on the Zeeman interaction. In the isotropic phase the deuterium spectrum consists of a single line because  $\langle H_Q \rangle = 0$ , while in the nematic phase it consists of a doublet separated by  $2\nu_Q$ .

## 2.2 Spin Dynamics

An NMR spectrometer creates radio frequency (rf) pulses, couples this radiation to a sample, and observes the response. State of the art spectrometers are capable of regulating the rf amplitude, phase, duration, and frequency. The pulsed radio frequency current passes through a coil, generating an alternating magnetic field,  $B_1(t)$ , and this field penetrates a sample inside the coil. The response of the nuclear spins in the sample to this changing magnetic field can be understood in terms of a density matrix formalism described in the following section.

Consider a system of  $N$  noninteracting spins described by the wave function  $\psi(t)$ . Assuming  $\psi(t)$  can be expanded in a complete set of time independent orthonormal wave functions  $\phi_n$  with time dependent coefficients  $c_n(t)$ ,

$$\psi(t) = \sum_n c_n(t) \phi_n. \quad (2.9)$$

The ensemble averaged expectation value of an operator  $\hat{O}$  is

$$\begin{aligned} \bar{O} &= \overline{\int \psi^* \hat{O} \psi d\tau} = \overline{\left\langle \sum_m c_m^*(t) \phi_m \mid \hat{O} \mid \sum_n c_n(t) \phi_n \right\rangle} \\ &= \sum_{m,n} \overline{c_n(t) c_m^*(t)} \langle \phi_m \mid \hat{O} \mid \phi_n \rangle. \end{aligned} \quad (2.10)$$

The matrix formed by the product of ensemble averaged expansion coefficients is defined to be the density matrix

$$\langle n \mid \rho \mid m \rangle = \overline{c_n(t) c_m^*(t)}. \quad (2.11)$$

Given the density matrix  $\rho$ , the ensemble averaged expectation value of any given operator  $\hat{O}$  can be calculated,



$$\bar{O} = \sum_{m,n} \langle n | \rho | m \rangle \langle m | \hat{O} | n \rangle = \text{Tr}(\rho \hat{O}) \quad (2.12)$$

where  $\text{Tr}$  is the trace and it is assumed that the states  $|n\rangle$  and  $|m\rangle$  are members of an orthonormal basis set which spans the state space. Since the diagonal elements of  $\rho$  represent a probability of the system being in a given state, normalization requires that  $\text{Tr}(\rho) = 1$ .

Since the density matrix completely determines the state of an ensemble, its time evolution will describe the behavior of the system. To determine how the density matrix evolves in time, first consider the time-dependent Schrödinger equation:

$$\frac{\hbar}{i} \frac{\partial \psi}{\partial t} = H \psi. \quad (2.13)$$

Expanding  $\psi$  using Eqn. (2.9), multiplying by  $\phi_k^*$ , and integrating gives

$$\frac{-\hbar}{i} \frac{\partial c_k(t)}{\partial t} = \sum_n c_n(t) \langle k | H | n \rangle. \quad (2.14)$$

Taking the time derivative of each element of the density matrix,

$$\begin{aligned} \frac{\partial \langle k | \rho | n \rangle}{\partial t} &= c_m^* \frac{\partial c_k}{\partial t} + c_k \frac{\partial c_m^*}{\partial t} \\ &= \frac{i}{\hbar} \langle k | [\rho H - H \rho] | m \rangle. \end{aligned} \quad (2.15)$$

In operator form, this is the Liouville-von Neumann equation

$$\frac{\partial \rho}{\partial t} = \frac{i}{\hbar} [\rho, H]. \quad (2.16)$$

If the Hamiltonian is time independent, it is easy to verify that a formal solution to this

equation is

$$\rho(t) = e^{-\frac{i}{\hbar}Ht} \rho(0) e^{+\frac{i}{\hbar}Ht}. \quad (2.17)$$

Deuterium, a spin  $I = 1$  nucleus, has three spin states ( $m = -1, 0, 1$ ). Hence the density matrix has  $3 \times 3 = 9$  elements, but the normalization requirement,  $\text{Tr}(\rho) = 1$ , reduces the degrees of freedom to 8. Therefore, eight  $3 \times 3$  operators are required to span the spin space. The eight operators are not unique; one set, which is particularly useful for analyzing pulse sequences, is given below.

$$\begin{aligned} (1) \quad I_x &= I_+ + iI_- & (2) \quad I_y &= I_+ - iI_- & (3) \quad I_z \\ (4) \quad Q_x &= I_z I_x + I_x I_z & (5) \quad Q_y &= I_z I_y + I_y I_z & (6) \quad Q_z &= \frac{1}{3} (3I_z^2 - I \cdot I) \\ (7) \quad D_x &= I_x^2 - I_y^2 & (8) \quad D_y &= I_x I_y + I_y I_x \end{aligned} \quad (2.18)$$

Where the angular momentum operators satisfy the relations

$$\begin{aligned} I_{\pm} |I, m\rangle &= [I(I+1) - m(m \pm 1)]^{1/2} |I, m \pm 1\rangle \\ I_z |I, m\rangle &= m |I, m\rangle \\ I^2 |I, m\rangle &= I \cdot I |I, m\rangle = I(I+1) |I, m\rangle \end{aligned} \quad (2.19)$$

$(I_x, I_y, I_z)$  are scaled Cartesian angular momentum operators of rank 1 ( $J = \hbar I$  in ref. [73]),  $(Q_x, Q_y, Q_z)$  and  $(D_x, D_y)$  are Cartesian forms of second rank spherical tensor operators.

In theory, the time evolution of each of the eight operator basis set can be calculated using Eqn. (2.16) by solving the coupled differential equation. If the Hamiltonian is time independent, the problem is simplified considerably. The density matrix at time  $t$ ,  $\rho(t)$  can be calculated given the initial state  $\rho(0)$  and the Hamiltonian

using Eqn. (2.17) [74]. For deuterium nuclei on resonance, the Hamiltonian in a frame rotating at the Larmor frequency is given by

$$H = -h\nu_1 I_{x,y} - h\nu_Q Q_z \quad (2.20)$$

where  $\nu_1 = \gamma B_1$ .  $B_1$  gives the intensity of the magnetic field produced by the high power rf pulse applied at frequency  $\nu_0$ . For sufficiently strong pulses,  $\nu_1 \gg \nu_Q$ , and evolution under the quadrupole term in the Hamiltonian can be neglected when the pulses are on. State of the art, high power  $^2\text{H}$ -NMR spectrometers are capable of delivering an rf pulse which rotates the magnetization  $90^\circ$  in  $1.6 \mu\text{s}$ , corresponding to  $\nu_1 \approx 156 \text{ kHz}$ .

A simple example of a pulse sequence which can be used to obtain  $^2\text{H}$ -NMR spectra is a single, high power pulse at the Larmor frequency,  $\nu_0$ . If the phase of the pulse is set to rotate the spins about the x-axis, and the duration of the pulse is long enough to rotate the spins  $90^\circ$  (a  $90_x$  pulse in NMR jargon), the magnetization is rotated from pointing along the z-axis in equilibrium to along the y-axis just after the pulse. This magnetization is free to precess, inducing signal in the coil called the free induction decay (FID). This FID is digitized and the discrete Fourier transform of this time domain signal gives an approximation to the frequency spectrum. However, spectra collected in this manner are highly distorted because it is impossible to collect the weak signal immediately after the rf pulse, whose amplitude exceeds the signal by at least a factor of  $10^6$ . One way to avoid this  $20\mu\text{s}$  to  $40\mu\text{s}$  receiver "dead time" is to use a quadrupolar echo pulse sequence.

### 2.3 The Quadrupolar Echo Pulse Sequence

The quadrupole echo pulse sequence ( $90_x-\tau-90_y-\tau\text{-acq}$ ) is the standard

method for obtaining undistorted, full width  $^2\text{H-NMR}$  spectra. The reason for the popularity of this technique is that the free induction decay (FID) refocuses at a time  $\tau$  after the last pulse [75], as shown in Figure 2.2, which allows the digitizer to acquire the beginning of the FID. The time evolution of the density matrix  $\rho$  can be used to describe the spin dynamics during a quadrupolar echo pulse sequence. In equilibrium, the net magnetization points along the external magnetic field,  $\rho(0) \propto I_z$ . Immediately after the first pulse, the spins point along the y-axis (see Appendix II for a comprehensive list of the time evolution of the elements of the density matrix under quadrupole or rf pulse Hamiltonians)

$$\rho = e^{i\frac{\pi}{2}I_x} I_z e^{-i\frac{\pi}{2}I_x} = I_y. \quad (2.21)$$

In the time  $\tau$  between the first and second pulses, the density matrix evolves under the quadrupolar Hamiltonian

$$\rho(\tau) = e^{iQ_z\omega\tau} I_y e^{-iQ_z\omega\tau} = I_y \cos\omega_Q\tau + Q_x \sin\omega_Q\tau. \quad (2.22)$$

Just after the second pulse, the density matrix becomes

$$\begin{aligned} \rho &= e^{i\frac{\pi}{2}I_x} [I_y \cos\omega_Q\tau + Q_x \sin\omega_Q\tau] e^{-i\frac{\pi}{2}I_x} \\ &= I_y \cos\omega_Q\tau - Q_x \sin\omega_Q\tau. \end{aligned} \quad (2.23)$$

At time  $t$  after the second pulse, the density matrix is

$$\begin{aligned} \rho(t) &= e^{iQ_z\omega t} [I_y \cos\omega_Q\tau - Q_x \sin\omega_Q\tau] e^{-iQ_z\omega t} \\ &= \cos\omega_Q\tau [I_y \cos\omega_Q t - Q_x \sin\omega_Q t] \\ &\quad + \sin\omega_Q\tau [Q_x \cos\omega_Q t + I_y \sin\omega_Q t] \\ &= I_y \cos\omega_Q(t-\tau) - Q_x \sin\omega_Q(t-\tau). \end{aligned} \quad (2.24)$$

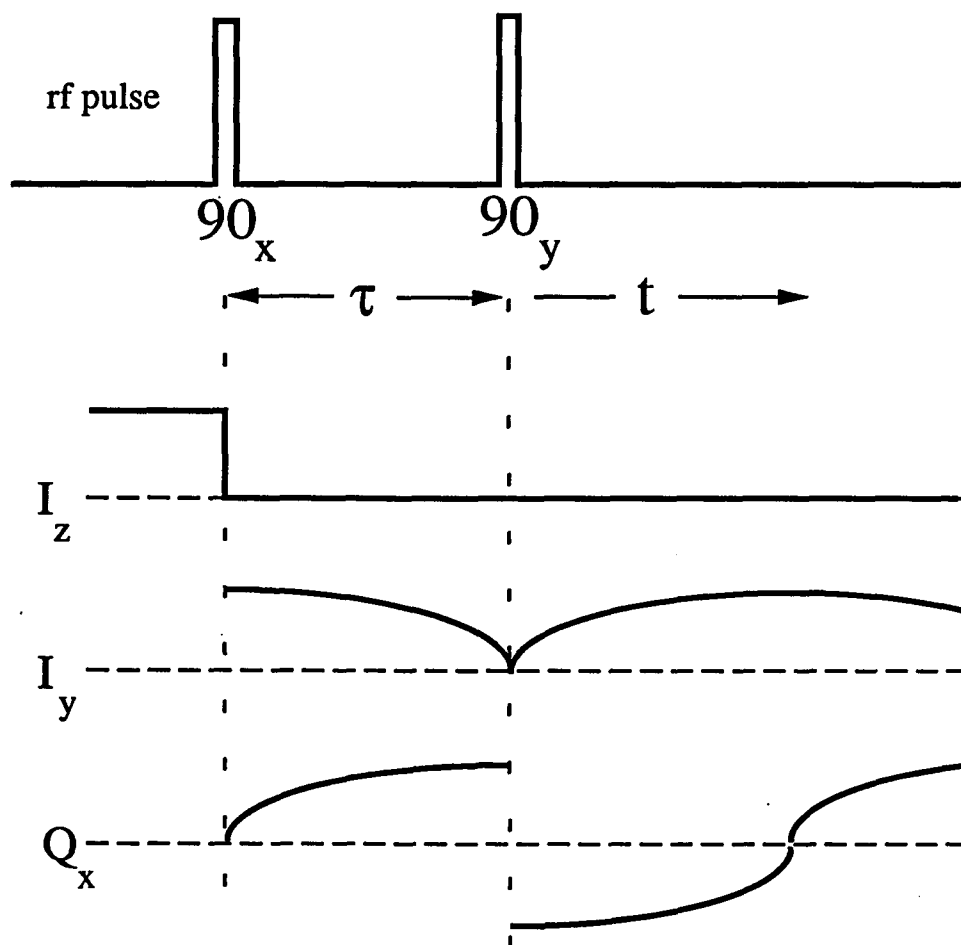


Figure 2.2 The quadrupole echo pulse sequence. The top line shows the pulsed rf used to manipulate the spins. Below, the time evolution of the three non-zero elements of the spin density matrix,  $I_z$ ,  $I_y$  and  $Q_x$ , is sketched. In this picture, the pulses are delta functions,  $\tau = 40 \mu\text{s}$ , and  $2\nu_Q = 125 \text{ kHz}$ .

At  $t = \tau$ , the two pulses have refocused the magnetization, this is the 'echo'. If  $\tau$  is chosen long enough (typically  $> 30 \mu\text{sec}$ ), the echo is formed outside the coil ring down time allowing complete digitization of the FID. A Fourier transform of this time domain data gives undistorted spectra in frequency space with a pair of symmetric peaks separated by  $2\nu_Q^i$  (in Hertz) for each non-equivalent deuteron site  $i$ . The next section will explain how these experimentally measured quadrupolar splittings are used to measure orientational order parameters of nematogens.

#### 2.4 $^2\text{H-NMR}$ Spectra of Molecules in Nematic Liquid Crystal Phases

Expressions for the frequency splittings need to be obtained in terms of the orientational order parameters  $Q$  and  $D$ . The frequency splittings observed in the spectra,  $2\nu_Q$ , correspond to transitions between the energy levels illustrated in Fig. 2.1.

$$2\nu_Q = \frac{6}{h} \langle T_{2,0}^L \rangle. \quad (2.25)$$

This expression requires the value of the quadrupole tensor in a laboratory fixed frame,  $\langle T_{2,0}^L \rangle$ . However, the explicit form of the electric field gradient tensor (EFG) is known only in the principal axis system (PAS):  $\langle T_{2,0}^P \rangle$ . The PAS is the frame in which the field gradient tensor is diagonal. For many deuterated sites on organic molecules, the z-axis of the PAS is aligned with the C- $^2\text{H}$  internuclear vector. In the PAS, the spherical tensor describing the electric field gradient is diagonal and traceless (Laplace's equation  $\nabla^2 V = 0$ ) and thus has only three non-zero elements:

$$\langle T_{2,0}^P \rangle = \frac{e^2 q_{zz} Q}{4} \quad (2.26)$$

$$\langle T_{2,\pm 1}^P \rangle = 0 \quad (2.27)$$

$$\langle T_{2,\pm 2}^P \rangle = \frac{\eta e^2 q_{zz} Q}{8} \quad (2.28)$$

Here  $q_{zz}$  is the vibrationally averaged z-component of the electric field gradient in the PAS,  $\langle V_{zz} \rangle$ , and  $\eta$  is the asymmetry parameter,  $\eta = \left\langle \frac{V_{xx} - V_{yy}}{V_{zz}} \right\rangle$ . The vibrationally averaged quadrupole coupling constant is defined to be  $\bar{\nu}_Q \equiv \left\langle \frac{e^2 q_{zz} Q}{h} \right\rangle$ . Typically, for C-D bonds the values of  $\bar{\nu}_Q$  for sp hybridization are  $200 \pm 5$  kHz, for sp<sup>2</sup> are  $182 \pm 5$  kHz, and for sp<sup>3</sup> are  $169 \pm 5$  kHz [76].

In order to derive expressions for the observed spectra in terms of the orientational order parameters, the Euler angles which describe the rotation from the PAS frame of the EFG tensor into the laboratory frame must be found. The advantage of spherical tensor operators is their behavior under coordinate transformations. Rotation of a spherical tensor from one coordinate system (CS1) to a second (CS2) using the y-convention Euler angles  $(\alpha, \beta, \gamma)$  is given by

$$\begin{aligned} CS1 &\rightarrow (\alpha, \beta, \gamma) \rightarrow CS2 \\ T_{l,m}^{CS2} &= \sum_{n=-l}^l D_{nm}^l(\alpha, \beta, \gamma) T_{l,n}^{CS1} \end{aligned} \quad (2.29)$$

where  $D_{nm}^l(\alpha, \beta, \gamma)$  is the n,m element of the l<sup>th</sup> rank Wigner rotation matrix. Elements of the second rank (l=2) rotation matrix are listed in Appendix III.

For rigid molecules, it is convenient to describe rotations from the

laboratory frame into the EFG principal axis frame in three steps. The first rotation  $(\alpha_1, \beta_1, \gamma_1)$  transforms the PAS frame of the electric field gradient tensor into the molecular axis frame. In rigid molecules, these angles are time independent. The second rotation  $(\alpha_2, \beta_2, \gamma_2)$  describes the time averaged position of the molecule with respect to the liquid crystal director's frame. The order parameters are functions of these Euler angles,  $Q = \left\langle \frac{3}{2} \cos^2 \beta_2 - \frac{1}{2} \right\rangle$  and  $D = \left\langle \frac{3}{2} \sin^2 \beta_2 \cos 2\alpha_2 \right\rangle$ . The last rotation  $(\alpha_3, \beta_3, \gamma_3)$  describes the orientation of the director of the nematic phase in the static external magnetic field. The director of nematogens spontaneously aligns along a strong external magnetic field, and thus  $(\alpha_3, \beta_3, \gamma_3) = (0, 0, 0)$ . Combining the three rotations, a compact expression for the field gradients in the lab frame can be derived in terms of the three sets of Euler angles:

$$\langle T_{2,0}^L \rangle = \sum_{p,q,r=-2}^2 \langle D_{p0}^2(\alpha_3, \beta_3, \gamma_3) D_{qp}^2(\alpha_2, \beta_2, \gamma_2) D_{rq}^2(\alpha_1, \beta_1, \gamma_1) \rangle \langle T_{2r}^P \rangle. \quad (2.30)$$

Rigorously, there is one ensemble average of the entire expression. If all motions are decoupled, the ensemble averages over  $\Omega_1$ ,  $\Omega_2$ , and  $\Omega_3$  can be performed independently. Combining equations (2.25) and (2.30), the following general expression for quadrupolar splittings can be derived:



$$\begin{aligned}
2v_e &= \frac{3}{2} \bar{v}_e \left\{ \frac{3}{2} \cos^2 \beta_3 - \frac{1}{2} \right\} \\
&\left\{ Q \left\langle \frac{3}{2} \cos^2 \beta_1 - \frac{1}{2} \right\rangle + \frac{1}{2} D \left\langle \sin^2 \beta_1 \cos 2\gamma_1 \right\rangle \right. \\
&\quad \left. + \frac{1}{2} \eta \left[ Q \left\langle \sin^2 \beta_1 \cos 2\gamma_1 \right\rangle \right. \right. \\
&\quad \left. \left. + \frac{1}{3} D \left\langle (1 + \cos^2 \beta_1) \cos 2\alpha_1 \cos 2\gamma_1 - 2 \cos \beta_1 \sin 2\alpha_1 \sin 2\gamma_1 \right\rangle \right] \right\}.
\end{aligned} \tag{2.31}$$

The rigid solute, p-Xy, is a highly symmetric molecule. There are two distinct deuteron sites on p-Xy: the methyl (Me) and aromatic (Ar). For the methyl groups, the expression for the quadrupole splitting is

$$2v_{\mathcal{Q}}^{Me} = \frac{3}{4} Q_2 \bar{v}_{\mathcal{Q}}^{Me} [3\cos^2(\beta_1^{Me}) - 1] \tag{2.32}$$

while the aromatic deuterons give

$$2v_{\mathcal{Q}}^{Ar} = \frac{3}{4} \bar{v}_{\mathcal{Q}}^{Ar} \left[ Q_2(3\cos^2\beta_1^{Ar} - 1) + D_2\sin^2\beta_1^{Ar} \right] \tag{2.33}$$

with  $\beta_1^{Me} = 70.5^\circ$ ,  $\beta_1^{Ar} = 60^\circ$ ,  $\bar{v}_{\mathcal{Q}}^{Ar} = 182 \text{ kHz}$ , and  $\bar{v}_{\mathcal{Q}}^{Me} = 169 \text{ kHz}$ . Since the asymmetry parameter in the electric field gradient tensor is typically small ( $\eta=0.00$  for rapidly rotating methyl sites, and  $\eta=0.04$  for aromatic sites), it has been neglected. This could be a potential problem for aromatic sites whose average orientation with respect to the magnetic field is close to the magic angle. If  $\theta$  is the angle between the C-D internuclear vector and the magnetic field, the 'magic angle' ( $54.7^\circ$ ) is the angle at which  $(3/2\cos^2\theta - 1/2) = 0$ . The contribution of these asymmetry terms to the theoretical prediction for the splittings will be investigated later.

Almost all liquid crystal molecules have flexible tails connected to rigid aromatic cores. In order to derive expressions for the splittings from deuterated sites on the rigid core of the liquid crystal FLOC, four independent rotations are used. The Euler angles  $(\alpha_1, \beta_1, \gamma_1)$ , which describe the relative orientation of the EFG PAS and core axis systems, are time independent. These Euler angles were measured using X-ray techniques [77], they are listed in Table 2.1 and shown in Fig. 2.3. The second rotation  $(\alpha_2, \beta_2, \gamma_2)$  from the core frame into the molecular frame is deceptively simple. Implicit in the definition of this molecule fixed frame is a statistical average over all conformations of the flexible alkyl chain. The third rotation  $(\alpha_3, \beta_3, \gamma_3)$  describes the time averaged position of the molecule with respect to the liquid crystal director's frame. The orientational order parameters are functions of  $\Omega_3$ . Finally, because the uniaxial nematic phase orients with the large static magnetic field, the director is always coincident with the external magnetic field and thus  $(\alpha_4, \beta_4, \gamma_4) = (0, 0, 0)$ . Combining the four rotations, a compact expression for the field gradients in the lab frame can be derived:

$$\begin{aligned} \langle T_{2,0}^L \rangle = & \sum_{p,q,r,s=-2}^2 \langle D_{p0}^2(\alpha_4, \beta_4, \gamma_4) \rangle \langle D_{qp}^2(\alpha_3, \beta_3, \gamma_3) \rangle \\ & \langle D_{rq}^2(\alpha_2, \beta_2, \gamma_2) \rangle \langle D_{sr}^2(\alpha_1, \beta_1, \gamma_1) \rangle \langle T_{2,s}^P \rangle. \end{aligned} \quad (2.34)$$

This summation is performed giving following theoretical expression for the quadrupolar splittings. To keep this expression tractable, all terms involving the asymmetry parameter are ignored.

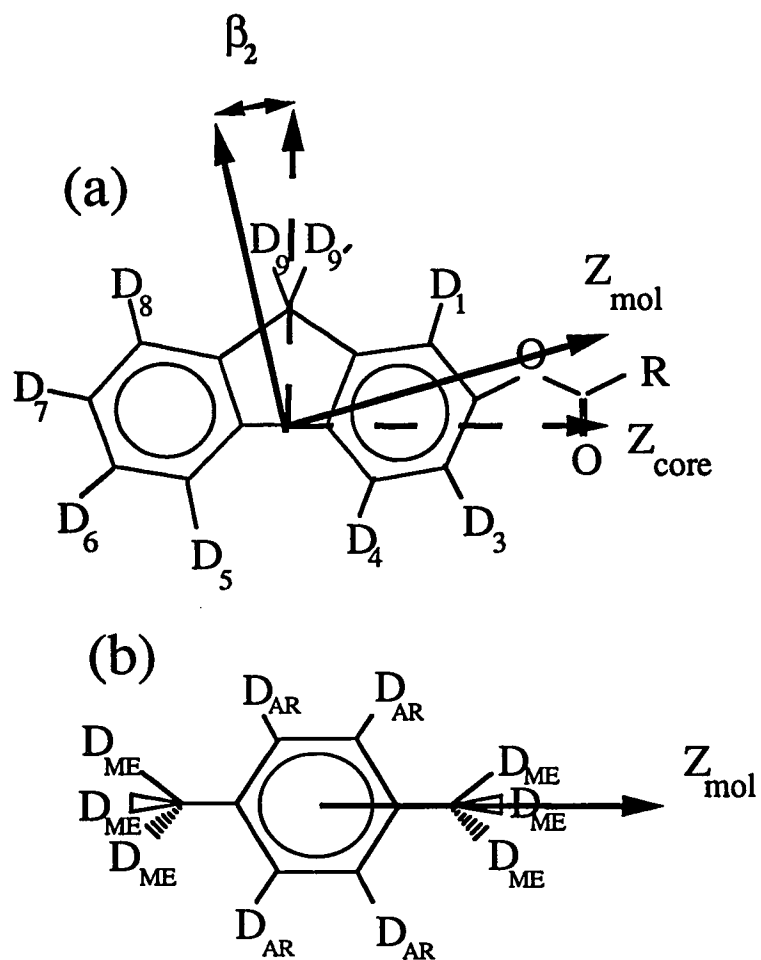


Figure 2.3 The fluorene moiety of the liquid crystal FLOC is pictured to illustrate the Eulerian angles described in the text. The principle axis of the EFG tensor is aligned along the C-D internuclear vector. X-ray analysis gives the orientation of these principle axis with respect to the dashed axis (Ref. 62). The angle  $\beta_2$ , which is fit using the quadrupole splittings (Ref. 58), gives average orientation of the molecular frame (solid axis). The site assignments are labeled for (a) FLOC and (b) p-Xy.

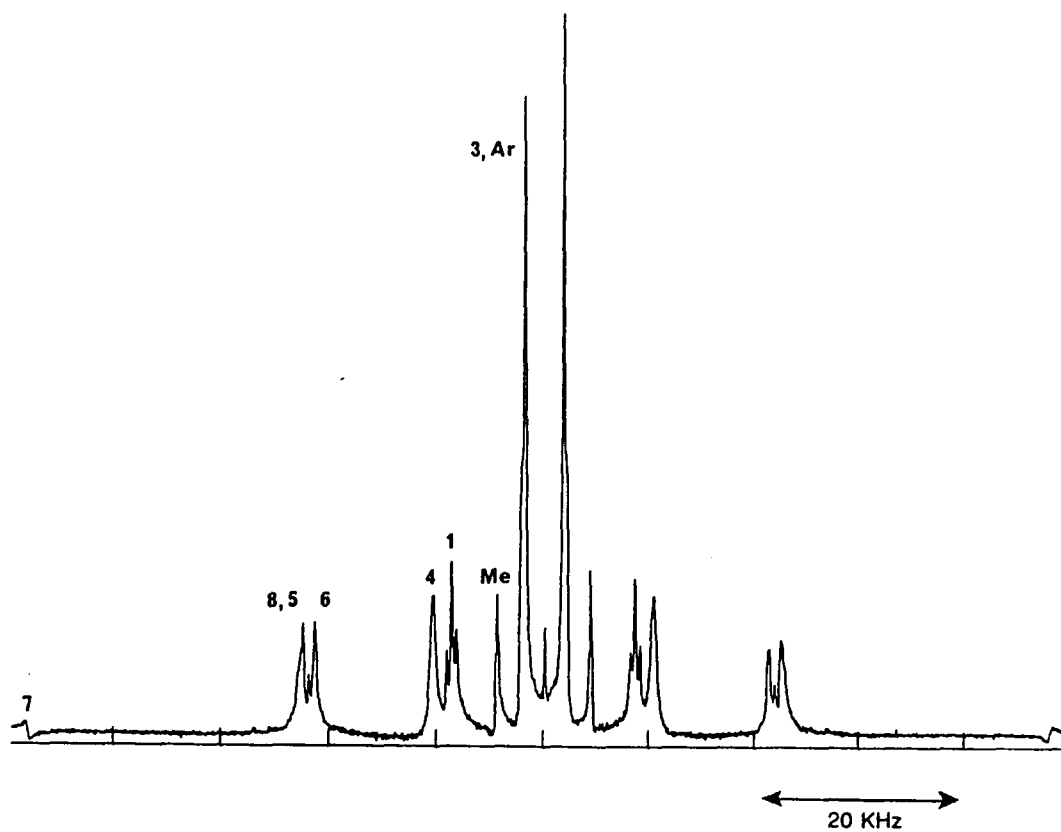


Figure 2.3(c) Site assignments on the  $^2\text{H}$ -NMR spectra of the FLOC : p-Xy mixture for an experiment performed at 93.82 °C.

Site No.	$\alpha_1$	$\beta_1$	$\gamma_1$
1 and 4	180°	71°	90°
3	0°	47.5°	270°
5 and 8	0°	71°	270°
6	180°	47.5°	90°
7	0°	10.5°	270°
9 and 9'	180°	90°	$\pm 144.735^\circ$

Table 2.1 X-ray studies of fluorene [62] give the location of the PAS of the EFG tensor in the core axis frame in terms of y-convention Euler angles.

$$\begin{aligned}
2v_{\rho} = \frac{3}{8} \bar{v}_{\rho} & \left\{ \frac{3}{2} \cos^2 \beta_4 - \frac{1}{2} \right\} \\
& \left\{ \left[ \frac{3}{2} \cos^2 \beta_3 - \frac{1}{2} \right] \right. \\
& \left[ (3 \cos^2 \beta_2 - 1) (3 \cos^2 \beta_1 - 1) \right. \\
& - 3 \cos(\alpha_2 + \gamma_1) \sin 2\beta_2 \sin 2\beta_1 + 3 \cos(2\alpha_2 + 2\gamma_1) \sin^2 \beta_2 \sin^2 \beta_1 \left. \right] \\
& + \left[ \frac{3}{2} \sin^2 \beta_3 \cos(2\alpha_3 + 2\gamma_2) \right] \\
& \left. \left[ \cos(2\alpha_2 + 2\gamma_1) (1 + \cos^2 \beta_2) \sin^2 \beta_1 \right. \right. \\
& \left. \left. + 2 \cos(\alpha_2 + \gamma_1) \cos \beta_2 \sin \beta_2 \sin 2\beta_1 + \sin^2 \beta_2 (3 \cos^2 \beta_1 - 1) \right] \right\} \quad (2.35)
\end{aligned}$$

FLOC is perdeuterated on the rigid fluorene moiety. From Table 2.1, it is observed that all seven of the aromatic sites (sites #1,#3-#8) are coplanar. For these sites, the influence of a finite asymmetry parameter ( $\eta \approx 0.04$ ) is expected to be small, unless the angle between the C-D bond z-axis and laboratory z-axis is close to the magic angle. Effects of this  $\eta=0$  approximation on the experimentally determined order parameters will be discussed in more detail later. Briefly, for both molecules p-Xy and FLOC, it appears that discrepancies between the theoretical fits and the experimental data are of the same order of magnitude as these neglected asymmetry terms. With zero asymmetry parameter, the expression for the  $j^{\text{th}}$  aromatic site in the plane of the fluorene core is given below

$$\begin{aligned}
2\nu_Q^j &= \left\{ \frac{3}{8} \bar{\nu}_Q^j \right\} \\
&\{ Q [ (3\cos^2\beta_2 - 1)(3\cos^2\beta_1^j - 1) \\
&\quad - 3\sin\alpha_2 \sin 2\beta_2 \sin 2\beta_1^j - 3\cos 2\alpha_2 \sin^2\beta_2 \sin^2\beta_1^j ] \\
&+ D [ \cos 2\alpha_2 \sin^2\beta_1^j (1 + \cos^2\beta_2) \\
&\quad - \sin\alpha_2 \sin 2\beta_2 \sin 2\beta_1^j + \sin^2\beta_2 (3\cos^2\beta_1^j - 1) ] \}
\end{aligned} \tag{2.36}$$

where  $\bar{\nu}_Q^j$  is taken to have an intrinsic value of 182 kHz for the aromatic deuterons on the fluorene core. For the  $j = 9$  site,

$$\begin{aligned}
2\nu_Q^9 &= \frac{3}{8} \bar{\nu}_Q^9 \{ Q [ 1 - 3\cos^2\beta_2 + 3\sin^2\beta_2 \cos(2\alpha_2 + 2\gamma_1) ] \\
&\quad + D [ \sin^2\beta_2 - (1 + \cos^2\beta_2) \cos(2\alpha_2 + 2\gamma_1) ] \}.
\end{aligned} \tag{2.37}$$

The quadrupolar coupling constant for this hybridized aliphatic deuteron,  $\bar{\nu}_Q^9$ , is taken to be 169 kHz, and the asymmetry parameter for the  $j = 9$  site is assumed to be zero.

The assumption that the asymmetry parameter in the quadrupolar tensor  $\eta$  has no effect will be explored in more detail by estimating the order of magnitude of the error introduced. For FLOC, the expression for the splittings are functions of the order parameters and two sets of Eulerian angles. Formally, the three successive rotations can be done in one equivalent rotation,

$$\mathfrak{R}(\Phi, \Theta, \Psi) = \mathfrak{R}(-\gamma_1, -\beta_1, -\alpha_1), \mathfrak{R}(-\gamma_2, -\beta_2, -\alpha_2), \mathfrak{R}(-\gamma_3, -\beta_3, -\beta_3) \tag{2.38}$$

These rotations can be expressed in terms of Cartesian rotation matrices in the  $y$ -convention. Exploiting the inversion symmetry of the phase [78], the expression for the splittings becomes

$$2v'_q = \bar{v}'_q \left[ \left( \frac{3}{2} \cos^2(\Theta) - \frac{1}{2} \right) + \frac{\eta'}{2} \left( \frac{3 \sin^2(\Theta) \cos(2\Psi)}{2} \right) \right] \quad (2.23)$$

This equation is useful for exploring the effect of neglecting  $\eta$  when determining the order parameters from  $^2\text{H-NMR}$  results.

### 2.5 Sample Preparation and Experimental Setup

The deuterated liquid crystal FLOC<sub>14-d<sub>10</sub></sub> was obtained from the organic synthesis group at the Liquid Crystal Institute at Kent State University. A detailed description of the chemical synthesis has been published [79]. Para-xylene-d<sub>10</sub> was supplied by Merck, Sharp and Dohme. A homogeneous mixture was obtained by micropipetting the p-Xy into the isotropic phase of FLOC and homogenizing with a vortex mixer. Because of the high temperature (~160°C) and the length of time before the 5 mm NMR tube was sealed, the concentration of p-Xy is expected to be lower than the gravimetrically determined value (20 mole %). Assuming complete deuteration, the integrated intensity of the  $^2\text{H-NMR}$  spectrum gives the concentration to be approximately 11 mole % [66].

The  $^2\text{H-NMR}$  experiments were performed using a home built pulse spectrometer constructed at William and Mary by Dr. Hoatson. It has the following components: (1) a radio frequency (rf) transmitter which creates high power rf pulses, (2) a probe to couple this radiation to the sample, (3) a receiver to amplify the response of the nuclear spins to the radiation, (4) a pair of analog to digital converters (ADC) to digitize the complex signal, and (5) a pulse programmer to interface the spectrometer with a computer (see the schematic in Figure 2.4). The transmitter has three parts: (1) a highly



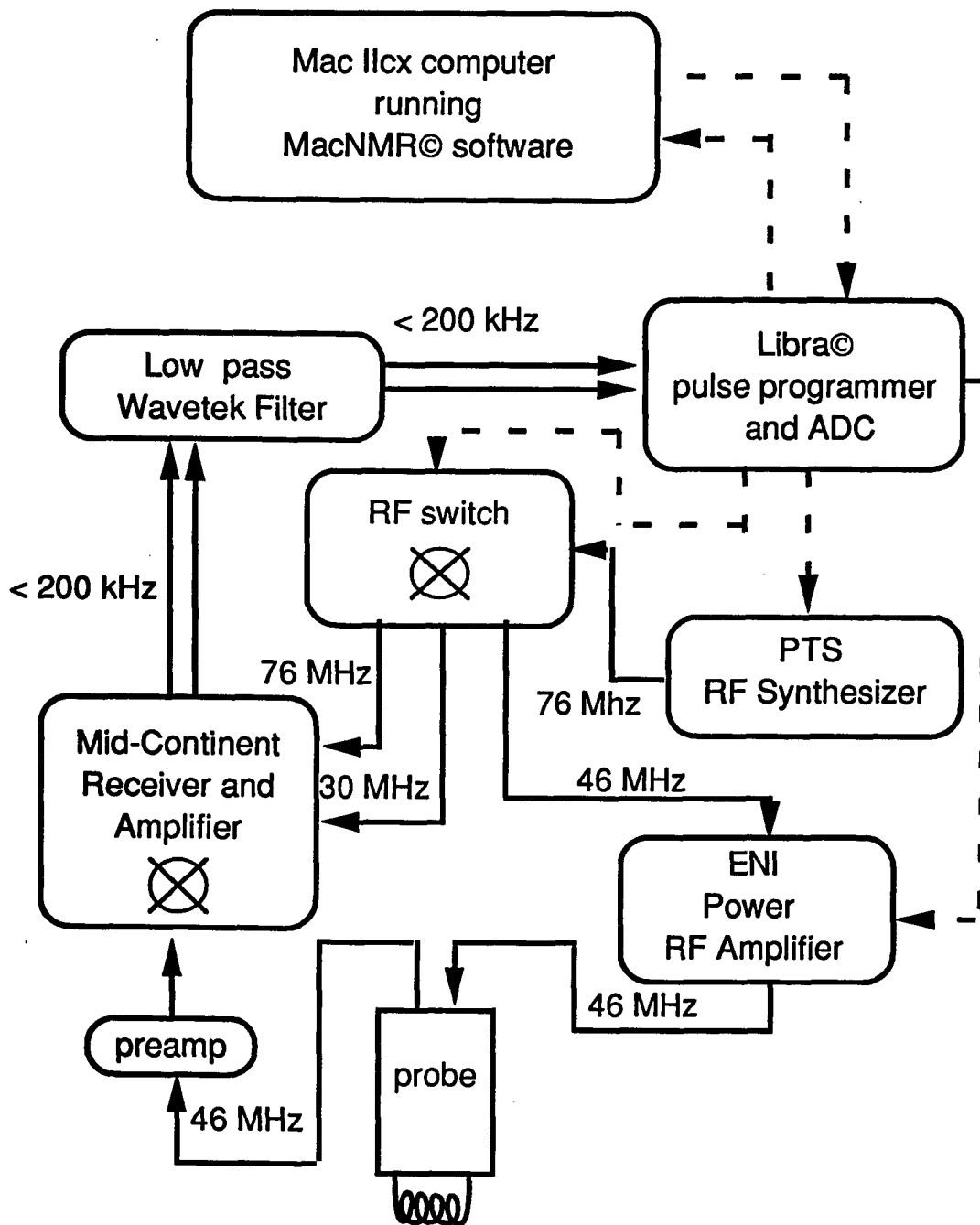


Figure 2.4 Block diagram of a pulsed NMR spectrometer.

stable rf frequency synthesizer which is gated by (2) an rf switch which feeds (3) a power rf amplifier. The phase and duration of the pulse is set using the rf switch. The power amplifier, which is capable of delivering short (1-10  $\mu\text{sec}$ ), high power ( $>1\text{kW}$ ) pulses, amplifies the gated signal from the rf switch. The pulsed signal is sent to the probe which houses a coil in a resonant circuit. This resonant L-C circuit is tuned with variable capacitors such that the probe impedance is strictly resistive ( $\phi=0$ ) matched to the line ( $|Z|=50\Omega$ ), insuring a minimum reflection of rf power. The quality factor Q of the L-C circuit is optimized such that the field induced in the coil ( $B_1 \sim 237$  Gauss) is large and the ringdown time (receiver dead time  $\sim 30\mu\text{s}$ ) is small. The response from nuclear spins in the sample to the induced magnetic field is received using the same coil. The receiver is comprised of a train of linear analog amplifiers which magnify the FID signal (as small as  $\mu\text{Volts}$ ) and a set of low pass filters used to eliminate high frequency background noise. After several amplifications, the ADCs digitize and store the signal. The digitized signal is sent to a computer (a Macintosh II CX) which runs software designed to read the digitized signal from the ADC and perform data processing. The computer is also connected to a pulse programmer which controls the three parts of the transmitter. Via this interface, the experimenter can set the duration, frequency, amplitude and phase of the pulsed rf used in excitation sequences.

## 2.6 $^2\text{H}$ -NMR Experimental Results

$^2\text{H}$ -NMR spectra for the binary mixture of FLOC:p-Xy were obtained by Dr. G. L. Hoatson using a 32.8 MHz spectrometer at the Liquid Crystal Institute [58,66]. All  $^2\text{H}$ -NMR spectra were recorded using the quadrupole echo pulse sequence with the

following relevant experimental parameters: 90° pulse length = 4.5 μs, echo delay  $\tau = 100\mu\text{s}$ , dwell time = 5μs, data size was 2K complex points giving a spectral width of  $\pm 100$  kHz, and 2500 scans with a 1s recycle time were used to signal average. The experimentally measured quadrupolar splittings are listed in Table 2.2 as a function of temperature.

The first step in analyzing  $^2\text{H}$ -NMR spectra is to assign the spectral lines to specific deuteron sites and to determine the relative signs of the quadrupole coupling constants. For pure FLOC, this assignment was made by Wu, Ziemnicka and Doane and is shown in figure 2.3(c) [80]. Values for the order parameters for FLOC in the mixture,  $Q_1$  and  $D_1$ , and the Euler angle  $\beta_2$ , which describes the orientation of FLOC's fluorene core, were obtained using a nonlinear least squares fitting routine. The routine minimized the function,

$$\chi^2 = \sum_j \frac{\left[ 2\nu_Q^{j,\text{exp}} - 2\nu_Q^{j,\text{fit}}(\beta_1^j; Q_1, D_1, \beta_2) \right]^2}{\sigma_j^2}. \quad (2.41)$$

Where  $2\nu_Q^{j,\text{exp}}$  are experimentally measured spectral widths for the  $j^{\text{th}}$  site listed in Table 2.2,  $2\nu_Q^{j,\text{fit}}$  are the spectral widths calculated using Eqn. (2.36), and  $\sigma_j$  is the estimated uncertainty in the measurement of the spectral width. Data from the five independent experimental sites on the fluorene core were used. The resulting order parameters are presented in Table 2.3 and plotted as a function of temperature in Figure 2.5. With  $\sigma_j < 1.5$  kHz, the convergence was unreliable, probably due to neglect of the asymmetry parameter in the theoretical expressions. Measured values of the quadrupolar splittings,  $2\nu_Q^{j,\text{exp}}$ , are considerably more precise, of the order  $\pm 0.4$  kHz. The correlations between

T (°C)	$2v_{\varrho}^1$	$2v_{\varrho}^3$	$2v_{\varrho}^4$	$2v_{\varrho}^5$	$2v_{\varrho}^6$	$2v_{\varrho}^7$	$2v_{\varrho}^8$	$2v_{\varrho}^{AR}$	$2v_{\varrho}^{ME}$
93.82	-34.08	7.47	-40.97	-88.77	84.13	191.84	-88.77	7.47	17.33
96.60	-33.59	7.54	-40.23	-87.60	83.35	188.87	-87.60	7.52	17.38
99.53	-32.81	7.57	-39.55	-86.13	82.52	187.06	-86.13	7.57	17.19
102.46	-31.98	7.62	-38.63	-84.77	81.54	183.98	-84.77	7.62	17.09
105.30	-31.01	7.44	-37.65	-83.01	80.37	181.30	-83.00	7.44	16.89
108.13	-29.93	7.67	-36.43	-81.10	78.61	177.00	-81.10	7.67	16.60
111.05	-28.17	7.62	-34.67	-76.56	76.56	173.09	-76.56	7.62	15.92
114.02	-28.86	7.52	-32.81	-73.88	73.88	164.46	-73.88	7.18	15.87
117.00	-20.75	7.72	-26.03	-61.57	63.10	143.26	-61.57	6.69	13.53
118.22	-19.82	7.67	-24.61	-59.10	60.84	137.74	-59.10	6.49	12.89
118.63	-19.87	7.59	-24.37	-58.06	59.96	135.25	-58.06	6.40	12.79
119.05	-19.04	7.57	-23.58	-56.99	58.84	133.40	-56.99	6.35	12.60
119.57	-18.75	7.52	-22.80	-56.20	57.81	132.37	-56.20	6.20	12.31
120.00	-18.46	7.47	-22.31	-54.83	56.98	129.78	-54.83	6.15	11.95
120.44	-17.92	7.37	-21.93	-53.27	55.67	127.69	-53.27	6.00	11.94
120.97	-17.14	7.23	-20.50	-51.45	54.25	124.51	-51.47	5.90	11.04
121.52	-16.41	7.08	-19.43	-49.71	52.78	121.97	-49.71	5.67	11.33
121.97	-16.98	6.98	-18.26	-47.5	51.86	119.19	-47.75	5.66	10.25
122.50	-15.67	6.79	-16.99	-45.51	50.34	115.87	-45.51	5.47	9.86
122.99	-14.68	6.59	-16.44	-42.99	48.49	113.28	-42.99	5.23	8.74
123.47	-13.08	6.49	-15.77	-40.58	47.56	110.30	-40.58	5.13	7.39
123.97	-12.79	6.40	-14.99	-41.16	45.31	105.02	-41.16	5.33	7.66

Table 2.2 The experimental data of quadrupole splittings,  $2v_{\varrho}^i$  (kHz), for the binary mixture FLOC : p-Xy.

T (°C)	$\chi^2$	$Q_1^a$	$D_1^b$	$\beta_2^c$	$Q_2^d$	$D_2^e$
93.82	0.1802	0.81	-0.057	6.901°	0.205	0.141
96.60	0.4399	0.80	-0.058	6.930°	0.206	0.142
99.53	0.2355	0.79	-0.060	6.924°	0.203	0.142
102.46	0.3981	0.78	-0.061	6.946°	0.202	0.142
105.30	0.1543	0.77	-0.062	6.960°	0.200	0.140
108.13	0.3701	0.75	-0.063	6.964°	0.197	0.140
111.05	0.1768	0.73	-0.071	6.909°	0.189	0.137
114.02	0.1394	0.69	-0.068	7.011°	0.188	0.133
117.00	0.8430	0.60	-0.074	6.889°	0.160	0.119
118.22	0.9017	0.58	-0.073	6.897°	0.152	0.114
118.63	0.5614	0.57	-0.072	6.901°	0.152	0.113
119.05	1.029	0.56	-0.073	6.895°	0.149	0.112
119.57	2.136	0.55	-0.074	6.874°	0.145	0.109
120.00	1.655	0.54	-0.074	6.875°	0.142	0.107
120.44	1.961	0.53	-0.074	6.821°	0.141	0.105
120.97	2.937	0.52	-0.076	6.837°	0.131	0.101
121.52	4.303	0.51	-0.077	6.834°	0.134	0.100
121.97	4.832	0.49	-0.080	6.857°	0.121	0.096
122.50	6.179	0.48	-0.083	6.874°	0.117	0.092
122.99	8.653	0.47	-0.084	6.775°	0.104	0.086
123.47	9.1134	0.45	-0.087	6.756°	0.088	0.079
123.97	5.9930	0.43	-0.076	6.834°	0.091	0.082

<sup>a</sup>  $\delta Q_1 = \pm 0.010$

<sup>b</sup>  $\delta D_1 = \pm 0.014$

<sup>c</sup>  $\delta \beta_2 = \pm 0.005^\circ$

<sup>d</sup>  $\delta Q_2 = \pm 0.018$

<sup>e</sup>  $\delta D_2 = \pm 0.021$

Table 2.3 Results of nonlinear least squares fits of the parameters for FLOC ( $Q_1$ ,  $D_1$  and  $\beta_2$ ) and p-Xy ( $Q_2$  and  $D_2$ ).

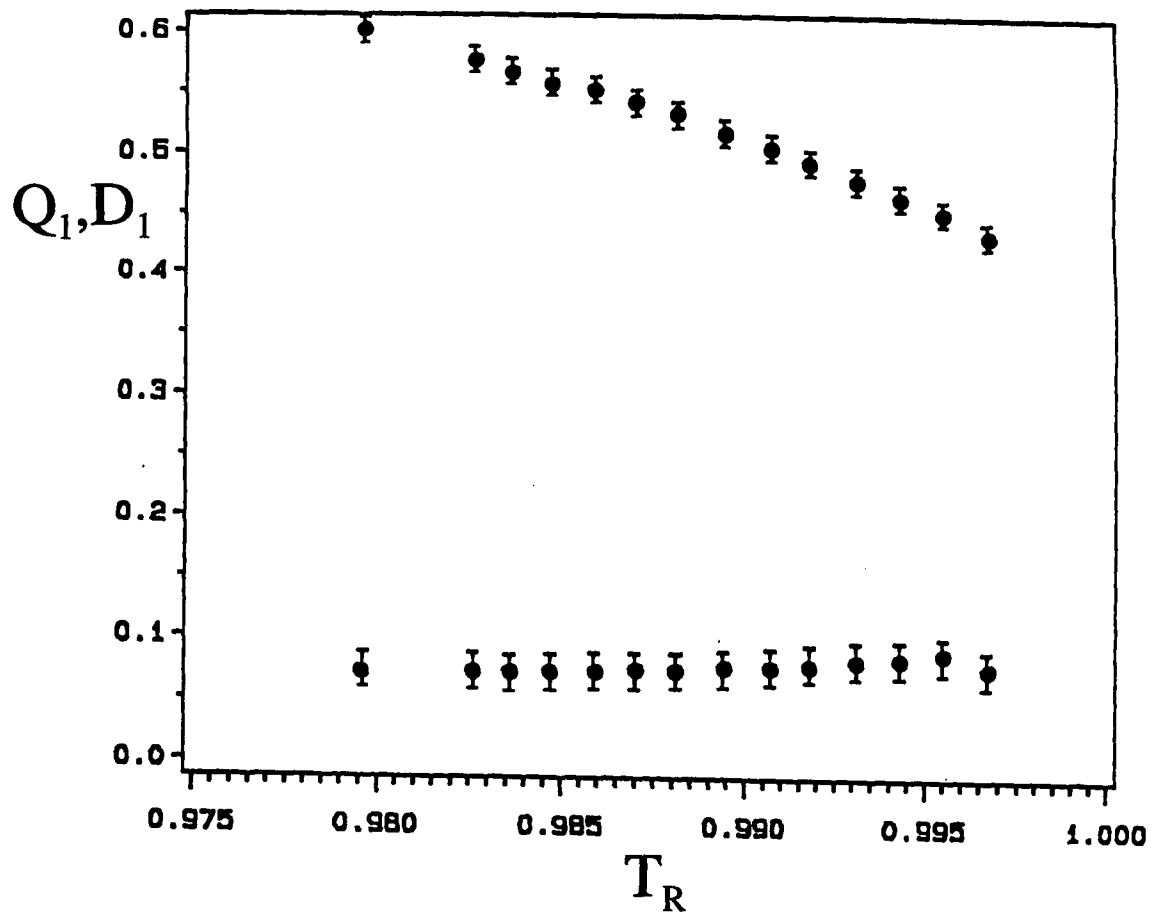


Figure 2.5 Molecular orientational order parameters of both components,  $Q_i$  and  $D_i$ , as a function of reduced temperature  $T_R$ .  
(a)  $i = 1$ , FLOC.

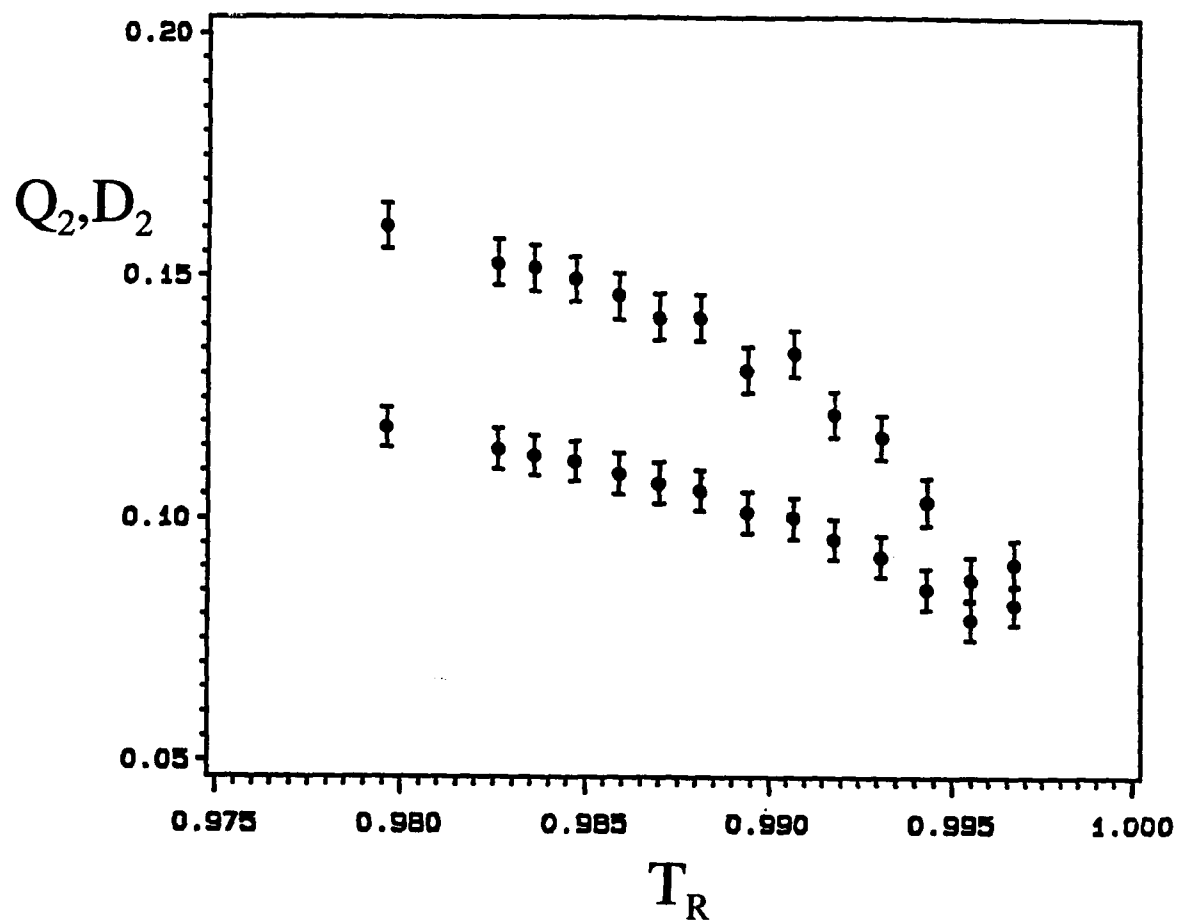


Figure 2.5 Molecular orientational order parameters of both components,  $Q_i$  and  $D_i$ , as a function of reduced temperature  $T_R$ .  
(b)  $i = 2$ , p-Xy.

parameters are reasonably small, with off diagonal elements of the inverse of the covariant matrix less than 0.3. The  $\chi^2$  were acceptable ( $\leq 1$ ) for the lower temperature data, but increased with increasing temperature. This is to be expected since with decreased splittings the contributions from a finite asymmetry parameter would become more significant.

Rather than making the assumption that the principal axes systems of the core and molecule are coplanar [80] this description includes the possibility of a twist in the relative orientation. In order to determine the twist angle,  $\alpha_2$ , the quadrupole splitting from the site  $j = 9$  is required since this is the only position with deuterons out of the plane of the core ( $\gamma_1 = -90^\circ$ ). By reanalyzing the published  $j = 9$  splittings pure FLOC [80], the angle  $\alpha_2$  was determined using eqn. (2.37). In the nematic range for pure FLOC (124.3°C to 136.3°C), the twist angle  $\alpha_2$  was found to be  $-88.8^\circ \pm 0.4^\circ$ . For the 46K range, including the both the nematic and the smectic-A phase,  $\alpha_2$  was found to be a monotonically decreasing function with temperature with a mean value of  $-87.6^\circ$ , and a total range of  $2.8^\circ$ . Thus deviations from planarity appear to be insignificant and the inclusion of the twist angle was found to have a negligible effect on the derived order parameters. Such insensitivity makes the additional parameterization difficult to justify. The FLOC used in the mixture was incompletely deuterated at the  $j = 9$  sites and the low intensities and poor accuracy of the measurements made derivation of  $\alpha_2$  unreliable. Thus, analysis of the binary mixture assumed a fixed value  $\alpha_2 = -90^\circ$ . This is expected on the basis of chemical intuition.

The role of the asymmetry in the electric field gradient tensor,  $\eta$ , has been



explored in detail. So far, the nine Euler angles in Eqn. (2.38) were determined by fitting the experimental data assuming the  $\eta$  terms were zero. Given these Euler angles, matrix multiplication of the Cartesian rotation matrices in Eqn. (2.38) allows the equivalent rotation,  $\mathfrak{R}(\Phi, \theta, \Psi)$ , to be determined. The first term in Eqn. (2.39) is equivalent to Eqns. (2.36) and (2.37), and it gives the theoretical splittings assuming  $\eta = 0$ . The second term provides a realistic estimate of the contribution to the splittings if the asymmetry parameter were finite,  $\eta=0.04$ . The theoretical splittings ( $2\nu_Q^{j/fit}$ ) and an estimate of the neglected asymmetry parameter on the size of the splittings ( $2\nu_Q^\eta$ ) are given in Table 2.4. It is interesting to note that the contribution from the asymmetry terms, most pronounced for smaller splittings, is sufficient to account for the discrepancies between experiment and theory. What is more important to determine is whether, in addition to better convergence, the inclusion of a finite asymmetry parameter in the calculation gives significantly different values for the order parameters. One estimate the magnitude of these effects can be made by attempting to compensate for the asymmetry parameter contributions. A typical value of the for the asymmetry was assumed,  $\eta = 0.04$ , and for the  $j = 3$  and 4 positions, the experimental splittings were replaced by the corrected values, ( $2\nu_Q^{j/fit} \pm 2\nu_Q^\eta$ ). The fitting procedure was repeated for all temperatures and the results show that, for either case, the new order parameters are within the reported errors (Table 2.3 and Figure 2.5). This confirms that neglect of  $\eta$  in no way compromises the orientational order parameters derived from the  $^2\text{H-NMR}$  experimental results. In order to do a completely rigorous analysis of the values of the quadrupole coupling constants,  $\bar{\nu}_Q^j$ , and asymmetry parameters,  $\eta^j$ , for each molecular site,  $j$ , should be determined and

T (°C)	$2\nu_{\rho}^{7,the}$	$2\nu_{\rho}^{7,asy}$	$2\nu_{\rho}^{8,the}$	$2\nu_{\rho}^{8,asy}$	$2\nu_{\rho}^{AR,asy}$
93.82	192.09	0.58	-88.45	4.35	1.20
96.60	189.23	0.58	-87.14	4.30	1.21
99.53	187.37	0.58	-85.84	4.26	1.20
102.46	184.39	0.58	-84.34	4.19	1.19
105.30	181.55	0.58	-82.74	4.13	1.18
108.13	177.35	0.57	-80.58	4.04	1.17
111.05	172.88	0.59	-76.96	3.95	1.13
114.02	164.71	0.57	-73.70	3.77	1.11
117.00	142.75	0.52	-61.43	3.28	0.97
118.22	137.20	0.51	-58.80	3.16	0.92
118.63	134.91	0.51	-57.80	3.10	0.92
119.05	132.90	0.51	-56.69	3.06	0.90
119.57	131.60	0.50	-55.86	3.03	0.88
120.00	129.10	0.50	-54.58	2.96	0.86
120.44	126.83	0.50	-53.29	2.92	0.86
120.97	123.52	0.50	-51.42	2.85	0.80
121.52	120.70	0.50	-49.80	2.79	0.82
121.97	117.85	0.50	-47.99	2.74	0.75
122.50	114.30	0.50	-45.94	2.66	0.73
122.99	111.30	0.50	-44.04	2.59	0.65
123.47	108.28	0.50	-42.09	2.57	0.57
123.97	103.53	0.46	-41.35	2.41	0.59

Table 2.4(b) Theoretical Splittings assuming the fit parameters are correct (  $2\nu_{\rho}^{j,the}$  ) and the asymmetry term contribution (  $2\nu_{\rho}^{j,asy}$  ) assuming  $\eta = 0.049$  (in kHz).

T (°C)	$2v_{\rho}^{3,the}$	$2v_{\rho}^{3,asy}$	$2v_{\rho}^{4,the}$	$2v_{\rho}^{4,asy}$	$2v_{\rho}^{6,the}$	$2v_{\rho}^{6,asy}$
93.82	7.02	3.06	-40.91	3.75	83.96	2.08
96.60	6.85	3.02	-40.09	3.70	82.99	2.05
99.53	7.07	2.99	-39.38	3.66	82.25	2.04
102.46	6.99	2.95	-38.48	3.61	81.19	2.01
105.30	7.05	2.91	-37.56	3.56	80.15	1.99
108.13	7.04	2.85	-36.47	3.48	78.42	1.95
111.05	8.04	2.79	-34.57	3.41	76.64	1.93
114.02	7.18	2.67	-32.64	3.26	73.61	1.84
117.00	8.08	2.33	-26.88	2.86	63.97	1.64
118.22	7.64	2.24	-25.58	2.75	61.68	1.59
118.63	7.78	2.21	-25.14	2.71	60.63	1.56
119.05	7.84	2.17	-24.59	2.67	59.79	1.54
119.57	7.98	2.16	-24.22	2.65	59.19	1.54
120.00	7.97	2.21	-23.57	2.60	58.16	1.51
120.44	8.14	2.08	-23.12	2.56	56.96	1.49
120.97	8.22	2.03	-22.05	2.50	55.75	1.46
121.52	8.33	1.99	-21.18	2.45	54.63	1.44
121.97	8.52	1.96	-20.06	2.40	51.86	1.42
122.50	8.63	1.91	-18.89	2.34	50.34	1.39
122.99	9.01	1.86	-18.19	2.29	48.49	1.39
123.47	9.29	1.82	-17.14	2.23	47.56	1.35
123.97	8.05	1.73	-17.04	2.12	45.31	1.27

Table 2.4(a) Theoretical Splittings assuming the fit parameters are correct (  $2v_{\rho}^{j,the}$  ) and the asymmetry term contribution (  $2v_{\rho}^{j,asy}$  ) assuming  $\eta = 0.049$  (in kHz).

explicitly included. These values have recently been measured from a single crystal of perdeuterated fluorene with  $^2\text{H-NMR}$  [81]. Fortunately, this daunting calculation does not appear to be necessary.

Analysis of the  $p\text{-Xy}$  splittings is comparatively straight forward because of the rigid molecular geometry. As discussed earlier, there are two distinct deuteron sites, methyl and aromatic. The splittings from the deuterated  $p\text{-Xy}$  sites,  $2\nu_Q^{Me}$  and  $2\nu_Q^{Ar}$ , were measured and Eqns. (2.32) and (2.33) were solved simultaneously to determine the orientational order parameters of  $p\text{-Xy}$  in the mixture,  $Q_2$  and  $D_2$ . The results, neglecting the asymmetry in the EFG tensor, are presented in Table 2.3 and Figure 2.5. The primary source of error is taken to be the accuracy of measuring the splittings ( $\pm 0.4$  kHz). Simple error propagation was used to estimate the errors in the order parameters.

## 2.7 A Mean Field Theory of Binary Mixtures

The temperature dependence of the experimentally measured order parameters ( $Q_1$ ,  $Q_2$ ,  $D_1$ , and  $D_2$ ) are interpreted using a mean field theory of binary mixtures of biaxial nematic liquid crystals [41]. The parameters of the theory are coupling constants,  $r_i$ , which gives a measure of how strongly a molecule couples to a given mean field,  $\Lambda$ . In the case of cylindrically symmetric molecules, this theory reduces to an existing mean field theory of binary mixtures [82,83]. This uniaxial theory predicts that the two orientational order parameters,  $Q_1$  and  $Q_2$ , are related by concentration and temperature independent curves.  $^2\text{H-NMR}$  experimental results, from a variety of mixtures over a wide range of temperatures and concentrations [84,85] have

confirmed these predictions. For biaxial molecules, unique relationships between all four order parameters  $Q_1$ ,  $D_1$ ,  $Q_2$  and  $D_2$ , are determined by the three anisotropic interaction strengths, the  $r_i$ 's,  $i = 1,3$ . The  $r_i$ 's will be determined by fitting the temperature dependence of the four experimentally determined order parameters.

Mean field theory gives the anisotropic part of the single particle pseudopotential of each component of the mixture,  $\epsilon_1$  and  $\epsilon_2$ . Using a geometric mean assumption, the general form of the single particle pseudopotential reduces to

$$\epsilon_1 = -\sqrt{U_{11}} \left[ \Lambda \left( q_1(\theta) - \frac{1}{2}Q_1 \right) - r_2 \Lambda \left( d_1(\theta, \psi) - \frac{1}{2}D_1 \right) \right] \quad (3.42)$$

for molecule 1 in the mixture, and

$$\epsilon_2 = -\sqrt{U_{11}} \left[ r_1 \Lambda \left( q_2(\theta) - \frac{1}{2}Q_2 \right) - r_3 \Lambda \left( d_2(\theta, \psi) - \frac{1}{2}D_2 \right) \right] \quad (2.43)$$

for particle 2. The Euler angles  $(\phi, \theta, \psi)$  describe the orientation of a molecule in the laboratory frame. The  $r_i$  parameters are functions of anisotropic coupling constants:

$$r_1 = \sqrt{\frac{U_{22}}{U_{11}}}, \quad r_2 = \sqrt{\frac{W_{11}}{U_{11}}}, \quad r_3 = \sqrt{\frac{W_{22}}{U_{11}}}. \quad (2.44)$$

A detailed derivation of this mean field will be presented in the next chapter. Coupling constant  $U_{ij}$  gives a measure of the strength of the coupling of the instantaneous orientation of the distinguished (major) axis of particles of species of  $i$  with the order parameter  $Q_j$ . Similarly,  $W_{ij}$  gives a measure of the strength of the interactions coupling the instantaneous orientation of the minor axis of species  $i$  to  $D_j$ . All particles couple to the same concentration dependent mean field,  $\Lambda$ , which is of the form,

$$\Lambda = \frac{2}{3} (\rho_1 \sqrt{U_{11}} Q_1 + \rho_2 \sqrt{U_{22}} Q_2 + \rho_1 \sqrt{W_{11}} D_1 + \rho_2 \sqrt{W_{22}} D_2) \quad (2.45)$$

where  $\rho_i$  is the number density of species  $i$ .

A nonlinear routine was written to fit the three parameters,  $r_i$ , successively and self consistently using these expressions for the pseudopotentials. The orientational order parameters can be determined by evaluation the following integrals numerically,

$$Q_1 = \frac{\int_{X=0}^1 (3X^2-1) \exp(\frac{9}{4}\Lambda X^2) I_0(\frac{9}{4}r_2\Lambda(1-X^2)) dX}{2 \int_{X=0}^1 \exp(\frac{9}{4}\Lambda X^2) I_0(\frac{9}{4}r_2\Lambda(1-X^2)) dX} \quad (2.46)$$

$$Q_2 = \frac{\int_{X=0}^1 (3X^2-1) \exp(\frac{9}{4}r_1\Lambda X^2) I_0(\frac{9}{4}r_3\Lambda(1-X^2)) dX}{2 \int_{X=0}^1 \exp(\frac{9}{4}r_1\Lambda X^2) I_0(\frac{9}{4}r_3\Lambda(1-X^2)) dX} \quad (2.47)$$

$$D_1 = \frac{\int_{X=0}^1 (1-X^2) \exp(\frac{9}{4}\Lambda X^2) I_1(\frac{9}{4}r_2\Lambda(1-X^2)) dX}{\frac{2}{3} \int_{X=0}^1 \exp(\frac{9}{4}\Lambda X^2) I_0(\frac{9}{4}r_2\Lambda(1-X^2)) dX} \quad (2.48)$$

and

$$D_2 = \frac{\int_{X=0}^1 (1-X^2) \exp\left(\frac{9}{4}r_1\Lambda X^2\right) I_1\left(\frac{9}{4}r_3\Lambda(1-X^2)\right) dX}{\frac{2}{3} \int_{X=0}^1 \exp\left(\frac{9}{4}r_1\Lambda X^2\right) I_0\left(\frac{9}{4}r_3\Lambda(1-X^2)\right) dX} \quad (2.49)$$

$I_0(\arg)$  is the modified Bessel function of the first kind and  $I_1(\arg)$  is the modified Bessel function of the first kind of order one.  $\Lambda$  is the concentration and orientational order parameter dependent nematic mean field given by Eqn. (2.46).

## 2.8 Interpretation of Fits To Mean Field Theory

In order to fit the temperature dependent order parameters and find the three  $r_i$  parameters,  $Q_1$  is defined to be the independent variable and the dependent variables are the three other orientational order parameters ( $Q_2, D_1, D_2$ ). At a given temperature,  $Q_1$  was used to calculate  $\Lambda$  by inverting equation (2.46). Given  $\Lambda$ , the dependent variables  $Q_2$ ,  $D_1$  and  $D_2$  were determined for a given  $r_1$ ,  $r_2$  and  $r_3$  by evaluating the integrals in Eqns. (2.47-2.49). A nonlinear least squares fitting routine was applied in successive stages. First,  $Q_2$  is fit as a function of  $Q_1$  to provide a value of  $r_1$  keeping  $r_2$  and  $r_3$  fixed. Then  $r_2$  is estimated from the  $D_1$  vs  $Q_1$  curve with  $r_1$  and  $r_3$  held constant. Finally,  $r_3$  is determined by fitting the function  $D_2$  with  $r_1$  and  $r_2$  held constant. This procedure was iterated until all parameters converged to within one part in  $10^6$ . The universal curves relating the order parameters are superimposed with the theoretical fits in Figure 2.6. The final values (90% confidence limits) were determined to be  $r_1 = 0.251 \pm 0.004$ ,  $r_2 = -0.16 \pm 0.01$  and  $r_3 = 0.084 \pm 0.002$ . It is clear from the figures that the second and third points deviate significantly from the least squares fits. This is thought

to be due to the fact that they correspond to data taken in the isotropic-nematic coexistence region where the splittings are small and the fractional errors are large. Using an identical procedure to reanalyze the data from pure FLOC [80] gives the value  $r_2 = 0.13 \pm 0.01$ .

In order for this theoretical description to be useful, it must provide a physical interpretation of the temperature dependence of the order parameters in terms of anisotropic interaction potentials ( $r_i$ 's). The temperature dependence of  $Q_1$  and  $Q_2$  indicate that the degree of orientation of the long axis of the small rigid non-mesogenic solute is much smaller than that of the liquid crystal ( $Q_1 > Q_2$ ). This behavior makes intuitive sense because the probe is not expected to interact as strongly with the mean field, and hence to orient to the same extent as the liquid crystal molecules. The parameter  $r_1$ , the ratio of the anisotropic interaction strength coupling the long axes of each molecule to the uniaxial order parameters, is much smaller than one. One of the most appealing results of mean field theory of nematic binary mixtures of *uniaxial* molecules is that the  $Q_2$  vs  $Q_1$  universal curve is completely determined by properties of the pure materials [82,83]

$$r_1 = \sqrt{\frac{T_{NI,2} \rho_1}{T_{NI,1} \rho_2}} \quad (2.50)$$

where  $T_{NI,i}$  is the Nematic-Isotropic transition temperature of species  $i$  and  $\rho_i$  is its number density. For *biaxial* molecules the corresponding theoretical parameter  $r_1$  exists but can no longer be rigorously defined by equation (2.50). However, for binary mixtures where the two components transition temperatures are defined the ratio of transition temperatures and number densities give an excellent initial guess at the parameter. Since pure FLOC



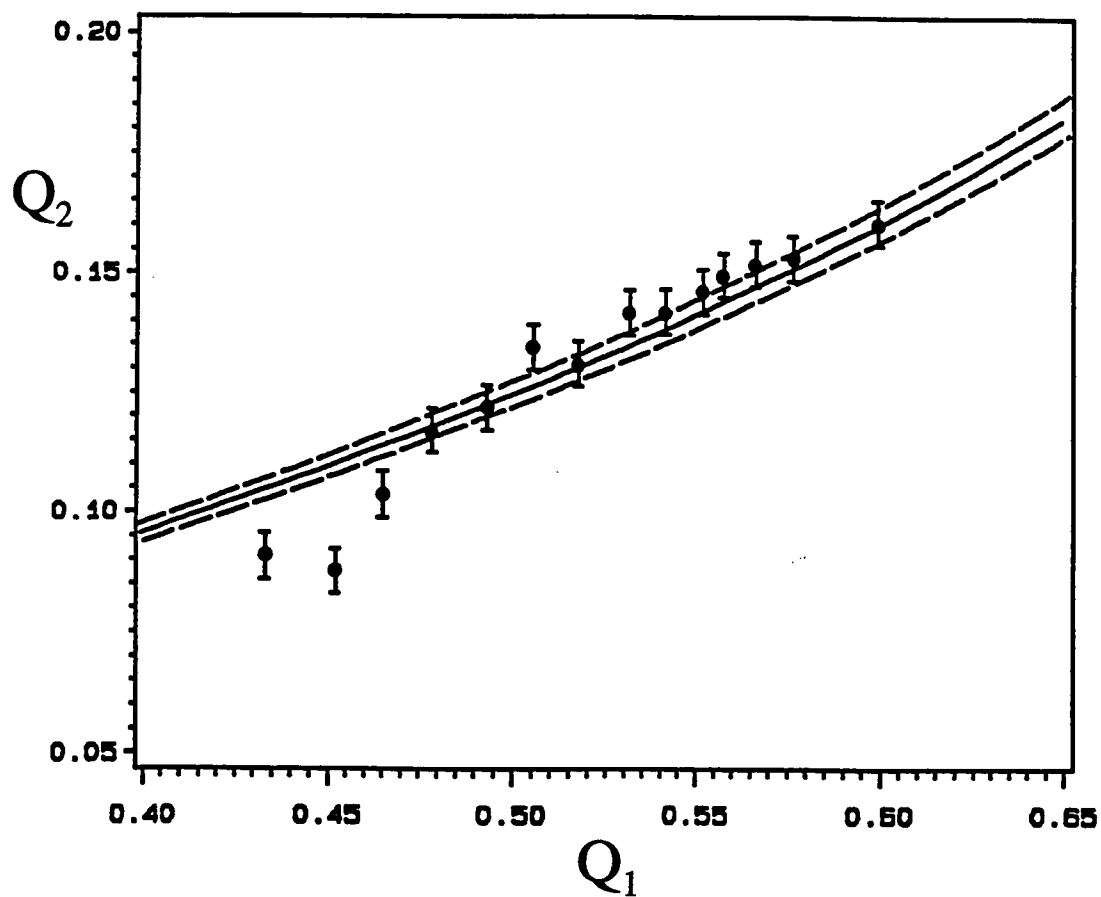


Figure 2.6 Interrelations of the orientational order parameters with the best non linear least squares fit to the ratios of interaction potentials,  $r_1 = 0.251 \pm 0.004$ .  
(a)  $Q_2$  vs.  $Q_1$ .

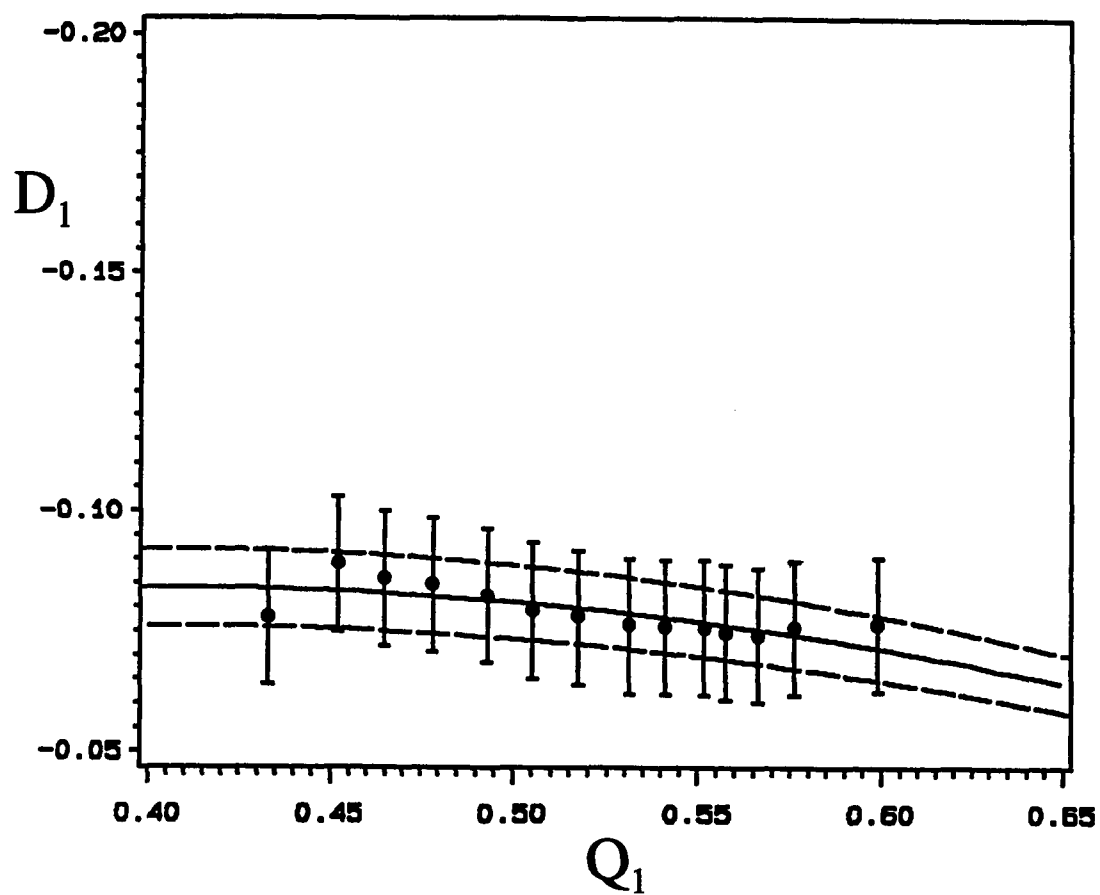


Figure 2.6 Interrelations of the orientational order parameters with the best non linear least squares fit to the ratios of interaction potentials,  $r_2 = -0.16 \pm 0.01$ .  
(b)  $D_1$  vs.  $Q_1$

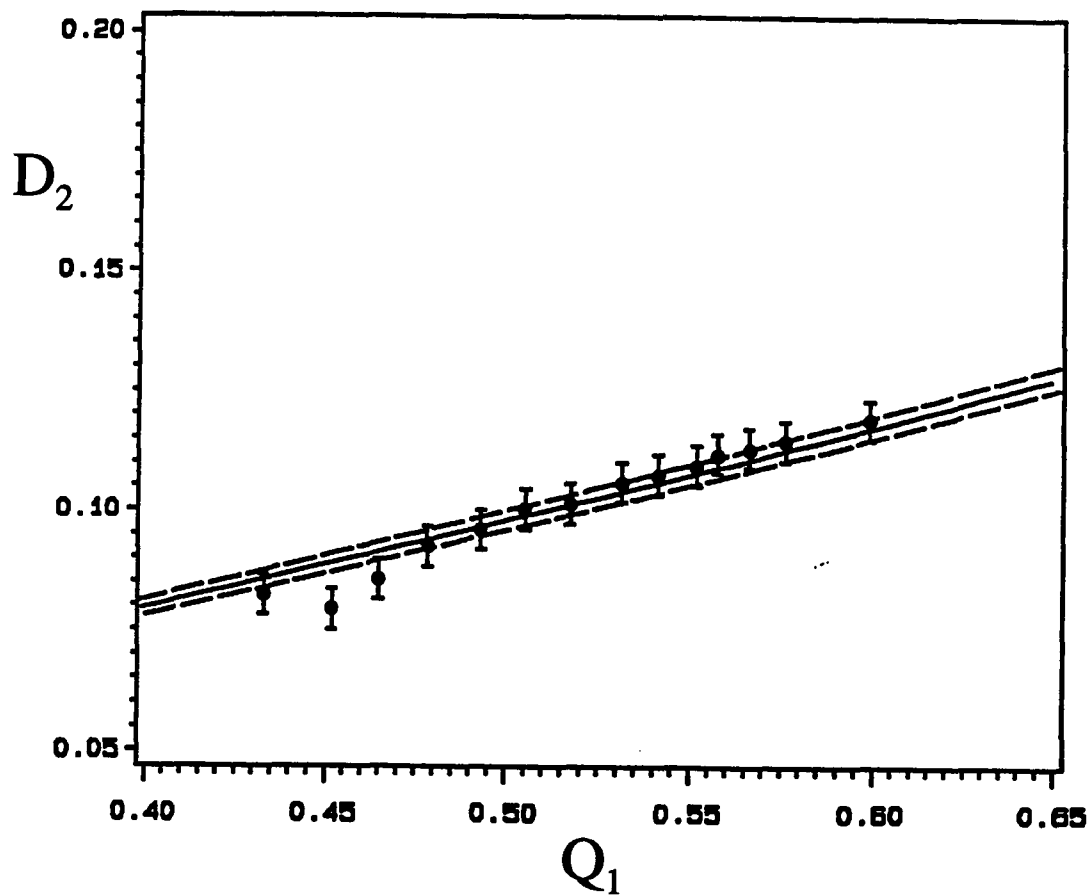


Figure 2.6 Interrelations of the orientational order parameters with the best non linear least squares fit to the ratios of interaction potentials,  $r_3 = 0.084 \pm 0.002$ .  
(c)  $D_2$  vs.  $Q_1$

has a  $T_{NI,1}^* = 409.70$  K, equation (2.50) can be applied assuming p-Xy and FLOC have the same molar volumes. This gives a virtual transition for p-Xy as  $T_{NI,2}^* = 25$ K, well below the crystallization temperature, as required for a non-mesogenic compound [58].

The experimental results also indicate that the molecular biaxiality of the p-Xy solute is larger than that of the liquid crystal FLOC ( $D_2 > D_1$ ). Initially, this seems contradictory to the premise that the biaxiality of molecules has a profound effect on the physical properties of liquid crystal phases. It is unclear why the ordering of p-Xy is more asymmetric than that of FLOC, but it seems reasonable that the symmetry and packing considerations will require a small, flat molecule to orient anisotropically. Obviously, the dimensions of the rigid core of FLOC are larger and this suggests that the orientation should be more asymmetric. The results indicate that this notion is inappropriately simplistic.

It is important to appreciate that in FLOC the fluorene core has a 14 carbon tail attached to it, and this has a profound effect on the location of the principal axes of the molecular order tensor. The alkoxy chain is flexible and can exist in many conformations ( $3^{12}$ ), each having a dramatically different geometry and hence orientational order. It is conceivable that in most conformers the rigid segment is more biaxial than the solute p-Xy. However, the observed molecular biaxiality is a statistical mechanical average over all possible conformations [86] and thus it appears that the core is incapable of dominating the ordering of the minor axis.

The theoretical parameter governing the coupling of the instantaneous orientation of the short axis with the biaxial order parameters,  $D_1$ , is given by  $r_2 =$

$(W_{11}/U_{11})^{1/2}$ . Since these interaction potentials are single particle properties they can, in principal, be derived from the behavior of pure materials.  $r_2$  is equivalent to the parameter  $\delta$  in a generalized mean field theory of pure nematogens proposed by Bergersen, Palfy-Muhoray and Dunmur [87]. It is encouraging that an identical analysis on pure FLOC [58,66] gave a value of  $r_2 = -0.13 \pm 0.01$ , which although not quite within experimental error is at least consistent with that obtained from the mixture.

The third parameter,  $r_3$ , determines the ratio of anisotropic interaction potentials coupling the short and long axes of unlike species. This parameter is unique to this treatment of binary mixtures of biaxial particles. It should be stressed that there is a lack of reciprocity in these coupling constants [41], and hence it is incorrect to assume a single interaction strength, even in the infinite dilution limit [88]. In the treatment of Emsley et al. the parameter  $r_2$  (corresponding to  $\lambda$ ) is a molecular property and thus explicitly temperature independent [88]. If the binary mixture consisted of two similar liquid crystal molecules then  $r_2$  would be expected to be approximately constant regardless of the species considered (ie.  $r_2 = [W_{11}/U_{11}]^{1/2} = [W_{22}/U_{22}]^{1/2}$ ) and under these circumstances the theoretical parameters would satisfy the relationship  $r_3 = \pm r_1 r_2$ . The results for the mixture of the nonmesogenic probe *p*-Xy and the liquid crystal FLOC show clearly that this relationship does not hold. It would be interesting to investigate this in more detail by performing experiments on mixtures containing two nematogens.

In conclusion, NMR is the only technique capable of confirming predictions and interrelations between the order parameters  $Q_1$ ,  $D_1$ ,  $Q_2$  and  $D_2$ , and thus has the potential to make significant contribution to the understanding of liquid crystal

mixtures. These  $^2\text{H}$ -NMR results are the first experimental observation of all four component order parameters in a binary mixture of biaxial molecules in the nematic phase [58,66]. The temperature dependence of the order parameters has been obtained from these experiments and this provides information on the order, asymmetry and flexibility of the liquid crystal molecules. These results were interpreted using a new mean field theory of binary mixtures of biaxial nematic liquid crystals. If the geometric mean assumption is made all particles couple to an identical mean field. This theory is the first to allow for calculation of the free energy explicitly, to include concentration dependence and to allow for biaxial nematic phases. The results show that mixtures and pure materials are fundamentally different and it is incorrect to assume that probe molecules are capable of monitoring a system in an unbiased manner.

### 3. PHASE DIAGRAMS OF NEMATIC BINARY MIXTURES

Molecules which form nematic liquid crystal phases come in a wide variety of shapes and sizes. It would be valuable to be able to predict how mixtures of these very different molecules might behave. A mean field theory has been proposed to describe binary mixtures of nematic liquid crystals with arbitrary shapes [41]. Using this formalism, a complete theoretical description of phase stability and orientational order in binary mixtures of biaxial molecules has been obtained. For a single component, one anisotropic coupling parameter is required to predict the temperature dependence of the four orientational order parameters (Q,D,P,C). Given the order parameters, the stability of the isotropic (I), uniaxial (U), and biaxial (B) nematic phase is ascertained by calculating the free energy density. For binary mixtures, three anisotropic interaction strengths,  $r_1$ ,  $r_2$ , and  $r_3$ , are needed to calculate the four order parameters of each component as a function of concentration and temperature. The free energies and chemical potentials of each phase are calculated to assess stability of the mixture, and the results are often presented in phase diagrams [63]. One question, which has been a topic of debate for researchers studying nematic liquid crystal mixtures, is whether binary mixtures can form stable biaxial nematic liquid crystal phases [89]. The results of this computational study suggest that binary mixtures of molecules with suitably asymmetric shapes might display a stable biaxial nematic phases [63].

#### 3.1 Symmetry of the Nematic Phase

Liquid crystal molecules are often modeled as rigid, asymmetric molecules

possessing  $D_{2h}$  symmetry. Particles with  $D_{2h}$  symmetry have three mutually orthogonal planes of mirror symmetry, examples include ellipsoids of revolution, elliptic cylinders, and regular parallelepipeds or "bricks" [90]. The distribution function,  $\rho(\Omega)$ , can be given as an expansion in terms of the standard Wigner rotation matrix elements:

$$\rho(\Omega) = \sum_{J,m,n} a_{mn}^{(J)} D_{mn}^{(J)*}(\Omega). \quad (3.1)$$

Where  $\Omega = (\alpha, \beta, \gamma)$  are the y-convention Euler angles describing the rotations needed to transform from the laboratory to the molecular coordinate system, and the sum runs over  $J$ ,  $m$  and  $n$  in their appropriate ranges ( $J$  from 0 to  $\infty$ , and  $m, n$  from  $-J$  to  $J$ ). The assumption that both the phase and the particles possess  $D_{2h}$  symmetry leads to the following restrictions on the expansion coefficients,  $a_{mn}^{(J)}$  [91]:

- (i) only terms with  $J$ ,  $m$ , and  $n$  even contribute
- (ii) the expansion coefficients satisfy the identities.

$$a_{mn}^{(J)} = a_{m-n}^{(J)} = a_{-mn}^{(J)} = a_{-m-n}^{(J)}. \quad (3.2)$$

$$Q_{mn}^{(J)}(\Omega) = \left(\frac{\sqrt{2}}{2}\right)^{2+\delta_{m0}+\delta_{n0}} [D_{mn}^{(J)}(\Omega) + D_{m-n}^{(J)}(\Omega) + D_{-nm}^{(J)}(\Omega) + D_{-m-n}^{(J)}(\Omega)],$$

the expression for the distribution function, Eqn. (3.1), can be rewritten (3.3)

$$[D_{mn}^{(J)}(\Omega) + D_{m-n}^{(J)}(\Omega) + D_{-nm}^{(J)}(\Omega) + D_{-m-n}^{(J)}(\Omega)],$$

the expression for the distribution function, Eqn. (3.1), can be rewritten

$$\rho(\Omega) = \sum q_{mn}^{(J)} Q_{mn}^{(J)}(\Omega). \quad (3.4)$$

where  $J$ ,  $m$ , and  $n$  are even, non-negative integers.

There are four second rank ( $J = 2$ ) expansion terms:



$$\begin{aligned}
q &\equiv Q_{00}^{(2)} = \frac{1}{2} (3\cos^2\beta - 1) \\
p &\equiv \sqrt{3} Q_{20}^{(2)} = \frac{3}{2} \sin^2\beta \cos 2\alpha \\
d &\equiv \sqrt{3} Q_{02}^{(2)} = \frac{3}{2} \sin^2\beta \cos 2\gamma \\
c &\equiv 3Q_{22}^{(2)} = \frac{3}{2} ( (1+\cos^2\beta) \cos 2\alpha \cos 2\gamma - 2\cos\beta \sin 2\alpha \sin 2\gamma )
\end{aligned} \tag{3.5}$$

Ensemble averages of these functions ( $\langle q \rangle = Q$ ,  $\langle d \rangle = D$ ,  $\langle p \rangle = P$ ,  $\langle c \rangle = C$ ) give the four second rank order parameters which completely characterize orientational order of biaxial particles of  $D_{2h}$  symmetry. These are, apart from some arbitrary normalization constants, the four order parameters introduced by Straley [20] to describe orientational order in biaxial nematic liquid crystals. All four order parameters are zero in the isotropic phase. The uniaxial nematic phase has azimuthal symmetry about the director (laboratory z-axis); therefore, the distribution is not a function of the angle  $\alpha$ , and the orientational order parameters  $P$  and  $C$  vanish. In the uniaxial phase,  $D$  is finite if the particles are lack cylindrically symmetry. In the biaxial phase, either  $P$  and/or  $C$  are finite.

### 3.2 Cartesian Order Tensors

An alternative representation of orientational order in nematic systems uses Cartesian tensors. Expressions for these tensors can be derived by considering the polarizability of a biaxial particle. Assuming that a liquid crystal molecule possessing  $D_{2h}$  symmetry has principle polarizabilities  $k_{11}$ ,  $k_{22}$  and  $k_{33}$ , the polarizability tensor  $k_{\alpha\beta}$  in the lab frame is

$$k_{\alpha\beta} = \bar{k}\delta_{\alpha\beta} + \frac{1}{2} (k_{33} - \bar{k}) (3n_{3\alpha}n_{3\beta} - \delta_{\alpha\beta}) + \frac{1}{2} (k_{11} - k_{22}) (n_{1\alpha}n_{1\beta} - n_{2\alpha}n_{2\beta}), \quad (3.6)$$

where the isotropic value is

$$\bar{k} = (k_{11} + k_{22} + k_{33}) \quad (3.7)$$

The orientation of the particle enters this expression for the polarizability through the quantities

$$\sigma_{\alpha\beta} = \frac{1}{2} (3n_{3\alpha}n_{3\beta} - \delta_{\alpha\beta}) \quad (3.8)$$

and

$$\tau_{\alpha\beta} = \frac{3}{2} (n_{1\alpha}n_{1\beta} - n_{2\alpha}n_{2\beta}), \quad (3.9)$$

where  $n_{1\alpha}$  is the projection of the unit vectors ( $n_{1\alpha} = \hat{e}_1 \cdot \hat{e}_\alpha$ ). Orientational order tensors  $S_{\alpha\beta}$  and  $T_{\alpha\beta}$  can be defined as thermal average values of these tensorial quantities. If it is assumed that  $S_{\alpha\beta}$  and  $T_{\alpha\beta}$  can be diagonalized simultaneously, as is expected for reasons of symmetry [92], then in the principal axis frame of the liquid crystal phase,

$$\langle \sigma_{\alpha\beta} \rangle = S_{\alpha\beta} = \begin{bmatrix} -\frac{1}{2}(Q-P) & 0 & 0 \\ 0 & -\frac{1}{2}(Q+P) & 0 \\ 0 & 0 & Q \end{bmatrix} \quad (3.10)$$

$$\langle \tau_{\alpha\beta} \rangle = T_{\alpha\beta} = \begin{bmatrix} -\frac{1}{2}(D-C) & 0 & 0 \\ 0 & -\frac{1}{2}(D+C) & 0 \\ 0 & 0 & D \end{bmatrix} \quad (3.11)$$

### 3.3 The Orienting Potential

Four order parameter tensors are needed to describe orientational order of both components (1 and 2) of a binary mixture  $S_{1\alpha\beta}$ ,  $T_{1\alpha\beta}$ ,  $S_{2\alpha\beta}$  and  $T_{2\alpha\beta}$ . The first step in deriving a mean field theory of binary mixtures is to choose a form for the orienting potential. To lowest order, a single particle pseudopotential of species 1 is formed by taking the scalar products of orientational dependent terms,  $\sigma_{\alpha\beta}$  and  $\tau_{\alpha\beta}$ , and the order parameters,  $S_{\alpha\beta}$  and  $T_{\alpha\beta}$ . For species 1, the orienting potential  $\epsilon_1(\Omega_1)$  is:

$$\begin{aligned} \epsilon_1(\Omega_1) = & -\frac{1}{2}\rho_1\gamma_{11} - \frac{1}{2}\rho_2\gamma_{12} \\ & -2/3 [\rho_1 U_{11} S_{1\alpha\beta} \sigma_{1\alpha\beta} + \rho_2 U_{12} S_{2\alpha\beta} \sigma_{1\alpha\beta} + \rho_1 U_{11}' S_{1\alpha\beta} S_{1\alpha\beta} + \rho_2 U_{12}' S_{2\alpha\beta} S_{1\alpha\beta} \\ & + \rho_1 V_{11} S_{1\alpha\beta} \tau_{1\alpha\beta} + \rho_2 V_{12} S_{2\alpha\beta} \tau_{1\alpha\beta} + \rho_1 V_{11}' S_{1\alpha\beta} T_{1\alpha\beta} + \rho_2 V_{12}' S_{2\alpha\beta} T_{1\alpha\beta} \\ & + \rho_1 \Pi_{11} T_{1\alpha\beta} \sigma_{1\alpha\beta} + \rho_2 \Pi_{12} T_{2\alpha\beta} \sigma_{1\alpha\beta} \\ & + \rho_1 W_{11} T_{1\alpha\beta} \tau_{1\alpha\beta} + \rho_2 W_{12} T_{2\alpha\beta} \tau_{1\alpha\beta} + \rho_1 W_{11}' T_{1\alpha\beta} T_{1\alpha\beta} + \rho_2 W_{12}' T_{2\alpha\beta} T_{1\alpha\beta}] \end{aligned} \quad (3.12)$$

where  $\Omega_1$  is the generalized orientational coordinate of particle one,  $\rho_i$  is the number density of species  $i$ ,  $\gamma_{ij}$  are isotropic coupling constants, and  $U_{ij}$ ,  $U_{ij}'$ ,  $V_{ij}$ ,  $V_{ij}'$ ,  $\Pi_{ij}$ ,  $W_{ij}$ , and  $W_{ij}'$  are anisotropic coupling constants. Here summation over repeated Greek indices is implied. The pseudopotential of a particle of species 2 is obtained by interchanging the indices 1 and 2.

The configurational free energy density of the system is given by [93]

$$\begin{aligned} f = & -\rho_1 k_B T \ln \left[ \frac{1}{\rho_1} \int \exp\left(-\frac{\epsilon_1(\Omega_1)}{k_B T}\right) d\Omega_1 \right] \\ & -\rho_2 k_B T \ln \left[ \frac{1}{\rho_2} \int \exp\left(-\frac{\epsilon_2(\Omega_2)}{k_B T}\right) d\Omega_2 \right] \end{aligned} \quad (3.13)$$

where  $k_B$  is Boltzmann's constant,  $T$  is temperature in Kelvin, and  $d\Omega = d(\cos\beta) d\alpha d\gamma$ .

Since at equilibrium the free energy density  $f$  is a minimum, its derivative with respect

to the order parameters must vanish. This minimum free energy requirement yields relationships between the coupling constants, (e.g.  $U_{11}' = -\frac{1}{2} U_{11}$ ,  $\Pi_{11} = V_{11}$ ) which simplify the expressions for the pseudopotentials to

$$\begin{aligned} \varepsilon_1(\Omega_1) = & -\frac{1}{2}\rho_1\gamma_{11} - \frac{1}{2}\rho_2\gamma_{12} \\ & -\frac{2}{3}(\rho_1 U_{11} S_{1\alpha\beta} + \rho_2 U_{12} S_{2\alpha\beta} + \rho_1 V_{11} T_{1\alpha\beta} + \rho_2 V_{21} T_{2\alpha\beta})(\sigma_{1\alpha\beta} - \frac{1}{2} S_{1\alpha\beta}) \\ & -\frac{2}{3}(\rho_1 V_{11} S_{1\alpha\beta} + \rho_2 V_{12} S_{2\alpha\beta} + \rho_1 W_{11} T_{1\alpha\beta} + \rho_2 W_{12} T_{2\alpha\beta})(\tau_{1\alpha\beta} - \frac{1}{2} T_{1\alpha\beta}) \\ & -\frac{1}{3}\rho_2 V_{21} T_{2\alpha\beta} S_{1\alpha\beta} + \frac{1}{3}\rho_2 V_{12} S_{2\alpha\beta} T_{1\alpha\beta} \end{aligned} \quad (3.14)$$

and a similar expression can be derived for  $\varepsilon_2(\Omega_2)$ .

The parameters of the pseudopotential which measure the strength of the attractive intermolecular potential between species  $i$  and  $j$ . The coupling constant  $U_{ij}$  gives a measure of the strength of the interaction coupling the average orientation of the distinguished (major) axis of particle  $i$  with the instantaneous orientation of the major axis of  $j$ . Similarly  $W_{ij}$  gives a measure of the strength of interaction coupling the average orientation of the minor axis of particle  $i$  with instantaneous orientation of the minor axis of  $j$ . Using the minimum free energy criterion, it can be shown that  $\gamma_{ij} = \gamma_{ji}$ ,  $W_{ij} = W_{ji}$  and  $U_{ij} = U_{ji}$ . Finally,  $V_{ij}$  gives a measure of the interaction strength coupling the average orientation of the minor axis of species  $i$  with the instantaneous orientation of the major axis of species  $j$ . In this case, no reciprocal relation can be found by minimizing the free energy, and in general  $V_{ij} \neq V_{ji}$ .

### 3.4 The Geometric Mean Assumption

For the most general case of the binary mixture, there are 13 independent coupling constants ( $\gamma_{11}$ ,  $\gamma_{22}$ ,  $\gamma_{12}$ ,  $U_{11}$ ,  $U_{22}$ ,  $U_{12}$ ,  $V_{11}$ ,  $V_{22}$ ,  $V_{12}$ ,  $V_{21}$ ,  $W_{11}$ ,  $W_{22}$ ,  $W_{12}$ ). In order

to reduce the number of parameters in this description, the geometric mean assumption is made. That is, the coupling constant for interactions between particles of different species is assumed to be the geometric mean of the corresponding interactions between like particles. Specifically,

$$\begin{aligned} U_{12} &= \sqrt{U_{11}U_{22}} & W_{12} &= \sqrt{W_{11}W_{22}} & V_{11} &= \sqrt{W_{11}U_{11}} \\ V_{12} &= \sqrt{W_{11}U_{22}} & V_{21} &= \sqrt{W_{22}U_{11}} & V_{22} &= \sqrt{W_{22}U_{22}} \end{aligned} \quad (3.15)$$

Making use of these relations, the pseudopotential for particle 1,  $\epsilon_1(\Omega_1)$ , simplifies to the following expression:

$$\begin{aligned} \epsilon_1(\Omega_1) &= -\frac{1}{2} \sqrt{\gamma_{11}} \Gamma - \sqrt{U_{11}} \Lambda_{\alpha\beta} \left( \sigma_{1\alpha\beta} - \frac{1}{2} S_{1\alpha\beta} \right) \\ &\quad - \sqrt{W_{11}} \Lambda_{\alpha\beta} \left( \tau_{1\alpha\beta} - \frac{1}{2} T_{1\alpha\beta} \right). \end{aligned} \quad (3.16)$$

Replacing the subscript 1 by 2 gives  $\epsilon_2(\Omega_2)$ . The isotropic mean field is

$$\Gamma = \rho_1 \sqrt{\gamma_{11}} + \rho_2 \sqrt{\gamma_{22}}, \quad (3.17)$$

and the anisotropic mean field is

$$\Lambda_{\alpha\beta} = \frac{2}{3} (\rho_1 \sqrt{U_{11}} S_{1\alpha\beta} + \rho_2 \sqrt{U_{22}} S_{2\alpha\beta} + \rho_1 \sqrt{W_{11}} T_{1\alpha\beta} + \rho_2 \sqrt{W_{22}} T_{2\alpha\beta}). \quad (3.18)$$

In the geometric mean approximation, therefore, all particles feel the same isotropic ( $\Gamma$ ) and anisotropic ( $\Lambda_{\alpha\beta}$ ) mean fields. How strongly a given species couples to these fields is characterized by the isotropic ( $\gamma_{ii}$ ) and anisotropic ( $U_{ii}$  and  $W_{ii}$ ) interaction strengths. The parameters of the theory are ratios of these coupling constants:

$$r_0 = \sqrt{\frac{\gamma_{22}}{\gamma_{11}}}, \quad r_1 = \sqrt{\frac{U_{22}}{U_{11}}}, \quad r_2 = \sqrt{\frac{W_{11}}{U_{11}}}, \quad r_3 = \sqrt{\frac{W_{22}}{U_{11}}}. \quad (3.19)$$

Now the pseudopotentials  $\epsilon_1$  and  $\epsilon_2$  can be expressed in terms of the scalar order

parameters  $(Q_i, D_i, P_i, C_i)$ , the Euler angles  $\Omega_i = (\alpha_i, \beta_i, \gamma_i)$  with  $i=1,2$ , and the four coupling parameters  $r_j$  with  $j = 0$  to 3.

$$\begin{aligned} \varepsilon_1(\Omega_1) = & -\frac{3}{2} \Lambda \left[ q_1(\theta_1) + r_2 d_1(\theta_1, \psi_1) - \frac{1}{2} Q_1 - \frac{1}{2} r_2 D_1 \right] \\ & - \frac{3}{2} \Lambda' \left[ p_1(\phi_1, \theta_1) + r_2 c_1(\phi_1, \theta_1, \psi_1) - \frac{1}{2} P_1 - \frac{1}{2} r_2 C_1 \right] \\ & - \frac{1}{2} \Gamma. \end{aligned} \quad (3.20)$$

and

$$\begin{aligned} \varepsilon_2(\Omega_2) = & -\frac{3}{2} \Lambda \left[ r_1 q_2(\theta_2) + r_3 d_2(\theta_2, \psi_2) - \frac{1}{2} r_1 Q_2 - \frac{1}{2} r_3 D_2 \right] \\ & - \frac{3}{2} \Lambda' \left[ r_1 p_2(\phi_2, \theta_2) + r_3 c_2(\phi_2, \theta_2, \psi_2) - \frac{1}{2} r_1 P_2 - \frac{1}{2} r_3 C_2 \right] \\ & - \frac{1}{2} r_0 \Gamma. \end{aligned} \quad (3.21)$$

Where the anisotropic mean fields are:

$$\Gamma = \gamma_{11} (\rho_1 + r_0 \rho_2), \quad (3.22)$$

$$\Lambda = \frac{2}{3} U_{11} (\rho_1 Q_1 + r_1 \rho_2 Q_2 + r_2 \rho_1 D_1 + r_3 \rho_2 D_2), \quad (3.23)$$

and

$$\Lambda' = \frac{2}{9} U_{11} (\rho_1 P_1 + r_1 \rho_2 P_2 + r_2 \rho_1 C_1 + r_3 \rho_2 C_2). \quad (3.24)$$

### 3.5 The Statistical Mechanics of Binary Mixtures

Statistical mechanics was used to calculate the order parameters of both species. The single particle partition function for the  $i^{\text{th}}$  species ( $Z_i$ ) and the orientational order parameters ( $\xi_i = Q_i, D_i, P_i, C_i$ ) may be calculated, for species  $i$ , by evaluating the integrals

$$Z_i = \int \exp\left(-\frac{\varepsilon_i(\phi, \theta, \psi)}{k_B T}\right) \sin(\theta) d\phi d\theta d\psi \quad (3.25)$$

$$\langle \xi_i \rangle = \frac{\int \xi_i \exp\left(-\frac{\varepsilon_i(\phi, \theta, \psi)}{k_B T}\right) \sin(\theta) d\phi d\theta d\psi}{Z_i} \quad (3.26)$$

Since the pseudopotentials are simply functions of the orientational order parameters of both species, this set of equations can be iterated until they converge to give self consistent solutions for all eight orientational order parameters.

The  $\alpha$  dimension of the integrals in Eqns. (3.25 and 3.26) was performed analytically. The remaining two dimensional forms of the ten integrals are given in Appendix IV in terms of spherical Bessel functions. For uniaxial phases, the integrands are independent of the angle  $\alpha$ , and in this case the integration over the angle  $\gamma$  can be performed analytically (see Eqns. 2.46-2.49) [58,94]. In the biaxial phase, all order parameters are nonzero, in this case Romberg's method was employed [95] to evaluate the ten 2-dimensional integrals required for each iteration in the order parameter calculation. The spherical Bessel functions were calculated using a polynomial expansion [96] which gave absolute errors of less than one part in  $10^7$ . The convergence criterion for integration in the  $\beta$  dimension required fractional accuracy of one part in  $10^6$ ; the second dimension,  $\gamma$ , required fractional errors of less than one part in  $10^5$ . The order parameters themselves are reiterated until they are consistent to within one part in  $10^4$ . The integrations were checked for a test case by comparing the results to Mathematica's [97] numerical evaluation of the actual three dimensional integrals, and the solution was

found to be correct to within the errors cited. When molecular biaxiality is ignored ( $D = C = 0$ ), this theory reduces to a mean field theory of binary mixtures of uniaxial particles. The numerical calculations were checked by reproducing phase diagrams which were constructed using this uniaxial theory [98]. Further verification of the results of the calculation included comparing the temperature dependence of the order parameters  $Q$  and  $D$ , calculated for prolate molecules in a uniaxial phase ( $N_{u,+}$ ), with previously published results [99], and reproducing Maier and Saupe's results for a single component, uniaxial system [24] when  $r_1=r_2=r_3=0$ .

Once the order parameters have converged, the configurational free energy density of the homogeneous mixture can be calculated using Eqn. (3.13). Other thermodynamic quantities can be evaluated, and those of particular interest include the thermal average energy densities  $\langle \epsilon_1 \rangle$ ,  $\langle \epsilon_2 \rangle$  and the entropy density  $\sigma$ ,

$$\langle \epsilon_1 \rangle = \langle \alpha \rangle \rho_1 + \langle \beta \rangle \rho_2 , \quad (3.27)$$

$$\langle \epsilon_2 \rangle = \langle \alpha' \rangle \rho_1 + \langle \beta' \rangle \rho_2 , \quad (3.28)$$

$$\frac{\sigma}{k_B T} = \langle \alpha \rangle , \quad (3.29)$$

where

$$\langle \alpha \rangle = - \frac{U_{11}}{2} (Q_1 + r_2 D_1)^2 - \frac{U_{11}}{6} (P_1 + r_2 C_1)^2 - \frac{\gamma_{11}}{2} , \quad (3.30)$$



$$\langle \beta \rangle = \langle \alpha \rangle = -\frac{U_{11}}{2}(Q_1+r_2D_1)(r_1Q_2+r_3D_2) - \frac{U_{11}}{6}(P_1+r_2C_1)(r_1P_2+r_3C_2) - r_0\frac{\gamma_{11}}{2}, \quad (3.31)$$

and

$$\langle \beta' \rangle = -\frac{U_{11}}{2}(r_1Q_2+r_3D_2)^2 - \frac{U_{11}}{6}(r_1P_2+r_3C_2)^2 - r_0^2\frac{\gamma_{11}}{2}. \quad (3.32)$$

For a pure component, if the entropy density jumps discontinuously at the transition, i.e. there is a finite entropy of transition, then the phase change is first order [100]. For second order transitions, the entropy changes continuously through the transition. Thus, the order of the transition can be determined by calculating  $\sigma$  just above and below the transition temperature.

For homogeneous mixtures, the chemical potentials for each component,  $\mu_i$ , ( $i = 1,2$ ) can be calculated. These chemical potentials are crucial for constructing temperature-concentration phase diagrams, since coexistence regions occur where the following chemical potentials of different species are equal. For a binary mixture,

$$\mu_1 = \frac{\partial F}{\partial N_1} = -k_B T \ln\left[\frac{1}{\rho_1} Z_1\right] + k_B T \rho_2 (v_2 - v_1) + \rho_2 \left[ \rho_1 v_2 \langle \alpha \rangle + (\rho_2 v_2 - \rho_1 v_1) \langle \beta \rangle - \rho_2 v_1 \langle \beta' \rangle \right] \quad (3.33)$$

and

$$\mu_2 = \frac{\partial F}{\partial N_2} = -k_B T \ln\left[\frac{1}{\rho_2} Z_2\right] + k_B T \rho_1 (v_1 - v_2) - \rho_1 \left[ \rho_1 v_2 \langle \alpha \rangle + (\rho_2 v_2 - \rho_1 v_1) \langle \beta \rangle - \rho_2 v_1 \langle \beta' \rangle \right]. \quad (3.34)$$

Where  $v_i$  is the molecular volume of the  $i^{\text{th}}$  species.

### 3.6 Temperature Dependence of Orientational Order in a Single Component System

Only one parameter,  $r_2$ , the ratio of the biaxial coupling strength to the uniaxial coupling strength, is needed to predict the temperature dependence of orientational order for a single component system. The temperature dependence of the nematic order parameters can be calculated. In the uniaxial phase, order parameters are calculated with  $P$  and  $C$  held fixed at 0. In this case, the algorithm converges to one of three states depending on the initial guesses for the order parameters. These three uniaxial solutions correspond to: (1) a solution describing the isotropic phase (I) with  $Q=P=C=D=0$ , (2) a solution with  $Q < 0$  corresponding to a discotic nematic phase ( $N_{U-}$ ), and (3) a solution with  $Q > 0$  indicating a calamitic nematic phase ( $N_{U+}$ ). In the biaxial phase ( $N_B$ ), all four order parameters are non-zero, and it is found that the self-consistent equations converge to the same orientational distribution independent of initial order parameter guess; however, the principal axis from which the Euler angles were defined depends on the initial conditions for the order parameters. For all phases, the scaled free energy density is calculated for a single component using Eqn. (3.14) with  $\rho_2 = 0$ . The solution for the order parameters which have the minimum orientational free energy gives the equilibrium phase of the system.

The temperature dependence of the four order parameters of a single component nematic for five different values of the biaxial coupling parameter,  $r_2$ , are presented in Figure 3.1. At each given temperature, Eqns. (3.25 and 3.26) were iterated to calculate the four order parameters. Depending on initial conditions and phase assumption, at most four solutions for the order parameters were found: a biaxial solution

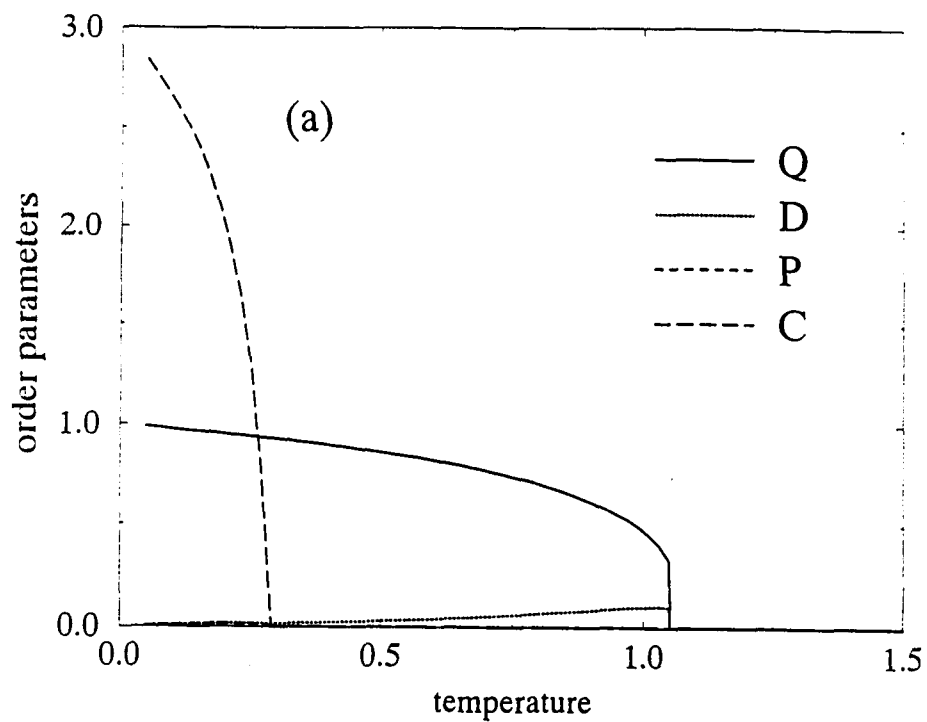


Figure 3.1(a) Orientational order parameters (Q,D,P,C) as a function of temperature for the biaxial coupling parameter  $r_2 = 0.20$ . Temperatures are normalized with respect to the Maier-Saupe transition temperature.

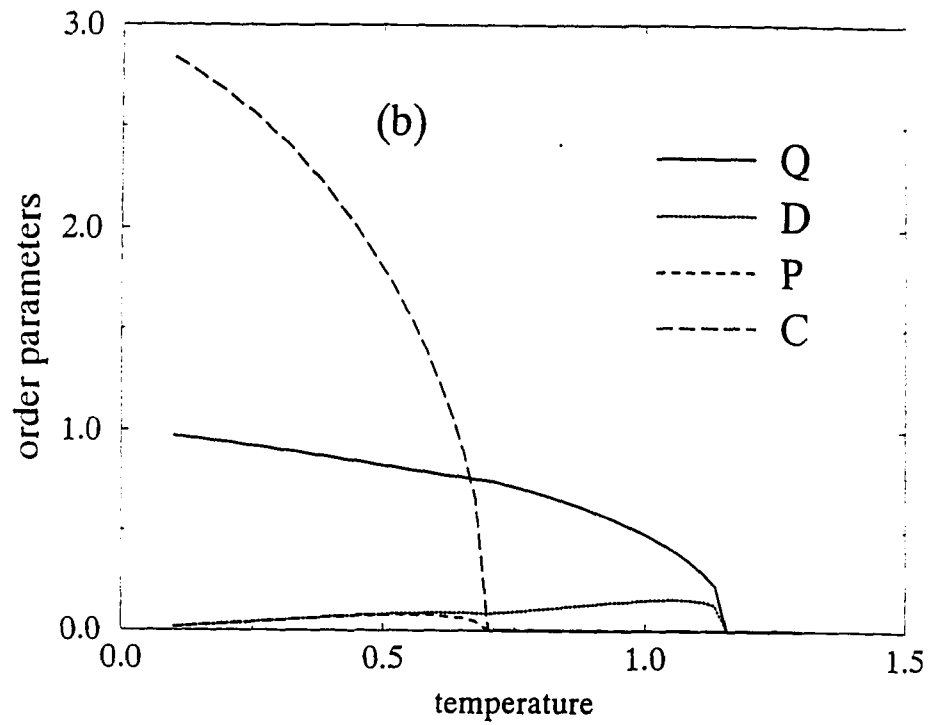


Figure 3.1(b) Orientational order parameters (Q,D,P,C) as a function of temperature for the biaxial coupling parameter  $r_2 = 0.30$ . Temperatures are normalized with respect to the Maier-Saupe transition temperature.

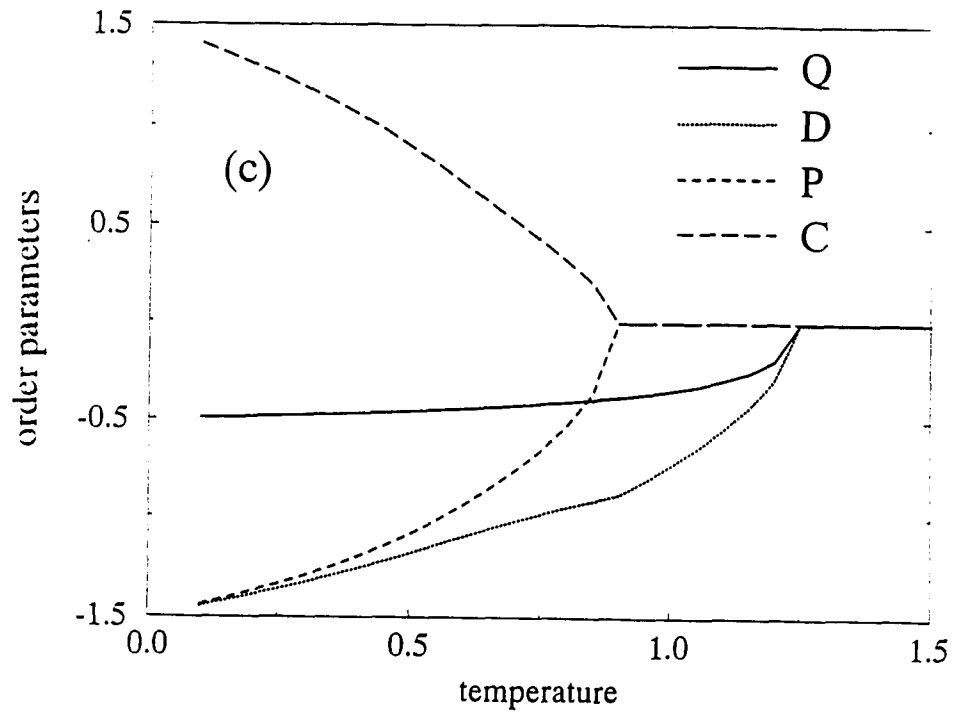


Figure 3.1(c) Orientational order parameters (Q,D,P,C) as a function of temperature for the biaxial coupling parameter  $r_2 = 0.35$ . Temperatures are normalized with respect to the Maier-Saupe transition temperature.

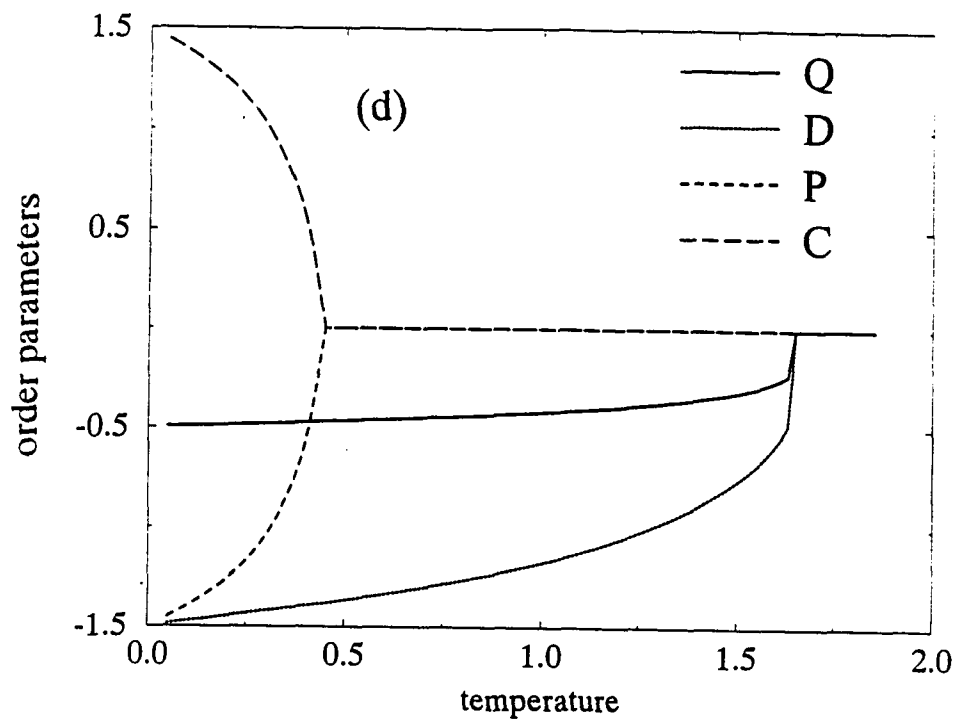


Figure 3.1(d) Orientational order parameters (Q,D,P,C) as a function of temperature for the biaxial coupling parameter  $r_2 = 0.50$ . Temperatures are normalized with respect to the Maier-Saupe transition temperature.

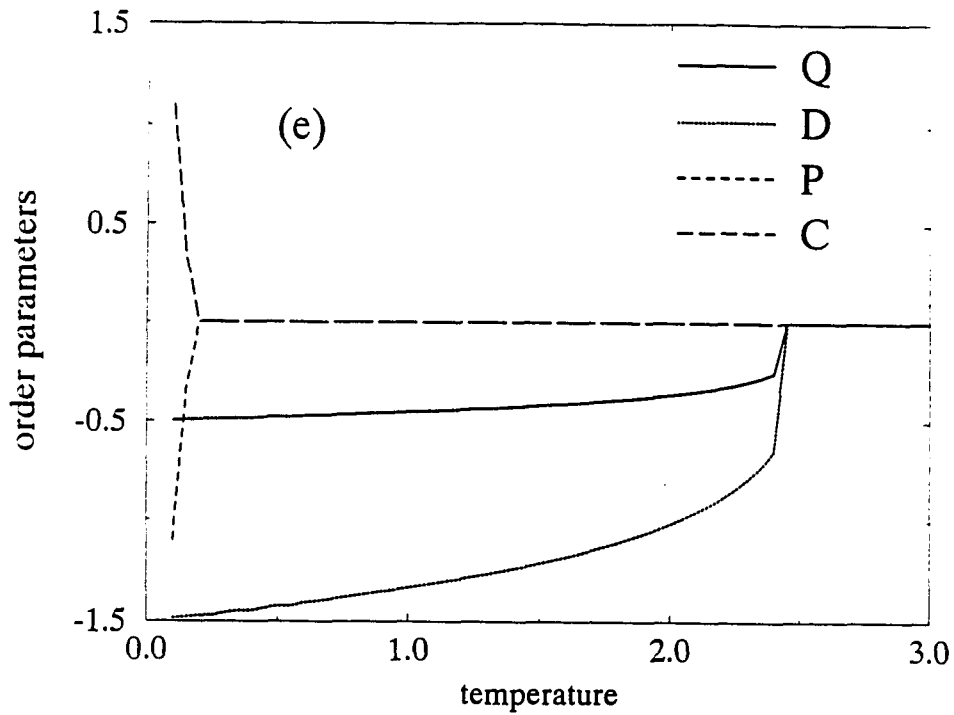


Figure 3.1(e) Orientational order parameters (Q,D,P,C) as a function of temperature for the biaxial coupling parameter  $r_2 = 0.70$ . Temperatures are normalized with respect to the Maier-Saupe transition temperature.

( $N_B$ ), a uniaxial solution of prolate objects ( $N_{U+}$ ), a uniaxial solution of oblate objects ( $N_{U-}$ ), and the isotropic phase solution (I). The equilibrium solution for the system was taken to be that of minimum free energy (Eqn. (3.13)). Small values of  $r_2$  ( $r_2 < 0.33$ ) describe rod-like or prolate molecules, while for  $r_2 = 0$  the rods are cylindrically symmetric and the Maier-Saupe results are reproduced [24]. Large values of  $r_2$  ( $r_2 > 0.33$ ) describe plate-like or oblate molecules, and larger values ( $r_2 > 1.0$ ) describe nearly cylindrically symmetric plates. A biaxial nematic phase is found near the isotropic-nematic transition temperature ( $T_{NI}$ ) for intermediate values of  $r_2$  ( $r_2 = 0.33$ ). This is in agreement with previous work [21,102-108] which predicted that low molecular weight thermotropic biaxial nematic liquid crystals should display characteristics of both rod-like and disk-like molecular shapes [109,110].

As the temperature is lowered, mean field theory predicts that a nematic liquid crystal becomes more ordered and follows the sequence I- $N_{U+}$ - $N_B$  (rods) or I- $N_{U-}$ - $N_B$  (disks). To illustrate this ordering as a function of temperature, an ensemble of 1000 molecules whose orientational distribution gives the order parameters are presented for  $r_2 = 0.3$  (Figure 3.2) and  $r_2 = 0.35$  (Figure 3.3). For prolate molecules, the order parameters converge to  $Q=1$ ,  $D=0$ ,  $P=0$  and  $C=3$  as the system cools to  $T = 0$ ; this gives an orientational distribution in the  $(\alpha, \beta, \gamma)$  space concentrating on the line  $\beta=0$  and  $\alpha=-\gamma$ . This distribution is one of complete alignment with the molecular z-axis parallel to the laboratory z-axis. As  $C$  becomes finite, the phase becomes biaxial, and the molecular x-axis aligns parallel to the lab x-axis. For oblate molecules, as the temperature lowers, the order parameters converge to  $Q=-0.5$ ,  $D=-1.5$ ,  $P=-1.5$  and  $C=1.5$ . Figure 3.3(c)



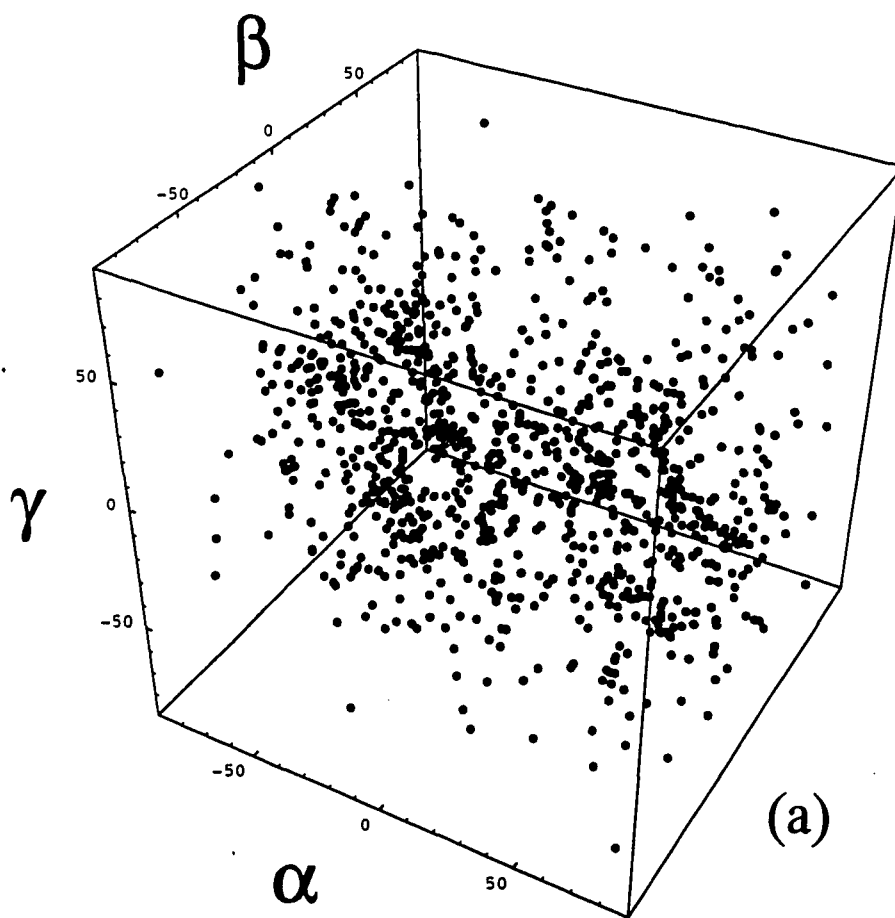


Figure 3.2(a) An ensemble of 1000 molecules whose orientational distribution gives the order parameters for rod-like liquid crystals with biaxial coupling parameter  $r_2=0.30$  for  $T = 0.700$

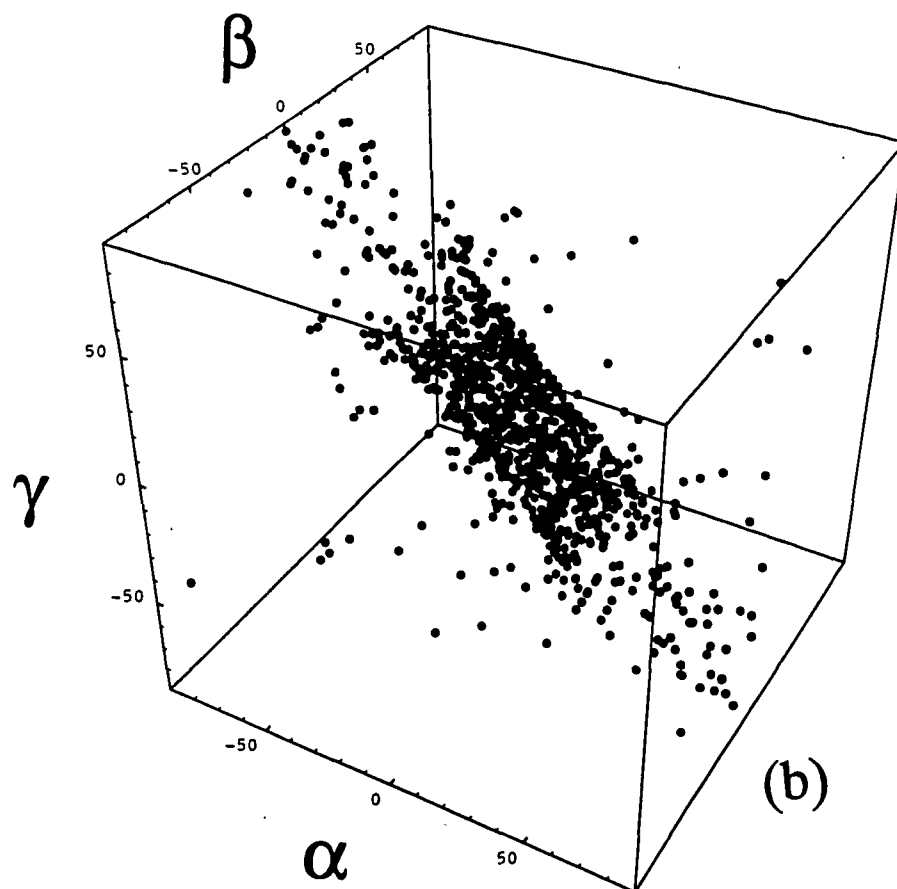


Figure 3.2(b) An ensemble of 1000 molecules whose orientational distribution gives the order parameters for rod-like liquid crystals with biaxial coupling parameter  $r_2=0.30$  for  $T = 0.316$ .

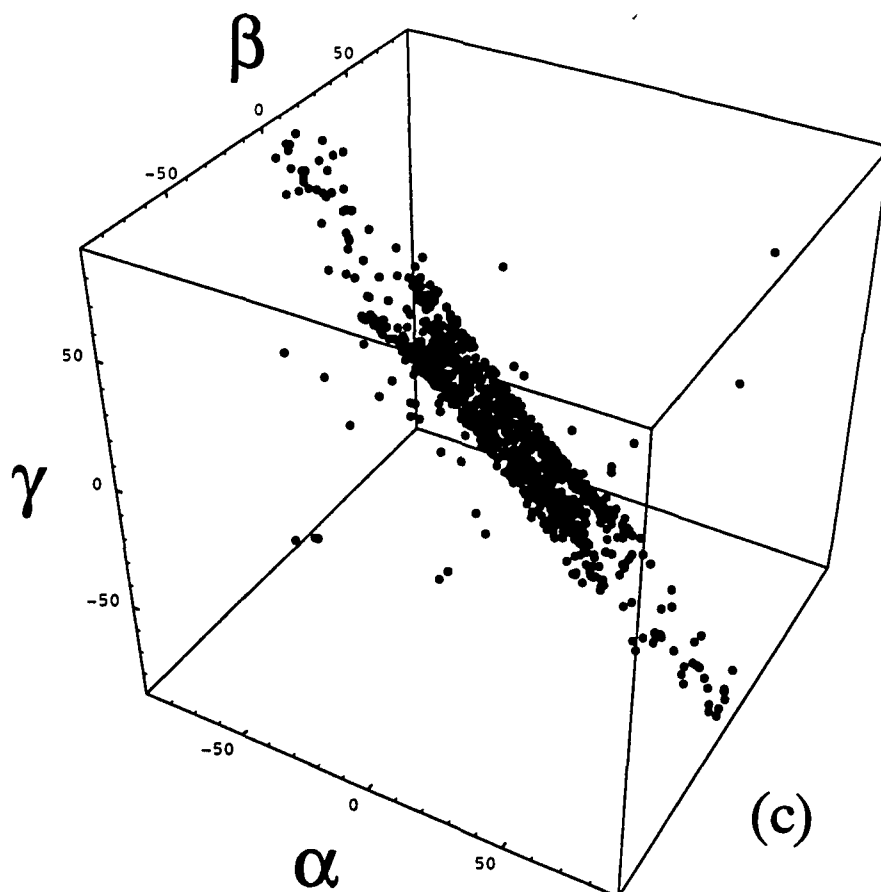


Figure 3.2(c) An ensemble of 1000 molecules whose orientational distribution gives the order parameters for rod-like liquid crystals with biaxial coupling parameter  $r_2=0.30$  for  $T = 0.100$ .

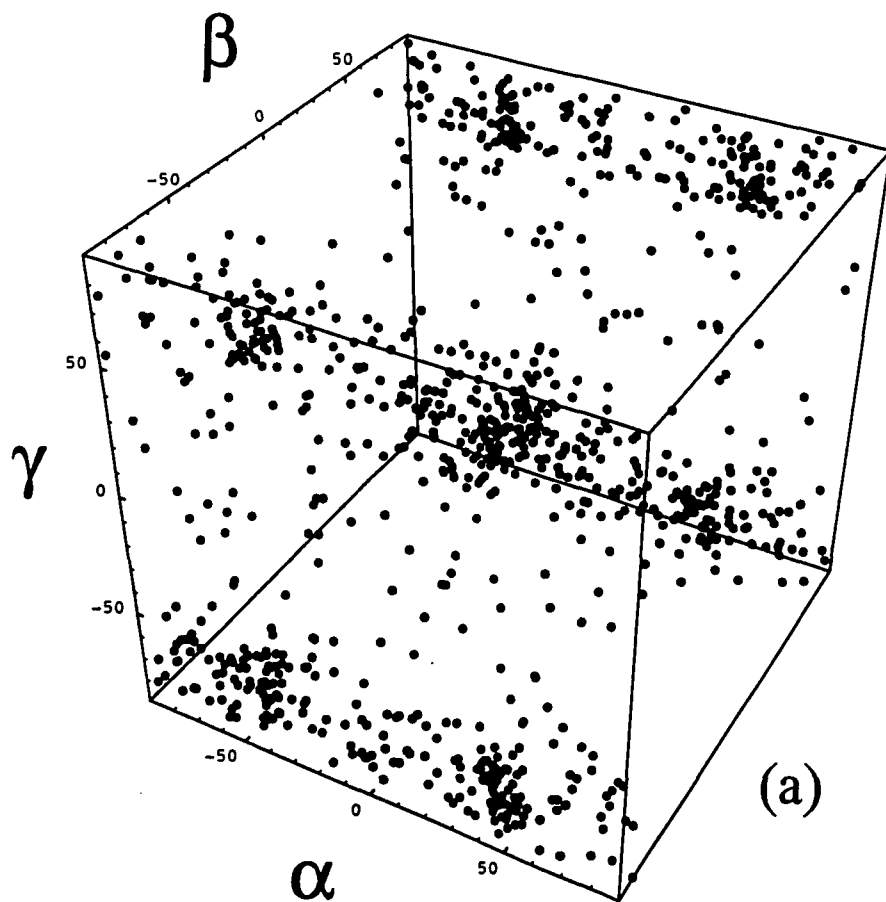


Figure 3.3(a) An ensemble of 1000 molecules whose orientational distribution gives the order parameters for disk-like liquid crystals with biaxial coupling parameter  $r_2=0.35$  for  $T = 0.900$ .

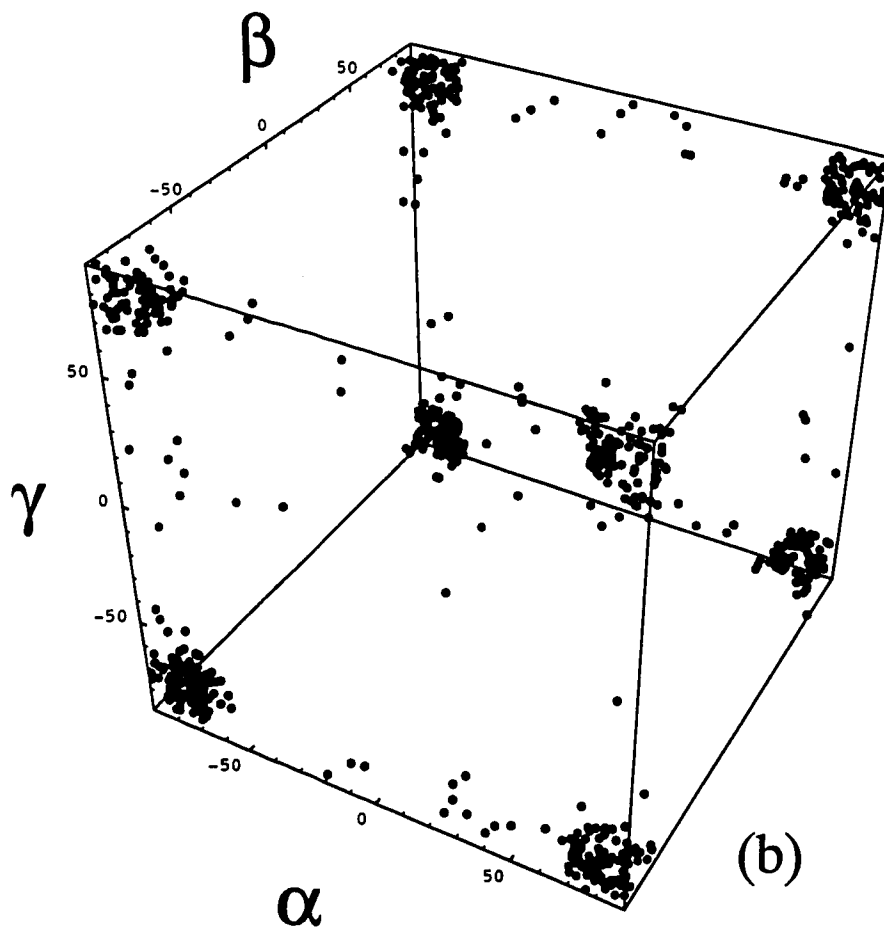


Figure 3.3(b) An ensemble of 1000 molecules whose orientational distribution gives the order parameters for disk-like liquid crystals with biaxial coupling parameter  $r_2=0.35$  for  $T = 0.400$ .

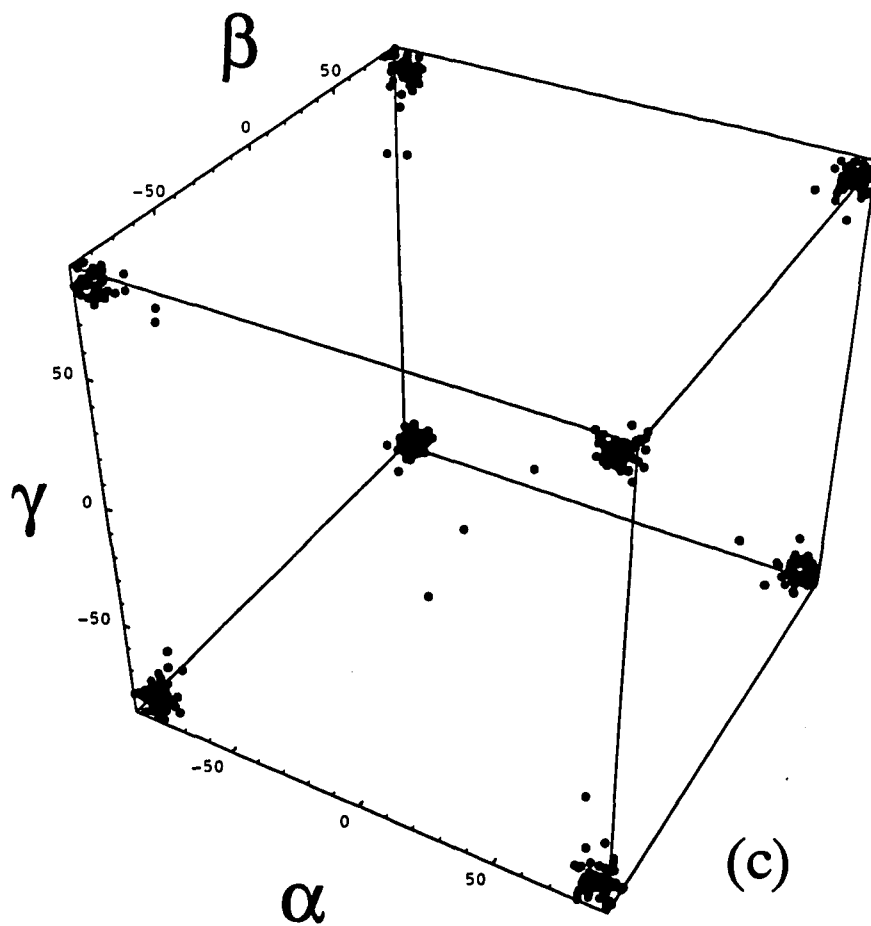


Figure 3.3(c) An ensemble of 1000 molecules whose orientational distribution gives the order parameters for disk-like liquid crystals with biaxial coupling parameter  $r_2=0.35$  for  $T = 0.100$ .

demonstrates that this distribution is also one of complete alignment except the molecular z-axis aligns along the laboratory y-axis. The entropy of transition was calculated using Eqn. (3.29) and the results indicate that the phase transition from the isotropic phase ( $Q=D=P=C=0$ ) to the uniaxial nematic phases ( $P=C=0$ ) is first order. The entropy of transition between the isotropic phase and the uniaxial nematic phase decreased as the molecular biaxiality parameter approached  $r_2=0.33$  from either above (I- $N_U$ ) or below (I- $N_{U+}$ ). The phase transition from the uniaxial nematic phase to the biaxial nematic phase ( $N_{U+}$ - $N_B$  and  $N_U$ - $N_B$ ) was found to be second order.

### 3.7 Temperature-Concentration Phase Diagrams of Binary Mixtures

After the behavior of pure components had been studied, binary mixtures of biaxial liquid crystals were investigated. For binary mixtures, phase separation occurs when the combined free energy of two phases is lower when the two components are apart than the free energy of the homogeneous mixture. Temperature-composition phase diagrams give the physical conditions where miscibility gaps occur [98,100,111]. It is of interest to calculate phase diagrams of different mixtures of molecules with a variety of uniaxial and biaxial coupling strengths. For a given temperature, once the free energy of a homogeneous mixture is known as a function of composition (Eqn. (3.13)), the minimum free energy phase of the system can be determined. If any line connecting two points on the homogeneous free energy curves lie below it, the composition range between the two points is unstable and phase separation will occur. The most stable configuration can be found by constructing a double tangent to the homogeneous mixture free energy curves [98,100]. An equivalent method to constructing this double tangent

involves the calculation of the chemical potential of both components (Eqns. (3.33) and (3.34)) [98,100]. When the chemical potentials of both components,  $\mu_i$ , are equal, the phases are in thermal and diffusive equilibrium and they can coexist. Therefore, the concentrations where the chemical potentials are equal gives the location of the miscibility gaps. Plotting the chemical potentials  $\mu_1$  against  $\mu_2$  and locating the point where the curve crosses itself gives a second, more numerically efficient, method of determining coexistence regions. In producing the temperature-concentration phase diagrams, the volumetric fraction ( $Y$ ) will be given in lieu of the number density (see Appendix IV). In all phase diagrams presented, the volume per molecule and the isotropic interaction strengths are set equal for both components to emphasize the effect of the anisotropic interaction strength.

For mixtures, three parameters are needed;  $r_1$ , which reduces in the uniaxial case to a ratio of transition temperatures ( $r_1 = (v_2 T_{NI2}/v_1 T_{NI1})^{1/2}$ ) [112],  $r_2$  which measures molecular biaxiality for component 1, and  $r_3$ , the biaxiality parameter for the second species ( $r_2$  for species 2 is  $r_3/r_1 = (W_{22}/U_{22})^{1/2}$ ). First, a mixture of rod-like liquid crystals was chosen with  $r_2$  approximately that expected for uniaxial nematogens, ( $r_1=0.632$ ,  $r_2=0.163$ ,  $r_3=0.158$ ). For the rod-like uniaxial nematogen FLOC<sub>14-d</sub>, the temperature dependence of  $Q$  and  $D$  were experimentally measured and fit to this theory to give  $r_2 = -0.16 \pm 0.01$  [58]. Comparison of results, shown in Figure 3.4, to an earlier study of binary mixtures of uniaxial, prolate liquid crystals ( $r_1=0.632$ ,  $r_2=r_3=0$ ) [98] shows that the effect of increasing molecular biaxiality is a decrease in the area of the  $N_{U^*}$ -I coexistence region and the appearance of an inhomogeneous mixture of two biaxial phases (at different



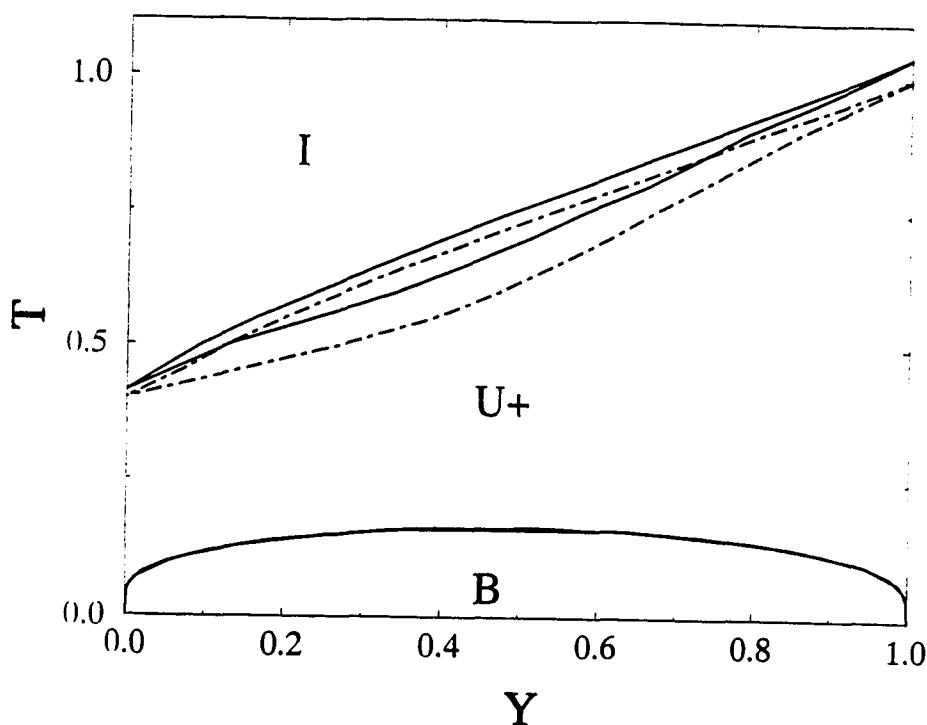


Figure 3.4 Temperature-concentration phase diagram for a biaxial binary mixture of rod-like liquid crystals with  $r_1=0.6325$ ,  $r_2=0.1633$ ,  $r_3=0.1581$ . The two solid lines on the top of the diagram are prolate nematic ( $N_{U+}$ ) - isotropic (I) coexistence curves. The dotted lines are the coexistence curves if the molecules were cylindrically symmetric ( $r_1=0.6325$ ,  $r_2=0.0$ ,  $r_3 = 0.0$ ). Below  $T = 0.17$ , biaxial solutions give the minimum free energy. The bottom line is a biaxial nematic ( $N_B$ ) - biaxial nematic ( $N_B$ ) coexistence region. For all phase diagrams,  $Y$  is the volumetric fraction of species  $i = 1$  and  $T$  is the temperature normalized such that  $T = 1.00$  is  $T_{NI}$  in Maier-Saupe theory.

concentrations) in the biaxial phase at lower temperatures. A mixture of disk-like liquid crystals ( $r_1=0.5$ ,  $r_2=0.7$ ,  $r_3=1.2$ ), presents qualitatively similar results, as shown in Figure 3.5. Figures 3.6 and 3.7 give the results of mixing rod-like with plate-like liquid crystal molecules, here  $r_1=1$ ,  $r_2=0.16$ ,  $r_3=0.7$ . This temperature-concentration phase diagram demonstrates that mixtures of prolate and oblate liquid crystals are unstable to spinodal decomposition into two coexisting uniaxial phases,  $N_{U+}$  and  $N_{U-}$ , even when the molecules are slightly perturbed from cylindrical symmetry. A mixture of a rod-like liquid crystal molecules with an asymmetrically shaped disk ( $r_1=0.632$ ,  $r_2=0.1633$ ,  $r_3=0.25$ ) has a small stable biaxial phase as demonstrated in Figure 3.8. The last temperature-concentration phase diagram (Figure 3.9) shows that for mixtures of liquid crystals with asymmetric shapes between that of rods and disks ( $r_1=1.0$ ,  $r_2=0.30$ ,  $r_3=0.35$ ), the homogeneous mixture in the biaxial phase is stable. The parameter  $r_2=0.30$  describes a flattened rod shaped molecule while  $r_3=0.35$  corresponds to a lopsided disk shaped one. The mixture of these two liquid crystals does not phase separate, a result which can be understood by comparing the free energy curves in Figure 3.10. For the mixture of nearly cylindrically symmetric rods and plates in Figure 3.10(a), a concave free energy envelope shows that a heterogeneous mixture minimizes the free energy. For the mixture shown in Figure 3.10(b), the free energy curve is convex which indicates that this mixture will not phase separate but remain a homogeneous mixture. The implications of this result are discussed below.

### 3.8 Conclusions

Predictions of the temperature dependence of all four order parameters

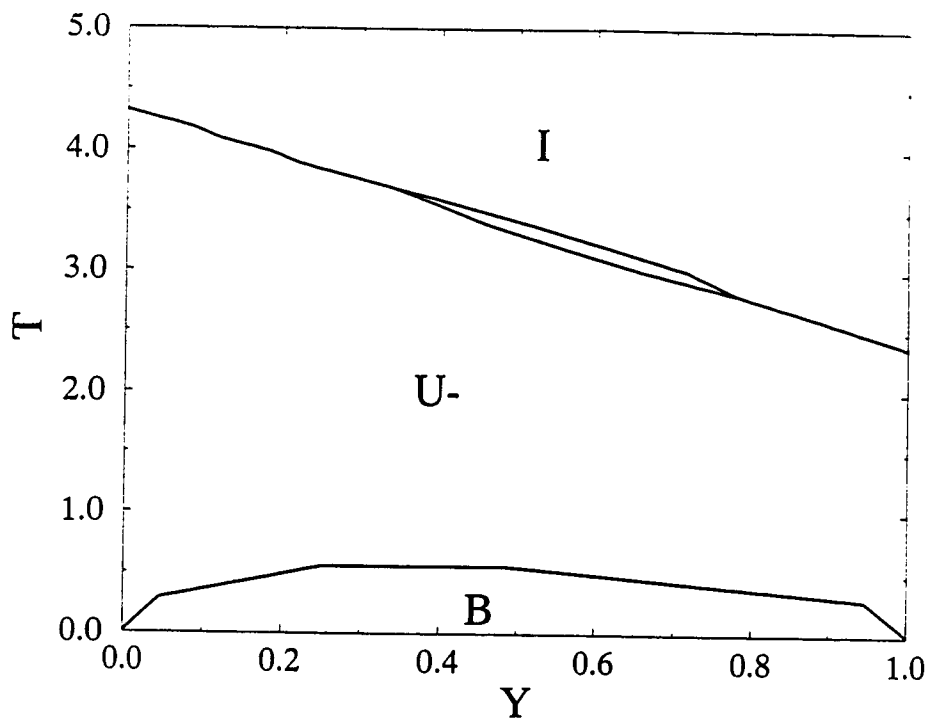


Figure 3.5 Temperature-concentration phase diagram for a biaxial binary mixture of disk-like liquid crystals with  $r_1=0.5$ ,  $r_2=0.7$ ,  $r_3=1.2$ . The two solid lines on the top of the diagram are oblate uniaxial nematic ( $N_{U-}$ ) - isotropic (I) coexistence curves. Below  $T=0.6$ , the system is biaxial. The bottom line is a biaxial nematic ( $N_B$ ) - biaxial nematic ( $N_B$ ) coexistence region.

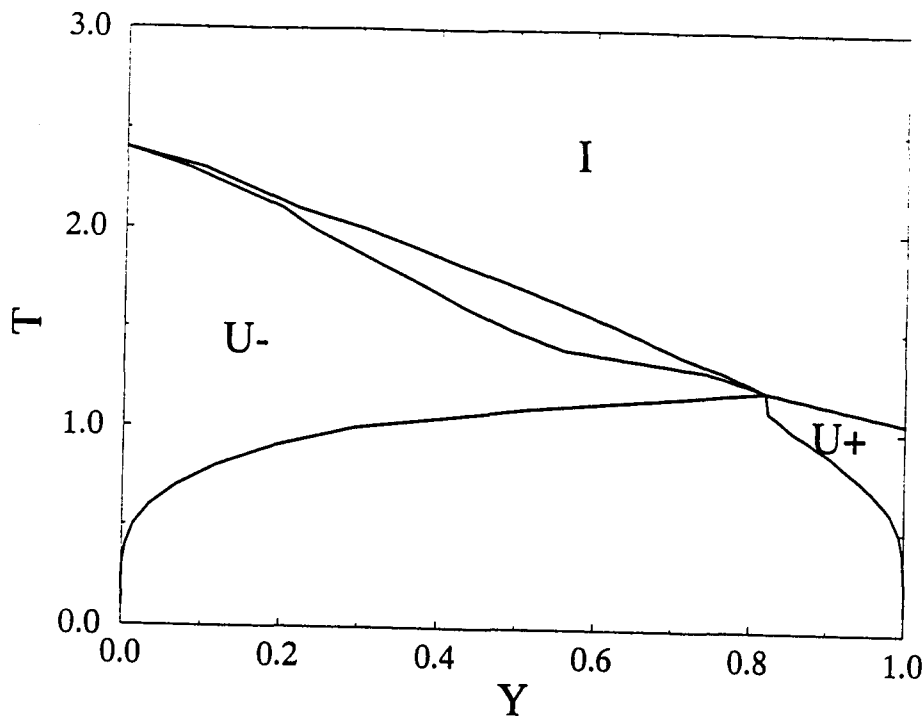


Figure 3.6 Temperature-concentration phase diagram for a biaxial binary mixture of disk-like liquid crystals with rod-like liquid crystals, here  $r_1=1.0$ ,  $r_2=0.166$ ,  $r_3=0.70$ . The two solid lines on the top of the diagram are oblate nematic ( $N_U$ ) - isotropic (I) coexistence curves. The bottom lines show that the biaxial nematic ( $N_B$ ) phase is unstable, and the mixture phase separates into two coexisting uniaxial nematic phases ( $N_{U+}$  and  $N_{U-}$ ).

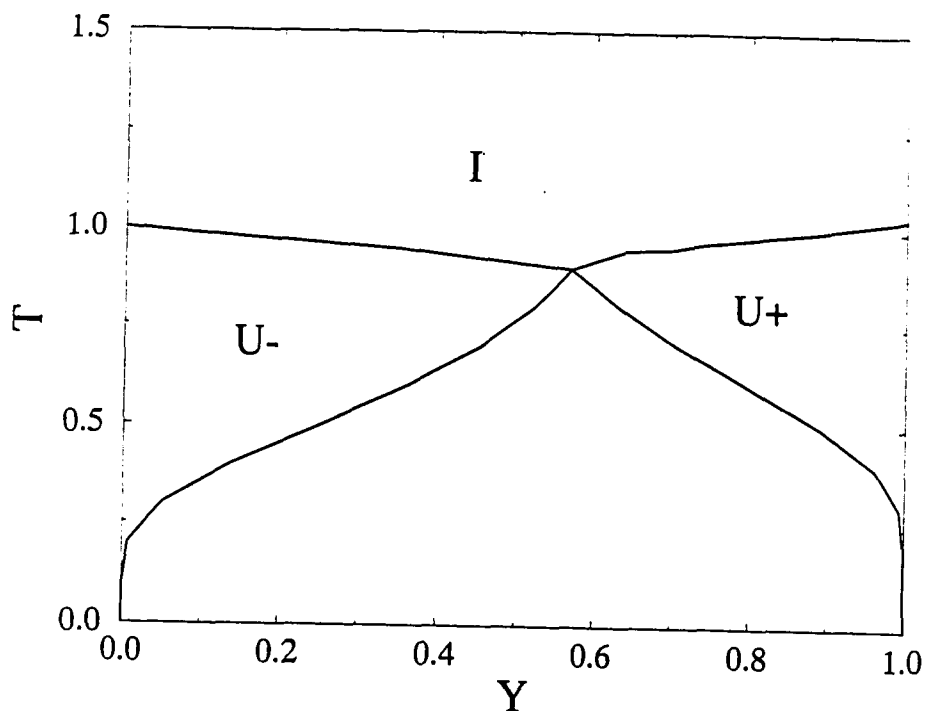


Figure 3.7 Temperature-concentration phase diagram for a biaxial binary mixture of disk-like liquid crystals with rod-like liquid crystals with  $r_1=0.5$ ,  $r_2=0.166$ ,  $r_3=0.50$ . The bottom lines again show that the biaxial nematic ( $N_B$ ) phase is unstable, and the mixture phase separates into two coexisting uniaxial nematic phases ( $N_{U+}$  and  $N_{U-}$ ). Here the two pure components have roughly equal isotropic-nematic transition temperatures close to the Maier-Saupe value  $T = 1.0$ .

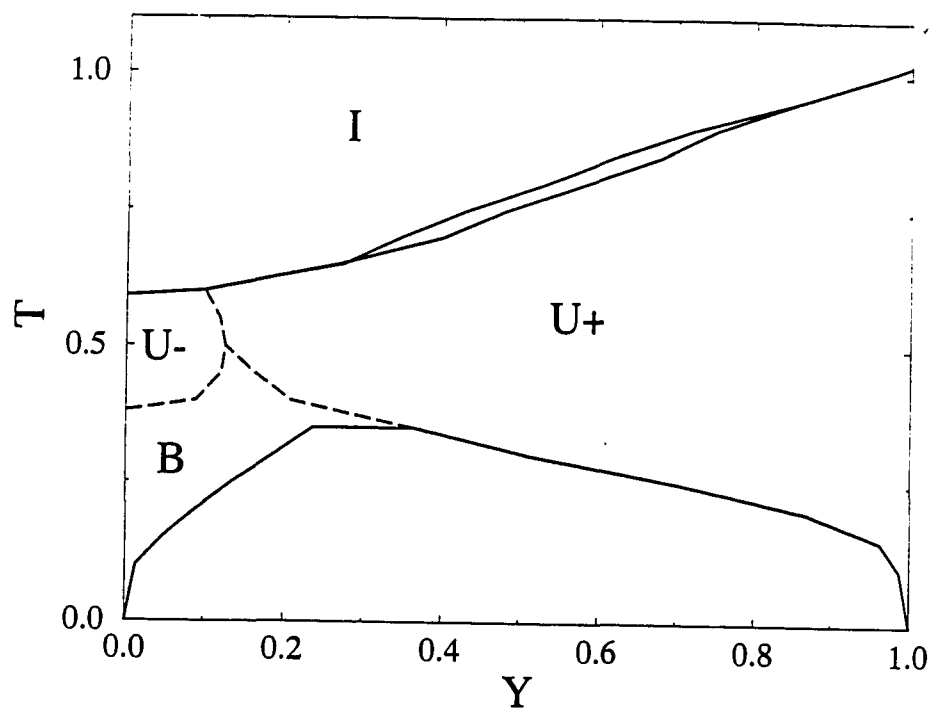


Figure 3.8 Temperature-concentration phase diagram for a binary mixture of rod-like nematogens with highly asymmetric disk-like molecules, here  $r_1=0.6325$ ,  $r_2=0.166$ ,  $r_3=0.25$ . A small region where the biaxial phase is stable exists. The dotted lines are not coexistence curves, but simply phase boundaries. The bottom line is a biaxial nematic ( $N_B$ ) - uniaxial nematic ( $N_{U+}$ ) coexistence region.

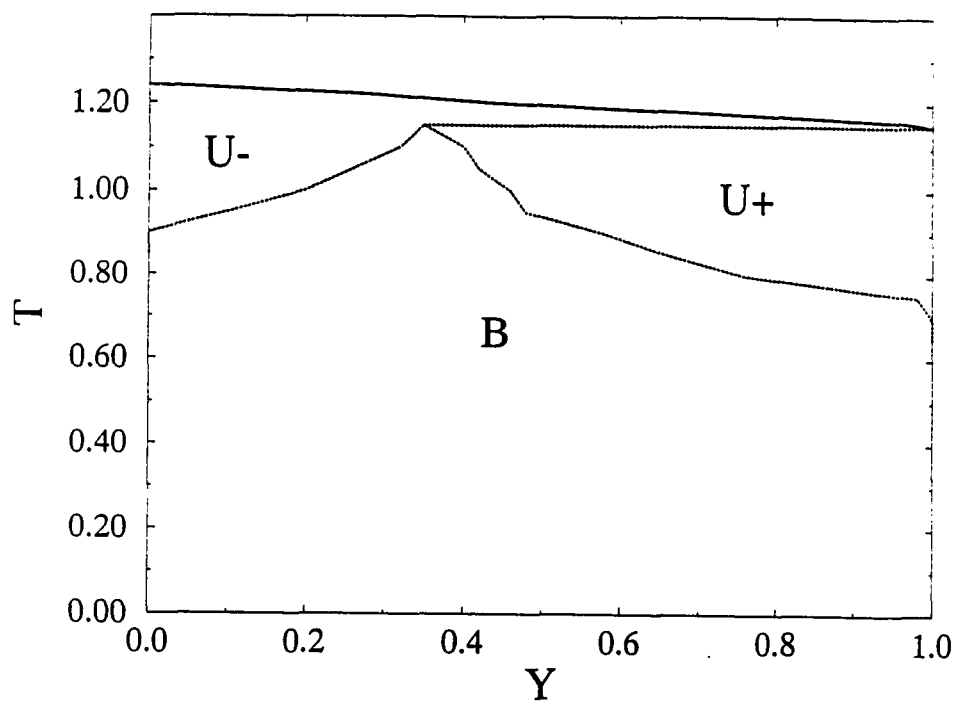


Figure 3.9 Temperature-concentration phase diagram for a biaxial binary mixture of flattened rod-like liquid crystals with lopsided disk-like liquid crystals,  $r_1=1.0$ ,  $r_2=0.3$ ,  $r_3=0.35$ . The dotted lines are not coexistence curves, but simply phase boundaries. For this mixture the biaxial phase is stable and is found close to the nematic - isotropic transition temperature ( $T_{NI}$ ) for  $Y=0.33$ .

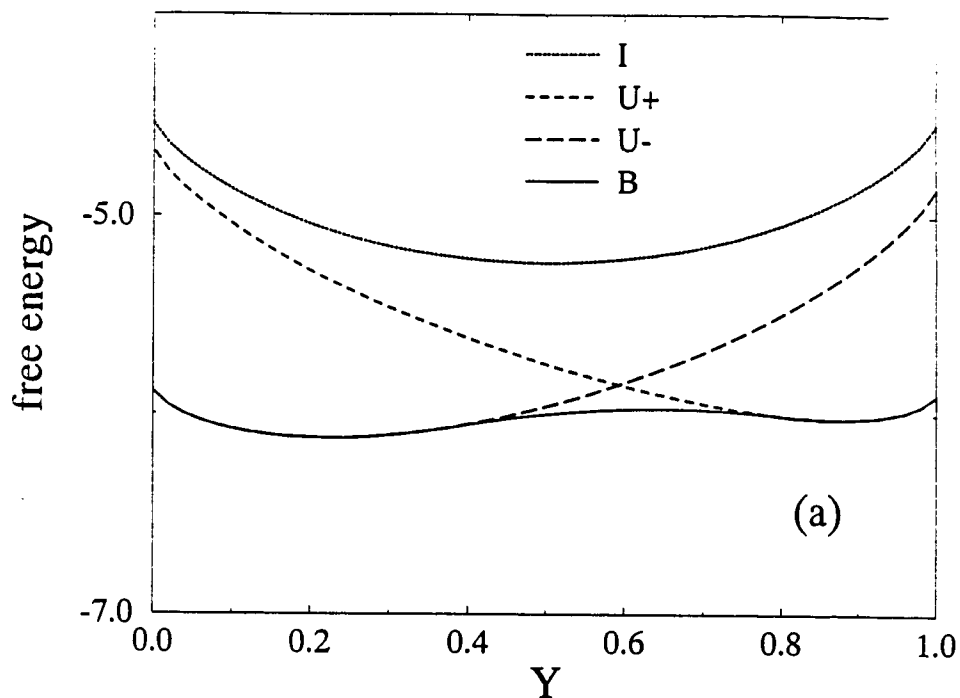


Figure 3.10(a) The free energy density at a fixed temperature is plotted as a function of concentration for the four possible phases of the mixture: isotropic (I), prolate uniaxial ( $N_{U_+}$ ), oblate uniaxial ( $N_{U_-}$ ) and biaxial ( $N_B$ ). For the system illustrated in Figure 3.7 at  $T = 0.50$ , the free energy density of all four phases is shown in Figure 3.10(a). To obtain the minimum free energy, the mixture phase separates into two uniaxial components.



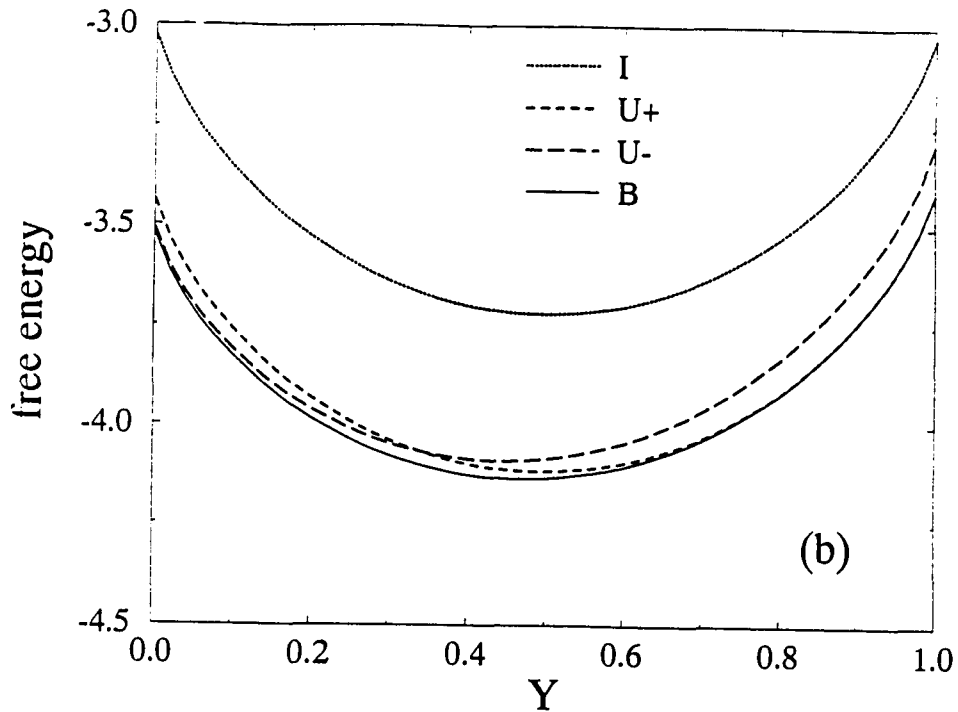


Figure 3.10(b) The free energy density at a fixed temperature is plotted as a function of concentration for the four possible phases of the mixture: isotropic (I), prolate uniaxial ( $N_{U+}$ ), oblate uniaxial ( $N_{U-}$ ) and biaxial ( $N_B$ ). For the system illustrated in Figure 3.9 at  $T = 0.85$ , the free energy density of all four phases is shown in Figure 3.10(b). The minimum free energy corresponds to a homogeneous biaxial phase.

describing a biaxial nematic phase in a single component liquid crystal have been presented for the first time [63]. The general result that asymmetric liquid crystals exhibit a second order phase transition between uniaxial and biaxial nematic phases is consistent with previous predictions [21,101-108]. These theoretical results motivated searches for low molecular weight biaxial nematogens [109,110,113-115]. The success of these searches is a topic of debate [116]. Experimental investigations of single component biaxial nematogens in the uniaxial calamitic phase have been performed in which the temperature dependence of the order parameters was successfully fit using this model [58]. It would be interesting to perform analogous experiments on the newly reported biaxial nematic liquid crystal systems to determine if they are truly biaxial nematic phases.

Behavior of biaxial nematogens in binary mixtures has also been predicted using mean field theory. Temperature-composition phase diagrams of a number of binary mixtures have been calculated in order to explore the behavior of biaxial molecules in nematic liquid crystal phases. Previous work on nematic mixtures have suggested that it may be possible to achieve phase biaxiality by mixing rod-like nematogens and plate-like nematogens [89]. Mean field calculations of cylindrically symmetric molecules ( $D_{2h}$  symmetry) concluded that for binary mixtures of prolate and oblate liquid crystal molecules, the biaxial phase is unstable to spinodal decomposition into separate inhomogeneous mixtures of uniaxial phases ( $N_{U+}$  and  $N_{U-}$ ) [98]. In the present study it has been shown that the inclusion of slight molecular biaxiality into the theory does not affect this conclusion. A mixture of a plate-like liquid crystal and a rod-like liquid

crystal (with a shape anisotropy comparable to those observed in real uniaxial rod-like liquid crystal systems [58]) is predicted to phase separate into two uniaxial phases, rather than to produce a stable biaxial nematic. Only mixtures composed of extremely asymmetric or lopsided molecules prefer the biaxial nematic phase. And, for binary mixtures the interesting result that a blend of highly asymmetric molecules with opposite shape anisotropy (asymmetric rods with disks) form a more stable, higher temperature biaxial nematic phase than either pure component alone.

#### 4. Molecular Motion of Nematic Liquid Crystals

The anisotropic intermolecular forces which cause liquid crystals to align also have a strong influence on their molecular motion.  $^2\text{H}$ -NMR relaxation experiments have been used to investigate the anisotropic molecular motion of nematic liquid crystals. Relaxation experiments measure how fast a spin system undergoes the transitions necessary to return it to thermal equilibrium. Spontaneous transitions between magnetic energy levels are hopelessly slow (e.g. for deuterons in a 7 Tesla magnetic field, the transition rate is  $W \approx 10^{-21} \text{ s}^{-1}$ ). Therefore, transitions between magnetic energy levels occur by stimulated absorption and emission. Thermal photons can induce transitions. However, this coupling also gives negligible transition rates ( $W \approx 10^{-9} \text{ s}^{-1}$  for deuterons in a 7 Tesla magnetic field in a coil with a  $Q = 100$ , volume of the sample =  $10^{-6} \text{ m}^3$ , and  $T = 300 \text{ K}$ ) [117]. Since coupling with the radiation field is inadequate as a relaxation mechanism, interactions of the spin system with its surrounding environment, the 'lattice', must be invoked to explain the observed relaxation rates. For  $^2\text{H}$ -NMR of liquid crystals, reorientational motion of the molecules give rise to rapidly fluctuating terms in the quadrupolar Hamiltonian which induce transitions. The rate at which a spin system relaxes to thermal equilibrium can be expressed in terms of spectral density functions which characterize the spectrum of the fluctuations [118]. Proper selection of relaxation experiments allows the determination of these individual spectral densities of motion as a function of frequency and temperature [119]. These spectral densities can be interpreted using various models of the molecular motion. In this chapter of the thesis, spectral

density data from both pure FLOC and a FLOC:p-Xy binary mixture will be interpreted by fitting experimentally measured spectral densities to a composite diffusion model of molecular motion in a nematic liquid crystal [61,65].

#### 4.1 Pulse Sequences

The measurement of deuteron relaxation rates in liquid crystals requires the use of sophisticated pulse sequences. Examples of the pulse sequences for a number of relaxation experiments are given in Figure 4.1. Assuming the system starts from thermal equilibrium, individual magnetizations or higher order coherences are established using a series of rf pulses and delays in the **preparation** part of the pulse sequence. Any of the eight quantum operators, ( $I_x$ ,  $I_y$ ,  $I_z$ ,  $Q_x$ ,  $Q_y$ ,  $Q_z$ ,  $D_x$ ,  $D_y$ ) [120], can be excited using a suitable pulse sequence. Pulse sequences which are used to establish spin order include the Jeener-Broekaert sequence which [121,122] creates quadrupolar order ( $Q_z$ ), an inversion-recovery experiment [123,124] in which Zeeman order ( $-I_z$ ) is excited, and an experiment [125,126] in which double quantum coherences ( $D_x$  or  $D_y$ ) are established. After the coherence has been prepared, the system is allowed to evolve for a given period of time,  $T$ , during which the spin system relaxes back to thermal equilibrium. The **evolution** of the operators can only be detected if **mixing** pulses are applied to create single quantum coherence. A measure of the decay of the order or coherence in the time,  $T$ , gives the relaxation rates, i.e. the decay of  $Q_z$  gives  $T_{1Q}$ , the decay of  $I_z$  gives  $T_{1Z}$  and the decay of  $D_x$  or  $D_y$  give  $T_{DQ}$ .

A simple example of a pulse sequence used to measure relaxation rates is the inversion-recovery pulse sequence with quadrupolar echo detection (IRQE). As

shown in Figure 4.1, the preparation part consists of a high power  $180^\circ$  pulse which inverts all the spins. After this pulse, the system is allowed to evolve freely for a time  $T$ . The mixing sequence is a conventional quadrupolar echo pulse sequence ( $90_x$ - $\tau$ - $90_y$ - $\tau$ -acq).

The time evolution of the density matrix during the IRQE experiment can be calculated starting from the thermal equilibrium distribution:  $\rho(0) = I_z$ . An rf voltage is applied across the coil at the Larmor frequency,  $\nu_0$ , with the intensity  $\omega_1 = \gamma\hbar H_1$  for a time  $t_p$ , such that  $\omega_1 t_p = \pi$ . The resulting density matrix is (see Appendix III)

$$\begin{aligned}\rho(t) &= \exp(iI_x \omega_1 t_p) I_z \exp(-iI_x \omega_1 t_p) \\ &= I_z \cos(\pi) - I_y \sin(\pi) \\ &= -I_z.\end{aligned}\quad (4.1)$$

The Zeeman order relaxes back to equilibrium exponentially during the time  $T$ ,

$$\rho(T) = -I_z \left[ 1 - 2 \exp\left(-\frac{T}{T_{1z}}\right) \right] \quad (4.2)$$

The quadrupole echo pulse sequence is used to create the detected signal quantum coherence [60]. Here, the first pulse projects the magnetization onto the x-y plane, and after a time,  $\tau$ , the second pulse refocuses precession due to the quadrupole Hamiltonian. To obtain the most accurate values of the relaxation rate,  $T_{1z}$ , the inversion-recovery sequence requires uniform initial inversion. When pulse power is limited ( $\omega_1 \leq \omega_Q$ ), composite  $90^\circ$  and  $180^\circ$  pulses are often used to acquire undistorted spectra [123,127].

Most measurements of deuterium quadrupolar order relaxation in liquid crystal systems have used the conventional Jeener-Broekaert (JB) pulse sequence [119-122]. The preparation sequence for a conventional JB experiment is  $90_x$ - $\tau$ - $45_y$ . Starting

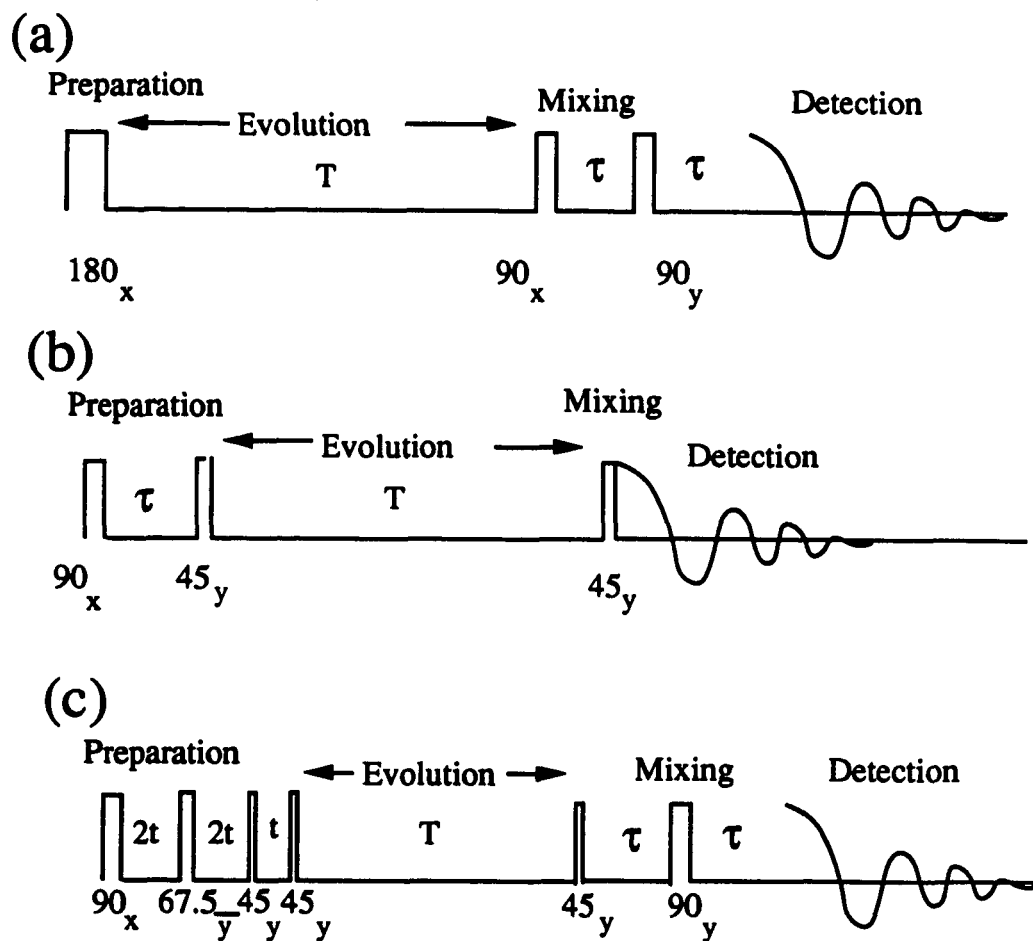


Figure 4.1 Three pulse sequences used to investigate molecular motion using  $^2\text{H}$ -NMR. The sequences pictured are (a) an inversion recovery experiment with a quadrupolar echo (IRQE) which is used to measure the rate of decay of Zeeman order  $T_{1z}$ , (b) the Jeener-Broekaert pulse sequence used to measure  $T_{1z}$  and rate of decay of quadrupolar order  $T_{1Q}$ , and (c) the broad band Jeener-Broekaert pulse sequence used to measure  $T_{1Q}$ .

from equilibrium,  $\rho(0) = I_z$ . After the  $90_x$  pulse has been applied,  $\rho(t) = I_y$ . This transverse magnetization is allowed to evolve under the quadrupolar Hamiltonian for some time  $\tau$ :

$$\rho(\tau) = \exp(iQ_z\omega_Q\tau) I_y \exp(-iQ_z\omega_Q\tau) = I_y \cos(\omega_Q\tau) + Q_x \sin(\omega_Q\tau). \quad (4.3)$$

If  $\tau$  is chosen such that  $2\omega_Q\tau = (2n+1)\pi$ , then  $\rho = \pm Q_x$ . Supposing a y-pulse is applied at this time, the density matrix becomes

$$\begin{aligned} \rho &= \exp(iI_y\omega_1 t_p) Q_x \exp(-iI_y\omega_1 t_p) \\ &= Q_x \cos(2\omega_1 t_p) + \frac{1}{2} (3Q_z - D_x) \sin(2\omega_1 t_p). \end{aligned} \quad (4.4)$$

Choosing  $t_p$  such that  $\omega_1 t_p = \pi/4$  gives  $\rho = 1/2(3Q_z - D_x)$ . Next, the system is allowed to relax back to equilibrium for a time  $T$  after the second pulse,

$$\rho(T) = I_z [1 - \exp(-\frac{T}{T_{1z}})] + \frac{3}{2} Q_z \exp(-\frac{T}{T_{1Q}}) + \frac{1}{2} D_x \exp(-\frac{T}{T_{DQ}}), \quad (4.5)$$

where  $T_{DQ}$  is the double quantum relaxation rate. In the mixing part of the JB sequence, a pulse is applied along the x-direction;  $\theta = \omega_1 t_p$  gives

$$\begin{aligned} \rho &= \left\{1 - \exp(-\frac{T}{T_{1z}})\right\} \left\{I_z \cos\theta + I_y \sin\theta\right\} \\ &+ \frac{3}{2} \exp(-\frac{T}{T_{1Q}}) \left\{\frac{1}{2} Q_z (3\cos^2\theta - 1) - Q_y \sin\theta \cos\theta - \frac{1}{2} D_x \sin^2\theta\right\} \\ &+ \frac{1}{2} \exp(-\frac{T}{T_{DQ}}) \left\{-Q_y \sin\theta \cos\theta - \frac{3}{2} Q_z \sin^2\theta + \frac{1}{2} D_x (1 + \cos^2\theta)\right\}. \end{aligned} \quad (4.6)$$

If the flip angle,  $\theta$ , is chosen to be  $45^\circ$ , a maximum amount of  $Q_y$  is produced from  $Q_z$ . Notice, however, that this choice of flip angle reduces the amplitude of the Zeeman order,  $I_z$ , by a factor of  $\sqrt{2}$ . Phase cycling can be used to cancel the double quantum coherence [60,119], this leaves the following measurable part of the density matrix:



$$\rho = \frac{\sqrt{2}}{2} [1 - \exp(-\frac{T_1}{T_{1z}})] I_y - \frac{3}{4} \exp(-\frac{T_1}{T_{1Q}}) Q_y. \quad (4.7)$$

The relaxation rates,  $T_{1z}$  and  $T_{1Q}$ , can be measured by measuring the sum (to get  $I_y$ ) and the difference (to get  $Q_y$ ) of intensities of the quadrupolar doublets as a function of relaxation time,  $T$ . Denoting the intensity of left and right absorption peaks by  $m_l(T)$  and  $m_r(T)$  respectively, the signal is  $\text{Tr}(\rho I^*) = m_l(T) + m_r(T)$ . An automated procedure which uses nonlinear least squares fitting was developed [128] for determining the relaxation rates based on the relations

$$S(T) = m_l(T) + m_r(T) \quad (4.8)$$

$$D(T) = m_l(T) - m_r(T) \quad (4.9)$$

$$S(T) = [S(0) - S(\infty)] \exp(-\frac{T}{T_{1z}}) + S(\infty) \quad (4.10)$$

$$D(T) = D(0) \exp(-\frac{T}{T_{1Q}}), \quad (4.11)$$

where  $S(\infty)$  and  $S(0)$  are the equilibrium and initial sum intensities respectively, and  $D(0)$  is the initial difference intensity. Obtaining the relaxation rates with this conventional Jeener-Broekaert pulse sequence is called the sum and difference (SAD) method [119,124].

For the SAD experiment, digitation is started immediately after the last pulse. Finite spectrometer recovery time precludes this, and distortions appear in the spectrum. Also, the conventional JB experiment only creates quadrupolar order with maximum intensity for specific frequencies  $\nu_Q$ , such that  $\tau = (2n+1)/(4\nu_Q)$ . In general, however, there is a distribution of  $2\nu_Q$  values in the  $^2\text{H-NMR}$  spectrum, and the value of  $\tau$  chosen will be a compromise which leads to less than optimal excitation of quadrupolar

order for some values of  $2\nu_Q$ .

Broadband Jeener-Broekaert experiments have been proposed by Wimperis [129-131] to help overcome this problem. One such pulse sequence is  $90_x - 2\tau - 67.5_y - 2\tau - 45_y - \tau - 45_y$ . [129]. A spin density matrix calculation of this multiple pulse sequence demonstrates the creation of broadband quadrupolar excitation [129-133]. The quadrupolar order,  $Q_z$ , is measured as a function of relaxation time,  $T$ , using a final  $45_y$  mixing pulse. Because of the dead time of the receiver, this method produces similar spectral artifacts as the traditional JB pulse sequence. To avoid this problem, a  $90_y$  pulse is inserted after the  $45_y$  mixing pulse to refocus the single quantum coherence [59]. This refocusing is analogous to the quadrupolar echo. The symmetries of the refocusing pulse required for Zeeman and quadrupolar order are incompatible; that is, the phase cycle which maximizes quadrupolar order suppresses Zeeman order, and vice-versa [59,60]. As a result, two separate experiments need to be performed: a broadband Jeener Broekaert (BBJB) and an inversion recovery experiment quadrupolar echo detection (IRQE). It has been shown that this approach (BBJB and IRQE) yields relaxation rates,  $T_{1Z}$  and  $T_{1Q}$ , with significantly greater precision and accuracy than those determined using a conventional Jeener-Broekaert experiment [60]. Examples of stacked plots created using this sequence of experiments are shown in Figure

4.2

#### 4.2 Relaxation Theory

Having measured the decay rate of quadrupolar and Zeeman order ( $T_{1Q}$  and  $T_{1Z}$ ), the results of these experiments need to be interpreted. The first step in this process

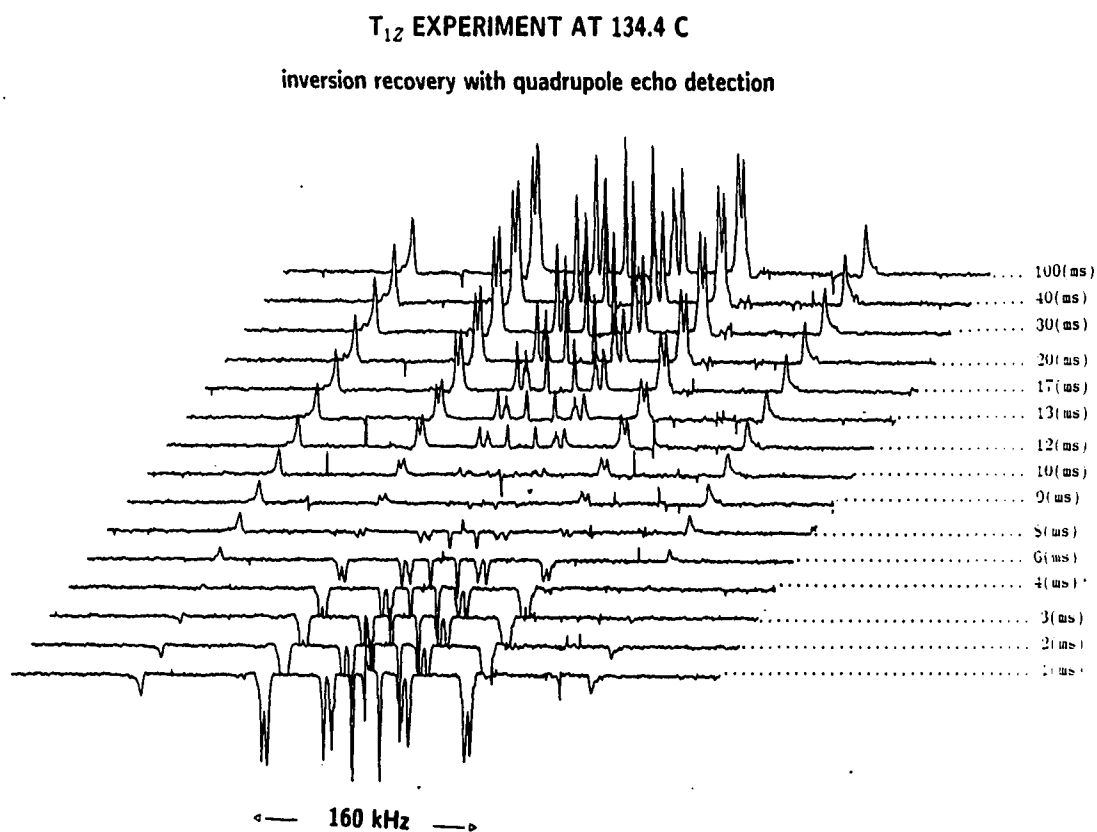


Figure 4.2(a) Stacked plots from an inversion-recovery experiment (IRQE) performed on pure FLOC.

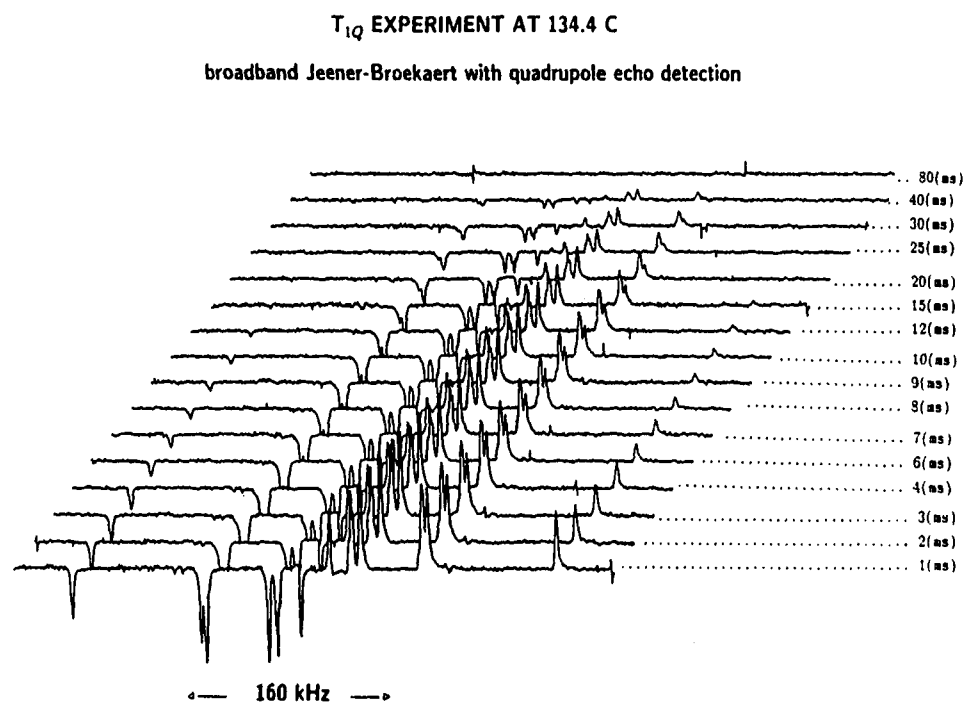


Figure 4.2(b) Stacked plots from a broad-band Jeener-Broekaert experiment (BBJB) performed on pure FLOC.

is to derive a theoretical description of relaxation in spin  $I=1$  systems. In the fast motion regime, these relaxation rates are expressed in terms of spectral density functions ( $J_M(M\omega_0)$ ) which characterize the molecular motion. Two different relaxation experiments (BBJB and IRQE) allows the determination of the individual spectral densities. These spectral densities represent the maximum amount of information available on molecular motion from magnetic resonance experiments [59,60,119].

When a time dependent perturbation is present, the Hamiltonian can be written as:

$$H = H_0 + H'(t) \quad (4.12)$$

where the time independent term  $H_0$  is responsible for the  $^2\text{H}$ -NMR spectrum and includes the static Zeeman, quadrupolar, dipolar and scalar couplings.  $H'(t)$  describes time dependent interactions and is defined to have a zero time average,  $\langle H'(t) \rangle = 0$ . Suppose  $\phi_n$  is an eigenvector of  $H_0$  with eigenvalue  $\hbar\omega_n$ , then a general solution of the time dependent Schrödinger equation can be written in the form

$$i\hbar \frac{\partial}{\partial t} \Psi = H \Psi \quad (4.13)$$

$$\Psi = \sum_n c_n(t) \phi_n = \sum_n a_n(t) e^{-i\omega_n t} \phi_n. \quad (4.14)$$

A time dependent density matrix operator  $\rho'$  can be defined:

$$\begin{aligned} (4.15) \quad \rho'_{nm} &= \langle a_n(t) a_m^*(t) \rangle \\ &= \rho_{nm} e^{i(\omega_n - \omega_m)t} \end{aligned}$$

Time dependent perturbation theory [132] gives expressions for the expansion coefficients at time  $t+\Delta t$ ,  $a_n(t+\Delta t)$ , given  $a_n(t)$ .

$$a_n(t+\Delta t) = \sum_i a_n^{(i)}(t+\Delta t) \quad (4.16)$$

To order zero, the coefficients are static in time

$$a_n^{(0)}(t+\Delta t) = a_n(t), \quad (4.17)$$

and higher order terms describe the time dependence of the expansion coefficients

$$a_n^{(i+1)}(t+\Delta t) = -i \sum_l \int_l^{t+\Delta t} a_l^{(i)}(t') \langle n | H'(t') e^{-i(\omega_n - \omega_l)t'} | l \rangle dt'. \quad (4.18)$$

Expanding the density matrix to second order (i=2) gives

$$\begin{aligned} \rho_{nm}'(t+\Delta t) &= \langle \sum_i a_n^{(i)}(t+\Delta t) \sum_j a_m^{(j)*}(t+\Delta t) \rangle \\ &= \rho_{nm}'(t) + \langle a_n(t) a_m^{(1)*}(t+\Delta t) \rangle + \langle a_n^{(1)}(t+\Delta t) a_m^*(t) \rangle \\ &\quad + \langle a_n(t) a_m^{(2)*}(t+\Delta t) \rangle + \langle a_n^{(2)}(t+\Delta t) a_m^*(t) \rangle \\ &\quad + \langle a_n^{(1)} a_m^{(1)*}(t+\Delta t) \rangle \end{aligned} \quad (4.19)$$

This expansion can be used to derive an expression for the time dependence of the elements of the density operator. For the second order expansion to be valid, the density operator  $\rho_{nm}'(t)$  must not change appreciably in the time  $\Delta t$ , otherwise, higher order terms need to be included. In the interaction representation (a frame rotating at  $\nu_0$  about the laboratory z-axis), the time dependent terms in the density matrix change at frequencies  $\pm\nu_Q$ . This implies that  $\Delta t \ll 1/\nu_Q$  in order for the second order expansion to remain valid. In addition, the definition of a spectral density requires that  $\Delta t \gg \tau_c$ , where  $\tau_c$  is the correlation time for molecular motion. Physically, these two conditions are met for any system where the rotational motion of the molecule changes on time scales much smaller than  $1/\nu_Q$ , i.e.  $1/\nu_Q \gg \tau_c$ . In this motional regime, Redfield theory describes the time dependence of the density matrix [133-136].

$$\frac{\partial \rho_{nm}'(t)}{\partial t} = \sum_{lk} e^{i(\omega_n - \omega_m + \omega_l - \omega_k)t} R_{nmik} [\rho_{lk}'(t) - \rho_{lk}'(\infty)] \quad (4.20)$$

The elements of the relaxation superoperator are

$$R_{nmik} = J_{nlmk}(\omega_k - \omega_m) + J_{nlmk}(\omega_n - \omega_l) - \delta_{mk} \sum_{\gamma} J_{\gamma l \gamma n}(\omega_n - \omega_{\gamma}) - \delta_{nl} \sum_{\gamma} J_{\gamma m \gamma k}(\omega_{\gamma} - \omega_m) \quad (4.21)$$

and the spectral densities are defined in terms of Fourier transforms of autocorrelation functions:

$$J_{nmik}(\omega_k - \omega_l) = \int_0^{\infty} G_{nmik} e^{i(\omega_k - \omega_l)\tau} d\tau \quad (4.22)$$

The autocorrelation function,  $G_{nmik}$ , of a time dependent perturbing Hamiltonian is defined to be

$$G_{nmik}(\tau) = \overline{\langle n | H'(t) | m \rangle \langle l | H'(t+\tau) | k \rangle} \quad (4.23)$$

This function is defined with the following two assumptions:

- (1)  $G(\infty) = 0$ , i.e.,  $H'(t)$  and  $H'(t+\tau)$  are statistically uncorrelated at long times.
- (2)  $G(\tau)$  is an even function of  $\tau$ .

The first assumption implies that there exists some correlation time  $\tau_c$  such that  $G(\tau_c) \ll G(0)$  for all  $\tau > \tau_c$ . The integral expressions for the spectral densities can be evaluated with an upper limit of infinity because  $G(\tau \gg \tau_c) = 0$ . Nonsecular terms with  $(\omega_n - \omega_m) \neq (\omega_l - \omega_k)$  will oscillate at high frequencies, and make a negligibly small contribution to  $R_{nmik}$ . Thus with this secular approximation, equation (4.20) is simplified to

$$\frac{\partial \rho_{nm}'(t)}{\partial t} = \sum_{lk} R_{nmik} [\rho_{lk}'(t) - \rho_{lk}'(\infty)]. \quad (4.24)$$

The  $R_{nmik}$  are elements of a four dimensional relaxation super-matrix often called the 'Redfield super-operator' which describes the time evolution of a density matrix

subject to a time dependent Hamiltonian  $H'(t)$ . Some of the elements have a simple physical interpretation;  $R_{nnmm}$  gives the probability per unit time that a transition from state  $m$  to state  $n$  will occur. The rate of depletion of state  $n$  is  $-R_{nnnn}$ , and conservation of populations requires

$$R_{nnnn} = -\sum_m R_{mnnm} \quad (4.25)$$

The spectral density  $J_{nmik}(\omega)$  is a generalized transition probability requiring fluctuations with frequency components at  $\omega$ . These spectral densities are one sided Fourier transforms of the correlation function of the perturbing Hamiltonian as shown in Eqn. (4.22). Given the time dependent part of the Hamiltonian in terms of spherical tensors,

$$H'(t) = \sum_m (-1)^m A_{2,m} [T_{2,m}^L(t) - \overline{T_{2,m}^L}] \quad (4.26)$$

where the static part of the quadrupole Hamiltonian,  $\overline{T_{2,m}^L}$ , is subtracted off to insure that  $\langle H' \rangle = 0$ . Placing this Hamiltonian into (4.22) gives

$$\begin{aligned} J_{nmik}(\omega_k - \omega_m) &= \int_0^{\infty} \overline{\langle n | H'(t) | m \rangle \langle l | H'(t+\tau) | k \rangle^*} e^{i(\omega_k - \omega_m)\tau} d\tau \\ (4.27) \quad &= \sum_{M,N} (-1)^{M+N} \langle n | A_{2,-M} | l \rangle \langle m | A_{2,-N} | k \rangle^* \times \\ &\int_0^{\infty} \langle (T_{2,M}^L(t) - \overline{T_{2,M}^L})(T_{2,N}^L(t+\tau) - \overline{T_{2,N}^L}) \rangle e^{-i(\omega_k - \omega_m)\tau} d\tau, \end{aligned}$$

where  $T_{2,m}^L(t)$  are spatial derivatives of the electric potentials in the laboratory frame. These spatial derivatives are only known in the PAS of the EFG tensor  $T_{2,m}^{\text{PAS}}$ . Neglecting bond asymmetry, this is a frame with the z-axis points along the C-D bond:

$$T_{2,m}^L(t) = D_{m,0}^{(2)*}(\Omega(t)) T_{2,0}^B \quad (4.28)$$

where  $\Omega(t) = (\alpha(t), \beta(t), \gamma(t))$  are the time dependent Euler angles which rotate the laboratory



frame into the PAS frame of the EFG tensor. In this expression, the time dependence of the quadrupolar Hamiltonian is attributed to changes in the orientation of the C-D bond with respect to the laboratory frame. That is, the time dependence of  $H_Q'(t)$  results from molecular motions. For uniaxial liquid crystals, the orientational potential is independent of  $\alpha(t)$ , so  $M$  is constrained to be equal to  $N$  in equation (4.27)

$$J_{nmk}(\omega_k - \omega_l) = \sum_M \langle n | A_{2,-M} | m \rangle \langle l | A_{2,-M} | k \rangle^* \times \frac{12\pi}{8} \left( \frac{e^2 q_{zz} Q}{h} \right)^2 J_M(\omega_k - \omega_l) \quad (4.29)$$

where

$$J_M(\omega_k - \omega_l) = \int_0^\infty \left[ \langle D_{M0}^{(2)}(\Omega(t)) D_{M0}^{(2)*}(\Omega(t+\tau)) \rangle - \langle D_{M0}^{(2)} \rangle^2 \right] e^{i(\omega_k - \omega_l)\tau} d\tau. \quad (4.30)$$

The spectral density of motion,  $J_M(\omega)$ , is the value of the Fourier transform of the auto-correlation function of the Wigner rotation matrix elements  $D_{M0}^{(2)}(\Omega)$  at frequency  $\omega$ . Physically, the  $J_M(\omega)$ 's are a measure of the intensity of fluctuations in the electric field gradient at the frequency  $\omega$ .

Using the Zeeman basis set,  $|1\rangle = |I_z = +1\rangle$ ,  $|2\rangle = |I_z = 0\rangle$ , and  $|3\rangle = |I_z = -1\rangle$ , the non-zero spin operators  $A_{2,M}$  can be evaluated and are presented in Table 4.1. These results along with Eqn. (4.29) can be used to find  $J_{nmk}(\omega)$  in terms of the spectral densities  $J_M(\omega)$ . Of the 405 theoretically possible  $J_{nmk}(\omega)$ 's, symmetry requires that only 14 of them are non-zero [119], these are listed in Table 4.2. Combining these results, the Redfield relaxation matrix elements can be calculated explicitly in terms of spectral densities and these are presented in Table 4.3.

$\langle 1 A_{2,0} 1\rangle = 1$	$\langle 2 A_{2,0} 2\rangle = 2$	$\langle 3 A_{2,0} 3\rangle = -2$
$\langle 1 A_{2,1} 2\rangle = -\sqrt{2}$	$\langle 2 A_{2,1} 3\rangle = \sqrt{2}$	
$\langle 2 A_{2,-1} 1\rangle = \sqrt{2}$	$\langle 3 A_{2,-1} 2\rangle = -\sqrt{2}$	
$\langle 1 A_{2,2} 3\rangle = 2$	$\langle 3 A_{2,-2} 1\rangle = 2$	

Table 4.1 The non-zero matrix elements of the spin operators  $A_{2,M}$ .

$J_{1111} = J_{3333} = J_{1133} = \frac{1}{6} J_0(0)$
$J_{2222} = \frac{2}{3} J_0(0)$
$J_{1122} = J_{2233} = -\frac{1}{3} J_0(0)$
$J_{1212} = J_{2323} = J_{2121} = J_{3232} = \frac{1}{2} J_1(\omega_0)$
$J_{1223} = J_{2132} = -\frac{1}{2} J_1(\omega_0)$
$J_{1313} = J_{3131} = J_2(2\omega_0)$

Table 4.2 The 14 non-zero matrix elements of the spectral densities in units of  $\frac{3\pi^2}{2} \left( \frac{e^2 q_{iz} Q}{h} \right)^2$

$$\begin{aligned}
 R_{1313} &= R_{3131} = -J_1(\omega_0) - 2J_2(2\omega_0) \\
 R_{3333} &= R_{1111} = -J_1(\omega_0) - 2J_2(2\omega_0) \\
 R_{2222} &= -2J_1(\omega_0) \\
 R_{1212} &= R_{2121} = R_{2323} = R_{3232} = -\frac{1}{2} [3J_0(0) - 3J_1(\omega_0) - 2J_2(2\omega_0)] \\
 R_{1122} &= R_{2211} = R_{3322} = R_{2233} = J_1(\omega_0) \\
 R_{1133} &= R_{3311} = 2J_2(2\omega_0) \\
 R_{1223} &= R_{2132} = R_{2312} = R_{3231} = -J_1(\omega_0)
 \end{aligned}$$

Table 4.3 Redfield relaxation matrix elements for  $I = 1$  in units of  $\frac{3\pi^2}{2} \left( \frac{e^2 q_{zz} Q}{h} \right)^2$ .

### 4.3 Relaxation Rates and Spectral Densities

Finally, the connection between the relaxation rates ( $T_{1Z}$ ,  $T_{1Q}$ ) and the spectral densities  $J_M(\omega)$  needs to be made. The equation governing the decay of Zeeman order is

$$\frac{d \langle I_z \rangle}{dt} = - \frac{\langle I_z \rangle - \langle I_z(\infty) \rangle}{T_{1Z}} \quad (4.31)$$

Recalling the definition of the expectation value in terms of the trace in Eqn. (2.12), and given that the equilibrium density matrix is proportional to  $I_z$  gives,

$$\langle I_z \rangle = \text{Tr}(\rho I_z) = (\rho_{11} - \rho_{33}). \quad (4.32)$$

Substituting (4.32) into (4.31), applying Redfield's equation of motion (4.24), and taking into account that  $R_{3333} = R_{1111}$  and  $R_{1133} = R_{3311}$  gives

$$\begin{aligned} \frac{d \langle I_z \rangle}{dt} &= \frac{d (\rho_{11} - \rho_{33})}{dt} = R_{1111} (\rho_{11} - \rho_{11}(\infty)) + R_{1133} (\rho_{33} - \rho_{33}(\infty)) \\ &\quad - R_{3311} (\rho_{11} - \rho_{11}(\infty)) - R_{3333} (\rho_{33} - \rho_{33}(\infty)) \\ &= (R_{1111} - R_{1133}) [ (\rho_{11} - \rho_{33}) - (\rho_{11}(\infty) - \rho_{33}(\infty)) ] \\ &= (R_{1111} - R_{1133}) [ \langle I_z \rangle - \langle I_z(\infty) \rangle ]. \end{aligned} \quad (4.33)$$

therefore

$$\frac{1}{T_{1Z}} = R_{1133} - R_{1111}. \quad (4.34)$$

Using Table 4.3, an expression for the relaxation rate in terms of the spectral density of motion can be derived

$$\frac{1}{T_{1Z}} = \frac{3\pi^2}{2} \left( \frac{e^2 q_z Q}{h} \right)^2 [ J_1(\omega_0) + 4J_2(2\omega_0) ]. \quad (4.35)$$

Similarly, the decay of quadrupolar order

$$\frac{d \langle Q_z \rangle}{dt} = -\frac{\langle Q_z \rangle}{T_{1Q}}, \quad (4.36)$$

can be expressed in terms of the expectation values of the density matrix elements:

$$\langle Q_z \rangle = \text{Tr}(\rho Q_z) = \frac{1}{3} (\rho_{11} - 2\rho_{22} + \rho_{33}). \quad (4.37)$$

This gives

$$\begin{aligned} \frac{d \langle Q_z \rangle}{dt} &= \frac{d}{dt} \left( \frac{\rho_{11} - 2\rho_{22} + \rho_{33}}{3} \right) \\ &= (R_{1111} - 2R_{1122} + R_{1133}) \left( \frac{\rho_{11} - 2\rho_{22} + \rho_{33}}{3} \right) \\ &= (R_{1111} - 2R_{1122} + R_{1133}) \langle Q_z \rangle. \end{aligned} \quad (4.38)$$

Thus the relaxation rate is,

$$\begin{aligned} \frac{1}{T_{1Q}} &= -R_{1111} + 2R_{1122} - R_{1133} \\ &= \frac{9\pi^2}{2} \left( \frac{e^2 q_{zz} Q}{h} \right)^2 3J_1(\omega_0). \end{aligned} \quad (4.39)$$

Given the quadrupole coupling constant ( $e^2 q_{zz} Q/h$ ), the spectral densities of motion  $J_1(\omega_0)$  and  $J_2(2\omega_0)$  can be obtained. In the next section, motional models of liquid crystals are used to interpret these experimental relaxation times.

#### 4.4 Models of Molecular Reorientation

In order to interpret the spectral density data, a theoretical expression for the autocorrelation function of the Wigner rotation matrix elements (Eqn. 4.30) needs to be calculated. If the molecular motion is considered to be a stationary Markovian process, probability theory can be used to derive an expression for the time dependence

of the correlation function [137]. A stationary Markovian process is a stochastic process having statistical parameters which are invariant to changes in the time origin.

Defining  $E_{mk}(\Omega)$ ,

$$E_{mk}(\Omega(t)) \equiv D_{mk}^{(2)}(\Omega(t)) - \langle D_{mk}^{(2)}(\Omega(t)) \rangle. \quad (4.40)$$

The general form of the autocorrelation function is given below [65,138,139]

$$\langle E_{mk}^{(2)}(\Omega(t)) E_{mk'}^{(2)*}(\Omega(t+\tau)) \rangle = \int d\Omega_0 \int d\Omega p(\Omega_0) P(\Omega_0; \Omega, \tau) E_{mk}(\Omega_0) E_{mk'}(\Omega(\tau)), \quad (4.41)$$

where  $p(\Omega_0)$  is the equilibrium orientational probability distribution function, and  $P(\Omega_0; \Omega, \tau)$  is the conditional probability of finding the molecule at the angle  $\Omega$  at time  $\tau$  when the initial orientation is  $\Omega_0$  at time  $\tau = 0$ . Implicit in this definition of the autocorrelation function is the assumption that no correlation exists between components of the molecular angular momentum  $L$  at any time, i.e. each collision randomizes the angular momentum of the molecule [138]. Specific models of molecular motion can be used to provide equations governing the time evolution of the conditional probability function  $P(\Omega_0; \Omega, \tau)$ .

The two extreme models of reorientational dynamics are strong collision and small step rotational diffusion. With the strong collision model, motion of the molecule is assumed to occur in uncorrelated, large angle jumps. The orientation after the collision is assumed to be independent of the orientation before the collision and the duration of collisions is assumed to be negligible when compared to the residence time in any given orientation [138-141]. This model is well suited for small solute molecules dissolved in a solvent of larger, rigid molecules. Strong collision models are also used to describe rotations of rod-like liquid crystals about the long molecular axis [65]. The

second limiting case, small step rotational diffusion, describes the situation when molecules rotate in small angular steps and a strong correlation between orientations before and after each collisions exist [138,139,142-144].

For small step Brownian motion in isotropic medium, the time dependence of the conditional probability function  $P(\Omega_0; \Omega, \tau)$  is given by solutions of the rotational diffusion equation. If the diffusion is isotropic, the rotational diffusion equation is given below [139]

$$\frac{\partial P(\Omega_0; \Omega, \tau)}{\partial \tau} = -D \nabla^2 P(\Omega_0; \Omega, \tau) \quad (4.42)$$

The diffusion constant,  $D$ , can be calculated hydrodynamically using the Stokes-Einstein model. With this model, the molecule is viewed as a sphere of radius  $a$  in a continuous, stationary, homogenous medium [139], and

$$D = \frac{k_B T}{8\pi a^3 \eta} \quad (4.43)$$

where  $\eta$  is the viscosity of the medium.

Using this model, analytic expressions for the autocorrelation functions of the Wigner rotation matrix elements  $\langle E_{mk}^{(2)}(\Omega(t)) E_{mk}^{(2)}(\Omega(t+\tau)) \rangle$  and the spectral densities  $J_M(M\omega_0)$  are easily derived. The solution for the conditional probability is assumed to be of the form

$$P(\Omega_0; \Omega, \tau) = \sum_{j,m,k} C_{mk}^{(j)}(\tau) D_{mk}^{(j)}(\Omega). \quad (4.44)$$

Assigning the time dependence to the expansion coefficients

$$\frac{\partial P(\Omega_0; \Omega, \tau)}{\partial \tau} = \sum_{j,m,k} \frac{\partial C_{mk}^{(j)}(\tau)}{\partial \tau} D_{mk}^{(j)}(\Omega), \quad (4.45)$$

and applying the Laplacian operator gives [145]

$$\nabla^2 D_{mk}^{(j)}(\Omega) = -j(j+1) D_{mk}^{(j)}(\Omega). \quad (4.46)$$

Multiplying the resulting equation by  $D_{m'k'}^{(j)'}(\Omega)$  and integrating over the Euler angles gives

$$\frac{\partial C_{mk}^{(j)}(\tau)}{\partial \tau} = -j(j+1) D C_{mk}^{(j)}(\tau). \quad (4.47)$$

The orthonormality properties of the Wigner rotation matrix elements [146] requires that

$$\int d\Omega D_{\mu_1 m_1}^{(j_1)'}(\Omega) D_{\mu_2 m_2}^{(j_2)}(\Omega) = \frac{8\pi^2}{(2j_1+1)} \delta_{\mu_1 \mu_2} \delta_{m_1 m_2} \delta_{j_1 j_2} \quad (4.48)$$

These simple uncoupled differential equation can be solved with the initial condition

$$\begin{aligned} P(\Omega_0; \Omega, 0) &= \delta(\Omega_0 - \Omega) \\ &= \sum_{jmk} \frac{2j+1}{8\pi^2} D_{mk}^{(j)'}(\Omega_0) D_{mk}^{(j)}(\Omega) \end{aligned} \quad (4.49)$$

giving

$$P(\Omega_0; \Omega, \tau) = \sum_{jmk} \frac{2j+1}{8\pi^2} D_{mk}^{(j)'}(\Omega_0) D_{mk}^{(j)}(\Omega) \exp(-j(j+1)D\tau). \quad (4.50)$$

The that conditional probability for an isotropic distribution is  $p(\Omega_0) = 1/8\pi^2$ ,

$$\langle E_{mk}^{(2)}(\Omega(t)) E_{m'k'}^{(2)'}(\Omega(t+\tau)) \rangle = \frac{1}{5} e^{-6D\tau} \delta_{kk'}. \quad (4.51)$$

The spectral densities can be calculated by taking a Fourier transform,

$$J_M(M\omega_0) = \frac{1}{5} \left[ \frac{1/6D}{1+(M\omega_0/6D)^2} \right] \quad (4.52)$$

In the extreme motional narrowing limit  $M\omega_0 \ll 1/6 D$  (in a 7 Tesla magnetic field,  $1/6 D \ll 20,000$  ps, a condition typically satisfied by most liquids). The spectral densities are



predicted to be equal with  $J_1(\omega_0) = J_2(2\omega_0) = 1/30 D$ .

All liquid crystal molecules lack spherical symmetry. In order to model the molecular motion of cylindrical molecules, the diffusion equation can be generalized

$$\frac{\partial P(\Omega_0; \Omega, \tau)}{\partial \tau} = \mathbf{L} \cdot \mathbf{D} \cdot \mathbf{L} P(\Omega_0; \Omega, \tau), \quad (4.53)$$

where  $\mathbf{L}$  is a scaled angular momentum vector  $\mathbf{L} = (i\partial/\partial x, i\partial/\partial y, i\partial/\partial z)$ , and  $\mathbf{D}$  is the second rank Cartesian diffusion tensor. This tensor is assumed to be diagonal in the molecular frame [139]. For an axially symmetric rotor  $D_{zz} = D_{\parallel}$ , and  $D_{xx} = D_{yy} = D_{\perp}$ , thus

$$\frac{\partial P(\Omega_0; \Omega, \tau)}{\partial \tau} = [D_{\perp} L^2 + (D_{\parallel} - D_{\perp}) L_z^2] P(\Omega_0; \Omega, \tau). \quad (4.54)$$

This can be solved to yield the conditional probability [65,139]

$$P(\Omega_0; \Omega, \tau) = \sum_{jmk} \frac{2j+1}{8\pi^2} D_{mk}^{(j)}(\Omega_0) D_{mk}^{(j)}(\Omega) \exp\left(-\frac{\tau}{T_{jk}}\right), \quad (4.55)$$

where

$$T_{jk} = \frac{1}{j(j+1)D_{\perp} + k^2(D_{\parallel} - D_{\perp})}. \quad (4.56)$$

The next step is to calculate the Fourier transform of the autocorrelation functions

$$J_{Mk}(M\omega_0) = \int_0^{\infty} \langle D_{Mk}^{(2)}(\Omega(t)) D_{Mk}^{(2)*}(\Omega(t+\tau)) \rangle e^{iM\omega_0\tau} d\tau \quad (4.57)$$

given that  $\Omega$  represents the set of Euler angles which rotate the principal axis system of the EFG ( $\mathbf{P}$ ) into the laboratory frame ( $\mathbf{L}$ ):  $\Omega = \Omega_{\mathbf{P} \rightarrow \mathbf{L}}$ . If a molecular axis system ( $\mathbf{M}$ ) is defined, the orientation of the PAS of the EFG with respect to the laboratory frame can be described with two consecutive rotations:

$$D_{mk}^{(2)}(\Omega_{P-L}(t)) = \sum_{k'=-2}^2 D_{kk'}^{(2)*}(\Omega_{L \rightarrow M}(t)) D_{k'm}^{(2)*}(\Omega_{M \rightarrow P}) \quad (4.58)$$

where  $\Omega_{L \rightarrow M}(t)$  are the time dependent Euler angles which change as the molecule moves, and  $\Omega_{M \rightarrow P}$  are the time independent angles describing the relative orientation of the molecular axis and the PAS of the EFG tensor. Performing the Fourier transform of this autocorrelation functions gives

$$J_M(M\omega_0) = \sum_{k=-2}^2 J_{Mk}(M\omega_0) = \sum_{k=-2}^2 |D_{k0}^{(2)}(\Omega_{M-P})|^2 \frac{T_{2k}}{5[1+(M\omega_0 T_{2k})^2]} \quad (4.59)$$

Here, the asymmetry of the bond is assumed to be negligibly small ( $\eta = 0$ ).

For liquid crystal systems, the molecules are orientationally ordered, and models of molecular reorientation must be modified to include the orienting potential,  $U(\Omega_{L \rightarrow M})$ . Statistical mechanics gives the equilibrium probability distribution as

$$\rho(\Omega) = \frac{\exp\left(-\frac{U(\Omega)}{k_B T}\right)}{\int \exp\left(-\frac{U(\Omega)}{k_B T}\right) d\Omega} \quad (4.60)$$

The differential equation governing the time dependence of the conditional probability becomes [147]

$$\frac{\partial P(\Omega_0; \Omega, \tau)}{\partial \tau} = -L \cdot \mathcal{D} \cdot \left[ L + L \frac{U(\Omega)}{k_B T} \right] P(\Omega_0; \Omega, \tau) \quad (4.61)$$

The inclusion of an orienting potential in Eqn. 4.61 makes the solution for  $P(\Omega_0; \Omega, \tau)$  much more complicated. First, the orientational ordering of the molecules makes  $p(\Omega_0)$  angle dependent. Second, when solving the differential equation with this condition, the analog to Eqn. 4.47 is no longer a simple decoupled result;  $\partial C_{mk}^{(j)}/\partial \tau$  couples to  $C_{mk}^{(j \pm 1)}$ . As a result, an infinite set of coupled differential equations needs to be considered. These

coupled equations have been solved by constructing progressively larger basis until the results converge [65]. Freed and his coworkers have proposed a theory to describe the rotational motion of liquid crystals based on small step diffusion in the presence of a restoring potential [148-151]. In the "anisotropic viscosity" model, the diffusion tensor  $\mathbf{D}$  is assumed to be diagonal in the laboratory fixed frame. This theory can be applied to predict spectral densities given the uniaxial order parameter  $Q$ , and two rotational correlation times:  $\tau_\alpha$  for rotational motion of the molecular axis about the director, and  $\tau_\beta$  for rotational tumbling about an axis perpendicular to the director as depicted in Figure 4.3.

In 1988 a composite diffusion model of molecular reorientation of nematic liquid crystals was proposed [65] which combines Freed's anisotropic viscosity model with a statistically independent rotation of the liquid crystal molecule about the molecule fixed z-axis. This "third rate model" requires an additional correlation time describing the rate of rotation of the liquid crystal molecule about its axis of symmetry,  $\tau_\gamma$ , and a continuously variable collision parameter  $p$ . The collision parameter,  $p$ , is defined in the range  $0 \leq p \leq 1$ , where  $p = 0$  corresponds to the assumption of strong collision (arbitrary step size), while  $p = 1$  implies small step diffusion for the  $\gamma$ -motion. Using this model, the spectral densities  $J_M(M\omega_0)$  can be calculated from the following parameters: the angle  $\beta$  between the molecule z-axis and the principal axis of the bond, the uniaxial order parameter  $Q$ , the collision parameter  $p$ , and the three correlation times  $\tau_\alpha$ ,  $\tau_\beta$  and  $\tau_\gamma$ .

The "third rate" model of molecular motion in anisotropic fluids gives explicit forms for the spectral densities,

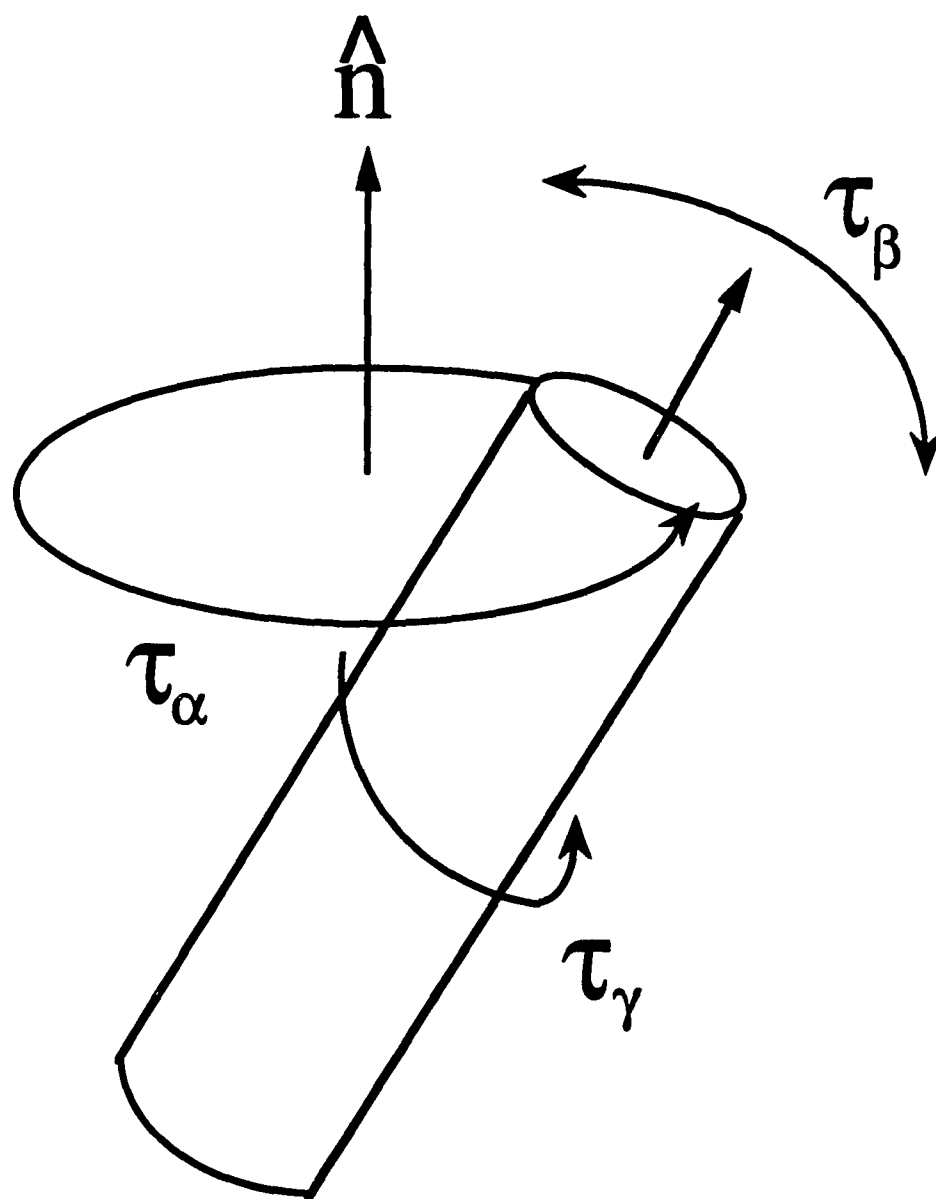


Figure 4.3 Molecular reorientational motion is described with the following correlation times: (1)  $\tau_\alpha$ , for rotations of the molecular z-axis about the director, (2)  $\tau_\beta$ , for rotations about axis perpendicular to the director, and (3)  $\tau_\gamma$  for spinning motion about the molecular z-axis.

$$J_m(\omega) = \int_0^{\infty} G_m(t) e^{-i\omega t} dt \quad (4.62)$$

with

$$G_m(t) = \sum_{k,k'=-2}^2 D_{0k}^{(2)}(\beta) D_{0k'}^{(2)*}(\beta) G_{mkk'}(t) \quad (4.63)$$

where the asymmetry in the field gradient tensor,  $\eta$ , is neglected. The individual correlation functions are given by

$$G_{mkk'}(\tau) = \int d\Omega_0 p(\Omega_0) \int d\Omega P(\Omega_0; \Omega, \tau) E_{mk}(\Omega_0) E_{m'k'}(\Omega) \quad (4.64)$$

Assuming that the motion of the long axis is uncorrelated with motions about this axis, the integrals above can be separated:

$$G_{mkk'}(\tau) = \Gamma_{kk'}(\tau) g_{mkk'}(\tau) \quad (4.65)$$

given

$$\Gamma_{kk'} = \int_0^{2\pi} d\gamma_0 p(\gamma_0) \int_0^{2\pi} d\gamma P(\gamma_0; \gamma, \tau) e^{-i(k\gamma - k'\gamma_0)} \quad (4.66)$$

and

$$g_{mkk'}(\tau) = \int_0^{2\pi} d\alpha_0 \int_{-1}^1 d(\cos\beta_0) p(\alpha_0, \beta_0) \times \int_0^{2\pi} d\alpha \int_{-1}^1 d(\cos\beta) P(\alpha_0, \beta_0; \alpha, \beta, \tau) E_{mk}(\alpha_0, \beta_0, 0) E_{m'k'}^*(\alpha, \beta, 0) \quad (4.67)$$

where  $\Gamma_{kk'}(t)$  are correlation functions for motions about the molecular z-axis and  $g_{mkk'}$  are correlation functions for motions of this axis.

The  $\tau_y$  motion is modeled with N equally spaced sites about the molecular axis. Equal probability jumps between any two sites gives an exponential correlation

function [152,153]

$$\begin{aligned} \Gamma_{kk}(t) &= \delta_{kk} e^{-\frac{t}{\tau_r}} & \text{if } k = 1,2 \\ &= \delta_{kk} & \text{if } k = 0 \end{aligned} \quad (4.68)$$

where  $\tau_r$  is the lifetime in any one orientation. For rotational diffusion, the jumps are restricted to be between nearest neighbors, and as the number of sites approaches infinity [152,154]

$$\Gamma_{kk}(t) = e^{-\frac{k^2 t}{\tau_r}}. \quad (4.69)$$

Therefore, the conditional probability for motions about the molecular z-axis is

$$\begin{aligned} \Gamma_{kk}(t) &= \delta_{kk} & \text{if } k = 0 \\ (4.70) \quad &= \delta_{kk} e^{-\frac{t}{\tau_r}} & \text{if } k = 1 \\ &= \delta_{kk} e^{-\frac{4t}{\tau_r}} & \text{if } k = 2. \end{aligned}$$

The conditional probability function for motions of the molecular z-axis in an ordered medium  $P(\alpha_0, \beta_0; \alpha, \beta, \tau)$  is obtained by solving equation (4.67) subject to the initial condition  $P(\alpha_0, \beta_0; \alpha, \beta, 0) = \delta(\Omega - \Omega_0)$ . In accord with Freed's anisotropic viscosity model, the principal components of the diffusion tensor refer to rotational motion about the space fixed x, y and z axis. Equation (4.61) is solved for a symmetric rotor ( $D_\alpha = 1/\tau_\alpha = D_\parallel$  and  $D_\beta = 1/\tau_\beta = D_\perp = D_{xx} = D_{yy}$ ) in a Maier-Saupe potential:  $U = -C Q (3/2 \cos^2 \beta - 1/2)$ . Details of the calculation are given in reference [65], here the correlation function  $g_{mkk}(t)$  is shown to be

$$g_{mkk}(t) = \delta_{kk} c_{mk}(Q) \sum_{i=1}^3 a_{mk}^{(i)}(Q) \exp\left(-\frac{t}{b_{mk}^{(i)}(Q) \tau_{2k}}\right) \quad (4.71)$$

Where  $c_{mk}(Q)$  is the initial amplitude of the correlation function,  $a_{mk}^{(i)}(Q)$  are the relative

weights of each exponential decay, and  $b_{mk}^{(i)}(Q)$  are coefficients which scale time constants for anisotropic diffusion in an isotropic medium,  $\tau_{2k}$  in Eqn. (4.56). The coefficients  $a_{mk}^{(i)}(Q)$ ,  $b_{mk}^{(i)}(Q)$  and  $c_{mk}^{(i)}(Q)$  are expressed as a power series expansion  $\sum q_n Q^n$  with the coefficients  $q_n$  [65].

In the following section, this composite diffusion model of molecular motion of nematic liquid crystal molecules is used to interpret the temperature and frequency dependence of the experimentally measured spectral densities  $J_1(\omega_0)$  and  $J_2(2\omega_0)$ . This "third rate model" of molecular reorientation, which assumes that the rotational diffusion tensor is diagonal in the laboratory frame, that the liquid crystal is well approximated by a symmetric rotor, and that molecular reorientation about the molecule's long axis is statistically independent. These approximations will be tested by fitting experimentally measured relaxation data.

#### 4.5 Experimental Determination of Rotational Dynamics

The liquid crystal studied (FLOC, the nematogen 2-fluorenyl-4'-tetradecyloxy benzoate-d<sub>9</sub>) is unique because of the large number of inequivalent deuterated sites on the rigid head group. This provides a wealth of information which can be used to provide a particularly rigorous test of the various motional models. In many previous studies, [154-159] the number of measured relaxation rates is equal to the number of variable parameters in the motional model. This makes rigorous, statistical estimations of the validity of the model and simultaneous determination of confidence limits for the parameters impossible. As shown in Figure (2.3), the deuterated rigid head group has seven inequivalent, deuterated sites. The signal to noise ratio for the 9,9'

deuterons was not sufficient to extract quantitative information from relaxation measurements. While the doublets from sites 1 and 4 are resolvable, the relaxation rates are the same within experimental error; thus, in the numerical analysis, data from site 4 was excluded. Even though results from only five of the sites were used, the abundance of experimental data provides a more stringent test of motional models than has been possible heretofore.

Pure FLOC<sub>14</sub>-d<sub>9</sub> was placed in a five millimeter sample tube, degassed using several freeze-pump-thaw cycles, and sealed under vacuum. Relevant experimental parameters include the following: 90° pulse width of 1.6 μsec, dwell time of 6.25 μsec (spectral width ± 80 kHz), 1K complex points, 250 ms recycle time, and 2K scans for signal averaging. The temperature was controlled to within 0.1°C between 120°C and 140°C using flowing nitrogen gas. The nitrogen was preheated to 110°C using a 32 watt continuously run, noninductively wired Nichrome preheater. The temperature of the sample was regulated by a 9000 Omega temperature controller with PID feedback to a 40 watt heater.

As discussed in section 4.1, the decay of quadrupolar order and the recovery of Zeeman order were measured in separate experiments. The inversion recovery experiment with a quadrupole echo was used to measure  $T_{12}^i$ , while  $T_{1Q}^i$  was determined using a broadband Jeener-Broekaert sequence with echo detection. This allows the two spectral densities  $J_1^i(\omega_0)$  and  $J_2^i(2\omega_0)$  to be obtained for each resolvable site  $i$  on the nematogen FLOC<sub>14</sub>-d<sub>9</sub>. Thus, these relaxation data from the five deuterated sites on the rigid fluorene moiety provide ten experimental spectral densities at each



temperature. The intensity of each peak was determined by having the computer search for a maximum intensity between two user-specified endpoints. A baseline for intensity measurements was established by averaging five neighboring points picked on either side of the endpoints and interpolating linearly to the position of the peak maximum. Peak separations ( $2\nu_Q^i$  listed in Table 4.4) were determined simultaneously for later use in order parameter determinations. Arrays of sum magnetizations (from the IRQE experiment) and difference magnetizations (from the BBJB experiment) for, typically, sixteen  $\tau$ -values were constructed and passed to iterative, nonlinear least squares routines [128].  $S(0)$  and  $S(\infty)$  were adjusted along with  $T_{1Z}$  in a three parameter fit to Eqn. (4.10), while  $D(0)$  and  $T_{1Q}$  were independently adjusted in a two parameter fit to Eqn. (4.11). All these procedures were incorporated into FELIX data processing software [160], and the user need only specify a list of  $\tau$ -values and an appropriate window width for the peak determination. The relaxation rates for all resolvable sites are listed in Tables 4.5 and 4.6.

As previously outlined, the quadrupolar splittings (listed in Table 4.4) were used to determine the temperature dependence of the static order parameters,  $Q$  and  $D$ , and these are listed in Table 4.4 and plotted in Fig. 4.4. The order parameters are the thermally averaged orientation of the long molecular axis (see Figure 2.3) relative to the laboratory fixed axes, and  $\beta_2$  refers to the orientation of the fluorene head group with respect to the long molecular axis.

In the fast motion regime, Redfield theory [133-136] applies and the relaxation times  $T_{1Z}$  and  $T_{1Q}$  can be related to the spectral density parameters  $J_1(\omega_0)$  and

temp (°C)	$2\nu_Q^3$ (kHz) <sup>a</sup>	$2\nu_Q^1$ (kHz)	$2\nu_Q^4$ (kHz)	$2\nu_Q^{5,8}$ (kHz)	$2\nu_Q^6$ (kHz)	$2\nu_Q^7$ (kHz)	$Q^b$	$D^c$	$\beta_2$ (deg) <sup>d</sup>
131.3	7.97	23.34	27.50	64.06	64.06	141.09	0.598	0.063	7.03
133.1	7.83	23.44	25.97	62.11	60.16	134.37	0.569	0.056	6.99
134.4	7.65	24.53	19.53	57.03	59.84	128.75	0.546	0.065	7.13
134.7	7.52	19.40	24.22	56.57	59.39	127.82	0.542	0.066	7.12
134.8	7.63	19.01	24.01	56.05	58.82	126.95	0.538	0.066	7.09
136.3	7.40	18.52	22.49	53.23	56.63	120.86	0.513	0.065	7.15
138.0	7.19	16.08	20.16	48.29	52.03	111.09	0.471	0.065	7.13
138.4	7.04	15.48	19.67	46.88	50.78	108.14	0.459	0.064	7.14
139.3	6.72	14.22	17.81	43.28	47.03	100.78	0.427	0.062	7.11
140.3	6.26	12.34	14.46	38.13	42.19	89.37	0.378	0.060	7.25

<sup>a</sup>  $2\nu_Q^j = \pm 0.4$  kHz

<sup>b</sup>  $\delta Q = \pm 0.010$

<sup>c</sup>  $\delta D = \pm 0.014$

<sup>d</sup>  $\delta\beta_2 = \pm 0.010$  deg

Table 4.4 The experimental quadrupole splittings  $2\nu_Q^j$  and order parameters of pure FLOC<sub>14</sub> in the nematic phase.

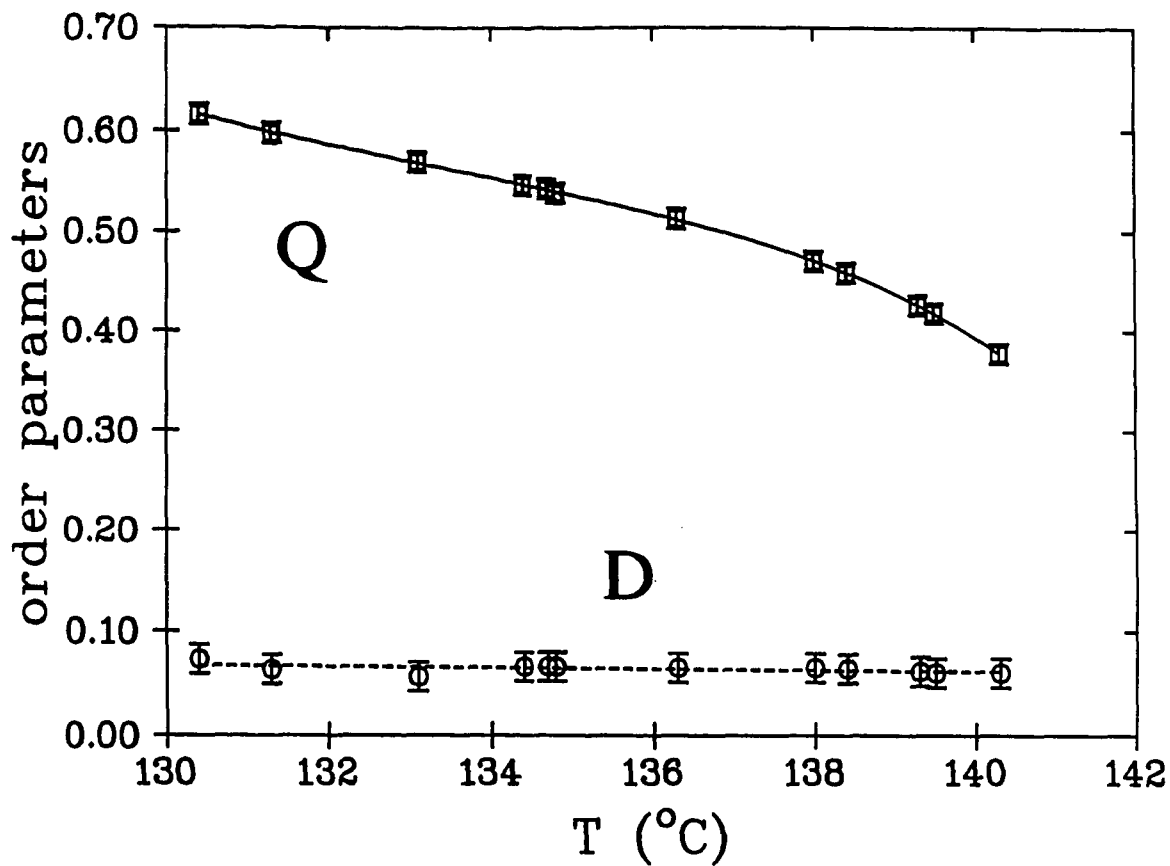


Figure 4.4 The uniaxial ( $Q$ ) and biaxial ( $D$ ) order parameters of FLOC<sub>14</sub> as a function of temperature in the nematic phase.

$J_2(2\omega_0)$  using eqs. (4.35) and (4.39). Here  $\langle e^2qQ/h \rangle$  is the vibrationally averaged quadrupole coupling in Hertz, estimated [66] to be 182 kHz for all aromatic deuterated sites in FLOC<sub>14</sub>-d<sub>9</sub>. The temperature dependence of the spectral density functions,  $J_1^i(\omega_0)$  and  $J_2^i(2\omega_0)$ , for different deuterated sites,  $i$ , are presented in Figs. 4.5(a)-4.5(f). Second order polynomial fits to the temperature dependence of the spectral densities for each site were made; the average deviation of the spectral density data from these polynomial fits ( $\delta J_1^i$  and  $\delta J_2^i$ ) is used to estimate random errors. It is these errors which are used in the calculation of  $\chi^2$  in the fit of the experimental data to the model of molecular motion.

The third rate model of molecular reorientation [65] was used to fit spectral density data for the five sites using a minimum  $\chi^2$  technique. This technique, which was used to find the four motional parameters  $\tau_\alpha, \tau_\beta, \tau_\gamma$  and  $p$ , from the spectral densities, involves calculating  $\chi^2$  defined by

$$\chi^2 = \sum_{i=1}^5 \frac{[J_1^i(\text{exp}) - J_1^i(\text{the})]^2}{[\delta J_1^i]^2} + \frac{[J_2^i(\text{exp}) - J_2^i(\text{the})]^2}{[\delta J_2^i]^2}. \quad (4.72)$$

$J_1^i(\text{exp})$  and  $J_2^i(\text{exp})$  are the experimentally measured spectral densities at  $\omega_0$  and  $2\omega_0$  respectively for the  $i^{\text{th}}$  site,  $J_1^i(\text{the})$  and  $J_2^i(\text{the})$  are the theoretically predicted spectral densities for the same site, and  $\delta J_1^i$  and  $\delta J_2^i$  are the estimated errors in the experimentally measured spectral density data.

Given the experimentally determined uniaxial order parameter ( $Q$ ), and a guess for the motional variables,  $(\tau_\alpha, \tau_\beta, \tau_\gamma, p)$ ,  $\chi^2$  was calculated on a grid in the four dimensional parameter space, and minimum values of  $\chi^2$  were found. The reduced chi squared parameter,  $\chi^2_{\text{RED}}$ , is defined to be the minimum chi squared divided by the

temp (°C)	site 3		site 1		site 1		site 4	
	$T_{12}$ (ms)	$T_{10}$ (ms)	$T_{12}$ (ms)	$T_{10}$ (ms)	$T_{12}$ (ms)	$T_{10}$ (ms)	$T_{12}$ (ms)	$T_{10}$ (ms)
131.3	13.79±0.59	13.50±0.76	14.40±0.18	15.09±0.62	14.05±0.18	16.40±0.49	14.05±0.18	16.40±0.49
133.1	13.05±0.63	11.21±0.43	13.72±0.71	13.53±0.57	13.60±0.73	13.80±0.64	13.60±0.73	13.80±0.64
134.4	15.20±0.30	14.09±0.45	14.63±0.25	16.43±0.38	14.63±0.25	16.43±0.38	14.63±0.25	16.43±0.38
134.7	13.81±0.46	16.05±0.58	14.14±0.56	18.94±0.55	14.07±0.51	18.60±0.45	14.07±0.51	18.60±0.45
134.8	14.34±0.24	14.61±0.76	14.13±0.38	17.14±0.52	15.04±0.19	16.60±0.63	15.04±0.19	16.60±0.63
136.3	14.84±0.57	14.84±0.62	15.66±0.63	17.29±0.61	15.12±0.56	17.47±0.49	15.12±0.56	17.47±0.49
138.0	16.18±0.42	19.12±0.36	16.59±0.39	20.15±0.53	16.33±0.38	19.78±0.60	16.33±0.38	19.78±0.60
138.4	15.76±0.17	16.89±0.97	17.09±0.27	20.37±0.73	16.43±0.21	20.53±0.63	16.43±0.21	20.53±0.63
139.3	16.58±0.09	18.56±0.79	17.10±0.26	20.80±0.89	16.74±0.18	20.78±0.41	16.74±0.18	20.78±0.41
140.3	...	20.3±1.8	16.42±0.39	23.1±1.5	16.00±0.35	21.69±1.1	16.00±0.35	21.69±1.1

Table 4.5 Experimental relaxation rates for sites 1, 3 and 4 on FLOC<sub>14</sub>.

temp (°C)	sites 8&5		site 6		site 6		site 7		site 7	
	$T_{12}$ (ms)	$T_{10}$ (ms)	$T_{12}$ (ms)	$T_{10}$ (ms)	$T_{12}$ (ms)	$T_{10}$ (ms)	$T_{12}$ (ms)	$T_{10}$ (ms)	$T_{12}$ (ms)	$T_{10}$ (ms)
131.3	13.02±0.20	13.43±0.43	13.65±0.24	12.37±0.99	10.46±0.34	10.46±0.34	6.07±0.43	6.07±0.43	10.46±0.34	6.07±0.43
133.1	12.13±0.60	8.48±1.08	12.77±0.72	13.41±0.70	9.01±0.93	9.01±0.93	5.46±0.89	5.46±0.89	9.01±0.93	5.46±0.89
134.4	13.38±0.25	15.17±0.43	14.82±0.80	10.19±0.75	9.69±0.47	9.69±0.47	4.73±0.35	4.73±0.35	9.69±0.47	4.73±0.35
134.7	12.76±0.50	16.47±0.48	12.87±0.84	11.93±0.93	8.35±0.48	8.35±0.48	5.69±0.25	5.69±0.25	8.35±0.48	5.69±0.25
134.8	12.93±0.22	15.58±0.73	12.72±0.30	8.47±1.09	9.39±0.29	9.39±0.29	5.47±0.70	5.47±0.70	9.39±0.29	5.47±0.70
136.3	13.21±0.56	14.87±0.74	13.45±0.57	9.70±0.96	8.68±0.59	8.68±0.59	4.44±0.47	4.44±0.47	8.68±0.59	4.44±0.47
138.0	13.89±0.42	15.42±0.43	14.55±0.95	9.8±3.8	8.12±0.46	8.12±0.46	5.13±0.65	5.13±0.65	8.12±0.46	5.13±0.65
138.4	14.35±0.27	16.99±0.85	14.31±0.57	10.0±2.3	8.3±1.0	8.3±1.0	4.1±1.2	4.1±1.2	8.3±1.0	4.1±1.2
139.3	14.40±0.24	16.75±0.57	16.9±2.8	13.90±0.84	6.22±0.70	6.22±0.70	6.9±1.1	6.9±1.1	6.22±0.70	6.9±1.1
140.3	13.21±0.56	14.87±0.74	13.45±0.57	9.70±0.96	8.68±0.59	8.68±0.59	4.44±0.47	4.44±0.47	8.68±0.59	4.44±0.47

Table 4.6 Experimental relaxation rates for sites 5,6,7 and 8 on FLOC<sub>14</sub>.

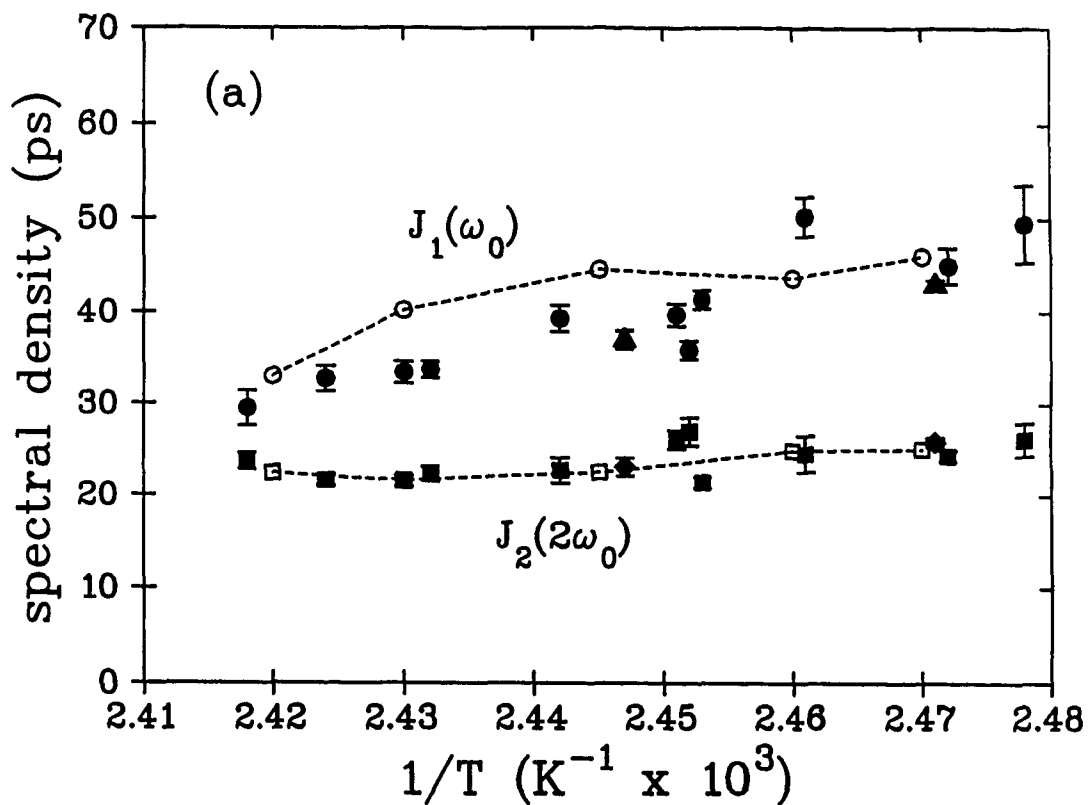


Figure 4.5(a) Site 1: Spectral densities measured as a function of inverse temperature for each deuterated site. Closed circles are  $J_1(\omega_0)$  measured at 46 MHz, closed triangles are  $J_1(\omega_0)$  measured at 38.4 MHz, closed squares are  $J_2(2\omega_0)$  measured at 46 MHz, and closed diamonds are  $J_2(2\omega_0)$  measured at 38.4 MHz. The open circles and squares, which are connected by a dotted line to guide the eye, are fits of the 46 MHz data to the third rate model of molecular reorientation.

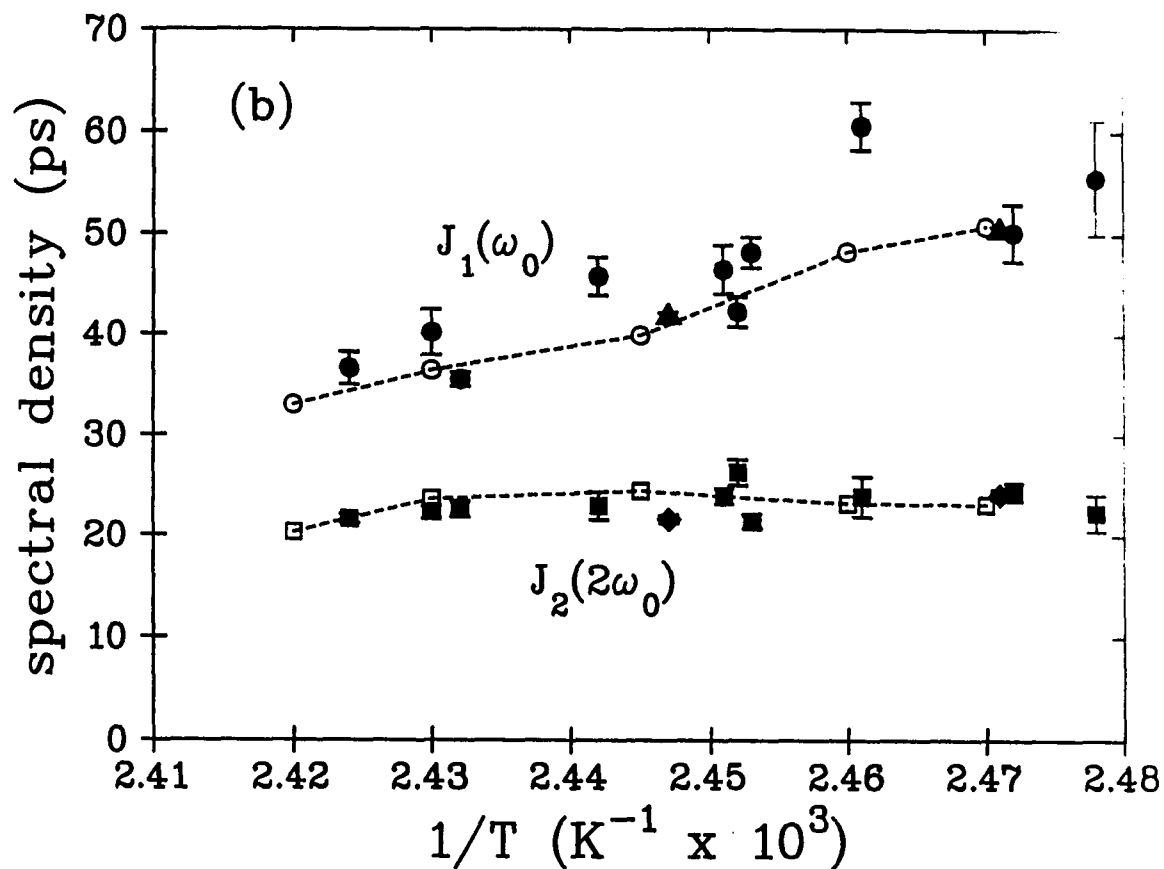


Figure 4.5(b) Site 3: Spectral densities measured as a function of inverse temperature for each deuterated site. Closed circles are  $J_1(\omega_0)$  measured at 46 MHz, closed triangles are  $J_1(\omega_0)$  measured at 38.4 MHz, closed squares are  $J_2(2\omega_0)$  measured at 46 MHz, and closed diamonds are  $J_2(2\omega_0)$  measured at 38.4 MHz. The open circles and squares, which are connected by a dotted line to guide the eye, are fits of the 46 MHz data to the third rate model of molecular reorientation.



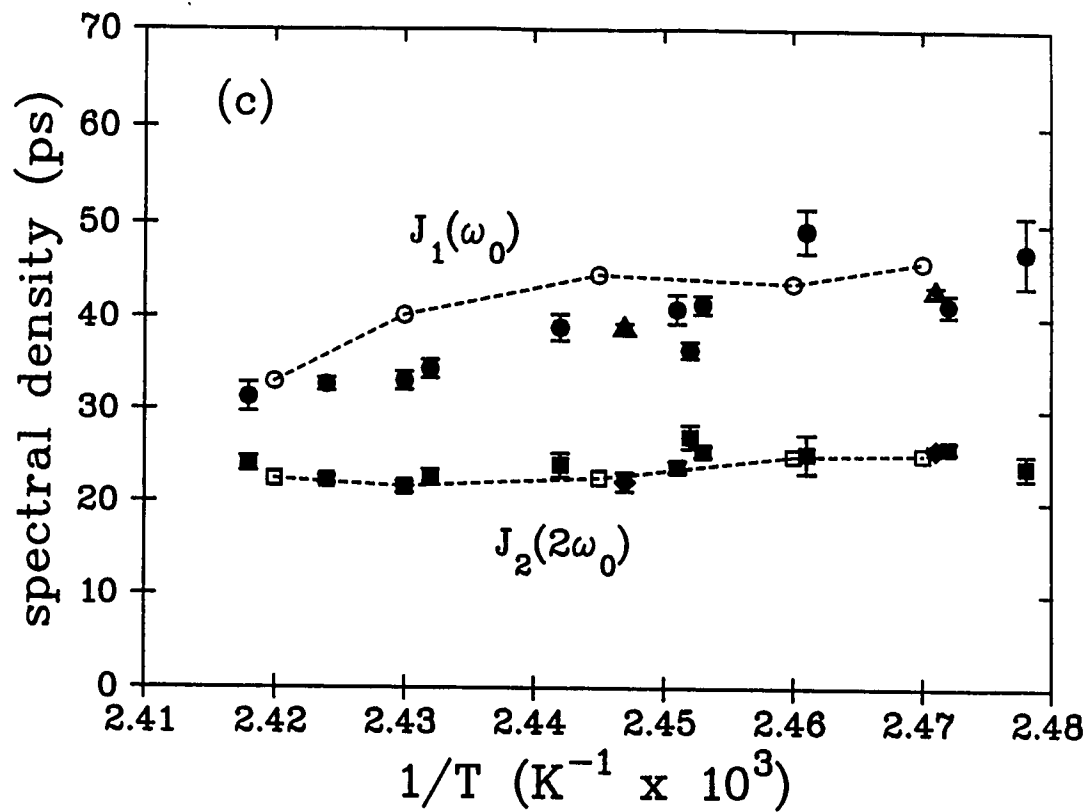


Figure 4.5(c) Site 4: Spectral densities measured as a function of inverse temperature for each deuterated site. Closed circles are  $J_1(\omega_0)$  measured at 46 MHz, closed triangles are  $J_1(\omega_0)$  measured at 38.4 MHz, closed squares are  $J_2(2\omega_0)$  measured at 46 MHz, and closed diamonds are  $J_2(2\omega_0)$  measured at 38.4 MHz. The open circles and squares, which are connected by a dotted line to guide the eye, are fits of the 46 MHz data to the third rate model of molecular reorientation.

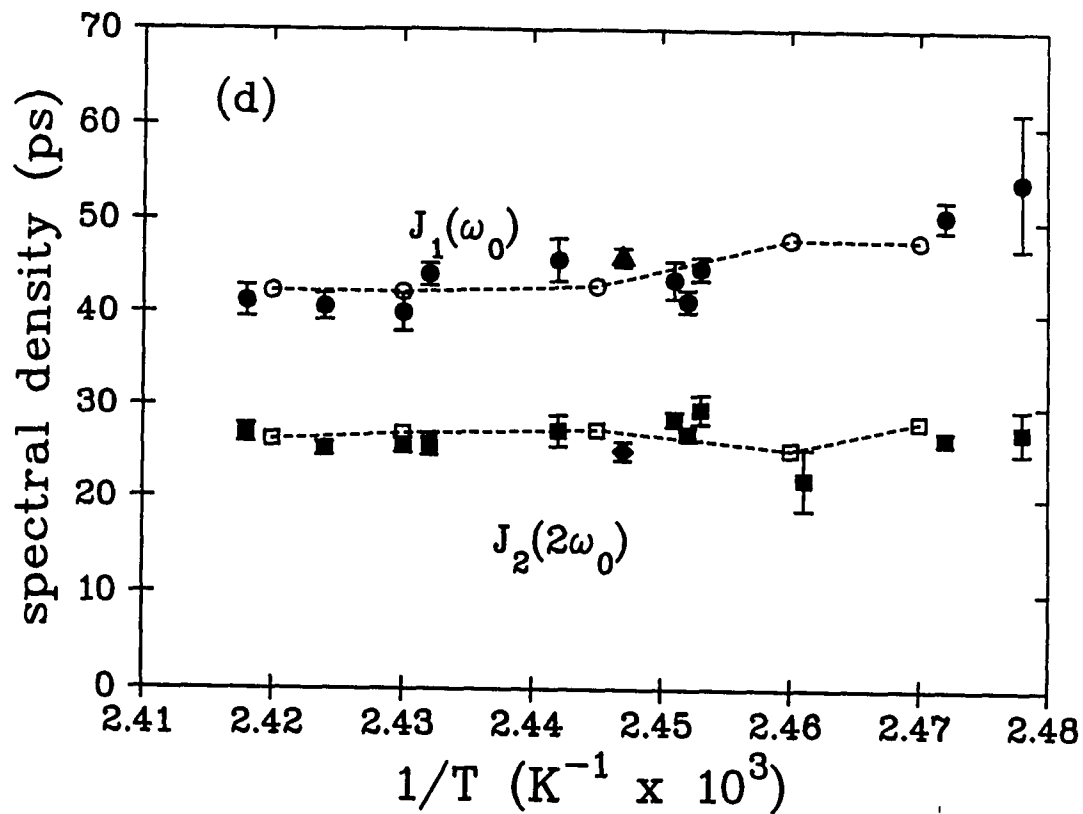


Figure 4.5(d) Sites 5 and 8: Spectral densities measured as a function of inverse temperature for each deuterated site. Closed circles are  $J_1(\omega_0)$  measured at 46 MHz, closed triangles are  $J_1(\omega_0)$  measured at 38.4 MHz, closed squares are  $J_2(2\omega_0)$  measured at 46 MHz, and closed diamonds are  $J_2(2\omega_0)$  measured at 38.4 MHz. The open circles and squares, which are connected by a dotted line to guide the eye, are fits of the 46 MHz data to the third rate model of molecular reorientation.

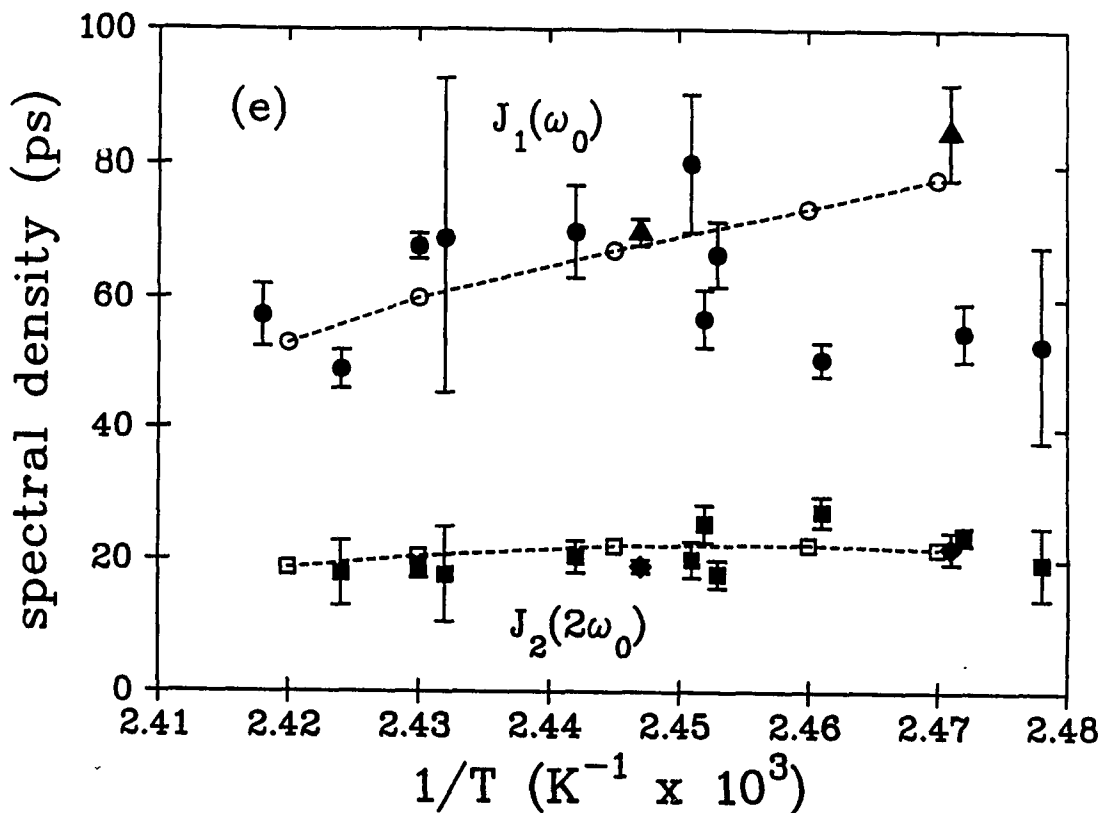


Figure 4.5(e) Site 6: Spectral densities measured as a function of inverse temperature for each deuterated site. Closed circles are  $J_1(\omega_0)$  measured at 46 MHz, closed triangles are  $J_1(\omega_0)$  measured at 38.4 MHz, closed squares are  $J_2(2\omega_0)$  measured at 46 MHz, and closed diamonds are  $J_2(2\omega_0)$  measured at 38.4 MHz. The open circles and squares, which are connected by a dotted line to guide the eye, are fits of the 46 MHz data to the third rate model of molecular reorientation.

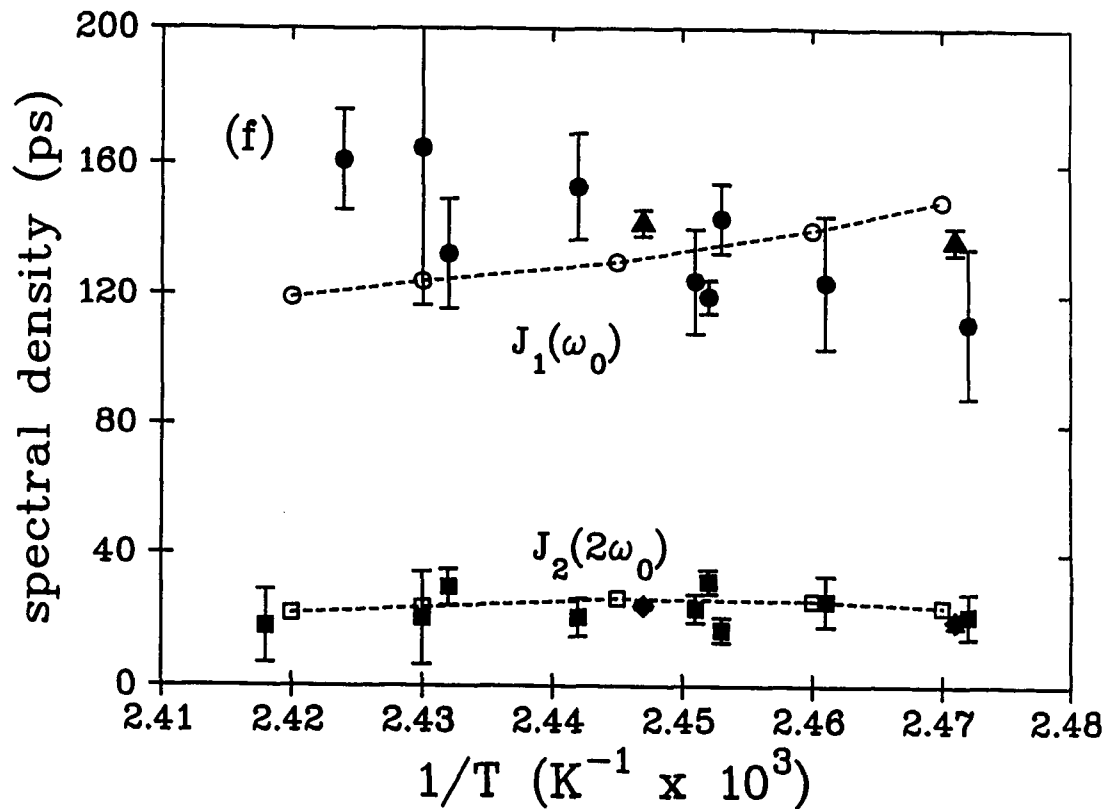


Figure 4.5(f) Site 7: Spectral densities measured as a function of inverse temperature for each deuterated site. Closed circles are  $J_1(\omega_0)$  measured at 46 MHz, closed triangles are  $J_1(\omega_0)$  measured at 38.4 MHz, closed squares are  $J_2(2\omega_0)$  measured at 46 MHz, and closed diamonds are  $J_2(2\omega_0)$  measured at 38.4 MHz. The open circles and squares, which are connected by a dotted line to guide the eye, are fits of the 46 MHz data to the third rate model of molecular reorientation.

degrees of freedom (six for the FLOC<sub>14</sub>-d<sub>9</sub> system).  $\chi^2_{\text{RED}}$  can be used to calculate the probability of measuring a given set of spectral densities [161]. A reasonably high probability gives the experimenter confidence that it is appropriate to use the model to interpret the data. Plots of the experimentally measured spectral densities and the  $J_1^i$ (the) and  $J_2^i$ (the) calculated with the motional parameters which give minimum  $\chi^2$  are presented in Fig. 4.5. The probabilities listed in Table 4.7 demonstrate that the model works best in the middle of the nematic range. Assuming that the model is correct, boundaries of confidence regions in the parameter space can be estimated [162]. For our experiment with six degrees of freedom, a contour of  $\Delta\chi^2 = 7.04$  give a 68.3% confidence level [163]. As examples, these boundaries are plotted in the three dimensional  $\tau$  space, for three different temperatures, in Fig. 4.6.

The ability of the third rate model to fit ten independent spectral densities with reasonable confidence in terms of four parameters is encouraging. The agreement between experiment and model is best for sites 3, 5 and 8 (Figs. 4.5(b) and 4.5(d)). These sites have the largest signal to noise ratios and the smallest experimental errors in the relaxation rates. Because the angle between the symmetry axis of the molecule and the principal axis of the EFG tensor is large for these sites, the motional parameters  $\tau_\gamma$  and  $p$  are largely determined by spectral densities measured for these sites. The sites 6 and 7 are more closely aligned with the molecular axis, and thus these sites play a dominant role in determining  $\tau_\alpha$  and  $\tau_\beta$ . The quadrupolar splittings for sites 6 and 7 are the largest and most temperature dependent (approximately 20 kHz per °C for the site 7). Because of incomplete deuteration and large quadrupolar splittings, these spectral peaks

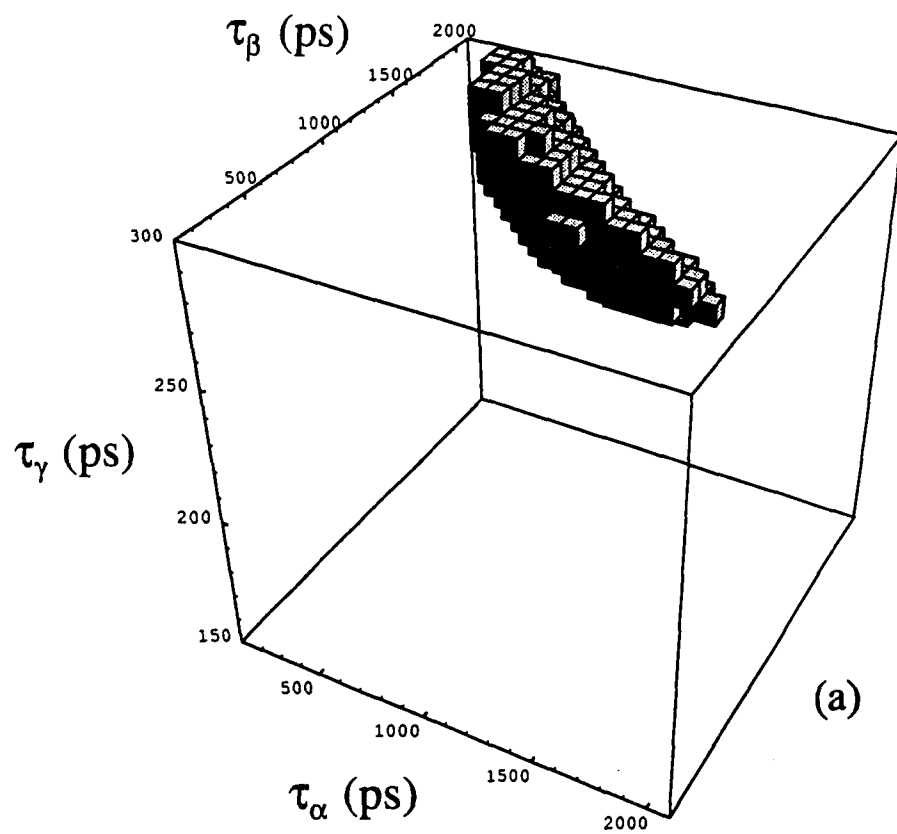


FIGURE 4.6(a) Constant  $\Delta\chi^2$  boundary of 68% confidence in the three dimensional parameter space of the third rate model<sup>7</sup> ( $\tau_\alpha, \tau_\beta, \tau_\gamma$ ) at 131.6 °C.

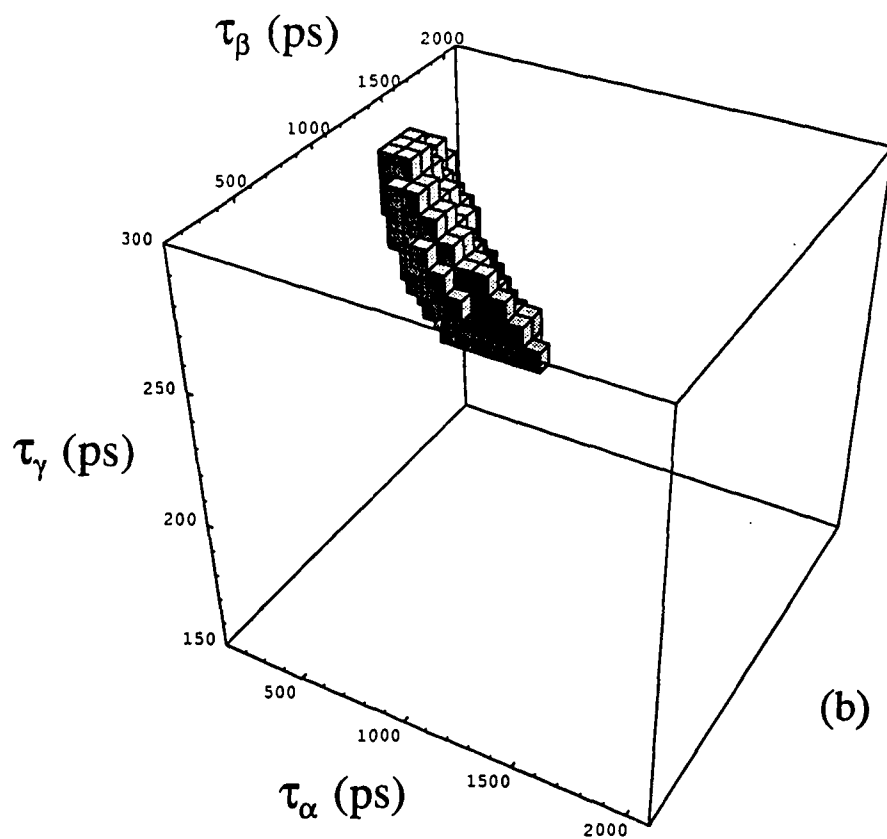


FIGURE 4.6(b) Constant  $\Delta\chi^2$  boundary of 68% confidence in the three dimensional parameter space of the third rate model<sup>7</sup> ( $\tau_\alpha, \tau_\beta, \tau_\gamma$ ) at 135.7 °C.

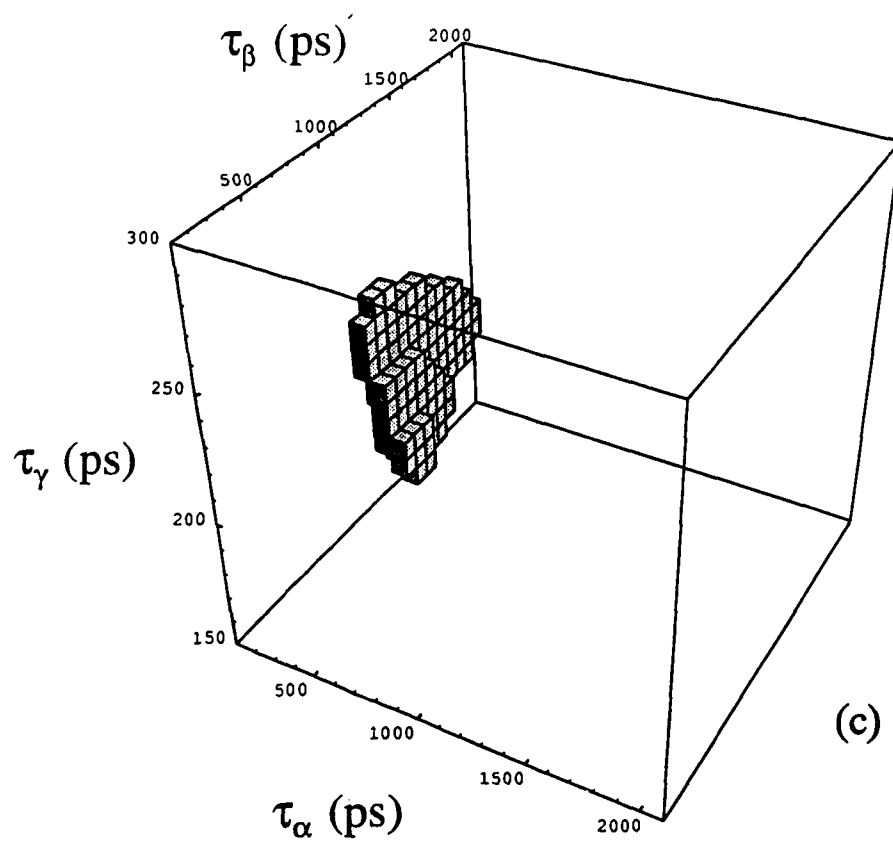


FIGURE 4.6(c) Constant  $\Delta\chi^2$  boundary of 68% confidence in the three dimensional parameter space of the third rate model<sup>7</sup> ( $\tau_\alpha, \tau_\beta, \tau_\gamma$ ) at 140.0 °C.



had smaller signal to noise ratios, consequently data for these sites had larger errors. Since it is more difficult for the model to fit the data for these sites (Figs. 4.5(e) and 4.5(f)), errors in  $\tau_\alpha$  and  $\tau_\beta$  are larger.

The correlation times obtained from the third rate model imply that the frequency dependence of the spectral densities is weak, and this was tested by comparison to experiments performed at 38.4 MHz [164]. These results (solid diamonds and solid triangles in Fig. 4.5) demonstrate that for two temperatures in the nematic range, there is no appreciable change in the spectral densities with Larmor frequency. This provides confirmation that the correlation times reported here are not seriously in error.

Attempts were made to improve the fit between calculated and experimental spectral densities by incorporating effects of nematic director fluctuations. According to a theory developed by several authors [148,165,166], director fluctuations contribute in first order exclusively to  $J_1(\omega_0)$ :

$$J_1^{DF}(\omega_0) = \frac{A Q^2 U(\omega_0/\omega_0)}{\omega_0^{1/2}} - A Q^2 \frac{\sqrt{8}}{\pi} \omega_c^{1/2} \tau_\beta. \quad (4.73)$$

where

$$A = \frac{3k_B T \eta^{1/2}}{4\sqrt{2} \pi K^{3/2}}$$

and

$$U(\omega_c/\omega_0) = \frac{1}{2\pi} \ln \left| \frac{(\omega_c/\omega_0) - (2\omega_c/\omega_0)^{1/2} + 1}{(\omega_c/\omega_0) + (2\omega_c/\omega_0)^{1/2} + 1} \right| \quad (4.74)$$

Where  $\eta$  and  $K$  are one constant approximations to the anisotropic viscosity and elastic tensors of the medium,  $\omega_c$  is a high frequency (short wavelength) cutoff parameter, and  $Q$  is the order parameter for the molecular z-axis relative to the nematic director. The cutoff function,  $U(\omega_0/\omega_c)$ , is unity at low frequency and becomes small for  $\omega_0 \gg \omega_c$  [167]. In accordance with Freed's original theory [148], a negative cross term has been included in Eqn. (4.73). Since viscosities and elastic constants have not been measured for FLOC<sub>14-d<sub>9</sub></sub>, it is not possible to obtain an accurate independent estimate of  $A$ . Hence, values appropriate for a 'typical' nematic liquid crystal (EBBA) were used, and  $A$  was assumed to be 1 to  $5 \times 10^{-6}$  s [167]. The cutoff frequency was taken to be 200 MHz (corresponding to a cutoff wavelength of molecular dimensions for the highest frequency director modes). These values of  $A$  and  $\omega_c$  were used with Eqn. (4.73) to calculate director fluctuation contributions at each temperature including the cross term. Resulting values for the best fit rotational correlation times did not differ appreciably from those reported in Table 4.7. It may be concluded that director fluctuations make negligible contributions to the spectral densities reported in the nematic phase of the liquid crystal FLOC.

This conclusion is in agreement with results of low frequency proton and deuterium relaxation measured with field cycling methods on other thermotropic nematics

[168-170] and lyotropic liquid crystals [171], but differs remarkably from results reported previously for small solute probes in nematics [158,159,168,171,172]. The resolution of this apparent paradox lies in the fact that the rotational correlation times for the liquid crystals themselves are typically much larger than those of the small solute probes. This has the effect of increasing the negative cross term, to the point where the total contribution from eqn. (4.73) approaches zero. For example, with  $A = 2 \times 10^6$  s,  $\omega_c = 200$  MHz and  $\tau_p = 500$  ps, the autocorrelation part (first term) of Eqn. (4.73) is found to be 23.7 ps at 46 MHz and the cross correlation term is -11.0 ps. But, when  $\tau_p$  is increased to 1200 ps, the second term increases to -24.0 ps and effectively cancels the first. It should be noted that in this regime, the assumptions on which Eqn. (4.73) is based are no longer valid, but a more rigorous generalized Langevin equation representation of the dynamics of a molecule [173,174] yields similar results to those reported here. It would be interesting to extend this theory [173] to asymmetric rotors like FLOC<sub>14</sub>-d<sub>9</sub> with off-axis deuterons to further explore the interaction between the rotational diffusion of liquid crystal molecules and the director fluctuations of liquid crystal systems when the time scales are comparable.

The temperature dependence of the correlation times fit using the  $\chi^2$  analysis is given in Table 4.7 and illustrated in Fig. 4.7. The collision parameter decreases with increasing temperature (Fig. 4.8), indicating that near the isotropic-nematic phase transition, the  $\tau_r$  motion is in the strong collision limit and proceeds by large angular jumps. As the temperature decreases, the nematogen rotates about its axis of symmetry with increasingly smaller angular jumps. Although this conclusion relies on

temp (°C)	Q <sup>a</sup>	$\tau_{\alpha}$ (ps) <sup>b</sup>	$\tau_{\beta}$ (ps) <sup>b</sup>	$\tau_{\gamma}$ (ps) <sup>b</sup>	P	$\chi^2_{RED}$	Prob( $\geq \chi^2$ ) (%)
131.6	.593	820 +700/-300	1400 +500/-300	280 +30/-30	0.70	4.57	<1
133.3	.565	900 +600/-400	1120 +300/-120	280 +30/-20	0.75	1.63	15
135.7	.523	610 +500/-200	1050 +300/-200	266 +25/-15	0.65	0.64	70
138.3	.463	390 +250/-150	1060 +500/-200	245 +40/-30	0.50	2.06	6
140.0	.395	270 +80/-90	1175 +800/-300	210 +40/-30	0.30	1.68	12

<sup>a</sup> The uniaxial order parameter (Q) estimated using a second order polynomial fit to the temperature dependence.

<sup>b</sup> The correlational times and the boundaries of 68% confidence are presented.

Table 4.7 Results of global least squares fit of experimental spectral density data to the third rate model of molecular reorientation.

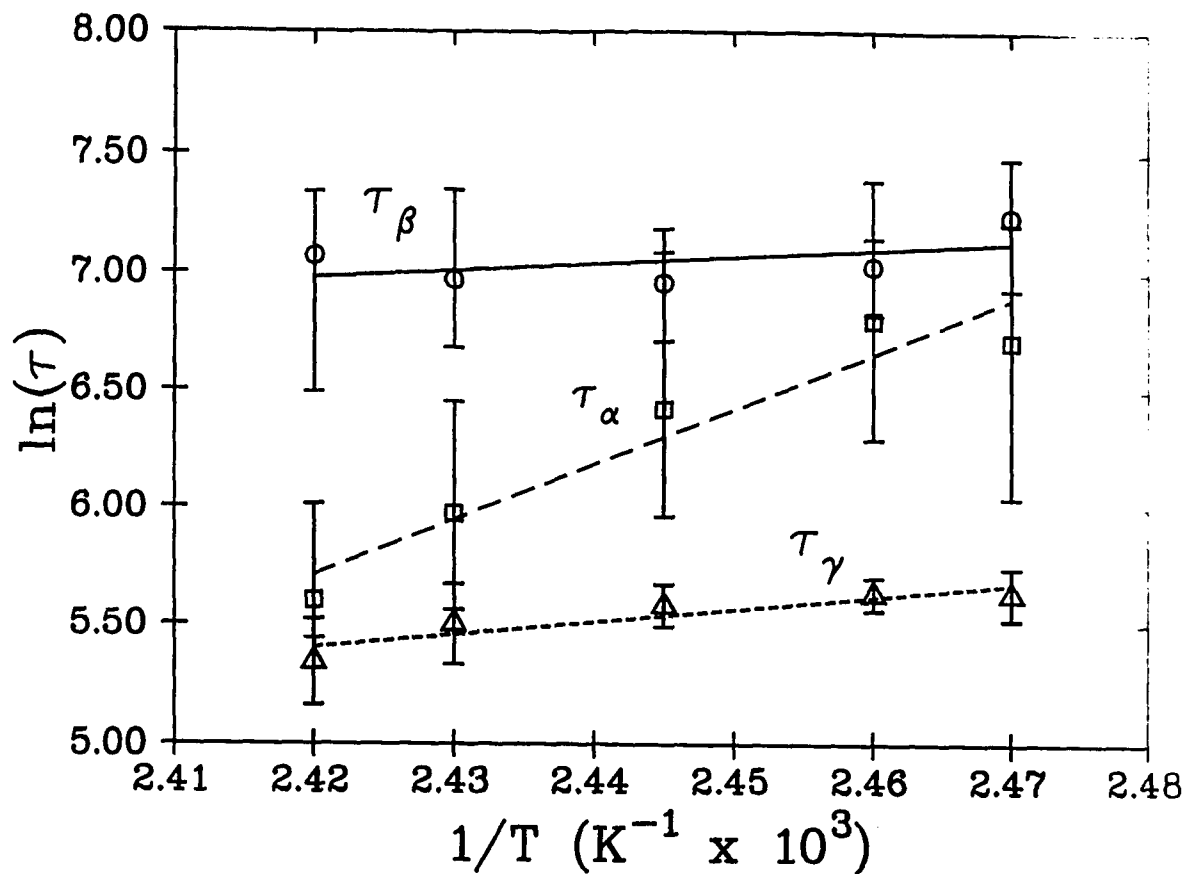


Figure 4.7 An Arrhenius plot of the temperature dependence of the motional correlation times showing 68% confidence boundaries for each parameter.  $\tau_\alpha$  data are squares,  $\tau_\beta$  data are circles, and  $\tau_\gamma$  data are triangles. The lines are least squares fits of the data to the Arrhenius equation,  $\tau = \tau_0 \exp(-E_A/k_B T)$ .

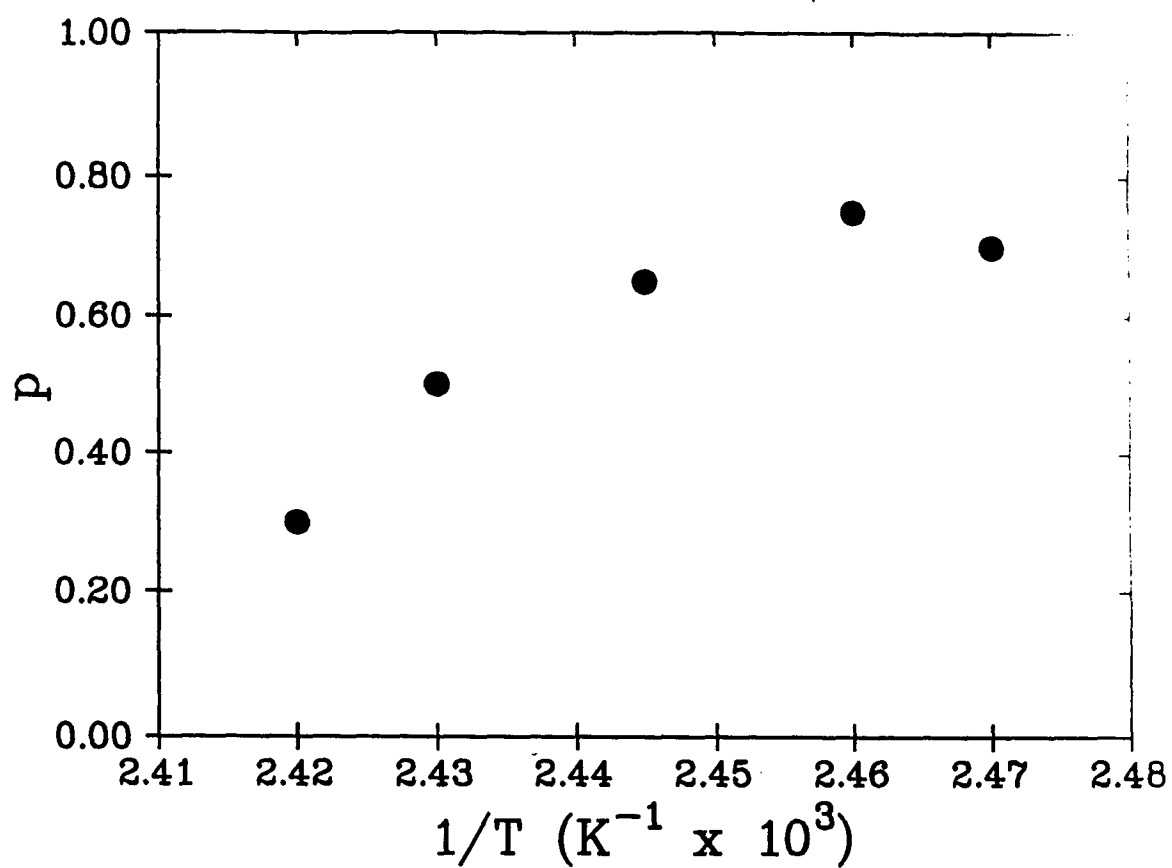


Figure 4.8 The collision parameter plotted as a function of inverse temperature.  $p = 0$  corresponds to strong collision and  $p = 1$  implies small step diffusion.

the assumption that  $\gamma$  motion and  $\alpha, \beta$  motions are statistically uncorrelated, it is physically plausible. If an Arrhenius temperature dependence is assumed, the  $\tau_\gamma$  values, yield activation energy  $E_A(\gamma) = 41 \pm 25$  kJ/mol over the 9.4 °C nematic temperature range investigated. FLOC<sub>14-d<sub>9</sub></sub> is a long molecule with a rather small molecular biaxial order parameter ( $D < 0.08$ ) in the nematic phase. Because motion about the molecular axis of symmetry is not hindered much by the shape of the rotating molecule, a comparatively low activation energy and short correlation time is expected. The  $\beta$  motion is about 5 to 7 times slower than the  $\gamma$  motion and also has a lower activation energy,  $E_A(\beta) = 12 \pm 47$  KJ/mol. This is surprising since a strong nematic aligning potential might be expected to give  $\tau_\beta$  a large temperature dependence. Large  $\tau_\beta$  and small  $E_A(\beta)$  is characteristic of several liquid crystals [175,176]. A possible explanation for the combination of long correlation time and small activation energy may be librational motion of the liquid crystal about an axis perpendicular to the director. The temperature dependence for  $\tau_\alpha$ , the correlation time for motion about the director, gives activation energy,  $E_A(\alpha) = 210 \pm 100$  kJ/mol. This seems anomalously high. Although error limits are large, a high activation energy is expected because this motion inevitably requires the displacement of many surrounding molecules.

The liquid crystal FLOC<sub>14-d<sub>9</sub></sub> presents a uniquely rich system for the investigation of molecular dynamics in the nematic phase. With many well resolved sites on the rigid fluorene moiety, the motion of the liquid crystal can be investigated in detail without complications introduced by the rotational degrees of freedom of the alkyl chain. A general, global least squares technique was developed to fit the relaxation data gathered

from five deuterated sites to the third rate model of molecular reorientation in ordered media. Uncertainties in the parameters of this model are larger than those of previous investigations, a result of insisting that the model fit the data from all measured sites. Much lower errors could be obtained by looking at only one or two sites. However, since the number of deuterated sites is greater than the number of motional parameters, confidence in the model can be estimated for the first time by the global fitting procedure and the results are encouraging. In the nematic phase, the third rate model adequately describes the molecular reorientation of the nematogen FLOC<sub>14-d<sub>6</sub></sub>, and there is no evidence for contributions to the relaxation from director fluctuations.

#### **4.6 Reorientational Dynamics in a Liquid Crystal Mixture**

A similar series of experiments were used to investigate the molecular motion of a binary mixture of the liquid crystal FLOC and the small, rigid molecule para-Xylene (p-Xy). The mixture was sealed in a 5mm tube after several freeze-pump-thaw cycles. One result of mixing the small, non-mesogenic probe in with the liquid crystal FLOC is a depressed nematic-isotropic transition temperature  $T_{NI}$ , and in this case  $T_{NI}$  fell by 50°C. As the sample was cooled, the phase changed from the isotropic to the nematic at  $T_{NI}^+ = 78.3^\circ\text{C}$  and from the nematic to the crystal phase at  $T_{NI}^- = 74.7^\circ\text{C}$ . Integrating the static  $^2\text{H-NMR}$  spectrum and assuming complete deuteration, it was discovered that only 30 mole % of the mixture becomes nematic, the rest stay in the isotropic state until the entire system crystallizes. Assuming that the concentration of FLOC in the isotropic phase is small, the integrated intensities were used to determine the molar concentration of molecules in the nematic phase: 50 mole % are FLOC and 50 mole % are p-Xy.



temp (°C)	$2\nu_0^3$ (kHz) <sup>a</sup>	$2\nu_0^1$ (kHz)	$2\nu_0^4$ (kHz)	$2\nu_0^{5,8}$ (kHz)	$2\nu_0^6$ (kHz)	$2\nu_0^7$ (kHz)	$Q_1^b$	$D_1^c$	$\beta_2^d$ (deg)	$Q_2^e$	$D_2^f$
74.20	6.73	18.4	22.8	53.3	53.3	122	.511	-.054	6.671	.119	.086
78.80	6.90	18.3	22.9	53.5	53.5	120	.506	-.053	6.848	.121	.086
75.50	6.72	17.8	22.1	51.6	51.6	117	.491	-.052	6.747	.117	.084
76.20	6.72	17.2	21.2	49.7	49.7	112	.471	-.500	6.764	.114	.083
77.50	6.40	16.0	20.1	46.4	46.4	105	.442	-.048	6.727	.107	.078
78.90	6.40	15.8	17.7	45.3	45.3	103	.432	-.047	6.673	.103	.076

<sup>a</sup>  $\delta(2\nu_0^j) = \pm 0.4$  kHz

<sup>b</sup>  $\delta Q_1 = \pm 0.010$

<sup>c</sup>  $\delta D_1 = \pm 0.016$

<sup>d</sup>  $\delta\beta_2 = \pm 0.010$  deg

<sup>e</sup>  $\delta Q_2 = \pm 0.005$

<sup>f</sup>  $\delta D_2 = \pm 0.004$

Table 4.8 The experimental quadrupole splittings  $2\nu_0^j$  and order parameters of FLOC and p-Xy in the nematic phase.

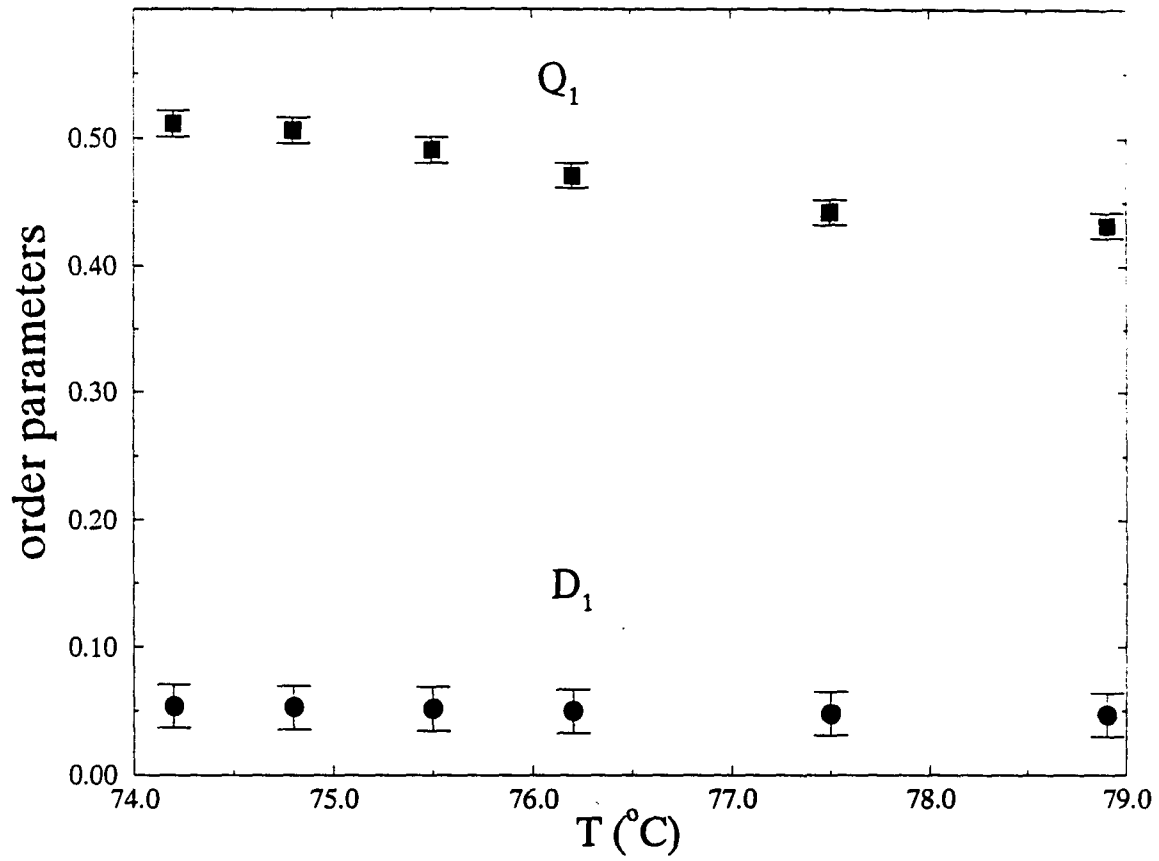


Figure 4.9(a) The uniaxial ( $Q_1$ ) and biaxial ( $D_1$ ) order parameters of FLOC as a function of temperature in the  $\text{FLOC}_{14}$  : p-Xy binary mixture.

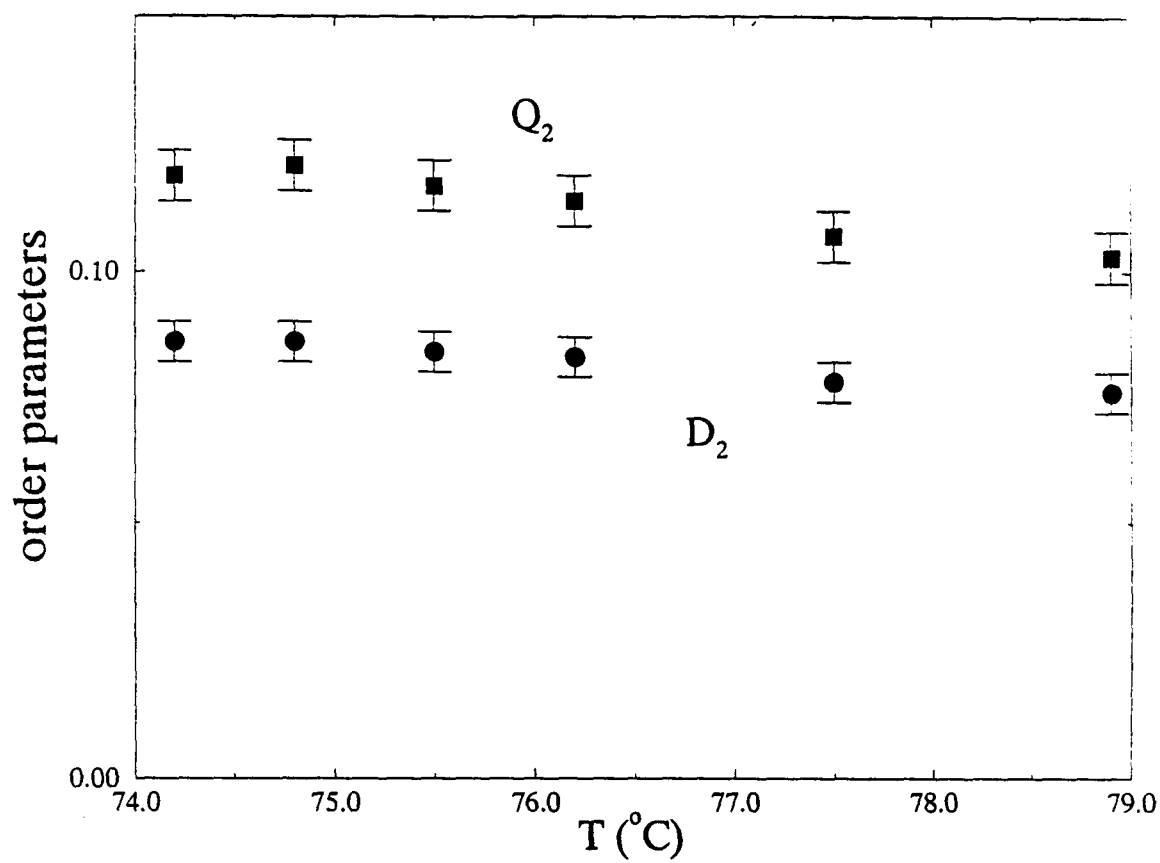


Figure 4.9(b) The uniaxial ( $Q_2$ ) and biaxial ( $D_2$ ) order parameters of p-Xy as a function of temperature in the FLOC<sub>14</sub> : p-Xy binary mixture.

The experimentally observed splittings were used to find the biaxial ( $D_i$ ) and uniaxial ( $Q_i$ ) order parameters of both components of the mixture. These are shown as a function of temperature for FLOC (Figure 4.9(a)) and p-Xy (Figure 4.9(b)), and they are listed in Table 4.8. Values for the order parameters are similar to those found previously for an 11 mole % binary mixture of p-Xy:FLOC, except that the temperature width of the phase is reduced from 12 °C to 3.5 °C.

The relaxation rates,  $T_{1Z}$  and  $T_{1Q}$ , for all sites on both molecules were determined using the same experimental techniques as described for the pure FLOC sample. The relaxation rates for the FLOC splittings were measured using 16 relaxation times with 1.6  $\mu$ sec 90° pulse widths, 100 ms recycle times and 4096 scans. The p-Xy lines had much longer relaxation rates and required a 3 sec recycle time and 256 scans were signal averaged. The relaxation rates are presented in figure 4.9 and 4.10, and the calculated spectral densities are presented as a function of temperature in 4.10 and Figure 4.10.

The spectral density data were fit to the third rate model with the same minimum  $\chi^2$  technique used in the investigation of pure FLOC, the results of the fit to the correlation times are given in Figure 4.11 and Table 4.11. These correlation times are in qualitative agreement with the results from pure FLOC. The general trend that  $\tau_\beta > \tau_\alpha > \tau_\gamma$  is followed, although  $\tau_\gamma$  is somewhat longer in the mixture. This slowing of the  $\tau_\gamma$  motion may be caused by collisions of the smaller p-Xy molecules with the core of the FLOC which serve to brake this rotational motion. The collision parameter for FLOC was found to be  $p = 0.50$  throughout the nematic range, this is in qualitative

temp (°C)	site 3		site 1		site 4	
	T <sub>1/2</sub> (ms)	T <sub>10</sub> (ms)	T <sub>1/2</sub> (ms)	T <sub>10</sub> (ms)	T <sub>1/2</sub> (ms)	T <sub>10</sub> (ms)
74.20	6.72±.17	6.00±.40	6.48±.16	8.62±.68	6.73±.15	8.99±.33
74.80	6.63±.71	6.20±.20	6.28±.11	7.91±.47	5.98±.19	8.67±.24
77.50	6.58±.07	7.37±.33	6.96±.09	8.99±.39	6.84±.14	9.13±.23
76.20	7.67±.33	7.93±.30	7.22±.07	8.85±.21	7.20±.15	9.25±.27
77.50	7.48±.20	8.05±.42	6.96±.12	9.98±.76	7.34±.09	8.95±.11
78.90	9.65±.78	12.2±1.50	9.71±.63	8.27±1.5	12.0±.60	4.99±1.1

Table 4.9 Experimental relaxation rates for sites 1, 3 and 4 on FLOC in the FLOC<sub>14</sub> : p-Xy binary mixture.

tmp (°C)	sites 8&5 T <sub>1/2</sub> (ms)	sites 8&5 T <sub>10</sub> (ms)	site 7 T <sub>1/2</sub> (ms)	site 7 T <sub>10</sub> (ms)	tmp (°C)	AR site T <sub>1/2</sub> (ms)	AR site T <sub>10</sub> (ms)	ME site T <sub>1/2</sub> (ms)	ME site T <sub>10</sub> (ms)
74.20	6.75±.20	10.20±.58	8.02±1.19	4.4±1.6	74.8	109±8	217±30	704±127	615±12
74.80	5.71±.22	8.26±.74	5.15±2.7	6.15±1.9	75.5	171±7	376±104	936±96	612±182
75.50	6.81±.09	9.65±.61	7.2±1.3	6.02±1.9	75.8	98±25	331±36	405±33	763±23
76.20	6.98±.11	10.04±1.31	5.36±.81	3.89±.68	77.0	168±16	278±42	685±79	551±47
77.50	6.74±.14	9.25±1.23	5.26±.30	5.80±.68	77.5	147±5	361±27	767±37	1100±143
78.90	9.56±.52	9.09±.52	7.52±.31	6.90±.24	78.2	147±6	298±13	482±49	712±60

Table 4.10 Experimental relaxation rates for sites 5,8 and 7 on FLOC<sub>14</sub> and the methyl and aromatic sites on p-Xy in the FLOC<sub>14</sub> : p-Xy binary mixture.

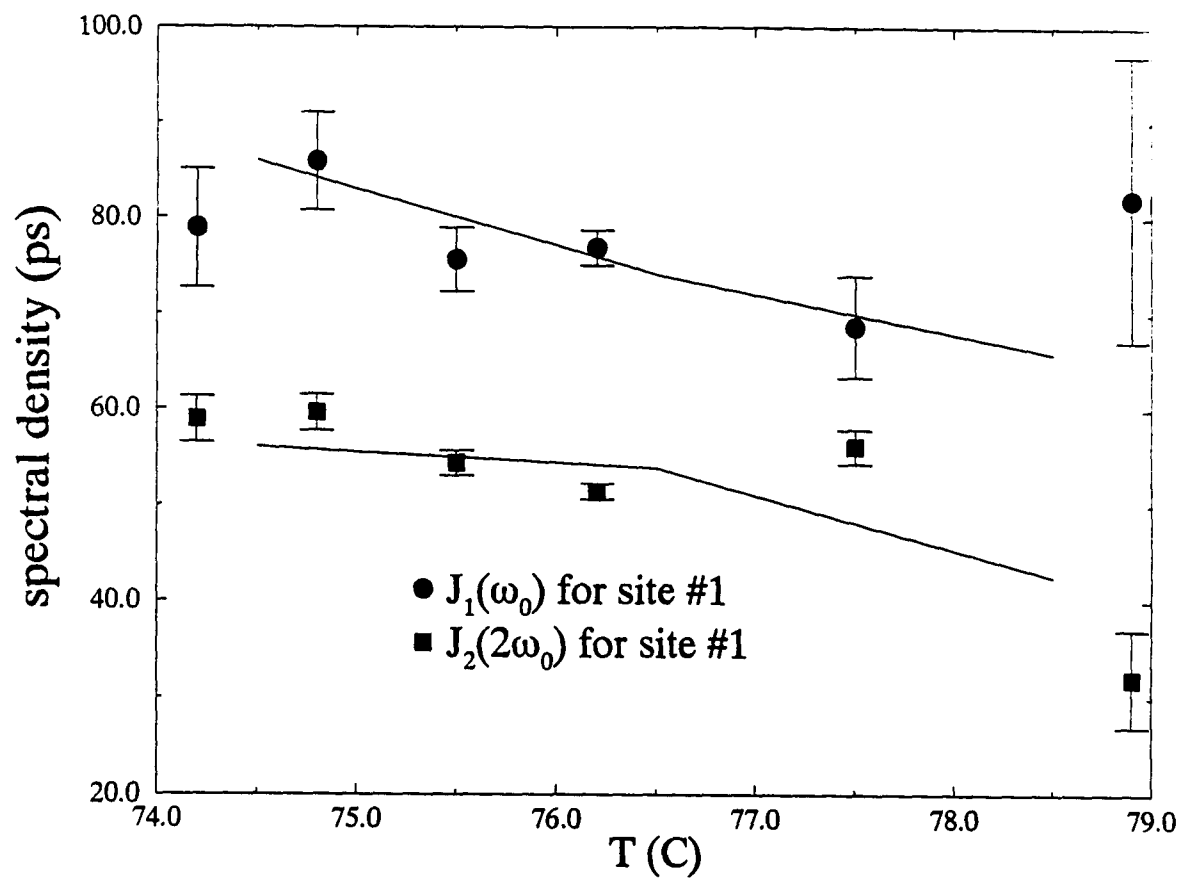


Figure 4.10(a) Site 1: Spectral densities measured as a function of inverse temperature for each deuterated site. Circles are  $J_1(\omega_0)$  measured at 46 MHz, squares are  $J_2(2\omega_0)$  measured at 46 MHz, and the lines are fits of the data to the third rate model of molecular reorientation.

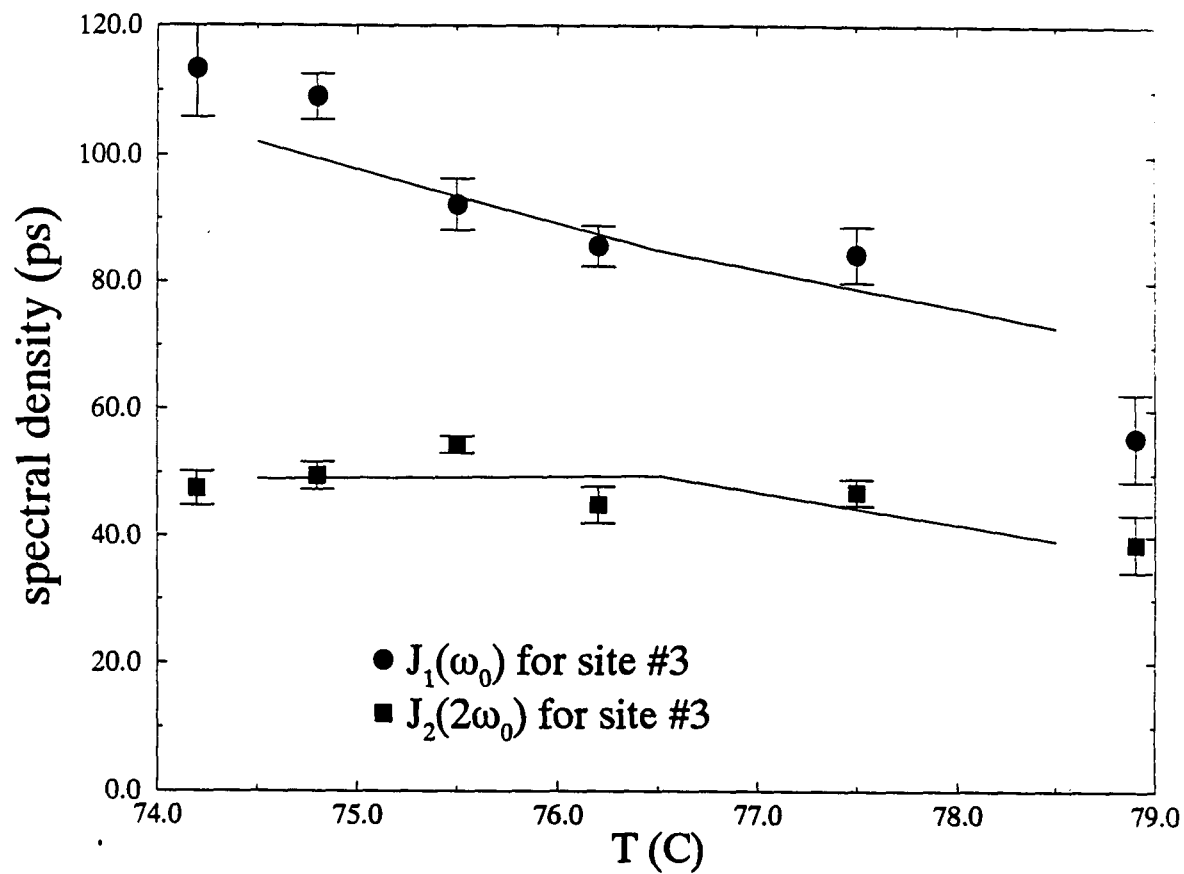


Figure 4.10(b) Site 3: Spectral densities measured as a function of inverse temperature for each deuterated site. Circles are  $J_1(\omega_0)$  measured at 46 MHz, squares are  $J_2(2\omega_0)$  measured at 46 MHz, and the lines are fits of the data to the third rate model of molecular reorientation.



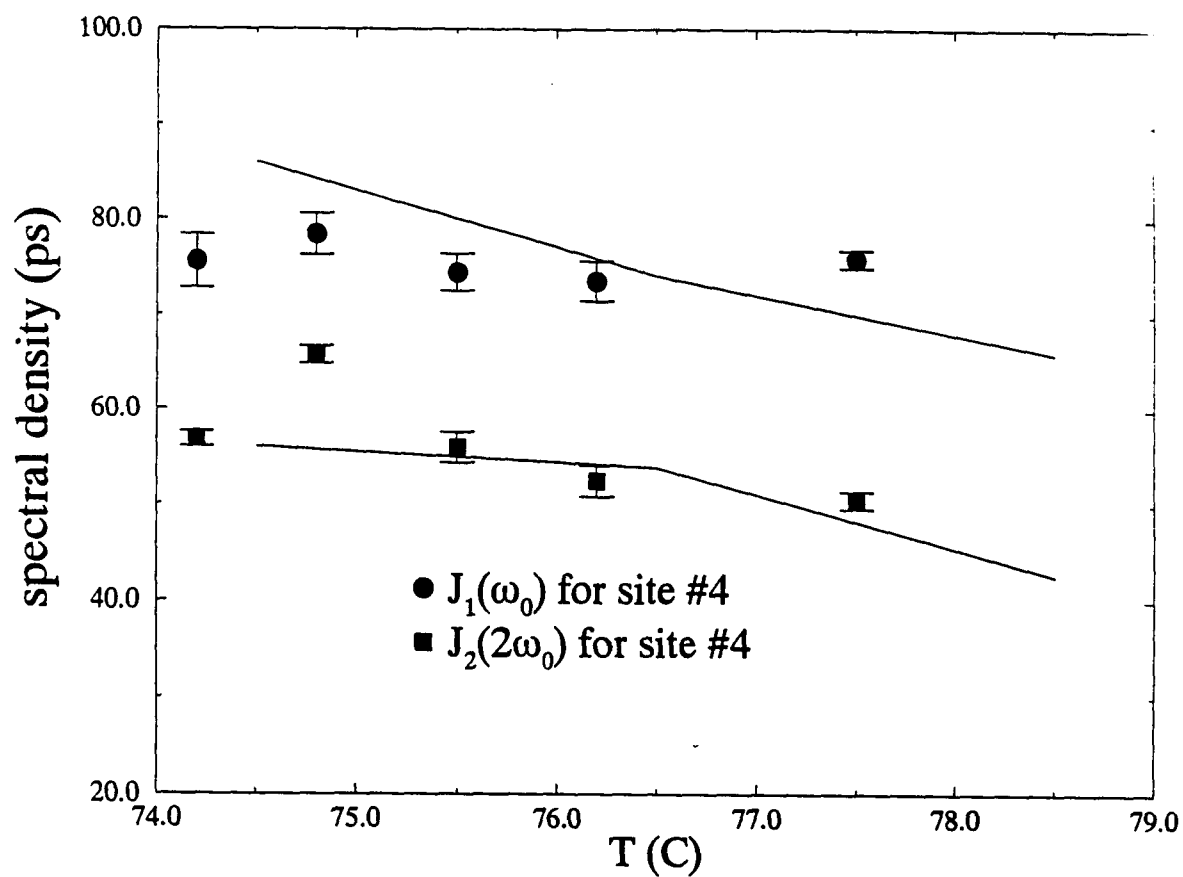


Figure 4.10(c) Site 4: Spectral densities measured as a function of inverse temperature for each deuterated site. Circles are  $J_1(\omega_0)$  measured at 46 MHz, squares are  $J_2(2\omega_0)$  measured at 46 MHz, and the lines are fits of the data to the third rate model of molecular reorientation.

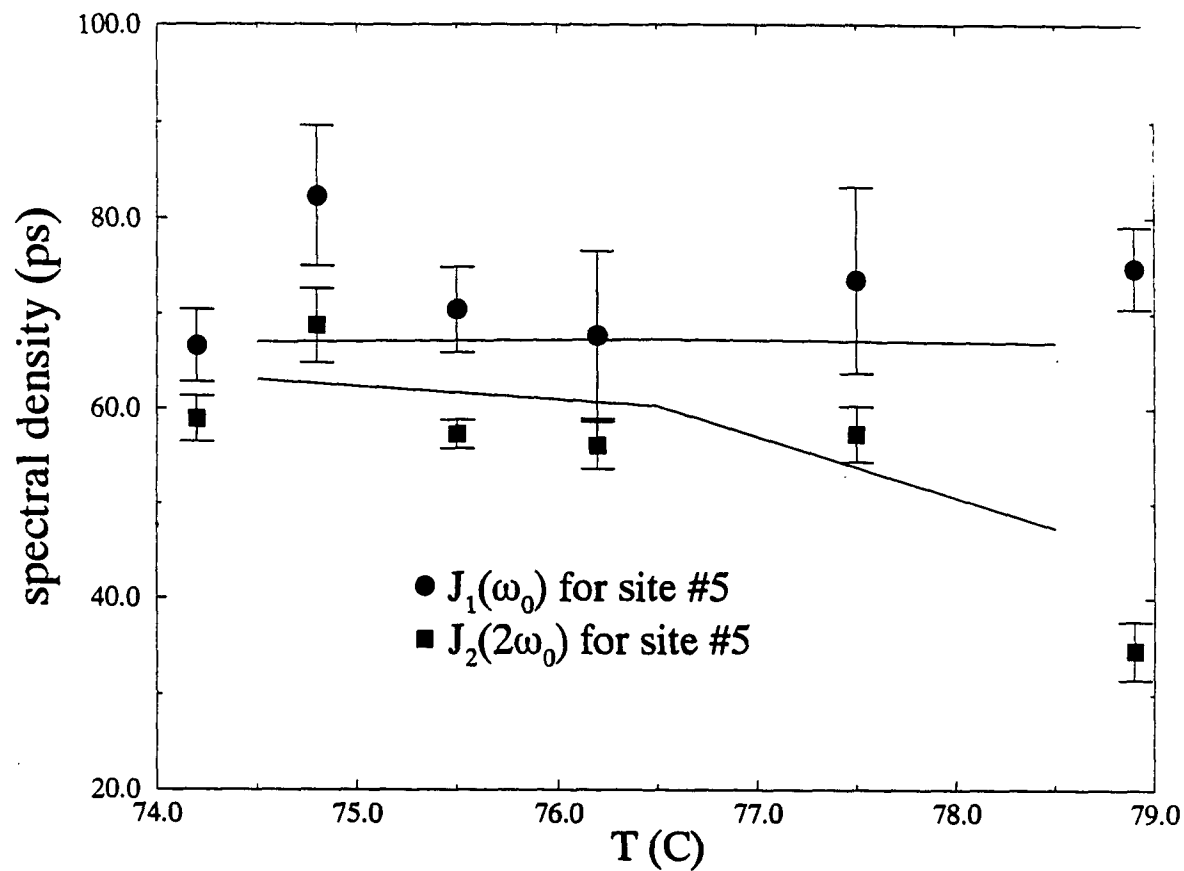


Figure 4.10(d) Site 5 and 8: Spectral densities measured as a function of inverse temperature for each deuterated site. Circles are  $J_1(\omega_0)$  measured at 46 MHz, squares are  $J_2(2\omega_0)$  measured at 46 MHz, and the lines are fits of the data to the third rate model of molecular reorientation.

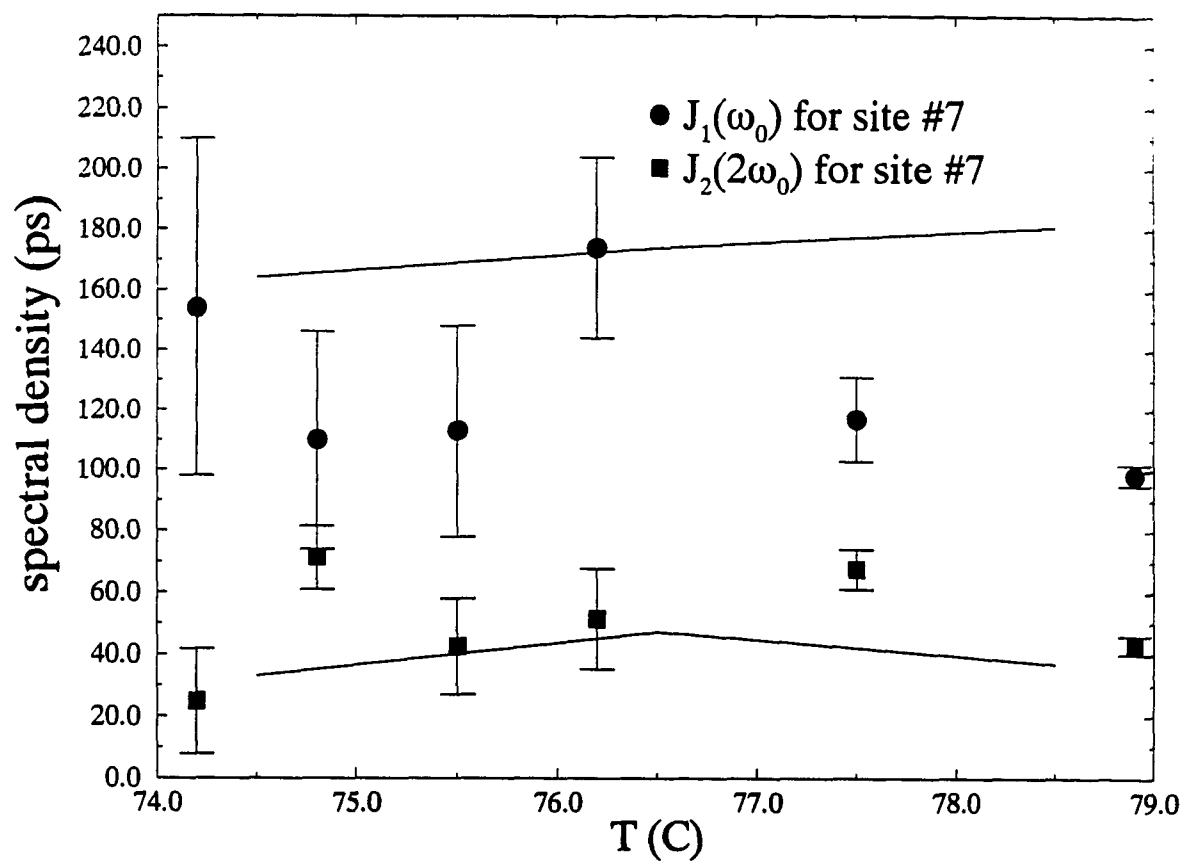


Figure 4.10(e) Site 7: Spectral densities measured as a function of inverse temperature for each deuterated site. Circles are  $J_1(\omega_0)$  measured at 46 MHz, squares are  $J_2(2\omega_0)$  measured at 46 MHz, and the lines are fits of the data to the third rate model of molecular reorientation.

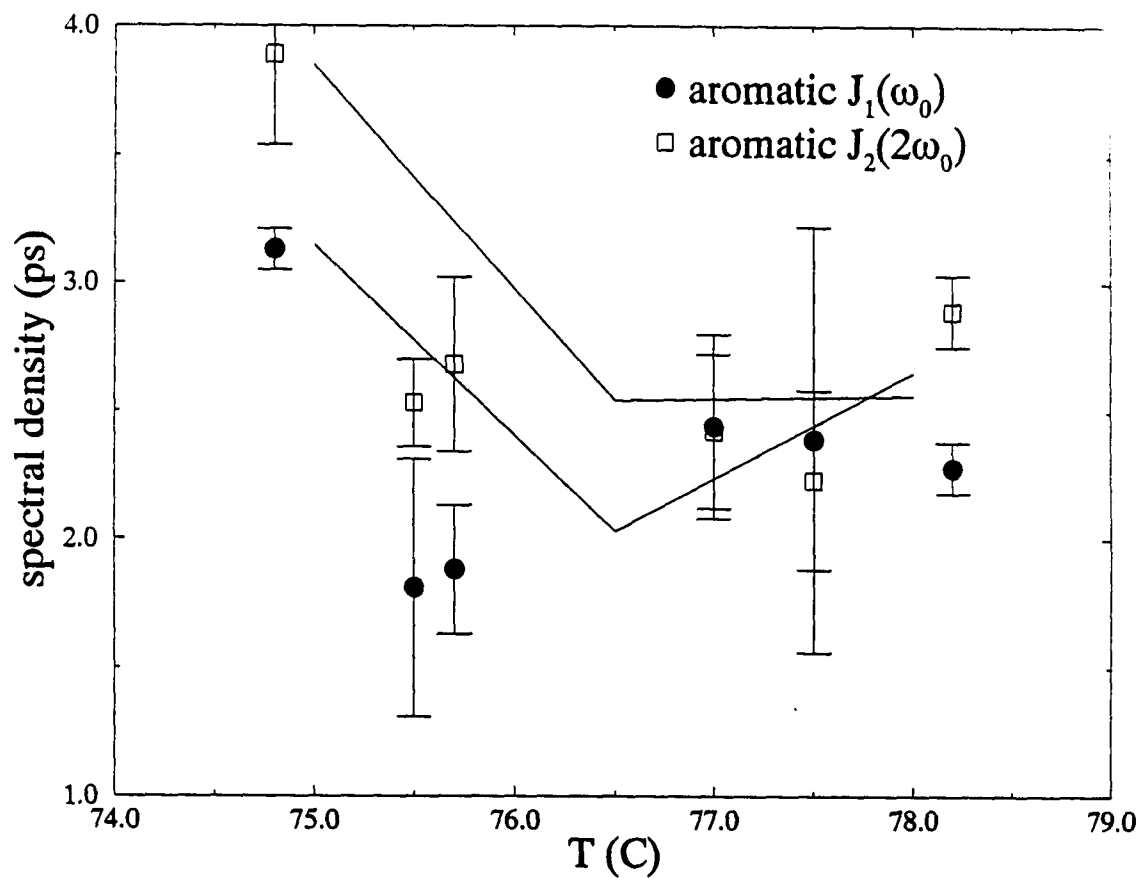


Figure 4.10(f) Aromatic Site on p-Xy: Spectral densities measured as a function of inverse temperature for each deuterated site. Circles are  $J_1(\omega_0)$  measured at 46 MHz, squares are  $J_2(2\omega_0)$  measured at 46 MHz, and the lines are fits of the data to the third rate model of molecular reorientation.

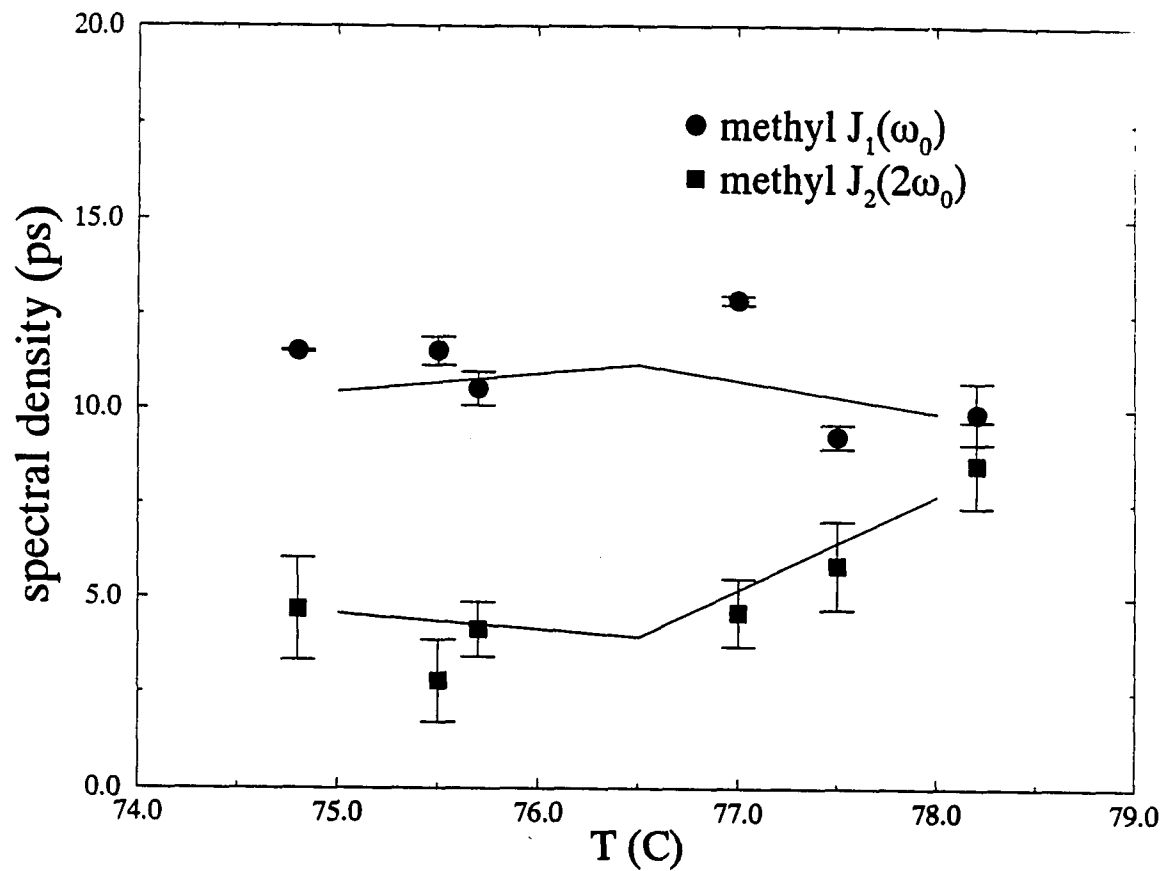


Figure 4.10(g) Methyl Site on p-Xy: Spectral densities measured as a function of inverse temperature for each deuterated site. Circles are  $J_1(\omega_0)$  measured at 46 MHz, squares are  $J_2(2\omega_0)$  measured at 46 MHz, and the lines are fits of the data to the third rate model of molecular reorientation.

agreement with the pure FLOC values. The temperature dependencies of the correlation times (Figure 4.11) were not used to find activation energies for either molecule in the mixture because of the small nematic temperature range and larger experimental uncertainties. The para-xylene data was fit to the third rate model assuming that fast spinning of the methyl groups motionally averages the quadrupolar coupling constant. For this motion, the principal axis of the effective field gradient tensor is along the spinning axis and is reduced by a factor of three [177]. The results of fits to the third rate model for p-Xy are presented in Table 4.12. The motions of this molecule are at least a factor of 10 faster than that of the larger liquid crystal host. The relative values of the correlation times of the para-xylene motion follow the general trend of the liquid crystal host, with  $\tau_\alpha > \tau_\beta > \tau_\gamma$ . The  $\tau_\gamma$  motion occurs by a strong collision mechanism as is observed for other small solute molecules [65,178-180].

These relaxation rates for molecular motion in the nematic phase were fit assuming that no exchange between molecules in the nematic phase and the coexisting nematic phase occurs on the time scale of the NMR experiment (100 ms for the FLOC<sub>14</sub> and 3 s for the p-Xy). This assumption was checked using a selective inversion-recovery experiment. In this experiment (shown in Figure 4.12), a low power, 180° pulse is used to invert the zero frequency line which originates from molecules in the isotropic phase. The system is then allowed to evolve for some time  $T_D$ . If molecules in the isotropic phase diffuse into the nematic phase during this time  $T_D$ , signal from inverted spins on the diffusing molecules should change the intensity of the quadrupolar doublets. By taking a difference between this experiment and one run without the inverting pulse, any

temp (°C)	$Q_1^a$	$\tau_{\alpha}$ (ps) <sup>b</sup>	$\tau_{\beta}$ (ps) <sup>b</sup>	$\tau_{\gamma}$ (ps) <sup>b</sup>	p	$\chi^2_{RED}$	Prob( $\geq \chi^2$ ) (%)
74.5	.508	660 +340/-160	1180 +520/-280	740 +160/-40	.50	2.08	6
76.5	.461	1000 +700/-400	1140 +360/-240	600 +100/-50	.50	2.01	6
78.0	.436	540 +260/-150	1560 +440/-460	500 +100/-50	.50	1.68	12

<sup>a</sup> The uniaxial order parameter ( $Q_1$ ) estimated using a second order polynomial fit to the temperature dependence.

<sup>b</sup> The correlational times and the boundaries of 68% confidence are presented.

Table 4.11 Results of global least squares fit of experimental spectral density data to the third rate model of molecular reorientation for FLOC<sub>14</sub> in the FLOC<sub>14</sub> : p-Xy binary mixture.

temp (°C)	$Q_2^*$	$\tau_\alpha$ (ps) <sup>b</sup>	$\tau_\beta$ (ps) <sup>b</sup>	$\tau_\gamma$ (ps) <sup>b</sup>	p
75.0	.120	24	60	31	0
76.5	.112	19	78	16	0
78.0	.099	51	45	17	0

- The uniaxial order parameter ( $Q_2$ ) estimated using a second order polynomial fit to the temperature dependence.
- The correlational times are presented.

Table 4.12 Results of global least squares fit of experimental spectral density data to the third rate model of molecular reorientation for p-Xy in the FLOC<sub>14</sub> : p-Xy binary mixture.



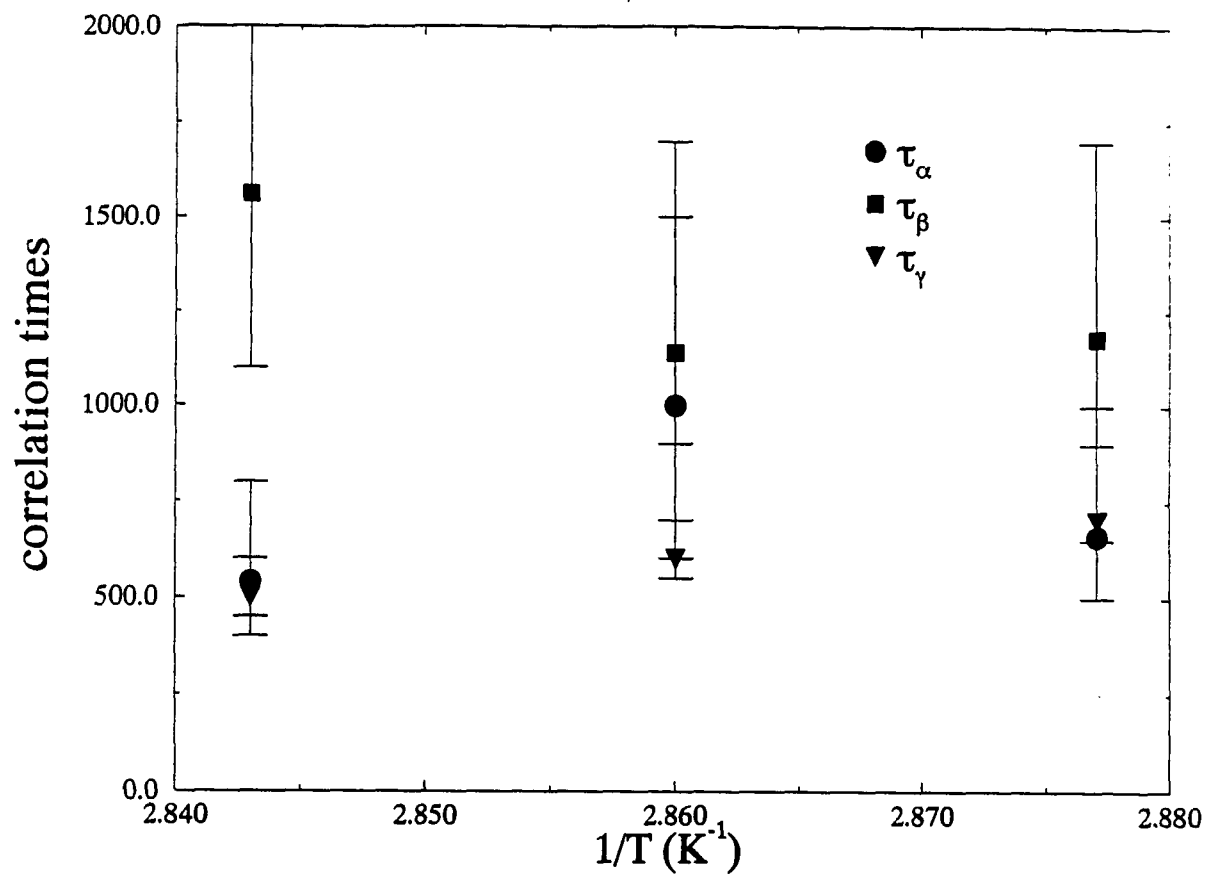


Figure 4.11 An Arrhenius plot of the temperature dependence of the motional correlation times of FLOC<sub>14</sub> molecular motion in the FLOC<sub>14</sub> : p-Xy binary mixture showing 68% confidence boundaries for each parameter.  $\tau_\alpha$  data are circles,  $\tau_\beta$  data are squares, and  $\tau_\gamma$  data are triangles.

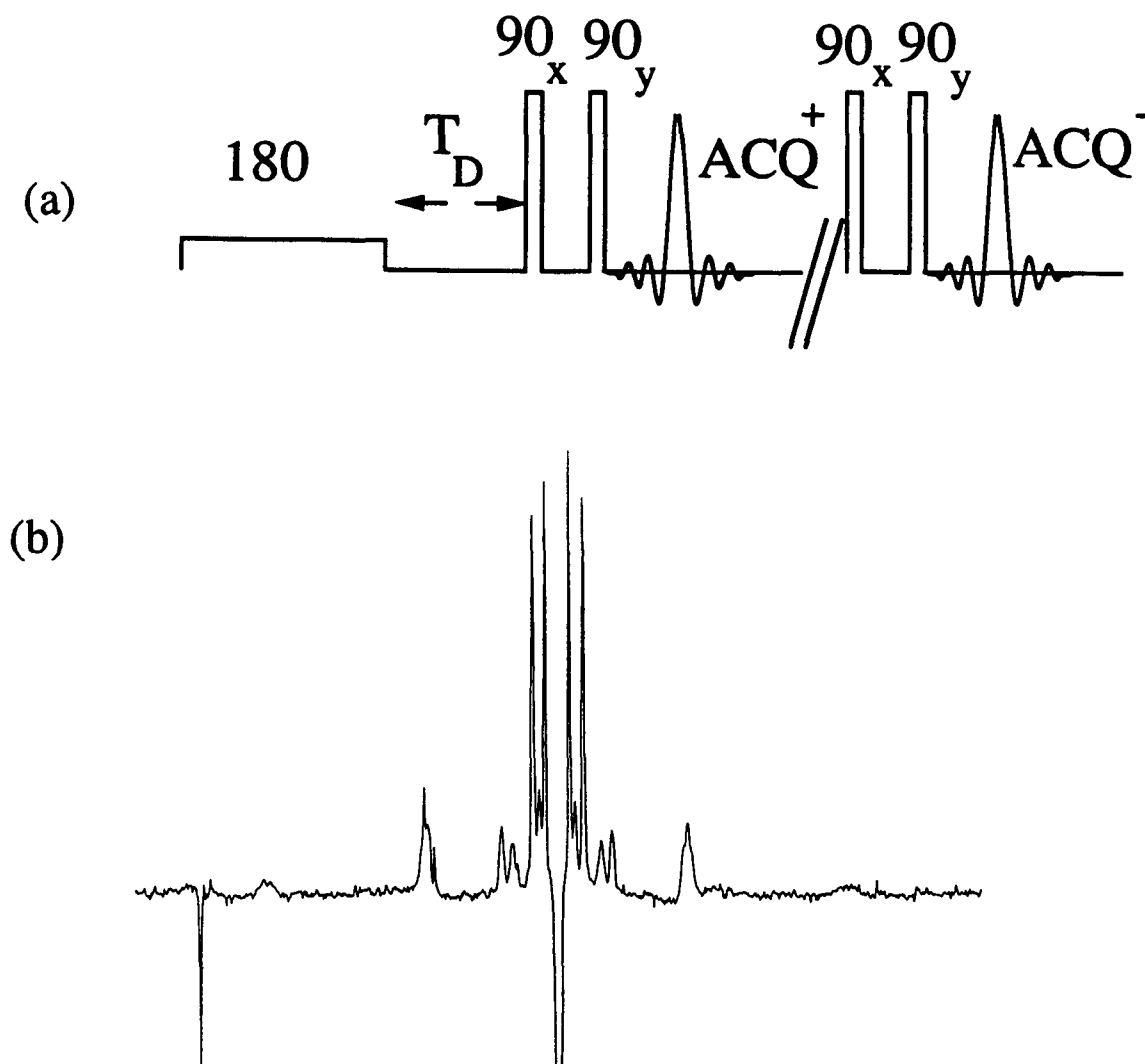


Figure 4.12 The selective inversion experiment is shown in Figure 4.12(a). A low power rf pulse is applied long enough ( $t_p = 800 \mu\text{s}$ ) to invert the low frequency signal ( $\omega_1 t_p = \pi$ ) as shown in 4.12 (b). The system is allowed to evolve during a time  $T_D$ , then a quadrupole echo pulse sequence is used to detect the magnetization. The difference between the this signal and one acquired using a standard quadrupolar echo is used to detect translational diffusion between molecules in coexisting nematic and isotropic phases.

off resonance signal would indicate translational diffusion between coexisting nematic and isotropic phases. No signal was detected away from the zero frequency isotropic peak in the difference spectrum. This negative result implies that the assumption that translational diffusion across the nematic-isotropic boundary is not occurring on the time scale of the NMR experiment is correct ( $T_D > 3s$ ).

In this chapter, the molecular motion of a liquid crystal and a liquid crystal binary mixture were investigated using  $^2H$ -NMR relaxation experiments analyzed with a composite diffusion model of molecular reorientation in an ordered medium. The results from the pure material showed that in the nematic phase, the third rate model adequately described the molecular reorientation of the nematogen FLOC<sub>14</sub> with no evidence of director fluctuations at 46 MHz. Curiously, no evidence for director fluctuations were found in the analysis of the relaxation data for a p-Xy:FLOC binary mixture. Although the experimental data for the mixture experiment are less accurate, previous studies of small molecules have reported that contributions to the spectral densities from director fluctuations are needed to interpret the relaxation data [170,180-183], especially at Larmor frequencies below 500 kHz. Both the low accuracy of the experimentally measured spectral densities and the high Larmor frequency of the experiment (46 MHz) do not allow for contributions to the spectral densities from director fluctuations to be estimated from the FLOC:p-Xy relaxation experiments. In fact, estimates using equation 4.73 and the results quoted in Table 4.12 show that the director fluctuation contribution to  $J_1(\omega_0)$  for the p-Xy deuterons is within experimental error. The motion of the smaller, rigid p-Xy occurs on a much faster time scale than that of the long, flexible liquid crystal. The

$\tau_y$  motion of FLOC is measurably different in the mixture compared to the pure material. The time scale for p-Xy motion differs from that of FLOC by an order of magnitude, this suggests that mixtures and pure materials are fundamentally different, and it is incorrect to assume that probe molecules are capable of monitoring a system without biasing it.

---

## APPENDIX I

$l$	$m$	$T_{lm}$
0	0	$-(1/3)[T_{xx}+T_{yy}+T_{zz}]$
1	0	$-(i/\sqrt{2})[T_{xy}-T_{yx}]$
1	$\pm 1$	$-(1/2)[T_{zx}-T_{xz} \pm i(T_{zy}-T_{yz})]$
2	0	$(1/\sqrt{6})[3T_{zz} - (T_{xx}+T_{yy}+T_{zz})]$
2	$\pm 1$	$\mp(1/2)[T_{xz}+T_{zx} \pm i(T_{yz}+T_{zy})]$
2	$\pm 2$	$(1/2)[T_{xx}-T_{yy} \pm i(T_{xy}+T_{yx})]$

Spherical Tensors. The spherical tensors  $T_{lm}$  are obtained from the nine elements of the Cartesian tensor  $T_{\alpha\beta}$  ( $\alpha, \beta = x, y, z$ ). The indices  $l$  and  $m$  denote the rank and component index of the spherical tensor, respectively.

APPENDIX II

m'/m	-2	-1	0	1	2
-2	$\frac{1}{4}(1+\cos\beta)^2 e^{i(\alpha+\gamma)}$	$\frac{1}{2}(1+\cos\beta) \sin\beta e^{i(2\alpha+\gamma)}$	$(\sqrt{3}/\sqrt{8})\sin^2\beta e^{i2\alpha}$	$\frac{1}{2}(1-\cos\beta) \sin\beta e^{-i(2\alpha+\gamma)}$	$\frac{1}{4}(1-\cos\beta)^2 e^{-2i(\alpha+\gamma)}$
-1	$-\frac{1}{2}(1+\cos\beta) \sin\beta e^{i(\alpha+2\gamma)}$	$\frac{1}{2}(1+\cos\beta) (2\cos\beta-1) e^{i(\alpha+\gamma)}$	$(\sqrt{3}/\sqrt{8}) \sin 2\beta e^{i\alpha}$	$\frac{1}{2}(1-\cos\beta) (2\cos\beta+1) e^{-i(\alpha+\gamma)}$	$\frac{1}{2}(1-\cos\beta) \sin\beta e^{-i(\alpha+2\gamma)}$
0	$(\sqrt{3}/\sqrt{8})\sin^2\beta e^{i2\gamma}$	$-(\sqrt{3}/\sqrt{8})\sin 2\beta e^{i\gamma}$	$1/2 (3\cos^2\beta-1)$	$(\sqrt{3}/\sqrt{8})\sin 2\beta e^{-i\gamma}$	$(\sqrt{3}/\sqrt{8})\sin^2\beta e^{-2i\gamma}$
1	$-\frac{1}{2}(1-\cos\beta) \sin\beta e^{i(\alpha+2\gamma)}$	$\frac{1}{2}(1-\cos\beta) (2\cos\beta+1) e^{i(\alpha+\gamma)}$	$-(\sqrt{3}/\sqrt{8}) \sin 2\beta e^{-i\alpha}$	$\frac{1}{2}(1+\cos\beta) (2\cos\beta-1) e^{-i(\alpha+\gamma)}$	$\frac{1}{2}(1+\cos\beta) \sin\beta e^{-i(\alpha+2\gamma)}$
2	$\frac{1}{4}(1-\cos\beta)^2 e^{i(\alpha+\gamma)}$	$-\frac{1}{2}(1-\cos\beta) \sin\beta e^{i(2\alpha+\gamma)}$	$(\sqrt{3}/\sqrt{8})\sin^2\beta e^{-i2\alpha}$	$\frac{1}{2}(1+\cos\beta) \sin\beta e^{-i(2\alpha+\gamma)}$	$\frac{1}{4}(1+\cos\beta)^2 e^{-2i(\alpha+\gamma)}$

Wigner Rotation Matrix elements  $D_{m'm}^{(2)}(\alpha, \beta, \gamma)$ . Rank 2 matrix elements given in terms of y-convention Euler angles  $\Omega=(\alpha, \beta, \gamma)$  [146].

## APPENDIX III

$$U(\hat{O}_a)\hat{O}_b = e^{-i\theta\hat{O}_a}\hat{O}_be^{i\theta\hat{O}_a}$$

$U(I_x)I_x = I_x\cos\theta - I_z\sin\theta$ $U(I_z)I_x = I_x\cos\theta + I_y\sin\theta$ $U(Q_z)I_x = I_x\cos\theta + Q_y\sin\theta$ $U(I_x)I_z = I_z\cos\theta + I_x\sin\theta$ $U(I_y)I_z = I_z\cos\theta + I_x\sin\theta$	$U(I_x)I_y = I_y\cos\theta + I_z\sin\theta$ $U(I_z)I_y = I_y\cos\theta - I_x\sin\theta$ $U(Q_z)I_y = I_y\cos\theta - Q_x\sin\theta$
$U(I_x)Q_x = Q_x\cos\theta - D_y\sin\theta$ $U(I_y)Q_x = Q_x\cos 2\theta$ $\quad + 1/2(3Q_z - D_x)\sin 2\theta$ $U(I_z)Q_x = Q_x\cos\theta + Q_y\sin\theta$ $U(Q_z)Q_x = Q_x\cos\theta + I_y\sin\theta$ $U(I_x)Q_z = 1/2Q_z(3\cos^2-1)$ $\quad - Q_y\sin\theta\cos\theta - 1/2D_x\sin^2\theta$ $U(I_y)Q_z = 1/2Q_z(3\cos^2-1)$ $\quad + Q_x\sin\theta\cos\theta + 1/2D_x\sin^2\theta$	$U(I_x)Q_y = Q_y\cos 2\theta$ $\quad + 1/2(2Q_z+D_x)\sin 2\theta$ $U(I_y)Q_y = Q_y\cos\theta + D_y\sin\theta$ $U(I_z)Q_y = Q_y\cos\theta - Q_x\sin\theta$ $U(Q_z)Q_y = Q_y\cos\theta - I_x\sin\theta$
$U(I_x)D_x = -Q_y\sin\theta\cos\theta - 3/2Q_z\sin^2\theta$ $\quad + 1/2D_x(1+\cos^2\theta)$ $U(I_y)D_x = -Q_x\sin\theta\cos\theta + 3/2Q_z\sin^2\theta$ $\quad + 1/2D_x(1+\cos^2\theta)$ $U(I_z)D_x = D_x\cos 2\theta + D_y\sin 2\theta$	$U(I_x)D_y = D_y\cos\theta + Q_x\sin\theta$ $U(I_y)D_y = D_y\cos\theta - Q_y\sin\theta$ $U(I_z)D_y = D_y\cos 2\theta - D_x\sin 2\theta$

Exponential operator commutation relations ( $\theta = \omega t$ ).

## APPENDIX IV

As explained in the text, integration of the expressions needed to calculate the order parameters (Eqns. (11) & (12)) can be performed analytically over the angular variable  $\alpha$ . This yields the following two dimensional integrals which must be evaluated numerically.

$$Z_1 = \frac{1}{2\pi} \int_{x=0}^1 \int_{\gamma=0}^{2\pi} \exp(a) I_0(\xi) dx d\gamma \quad (\text{A.1})$$

$$Q_1 Z_1 + \frac{1}{2} = \frac{3}{4\pi} \int_{x=0}^1 \int_{\gamma=0}^{2\pi} x^2 \exp(a) I_0(\xi) dx d\gamma \quad (\text{A.2})$$

$$D_1 Z_1 = -\frac{3}{4\pi} \int_{x=0}^1 \int_{\gamma=0}^{2\pi} (1-x^2) \frac{b}{\xi} \exp(a) I_1(\xi) dx d\gamma \quad (\text{A.3})$$

$$P_1 Z_1 = -\frac{3}{2\pi} \int_{x=0}^1 \int_{\gamma=0}^{2\pi} (1-x^2) \cos(\gamma) \exp(a) I_0(\xi) dx d\gamma \quad (\text{A.4})$$

$$C_1 Z_1 = \frac{3}{4\pi} \int_{x=0}^1 \int_{\gamma=0}^{2\pi} [b\cos(\gamma) + b\cos(\gamma)x^2 + 2cx\sin(\gamma)] \frac{I_1(\xi)}{\xi} dx d\gamma \quad (\text{A.5})$$

The integrals for species 2 are obtained by performing the following substitutions:

$$a \rightarrow r_1 a, \quad b \rightarrow \frac{r_3}{r_2} b, \quad c \rightarrow \frac{r_3}{r_2} c, \quad \xi \rightarrow \frac{r_3}{r_2} \xi.$$



The functions  $a$ ,  $b$ ,  $c$  and  $\alpha$  are given below.

$$a = \frac{3}{2} \Lambda \left( \frac{3}{2}x^2 - \frac{1}{2} \right) - \frac{9}{4} \Lambda' (1-x^2) \cos(\gamma) \quad (\text{A.6})$$

$$b = -\frac{9}{4} \Lambda r_2 (1-x^2) + \frac{9}{4} \Lambda' r_2 (1+x^2) \cos(\gamma) \quad (\text{A.7})$$

$$c = -\frac{9}{2} \Lambda' r_2 x \sin(\gamma) \quad (\text{A.8})$$

$$\alpha = \sqrt{b^2 + c^2} \quad (\text{A.9})$$

As a last note, the calculations are presented in the results and discussion section as functions of the volumetric fraction of molecule  $i=1$ . Given the volume per molecule of each component,  $v_1$  and  $v_2$  the number density,  $\rho$ , is related to the volumetric fraction,  $Y$ , by the following simple relations.

$$Y = Y_1 = \rho_1 v_1 \quad (\text{A.10})$$

$$(1-Y) = Y_2 = \rho_2 v_2 \quad (\text{A.11})$$

## REFERENCES

- [1] F. Reinitzer, *Monatsh. Chem.*, **9**, 421, 1888.
- [2] O. Lehmann, *Z. Physik. Chem.*, **4**, 462, 1889.
- [3] H. Kelker and P. Knoll, *Liq. Cryst.*, **5**, 19, 1989.
- [4] edited by G. G. Sprokel, *The Physics and Chemistry of Liquid Crystal Devices*, Plenum Press, N.Y., 1979).
- [5] E. Kaneko, *Liquid Crystal TV Displays*, (KTK Scientific Publishers, Tokyo, 1987).
- [6] D. Demus, *Liq. Cryst.*, **5**, 75, 1989.
- [7] S. Chandrasekhar, B. K. Sadashiva, K. A. Suresh, *Pramana*, **9**, 471, 1977.
- [8] J. Billard, J. C. Dubois, H-T Nguyen, A. Zann, *Nouveau J. Chim.*, **2**, 535, 1978.
- [9] J. Mathête, L. Liébert, A. M. Levelut, Y. Galerne, *Compte R. Ac. Sciences*, **303**, 1073, 1986.
- [10] S. Chandrasekhar, B. R. Ratna, B. K. Sadashiva, V. N. Raja, *Mol. Cryst. Liq. Cryst.*, **165**, 123, 1988.
- [11] K. Preafke, B. Kohne, B. Gündogan, D. Demus, S. Diele, G. Pelzi, *Mol. Cryst. Liq. Cryst. Lett.*, **7**, 27, 1990.
- [12] P. S. Pershan, *Structure of Liquid Crystal Phases*, (World Scientific, Singapore, 1988), Chap. 1, p. 7.
- [13] D. Demus and L. Richter, *Textures of Liquid Crystals*, (Verlag-Chemie, Berlin, 1978).
- [14] G. Vertogen and W. H. de Jeu, *Thermotropic Liquid Crystals, Fundamentals*, (Springer-Verlag, Berlin, 1988).
- [15] C. Zannoni, in *The Molecular Physics of Liquid Crystals*, edited by G. R. Luckhurst and G. W. Gray, (Academic Press, London, 1979), Chap. 3.
- [16] P. G. de Gennes, *The Physics of Liquid Crystals*, (Clarendon Press, Oxford, 1974).

- 
- [17] B. Bergersen, P. Palffy-Muhoray, and D. A. Dunmur, *Liquid Crystals*, **3**, 347, 1988.
- [18] L. L. Chapoy, D. B. Dupré, and E. T. Samulski, in *Liquid Crystals and Ordered Fluids*, edited by J. F. Johnson and R. S. Porter, (Plenum Press, N.Y., 1978), Vol. 3, pp. 177-189.
- [19] G. R. Luckhurst and R. Poupko, *Chem. Phys. Lett.*, **29**, 191, (1974).
- [20] J. P. Straley, *Phys. Rev. A*, **10**, 1881, 1974.
- [21] S. Romano in *Physics of Liquid Crystalline Materials*, edited by I. C. Khoo and F. Simoni, (Gordon and Breach Science Publishers, London, 1991), Chap. 3.
- [22] L. Onsanger, *Ann. N. Y. Acad. Sci.*, **51**, 627, 1949.
- [23] M. A. Cotter, in *The Molecular Physics of Liquid Crystals*, edited by G. W. Luckhurst and G. W. Gray, (Academic Press, N. Y., 1979), Chap. 7.
- [24] W. Maier and A. Saupe, *Z. Naturforsch.*, **14A**, 882, 1959.
- [25] G. R. Luckhurst, in *The Molecular Physics of Liquid Crystals*, edited by G. W. Luckhurst and G. W. Gray, (Academic Press, N. Y., 1979), Chap. 4.
- [26] P. J. Wojowicz, in *Introduction to the Molecular Theory of Liquid Crystals*, edited by E. B. Priestley, P. J. Wojtowicz, P. Sheng, (Plenum Press, N. Y., 1975), Chap. 3.
- [27] *Nobel Prize Winners, Supplement 1987-1991*, edited by P. McGuire, (The H. W. Wilson Company, New York, 1992).
- [28] P. A. Lebwohl and G. Lasher, *Phys. Rev. A*, **6**, 426, 1972.
- [29] C. Zannoni, in *The Molecular Physics of Liquid Crystals*, edited by G. W. Luckhurst and G. W. Gray, (Academic Press, N. Y., 1979), Chap. 9.
- [30] C. Chiccoli, P. Pasini and F. Semeria, *Mol. Cryst. Liq. Cryst*, **221**, 19, 1992.
- [31] M. Allen, *Liq. Cryst.*, **8**, 499, 1990.
- [32] Z. Y. Chen, J. M. Deutch, *J. Chem. Phys.*, **80**, 2151, 1984.
- [33] D. Frenkel and B. M. Mulder, *Mol. Phys.*, **55**, 1171, 1985.
-

- 
- [34] R. G. Calflisch, Y. G. Chen, A. N. Berker, J. M. Deutch, *Phys. Rev. A.*, **30**, 2562, 1984.
- [35] R. Alben, *J. Chem. Phys.*, **59**, 4299, 1973.
- [36] A. Stroobants and H. N. Lekkerkerk, *J. Phys. Chem.*, **88**, 3669, 1984.
- [37] Y. Rabin, W. E. McMullen, W. M. Gelbart, *Molec. Cryst. Liq. Cryst.*, **89**, 67, 1982.
- [38] D. E. Maitre and S. Ghodbane, *J. Phys. Chem.*, **91**, 6403, 1987.
- [39] P. Palfy-Muhoray, J. J. de Bruyn, D. A. Dunmur, *Molec. Cryst. Liq. Cryst.*, **127**, 301, 1985.
- [40] S. R. Sharma, P. Palfy-Muhoray, B. Bergersen, D. A. Dunmur, *Phys. Rev. A*, **32**, 3752, 1985.
- [41] P. Palfy-Muhoray and G. L. Hoatson, *Phys. Rev. A*, **44**, 5052, 1991.
- [42] W. H. de Jeu, *Physical Properties of Liquid Crystals*, (Gordon and Breach Science Publishers, London, 1980).
- [43] M. P. Fontana, *Physics of Liquid Crystalline Materials*, edited by I. C. Khoo and F. Simoni, (Gordon and Breach Science Publishers, London, 1980), Chap. 5.
- [44] M. P. Fontana, B. Rosi, N. Kirov, I. Dozov, *Phys. Rev. A.*, **33**, 4132, 1986.
- [45] I. Dozov, N. Kirov, M. P. Fontana, M. Mantredi, B. Rosi, R. Cywinski, *Liq. Cryst.*, **4**, 241, 1989.
- [46] A. Arcioni, F. Bertinelli, R. Tarroni and C. Zannoni, *Mol. Phys.*, **61**, 1161, 1987.
- [47] K. Brezinsky and B. J. Bulkin, in *Liquid Crystals and Ordered Fluids*, edited by J. F. Johnson and R. S. Porter, (Plenum Press, N.Y., 1978), Vol. 3, pp. 355-370.
- [48] A. J. Dianoux, F. Volino, H. Hervet, *Mol. Phys.*, **30**, 1181, 1975.
- [49] B. Rosi, *Physics of Liquid Crystalline Materials*, edited by I. C. Khoo and F. Simoni, (Gordon and Breach Science Publishers, London, 1980), Chap. 2.
-

- [50] D. Leporini, *Physics of Liquid Crystalline Materials*, edited by I. C. Khoo and F. Simoni, (Gordon and Breach Science Publishers, London, 1980), Chap. 7.
- [51] C. F. Polnaszek and J. H. Freed, *The Journal of Phys. Chem.*, **79**, 2283, 1975.
- [52] C. F. Polnaszek, G. V. Bruno and J. H. Freed, *J. Chem. Phys.*, **58**, 3185, 1973.
- [53] G. P. Drobney, in *NMR of Liquid Crystal Phases*, edited by J. W. Emsley, (D. Reidel Publishing Co., Dordrecht, Germany, 1985), pp. 289-314.
- [54] B. M. Fung, *J. Magn. Reson.*, **86**, 160, 1990.
- [55] *The CRC Handbook of Chemistry and Physics*, edited by D. R. Linde, 73<sup>rd</sup> edition, (CRC Press, Inc., Boca Raton, Florida, 1992).
- [56] J. W. Doane, in *Magnetic Resonance of Phase Transitions*, edited by F. J. Owens, C.P. Poole, Jr., H. A. Farach, (Academic Press, New York, 1979), Chap. 4.
- [57] G. B. Wu, B. Ziennicka, J. W. Doane, *J. Chem. Phys.*, **88**, 1373, 1988.
- [58] G. L. Hoatson and J. M. Goetz, *J. Chem. Phys.*, **94**, 3885, 1991.
- [59] G. L. Hoatson, *J. Magn. Reson.*, **94**, 152, 1991.
- [60] G. L. Hoatson, T. Y. Tse, R. L. Vold, *J. Magn. Reson.*, **98**, 1992.
- [61] J. M. Goetz, G. L. Hoatson, R. L. Vold, *J. Chem. Phys.*, **97**, 1306, 1992.
- [62] D. M. Burns and J. Iball, *Proc. R. Soc. London Ser. A*, **227**, 200, 1958.
- [63] J. M. Goetz and G. L. Hoatson, submitted to *Liq. Cryst.*, Feb. 1993.
- [64] A. G. Redfield, *Adv. Magn. Reson.*, **1**, 1, 1965.
- [65] R. R. Vold and R. L. Vold, *J. Chem. Phys.*, **88**, 1443, 1988.
- [66] G. L. Hoatson, J. M. Goetz, P. Palfy-Muhoray, G. P. Crawford and J.W. Doane, *Mol. Cryst. Liq. Cryst.*, **203**, 45, 1991.
- [67] *Nuclear Magnetic Resonance of Liquid Crystals*, edited by J. W. Emsley, (D. Reidel Publishing Co., Dordrecht, Germany, 1983).

- [68] *Physics of Liquid Crystalline Materials*, edited by I. C. Khoo and F. Simoni, (Gordon and Breach Science Publishers, Philadelphia, 1988).
- [69] *The Molecular Physics of Liquid Crystals*, edited by G. R. Luckhurst and G. W. Gray, (Academic Press, London, 1979).
- [70] *CRC Handbook of Chemistry and Physics, 69<sup>th</sup> edition*, (CRC Press, Boca Raton, Florida, 1988), page E-80.
- [71] C. P. Slichter, *Principles of Magnetic Resonance, 3rd edition*, (Springer-Verlag, Berlin, Germany, 1990), chapter 10.
- [72] M. Mehring, *Principles of High Resolution NMR in Solids*, (Springer-Verlag, Berlin, Germany, 1983), chapter 2.
- [73] L. Schiff, *Quantum Mechanics*, (McGraw-Hill Book Co., New York, 1968), chapter 7.
- [74] C. P. Slichter, *Principles of Magnetic Resonance, 3rd edition*, (Springer-Verlag, Berlin, Germany, 1990), chapter 2.
- [75] J. H. Davis, K. R. Jeffrey, M. Bloom, M. I. Valic and T. P. Higgs, *Chem. Phys. Lett.*, **42**, 390, 1976.
- [76] C. A. Veracini in *Nuclear Magnetic Resonance of Liquid Crystals*, edited by J. W. Emsley, (D. Reidel Publishing Co., Dordrecht, Germany, 1985).
- [77] D. M. Burns and J. Iball, *Proc. R. Soc. London, Ser. A*, **227**, 200, 1958.
- [78] J. W. Doane in *Magnetic Resonance of Phase Transitions*, edited by F. J. Owens, C. P. Poole Jr. and H. A. Farach, (Academic Press, New York, 1979).
- [79] B. Ziemnicka and J. W. Doane, *Mol. Cryst. Liq. Cryst.*, **150**, 361, 1987.
- [80] B. G. Wu, B. Ziemnicka and J. W. Doane, *J. Chem. Phys.*, **88**, 1373, 1988.
- [81] H. Vieth, private communication with A. Baugher at College of William and Mary.
- [82] P. Palffy-Muhoray, D. A. Dunmur, W. H. Miller and D. A. Balzarini in *Liquid Crystals and Ordered Fluids*, edited by A. C. Griffin and J. F. Johnson, (Plenum Press, New York, 1984).
-

- [83] P. Palffy-Muhoray, J. R. deBruyn and D. A. Dunmur, *Mol. Cryst. Liq. Cryst.*, **127**, 301, 1985.
  - [84] G. S. Bates, E.E. Burnell, G. L. Hoatson, P. Palffy-Muhoray and A. Weaver, *Chem. Phys. Lett.*, **134**, 161, 1987.
  - [85] G. S. Bates, P. A. Beckman, E. E. Burnell, G. L. Hoatson and P. Palffy-Muhoray, *Mol. Phys.*, **57**, 351, 1986.
  - [86] G. L. Hoatson, A. L. Bailey, A. J. Van der Est, G. S. Bates and E. E. Burnell, *Liq. Cryst.*, **3**, 347, 1988.
  - [87] B. Bergersen, P. Palffy-Muhoray and D. A. Dunmur, *Liq. Cryst.*, **3**, 347, 1988.
  - [88] J. W. Emsley, G. R. Luckhurst and S. Sachdev, *Liq. Cryst.*, **5**, 953, 1989.
  - [89] Y. Galerne, *Mol. Cryst. Liq. Cryst.*, **165**, 1988, 131, and references 8-14 therein.
  - [90] N. W. Ashcroft and N. D. Mermin, *Solid State Physics*, (W. B. Saunders Company, Philadelphia, Pa., 1976)
  - [91] B. M. Mulder, *Liq. Cryst.*, **1**, 539, 1986.
  - [92] B. J. Frisken, B. Bergersen and P. Palffy-Muhoray, *Mol. Cryst. Liq. Cryst.*, **148**, 45, 1987.
  - [93] P. Palffy-Muhoray, J. R. de Bruyn and D. A. Dunmur, *Mol. Cryst. Liq. Cryst.*, **127**, 301, 1985.
  - [94] G. R. Luckhurst in, *The Molecular Physics of Liquid Crystals*, edited by G. R. Luckhurst and G. W. Gray, (Academic Press, London, 1979).
  - [95] W. H. Press, B. P. Flannery, S. A. Teukolsky and W. T. Vetterling, *Numerical Recipes*, (Cambridge University Press, London, 1986).
  - [96] M. Abramowitz and I. A. Stegun, *Handbook of Mathematical Functions*, (Dover Publications, INC., 1965).
  - [97] S. Wolfram, 1991, *Mathematica*, (Addison-Wesley Publishing Co., New York, 1991).
-

- [98] P. Palffy-Muhoray, J. J. de Bruyn and D. A. Dunmur, *Mol. Cryst. Liq. Cryst.*, **127**, 301, 1985.
- [99] B. Bergersen, P. Palffy-Muhoray and D. A. Dunmur, *Liquid Crystals*, **3**, 347, 1988.
- [100] C. Kittel and H. Kroemer, *Thermal Physics*, (W.H. Freeman and Company, New York, 1980).
- [101] R. Alben, *Phys. Rev. Lett.*, **30**, 778, 1973.
- [102] M. J. Freiser, *Mol. Cryst. Liq. Cryst.*, **14**, 165, 1971.
- [103] B. Mulder, T. W. Ruijgrok, 1982, *Physica*, **113A**, 145, 1982.
- [104] C. Shih and R. Alben, *J. Chem. Phys.*, **57**, 3055, 1971.
- [105] G. R. Luckhurst and S. Romano, *Mol. Phys.*, **40**, 129, 1980.
- [106] R. G. Caflisch, Y. G. Chen, A. N. Berker and J. M. Deutch, *Phys. Rev. A*, **30**, 2562, 1984.
- [107] M. P. Taylor and J. Hertzfeld, *Phys. Rev. A*, **44**, 3742, 1991.
- [108] M. Allen, *Liquid Crystals*, **8**, 499, 1990.
- [109] S. Chandrasekhar, *Mol. Cryst. Liq. Cryst.*, **124**, 1, 1985..
- [110] K. Praefcke, B. Kohne, B. Gündogan, D. Singer, D. Demus, S. Diele, G. Pelzl and U. Bakowsky, *Mol. Cryst. Liq. Cryst.*, **198**, 393, 1991.
- [111] S. R. Sharma, P. Palffy-Muhoray, B. Bergersen and D. A. Dunmur, *Phys. Rev. A*, **32**, 3752, 1985.
- [112] P. Palffy-Muhoray, D. A. Dunmur, W. H. Miller and D. A. Balzarini in *Liquid Crystals and Ordered Fluids*, edited by A. C. Griffin and J. F. Johnson, (Plenum Press, N. Y., 1982).
- [113] J. Mathête, L. Liébert, A. M. Levelut and Y. Galerne, *Compte R. Ac. Sciences*, **303**, 1073, 1986.
- [114] S. Chandrasekhar, B. R. Ratna, B. K. Sadashiva and V. N. Raja, *Mol. Cryst. Liq. Cryst.*, **165**, 123, 1988.
-



- [115] K. Praefke, B. Kohne, B. Gündogan, D. Demus, S. Diele and G. Pelzi, *Mol. Cryst. Liq. Cryst. Lett.*, **7**, 27, 1990.
- [116] S. M. Fan, I. D. Fletcher, B. Gundogan, D. Demus, S. Diele, G. R. Luckhurst and K. Praefke, *Chem. Phys. Lett.*, **204**, 517, 1993.
- [117] A. Abragam, *The Principles of Nuclear Magnetism*, (Oxford University Press, Oxford, England, 1961), chapter 8.
- [118] R. L. Vold and R. R. Vold, *Israel J. Chem.*, **23**, 315, 1983.
- [119] R. R. Vold in *Nuclear Magnetic Resonance of Liquid Crystals*, edited by J. W. Emsley, (Reidel Publishing Co., Dordrecht, Germany, 1985).
- [120] M. S. Greenfield, Ph. D. Dissertation, University of California, San Diego, 1987.
- [121] J. Jeener and P. Broekaert, *Phys. Rev.*, **157**, 232, 1967.
- [122] R. L. Vold, W. H. Dickerson and R. L. Vold, *J. Magn. Reson.*, **43**, 213, 1981.
- [123] D. J. Sminovich and R. G. Griffin, *J. Magn. Reson.*, **62**, 99, 1985.
- [124] R. R. Vold and R. L. Vold, *Advances in Magnetic and Optical Resonance*, **16**, 85, 1991.
- [125] R. L. Vold, R. R. Vold, R. Poupko, and G. Bodenhausen, *J. Magn. Reson.*, **38**, 141, 1980.
- [126] D. Jaffe, R. L. Vold, and R. R. Vold, *J. Magn. Reson.*, **46**, 496, 1982.
- [127] H. J. Heaton, R. R. Vold, and R. L. Vold, *J. Magn. Reson.*, **77**, 572, 1988.
- [128] D. Jaffe, Ph.D. Dissertation, University of California, San Diego, 1982.
- [129] S. Wimperis, *J. Magn. Reson.*, **86**, 46, 1990.
- [130] S. Wimperis and G. Bodenhausen, *J. Magn. Reson.*, **69**, 264, 1986.
- [131] S. Wimperis and G. Bodenhausen, *Chem. Phys. Lett.*, **132**, 194, 1986.
- [132] J. R. Garbow, D. P. Wietekamp, A. Pines, *Chem. Phys. Lett.*, **93**, 504, 1982.
-

- [133] T. M. Barbara, R. Tyco, and D. P. Wietekamp, *J. Magn. Reson.*, **62**, 54, 1985.
- [132] L. I. Schiff, *Quantum Mechanics*, 3<sup>rd</sup> edition, (McGraw-Hill Book Co., New York, 1955), chapter 8.
- [133] C. P. Slichter, *Principles of Magnetic Resonance*, 3<sup>rd</sup> edition, (Springer-Verlag, Berlin, 1989).
- [134] R. R. Ernst, G. Bodenhausen, and A. Wokaun, *Principles of Nuclear Magnetic Resonance in One and Two Dimensions*, (Oxford University Press, Oxford, England, 1987).
- [135] A. G. Redfield, *IBM Journal of Research Developements*, **1**, 19, 1957.
- [136] A. G. Redfield, *Adv. Magn. Reson.*, **1**, 1, 1965.
- [137] R. Lenk, *Brownian Motion and Spin Relaxation*, (Elsevier Scientific Publishing, Amsterdam, 1977).
- [138] P. L. Nordio and U. Segre in *The Molecular Physics of Liquid Crystals*, edited by G. R. Luckhurst and G. W. Gray, Academic Press, London, 1979), chapters 16, 18, and 19.
- [139] W. T. Huntress Jr., *Adv. Magn. Reson.*, **4**, 1, 1970.
- [140] S. H. Glarum and J. H. Marshall, *J. Chem. Phys.*, **46**, 55, 1967.
- [141] R. D. Orwoll, C. G. Wade, and B. M. Fung, *J. Chem. Phys.*, **63**, 986, 1975.
- [142] F. Perrin, *J. Phys. Rad.*, **5**, 33, 1934.
- [143] L. B. Favro, *Phys. Rev.*, **119**, 119, 1960.
- [144] S. Chandrasekhar, *Rev. Mod. Phys.*, **15**, 1, 1943.
- [145] R. Tarroni and C. Zannoni, *J. Chem. Phys.*, **95**, 4550, 1991.
- [146] M. E. Rose, *Elementary Theory of Angular Momentum*, (Wiley Publishing Co., New York, 1957), chapter 4.
- [147] M. V. Smoluchowski, *Ann. der Physik*, **48**, 1103, 1916.
- [148] J. H. Freed, *J. Chem. Phys.*, **66**, 4183, 1977.
-

- [149] C. F. Polnaszek, G. V. Bruno, and J. H. Freed, *J. Chem. Phys.*, **58**, 31, 1973.
  - [150] C. F. Polnaszek and J. H. Freed, *J. Phys. Chem.*, **79**, 2283, 1975.
  - [151] W. J. Lin and J. H. Freed, *J. Phys. Chem.*, **83**, 379, 1979.
  - [152] R. A. Torchia and A. Szabo, *J. Magn. Reson.*, **49**, 107, 1982.
  - [153] R. J. Wittebort and A. Szabo, *J. Chem. Phys.*, **69**, 1722, 1978.
  - [154] R. E. London and J. Avitabile, *J. Am. Chem. Soc.*, **99**, 7765, 1977.
  - [155] L. S. Selwyn, R. R. Vold, and R. L. Vold, *Mol. Phys.* **55**, 287, 1985.
  - [156] R. Y. Dong, *J. Chem. Phys.* **76**, 5659, 1982.
  - [157] J. W. Emsley, K. Hamilton, G. R. Luckhurst, F. Sundholm, B. A. Timini, and D. L. Turner, *Chem. Phys. Lett.* **104**, 136, 1984.
  - [158] L. Plomp, A. C. Lohman, and J. Bulthuis, *J. Chem. Phys.* **84**, 6591, 1986.
  - [159] J. Voigt, and J. P. Jacobsen, *J. Chem. Phys.* **78**, 1693, 1983.
  - [160] Product of Hare Research, Inc. Bellevue, WA.
  - [161] P.R. Bevington, *Data Reduction and Error Analysis for the Physical Sciences*, (McGraw Hill, New York, 1969).
  - [162] W.E. Deming, *Statistical Adjustment of Data*, (Dover Publications, New York, 1969).
  - [163] W. H. Press, B. P. Flannery, S. A. Teukolsky, and W. T. Vetterling, *Numerical Recipes*, (Cambridge University Press, London, 1979).
  - [164] G. L. Hoatson and R. L. Vold, unpublished data.
  - [165] P. Pincus, *Solid State Commun.*, **7**, 4153, 1969.
  - [166] J. W. Doane, D. L. Johnson, *Chem. Phys. Lett.* **6**, 291, 1970.
  - [167] L.S. Selwyn, Ph.D. Dissertation, University of California, San Diego, 1984.
  - [168] F. Noack, *Prog. Nucl. Magn. Reson. Spectrosc.* **18**, 171, 1986.
-

- [169] E. Rommel, F. Noack, P.Meier, and G. Kothe, *J. Phys. Chem.* **92**, 2981, 1988.
  - [170] R. Kollner, K. H. Schweikert and F. Noack, *Liquid Crystals*, **13**, 483, 1993.
  - [171] R. L. Vold, and R.R. Vold, *J. Chem. Phys.* **71**, 1508, 1979.
  - [172] H. A. Lopes Cardozo, J. Bulhuis, and C. MacLean, *J. Magn. Reson.* **33**, 27, 1979.
  - [173] B.J. Gertner and K. Lindenberg, *J. Chem. Phys.*, in press.
  - [174] B.J. Gertner, D.A. Ikenberry, K. Lindenberg, R.L. Vold and R.R. Vold, submitted.
  - [175] R.Y. Dong, and G.M. Richards, *Mol. Crys. Liq. Cryst.* **141**, 335, 1987.
  - [176] T.M. Barbara, R.R. Vold, and R.L. Vold, *J. Chem. Phys.* **79**, 6338, 1983.
  - [177] H. W. Spiess, *Colloid and Polymer Science*, **261**, 193, 1983.
  - [178] S. H. Glarum and J. H. Marshall, *J. Chem. Phys.*, **46**, 55, 1967.
  - [179] G. R. Luckhurst and C. Zannoni, *J. of Mag. Reson.*, **23**, 153, 1976.
  - [180] J. P. Jacobsen, H. K. Bildsoe, and K. Schaumburg, *J. of Mag. Reson.*, **23**, 275, 1976.
  - [181] C. G. Wade, *Ann. Rev. Phys. Chem.*, **28**, 47, 1977.
  - [182] R. Y. Dong, *Israel J. Chem.*, **23**, 370, 1983.
  - [183] J. W. Emsley, J. C. Lindon, and G. R. Luckhurst, *Mol. Phys.*, **32**, 1187, 1976.
-

**VITA****Jon Michael Goetz**

Born in Madison, Wisconsin on July 26, 1964 to Dana and Gary Goetz. Graduated from Bradford High School in Kenosha, Wisconsin in 1982. Earned a B.S. in Physics from the University of Wisconsin at Madison in 1986. Was awarded a M.S. in Physics from the College of William and Mary in Williamsburg, Virginia in 1988, and a Ph.D. in Physics from the same institution in 1993. Has accepted a postdoctoral position at Washington University in St. Louis.